

# **Concrete Filled Fibre Reinforced Polymer Tubes for Structural Members**

A Project Report  
Presented to  
the Department of Civil Engineering  
Faculty of Engineering  
University of Manitoba

In Partial Fulfillment  
of the Requirements for the Degree  
Master of Science in Civil Engineering (M.Sc.(C.E.))

**THE UNIVERSITY OF MANITOBA**  
**FACULTY OF GRADUATE STUDIES**  
\*\*\*\*\*  
**COPYRIGHT PERMISSION**

**Concrete Filled Fibre Reinforced Polymer Tubes for Structural Members**

**BY**

**Bartlomiej Flisak**

**A Thesis/Practicum submitted to the Faculty of Graduate Studies of The University of  
Manitoba in partial fulfillment of the requirement of the degree**

**Of**

**MASTER OF SCIENCE**

**Bartlomiej Flisak © 2004**

**Permission has been granted to the Library of the University of Manitoba to lend or sell copies of this thesis/practicum, to the National Library of Canada to microfilm this thesis and to lend or sell copies of the film, and to University Microfilms Inc. to publish an abstract of this thesis/practicum.**

**This reproduction or copy of this thesis has been made available by authority of the copyright owner solely for the purpose of private study and research, and may only be reproduced and copied as permitted by copyright laws or with express written authorization from the copyright owner.**

A significant demand exists for stronger, more durable structural members for applications like marine piles and highway structures where aggressive chemicals quickly deteriorate traditional reinforced concrete and steel members. Concrete filled fibre reinforced polymer (FRP) tubes are a promising technology for such applications because they are strong, highly resistant to aggressive chemicals, and have service lives far longer than traditional materials.

This project investigates the structural behaviour of cylindrical concrete filled FRP tube members. An experimental program was performed to study the behaviour of two types of members subjected to axial loads, bending moments, and combinations of axial loads and bending moments. An analytical model was developed to predict the behaviour, and verified with the experimental results. The model incorporates calculations of FRP laminate effective elastic properties, evaluation of a variable confinement concrete stress-strain relationship depending on axial load eccentricity, determination of cross-section force and moment equilibrium using a numerical integration approach, and calculations for member deflection.

Further research on concrete filled FRP tube members will lead to the development of a wide knowledge base upon which design guidelines for the technology will be developed. Concrete filled FRP tube members will be a viable alternative to conventional timber, reinforced concrete, and steel members in the infrastructure of the future.

## **Table of Contents**

---

<b>Title</b>	<b>1</b>
<b>Abstract</b>	<b>2</b>
<b>Table of Contents</b>	<b>3</b>
<b>List of Figures</b>	<b>7</b>
<b>List of Tables</b>	<b>18</b>
<b>List of Symbols</b>	<b>19</b>

### **Chapter I: Introduction**

1.1 General	25
1.2 Objective and Scope	26
1.3 Acknowledgments	28

### **Chapter II: Background and Related Research**

2.1 Introduction	30
2.2 Fibre Reinforced Polymers	32
2.2.1 Composition of Fibre Reinforced Polymers	32
2.2.1.1 <i>Polymer Matrices</i>	32
2.2.1.1.1 Epoxy Polymers	34
2.2.1.1.2 Polyester Polymers	34
2.2.1.2 <i>Embedded Fibres</i>	35
2.2.2 Fibre Reinforced Polymer Fabrication Processes	37
2.2.2.1 <i>Filament Winding</i>	39
2.2.2.1.1 Filament Winding Process	40
2.2.2.1.2 Advantages of Filament Winding	42
2.2.2.1.3 Quality Control During Filament Winding	43
2.2.3 Fibre Reinforced Polymer Laminates	44
2.2.4 Advantages of Fibre Reinforced Polymers	45
2.3 Research Related to Hybrid FRP/Concrete Members	48
2.3.1 Performance of Concrete Filled Steel Tubular Members	48
2.3.1.1 <i>Concrete Filled Steel Tubular Columns</i>	50



2.3.1.2 Concrete Filled Steel Tubular Beams and Beam-columns	54
2.3.2 Performance of Fibre Reinforced Polymer Encased Concrete Members	57
2.3.2.1 Fibre Reinforced Polymer Wrapped Concrete Members	59
2.3.2.2 Axially Loaded Concrete Filled Fibre Reinforced Polymer Members	61
2.3.2.3 Concrete Filled Fibre Reinforced Polymer Beams and Beam-columns	64
2.3.2.4 Other Hybrid Fibre Reinforced Polymer/Concrete Members	67
2.3.3 Analytical Modelling of FRP Confined Concrete Behaviour	69

### **Chapter III: Experimental Program**

<b>3.1 Introduction</b>	<b>75</b>
<b>3.2 Materials Used to Fabricate the Test Specimens</b>	<b>76</b>
3.2.1 Fibre Reinforced Polymer Tubes	76
3.2.1.1 Effective Elastic Properties of FRP Laminates	78
3.2.2 Concrete Core	79
<b>3.3 Fabrication of Test Specimens</b>	<b>80</b>
<b>3.4 Experimental Phase I – Beam Tests</b>	<b>81</b>
3.4.1 Beam Test Specimens	81
3.4.2 Instrumentation of Beam Specimens	82
3.4.3 Beam Test Setup	82
<b>3.5 Experimental Phase II – Beam-column Tests</b>	<b>84</b>
3.5.1 Beam-column Test Specimens	84
3.5.2 Fabrication of Beam-column Test Specimens	85
3.5.3 Instrumentation of Beam-column Specimens	86
3.5.4 Beam-column Test Setup	87
<b>3.6 Experimental Phase III – Pure Axial Load Tests</b>	<b>88</b>

### **Chapter IV: Experimental Results and Discussion**

<b>4.1 Introduction</b>	<b>103</b>
<b>4.2 Material Properties</b>	<b>103</b>
4.2.1 Effective Elastic Properties of Fibre Reinforced Polymer Shells	103
4.2.2 Unconfined Concrete Compressive Strengths	105

4.2.3 Specimen Classification Based on Reinforcement Ratio	105
<b>4.3 Experimental Phase I: Flexural Tests</b>	<b>107</b>
4.3.1 Strengths and Failure Modes	108
4.3.2 Deflections and Concrete Cracking	110
4.3.3 Axial Strains and Neutral Axis Depths	113
4.3.4 Circumferential Strains and Concrete Confinement	115
<b>4.4 Experimental Phase II: Combined Axial Load and Bending Moment Tests</b>	<b>117</b>
4.4.1 Specimen BC-P-e10	117
4.4.2 Specimen BC-P-e30	121
4.4.3 Specimen BC-P-e100	124
4.4.4 Specimen BC-P-e200	126
4.4.5 Specimen BC-P-e300	127
4.4.6 Specimen BC-E-e30	129
4.4.7 Specimen BC-E-e100	131
4.4.8 Specimen BC-E-e200	133
4.4.9 Specimen BC-E-e300	135
<b>4.5 Experimental Phase III: Axial Compression Tests</b>	<b>137</b>
 <b>Chapter V: Analytical Model and Verification With Experimental Results</b>	
<b>5.1 Introduction</b>	<b>181</b>
<b>5.2 Analytical Model</b>	<b>183</b>
5.2.1 Overview	183
5.2.2 Modelling FRP Laminate and Concrete Material Properties	183
5.2.2.1 <i>Laminate Stiffness Model</i>	183
5.2.2.2 <i>Modelling Lamina and Overall Laminate Strengths</i>	193
5.2.2.2.1 Modelling Lamina and Overall Laminate Uniaxial Tensile Strengths	197
5.2.2.2.2 Modelling Lamina and Overall Laminate Biaxial Strengths	199
5.2.2.3 <i>Modelling Concrete Stress-strain Response</i>	201
5.2.2.3.1 Unconfined Concrete Stress-strain Model	201
5.2.2.3.2 Maximum Confinement Concrete Stress-strain Model	203

5.2.2.3.3 Proposed Intermediate Confinement Model	209
5.2.3 Modelling Concrete Filled FRP Tube Member Response to Applied Loads	212
5.2.3.1 Analysis Geometry	213
5.2.3.2 Cross-section Strain Distribution and Stress Calculations	215
5.2.3.3 Cross-section Equilibrium Analysis	219
5.2.3.3.1 Bending Moment Only Load Case	221
5.2.3.3.2 Combined Bending Moment and Axial Load Case	221
5.2.3.4 Calculation of Member Deflection	223
5.2.3.5 Modelling Member Failure	227
5.2.3.5.1 Laminate Failure in Pure Axial Load Cases	227
5.2.3.5.2 Laminate Failure in Load Cases with Bending Moment	228
5.2.4 Applying the Complete Analytical Model	230
5.2.4.1 Modelling a Pure Axial Load Case	231
5.2.4.2 Modelling a Pure Bending Moment Load Case	232
5.2.4.3 Modelling a Load Case with Bending Moment and Axial Load	235
<b>5.3 Verification of the Analytical Model</b>	<b>237</b>
5.3.1 Modelled Beam Specimen Tests	237
5.3.2 Modelled Axial Load Specimens	240
5.3.3 Modelled Combined Bending Moment and Axial Load Specimens	241
5.3.3.1 Specimens BC-P-e10 and BC-P-e30	241
5.3.3.2 Specimen BC-P-e100	242
5.3.3.3 Specimens BC-P-e200 and BC-P-e300	242
5.3.3.4 Specimens BC-E-e30 and BC-E-e100	243
5.3.3.5 Specimens BC-E-e200 and BC-E-e300	244
5.3.4 Comparing Behaviour Depending on Concrete Confinement Level	245
5.3.5 Interaction Diagrams	246
<b>5.4 Parametric Study</b>	<b>248</b>
 <b>Chapter VI: Conclusions and Recommendations</b>	 <b>293</b>
 <b>References</b>	 <b>299</b>

**Chapter I: Introduction**

<b>Figure 1.1:</b>	Concrete filled FRP tube members in marine piling applications.	29
--------------------	---	----

**Chapter II: Background and Related Research**

<b>Figure 2.1:</b>	Fibre reinforced polymer retrofitting and rehabilitation applications.	72
<b>Figure 2.2:</b>	Glass fibre bi-directional woven mats and unidirectional spooled roving.	72
<b>Figure 2.3:</b>	The FRP filament winding process.	73
<b>Figure 2.4:</b>	Orientation of lamina principal material coordinate axes.	74
<b>Figure 2.5:</b>	Orientation of laminate global coordinate axes with respect to lamina principal material axes.	74

**Chapter III: Experimental Program**

<b>Figure 3.1:</b>	The two types of FRP shells used to fabricate the test specimens.	93
<b>Figure 3.2:</b>	Longitudinal tension coupon.	93
<b>Figure 3.3:</b>	Typical longitudinal tension coupons after failure.	94
<b>Figure 3.4:</b>	Longitudinal compression coupon instrumentation.	94
<b>Figure 3.5:</b>	Local bearing failures at the top of the compression coupons.	95
<b>Figure 3.6:</b>	Concrete casting setup and procedure used to fabricate test specimens for the experimental program.	95
<b>Figure 3.7:</b>	Instrumentation for beam specimen tests.	96
<b>Figure 3.8:</b>	Roller support used in the beam specimen test setup.	97
<b>Figure 3.9:</b>	Beam specimen test setup.	98

<b>Figure 3.10:</b>	Cutting beam-column specimens from full-length members.	98
<b>Figure 3.11:</b>	Instrumentation for beam-column specimen tests.	99
<b>Figure 3.12:</b>	Configuration and dimensions of eccentric loading caps used in beam-column tests.	100
<b>Figure 3.13:</b>	Eccentric loading caps used in beam-column tests.	100
<b>Figure 3.14:</b>	Beam-column specimen test setup.	101
<b>Figure 3.15:</b>	Pure axial load specimen test setup and instrumentation.	102

#### **Chapter IV: Experimental Results and Discussion**

<b>Figure 4.1:</b>	Axial tensile properties of the FRP shells used in the experimental program.	143
<b>Figure 4.2:</b>	Axial tensile Poisson's ratios of the FRP shells used in the experimental program.	144
<b>Figure 4.3:</b>	Axial compressive properties of the FRP shells used in the experimental program.	145
<b>Figure 4.4:</b>	Axial compressive Poisson's ratios of the FRP shells used in the experimental program.	146
<b>Figure 4.5:</b>	Typical tensile failure of beam specimens BM-E-1 and BM-E-2.	146
<b>Figure 4.6:</b>	Specimen BM-P-1 and BM-P-2 failures by rupture of the FRP shell in tension.	147
<b>Figure 4.7:</b>	Load-deflection behaviours of the beam specimens.	148
<b>Figure 4.8:</b>	Moment-deflection behaviours of the beam specimens.	149
<b>Figure 4.9:</b>	Load-slip behaviours of beam specimens BM-E-1 and BM-P-1.	150
<b>Figure 4.10:</b>	Specimens with FRP shells removed to demonstrate the difference in shell interior surface profiles.	150

<b>Figure 4.11:</b>	FRP shell removed from half of specimen BM-P-2 to show the crack pattern in the concrete core.	151
<b>Figure 4.12:</b>	Moment-axial strain relationships of beams BM-E-1 and BM-E-2.	151
<b>Figure 4.13:</b>	Moment-axial strain behaviours of beams BM-P-1 and BM-P-2.	152
<b>Figure 4.14:</b>	Neutral axis depth-moment relationships of specimens BM-E-1 and BM-E-2, calculated from axial strains on the surface of the beams.	152
<b>Figure 4.15:</b>	Neutral axis depth-moment relationships of specimens BM-P-1 and BM-P-2, calculated from axial strains on the surface of the beams.	153
<b>Figure 4.16:</b>	Beam specimen concrete core appearance after failure, enabling visual determination of the neutral axis depth.	153
<b>Figure 4.17:</b>	Axial strain distributions across section depth at mid-span of specimen BM-E-1.	154
<b>Figure 4.18:</b>	Axial strain distributions across section depth at mid-span of specimen BM-P-1.	154
<b>Figure 4.19:</b>	Axial strain distributions across section depth at mid-span of specimen BM-E-2.	155
<b>Figure 4.20:</b>	Axial strain distributions across section depth at mid-span of specimen BM-P-2.	155
<b>Figure 4.21:</b>	Circumferential-axial strain behaviour of specimen BM-E-1.	156
<b>Figure 4.22:</b>	Circumferential-axial strain behaviour of specimen BM-P-1.	156
<b>Figure 4.23:</b>	Circumferential-axial strain behaviour of specimen BM-E-2.	157
<b>Figure 4.24:</b>	Circumferential-axial strain behaviour of specimen BM-P-2.	157

<b>Figure 4.25:</b>	Axial load-deflection behaviours of beam-column specimens BC-P-e10, BC-P-e30, BC-P-e100, BC-P-e200, and BC-P-e300.	158
<b>Figure 4.26:</b>	Moment-deflection behaviours of beam-column specimens BC-P-e10 and BC-P-e30.	158
<b>Figure 4.27:</b>	Initial delamination and buckling of FRP shell laminas in the maximum compression zone of specimen BC-P-e10.	159
<b>Figure 4.28:</b>	Axial load-moment behaviours of beam-columns BC-P-e10, BC-P-e30, and BC-P-e100.	159
<b>Figure 4.29:</b>	Moment-axial strain behaviours of beam-columns BC-P-e10 and BC-P-e30.	160
<b>Figure 4.30:</b>	Neutral axis depth-moment behaviours of beam-columns BC-P-e10, BC-P-e30, BC-P-e100, BC-P-e200, and BC-P-e300.	160
<b>Figure 4.31:</b>	Overall failure of specimen BC-P-e10 by propagation of delamination and buckling, splitting, and crushing of shell laminas.	161
<b>Figure 4.32:</b>	Deformation of concrete core in the maximum compression region of specimen BC-P-e10.	161
<b>Figure 4.33:</b>	Circumferential-axial strain behaviour of beam-column specimen BC-P-e10.	162
<b>Figure 4.34:</b>	Failure of outer laminas of specimen BC-P-e30.	162
<b>Figure 4.35:</b>	Maximum compression face of specimen BC-P-e30 at failure.	163
<b>Figure 4.36:</b>	Circumferential-axial strain behaviour of beam-column specimen BC-P-e30.	163
<b>Figure 4.37:</b>	Moment-deflection behaviours of beam-column specimens BC-P-e100, BC-P-e200, and BC-P-e300.	164
<b>Figure 4.38:</b>	Failure region at the maximum compression face of specimen BC-P-e100.	164
<b>Figure 4.39:</b>	Moment-axial strain behaviours of beam-column specimens BC-P-e100, BC-P-e200, and BC-P-e300.	165

<b>Figure 4.40:</b>	Circumferential-axial strain behaviour of beam-column specimen BC-P-e100.	165
<b>Figure 4.41:</b>	Axial load-moment behaviours of beam-column specimens BC-P-e200 and BC-P-e300.	166
<b>Figure 4.42:</b>	Tension failure of specimen BC-P-e200.	166
<b>Figure 4.43:</b>	Circumferential-axial strain behaviour of beam-column specimen BC-P-e200.	167
<b>Figure 4.44:</b>	Tension failure of specimen BC-P-e300 near the top eccentric loading cap.	167
<b>Figure 4.45:</b>	Circumferential-axial strain behaviour of beam-column specimen BC-P-e300.	168
<b>Figure 4.46:</b>	Axial load-deflection behaviours of beam-column specimens BC-E-e30, BC-E-e100, BC-E-e200, and BC-E-e300.	168
<b>Figure 4.47:</b>	Moment-deflection behaviours of beam-column specimens BC-E-e30, BC-E-e100, BC-E-e200, and BC-E-e300.	169
<b>Figure 4.48:</b>	Axial load-moment behaviours of beam-columns specimens BC-E-e30 and BC-E-e100.	169
<b>Figure 4.49:</b>	Failure location on specimen BC-E-e30.	170
<b>Figure 4.50:</b>	FRP shell compression failure on specimen BC-E-e30.	170
<b>Figure 4.51:</b>	Moment-axial strain behaviours of beam-column specimens BC-E-e30 and BC-E-e100.	171
<b>Figure 4.52:</b>	Circumferential-axial strain behaviour of beam-column specimen BC-E-e30.	171
<b>Figure 4.53:</b>	Neutral axis depth-moment behaviours of beam-column specimens BC-E-e30, BC-E-e100, BC-E-e200, and BC-E-e300.	172
<b>Figure 4.54:</b>	Failure location on specimen BC-E-e100.	172
<b>Figure 4.55:</b>	FRP shell tension failure on specimen BC-E-e100.	173



<b>Figure 4.56:</b>	Compression side of specimen BC-E-e100 after failure.	173
<b>Figure 4.57:</b>	Circumferential-axial strain behaviour of beam-column specimen BC-E-e100.	174
<b>Figure 4.58:</b>	Circumferential-axial strain behaviour of beam-column specimen BC-E-e200.	174
<b>Figure 4.59:</b>	Moment-axial strain behaviours of beam-column specimens BC-E-e200 and BC-E-e300.	175
<b>Figure 4.60:</b>	Axial load-moment behaviours of beam-column specimens BC-E-e200 and BC-E-e300.	175
<b>Figure 4.61:</b>	FRP shell tension failure of specimen BC-E-e200.	176
<b>Figure 4.62:</b>	Circumferential-axial strain behaviour of beam-column specimen BC-E-e300.	176
<b>Figure 4.63:</b>	FRP shell tension failure of specimen BC-E-e300.	177
<b>Figure 4.64:</b>	Load-axial strain behaviour of the E-glass/epoxy shell pure axial load specimen.	177
<b>Figure 4.65:</b>	Circumferential-axial strain behaviour of the E-glass/epoxy shell pure axial load specimen.	178
<b>Figure 4.66:</b>	Crushing of FRP shell near the top of the E-glass/epoxy shell pure axial load specimen.	178
<b>Figure 4.67:</b>	Failure of the FRP shell near the bottom of the E-glass/epoxy shell pure axial load specimen.	179
<b>Figure 4.68:</b>	Load-axial strain behaviour of the E-glass/polyester shell pure axial load specimen.	179
<b>Figure 4.69:</b>	FRP shell rupture on the E-glass/polyester shell pure axial load specimen.	180
<b>Figure 4.70:</b>	Circumferential-axial strain behaviour of the E-glass/polyester shell pure axial load specimen.	180

**Chapter V: Analytical Model and Verification With Experimental Results**

<b>Figure 5.1:</b>	Laminate global coordinate axes with respect to concrete filled FRP tube member geometry.	256
<b>Figure 5.2:</b>	Laminate geometry for calculating the laminate stiffness matrix.	256
<b>Figure 5.3:</b>	Uniaxial tensile stress at the tension side of an FRP shell of a concrete filled FRP tube member subjected to bending moment.	257
<b>Figure 5.4:</b>	Uniaxial multilinear stress-strain relationships for a general FRP laminate with two laminas.	258
<b>Figure 5.5:</b>	Biaxial state of stress on an FRP shell of a concrete filled FRP tube member subjected to an axial load.	259
<b>Figure 5.6:</b>	Lamina and overall laminate biaxial strength envelopes.	259
<b>Figure 5.7:</b>	Unconfined concrete stress-strain curves established using Thornfeldt, Tomaszewicz, and Jensen's model.	260
<b>Figure 5.8:</b>	Determining confined concrete elastic modulus during application of Fam and Rizkalla's variable confinement model.	260
<b>Figure 5.9:</b>	Confined concrete stress-strain relationships for a range of confining pressures, determined using Fam and Rizkalla's variable confinement model.	261
<b>Figure 5.10:</b>	Concrete stress-strain relationships from the intermediate confinement model for a variety of axial load eccentricities.	262
<b>Figure 5.11:</b>	Cross-section equilibrium analysis geometry.	263
<b>Figure 5.12:</b>	Cross-section axial compressive and tensile strains and stresses due to a general combination of applied axial load and bending moment.	263
<b>Figure 5.13:</b>	Calculating the applied bending moment on a member subjected to an eccentric axial load.	264

<b>Figure 5.14:</b>	Numerical integration of the curvature diagram to calculate deflection of a member subjected to bending moment.	264
<b>Figure 5.15:</b>	Calculating the member curvature diagram for use in cross-section deflection calculations.	265
<b>Figure 5.16:</b>	Detecting lamina and overall laminate failures in the compression zone of concrete filled FRP tube members subjected to pure axial load, pure bending moment, or combined axial load and bending moment.	266
<b>Figure 5.17:</b>	Effect of level of confinement on FRP shell biaxial stress paths and biaxial stresses at lamina failure in the compression zone.	267
<b>Figure 5.18:</b>	Model predicted moment-deflection behaviour of beam specimen BM-E-1.	268
<b>Figure 5.19:</b>	Model predicted moment-deflection behaviour of beam specimen BM-E-2.	268
<b>Figure 5.20:</b>	Model predicted moment-deflection behaviour of beam specimen BM-P-1.	269
<b>Figure 5.21:</b>	Model predicted moment-deflection behaviour of beam specimen BM-P-2.	269
<b>Figure 5.22:</b>	Predicted moment-axial strain behaviour of beam specimen BM-E-1.	270
<b>Figure 5.23:</b>	Predicted moment-axial strain behaviour of beam specimen BM-E-2.	270
<b>Figure 5.24:</b>	Predicted moment-axial strain behaviour of beam specimen BM-P-1.	271
<b>Figure 5.25:</b>	Predicted moment-axial strain behaviour of beam specimen BM-P-2.	271
<b>Figure 5.26:</b>	Model predicted axial load-axial strain behaviour of E-glass/epoxy shell pure axial load specimen.	272
<b>Figure 5.27:</b>	Model predicted axial load-axial strain behaviour of E-glass/polyester shell pure axial load specimen.	272

<b>Figure 5.28:</b>	Predicted axial load-deflection behaviour of beam-column specimen BC-P-e10.	273
<b>Figure 5.29:</b>	Predicted axial load-deflection behaviour of beam-column specimen BC-P-e30.	273
<b>Figure 5.30:</b>	Predicted moment-axial strain behaviour of beam-column specimen BC-P-e10.	274
<b>Figure 5.31:</b>	Predicted moment-axial strain behaviour of beam-column specimen BC-P-e30.	274
<b>Figure 5.32:</b>	Predicted moment-axial strain behaviour of beam-column specimen BC-P-e100.	275
<b>Figure 5.33:</b>	Predicted axial load-deflection behaviour of beam-column specimen BC-P-e100.	275
<b>Figure 5.34:</b>	Predicted moment-deflection behaviour of beam-column specimen BC-P-e100.	276
<b>Figure 5.35:</b>	Predicted axial load-deflection behaviour of beam-column specimen BC-P-e200.	276
<b>Figure 5.36:</b>	Predicted moment-deflection behaviour of beam-column specimen BC-P-e200.	277
<b>Figure 5.37:</b>	Predicted moment-axial strain behaviour of beam-column specimen BC-P-e200.	277
<b>Figure 5.38:</b>	Predicted axial load-deflection behaviour of beam-column specimen BC-P-e300.	278
<b>Figure 5.39:</b>	Predicted moment-deflection behaviour of beam-column specimen BC-P-e300.	278
<b>Figure 5.40:</b>	Predicted moment-axial strain behaviour of beam-column specimen BC-P-e300.	279
<b>Figure 5.41:</b>	Predicted load-deflection behaviour of beam-column specimen BC-E-e30.	279
<b>Figure 5.42:</b>	Predicted moment-deflection behaviour of beam-column specimen BC-E-e30.	280

<b>Figure 5.43:</b>	Predicted moment-axial strain behaviour of beam-column specimen BC-E-e30.	280
<b>Figure 5.44:</b>	Predicted axial load-deflection behaviour of beam-column specimen BC-E-e100.	281
<b>Figure 5.45:</b>	Predicted moment-deflection behaviour of beam-column specimen BC-E-e100.	281
<b>Figure 5.46:</b>	Predicted moment-axial strain behaviour of beam-column specimen BC-E-e100.	282
<b>Figure 5.47:</b>	Predicted moment-axial strain behaviour of beam-column specimen BC-E-e200.	282
<b>Figure 5.48:</b>	Predicted moment-axial strain behaviour of beam-column specimen BC-E-e300.	283
<b>Figure 5.49:</b>	Predicted axial load-deflection behaviour of beam-column specimen BC-E-e200.	283
<b>Figure 5.50:</b>	Predicted moment-deflection behaviour of beam-column specimen BC-E-e200.	284
<b>Figure 5.51:</b>	Predicted axial load-deflection behaviour of beam-column specimen BC-E-e300.	284
<b>Figure 5.52:</b>	Predicted moment-deflection behaviour of beam-column specimen BC-E-e300.	285
<b>Figure 5.53:</b>	Predicted interaction diagrams of beam-column specimens, plotted against experimental results.	285
<b>Figure 5.54:</b>	Modelled interaction diagrams for 300-mm diameter, 1:1 laminate concrete filled FRP tubes with varying shell thicknesses and concrete strengths.	286
<b>Figure 5.55:</b>	Modelled interaction diagrams for 300-mm diameter, 1:9 laminate concrete filled FRP tubes with varying shell thicknesses and concrete strengths.	287
<b>Figure 5.56:</b>	Modelled interaction diagrams for 300-mm diameter, 9:1 laminate concrete filled FRP tubes with varying shell thicknesses and concrete strengths.	288

<b>Figure 5.57:</b>	Modelled interaction diagrams for 300-mm diameter, 1-mm thick concrete filled FRP tubes with varying laminates and concrete strengths.	289
<b>Figure 5.58:</b>	Modelled interaction diagrams for 300-mm diameter, 6-mm thick concrete filled FRP tubes with varying laminates and concrete strengths.	290
<b>Figure 5.59:</b>	Modelled interaction diagrams for 300-mm diameter, 10-mm thick concrete filled FRP tubes with varying laminates and concrete strengths.	291
<b>Figure 5.60:</b>	Full confinement concrete stress-strain relationships for 300-millimetre diameter, 1:1 laminate concrete filled FRP tubes with varying FRP tube wall thicknesses and concrete compressive strengths.	292
<b>Figure 5.61:</b>	Modelled interaction diagrams for 300-mm diameter, 1:1 laminate concrete filled FRP tubes with varying wall thicknesses and concrete strengths.	292

**Chapter III: Experimental Program**

<b>Table 3.1:</b>	Laminate structure and characteristics of E-glass/epoxy laminate tubes used in the experimental program.	90
<b>Table 3.2:</b>	Laminate structure and characteristics of E-glass/polyester laminate tubes used in the experimental program.	90
<b>Table 3.3:</b>	Beam specimens tested in Phase I of the experimental program.	91
<b>Table 3.4:</b>	Beam-column specimens tested in Phase II of the experimental program.	92

**Chapter IV: Experimental Results and Discussion**

<b>Table 4.1:</b>	Effective elastic properties of the FRP tubes used in the experimental program.	141
<b>Table 4.2:</b>	Calculated reinforcement ratios and balanced reinforcement ratios for each specimen tested in the experimental program.	142

$A$	= Concrete filled FRP tube member cross-sectional area
$[A]$	= Extensional stiffness matrix
$(A_c)_i$	= Area of concrete within strip $i$
$(A_f)_i$	= Total area of FRP shell within strip $i$
$[B]$	= Coupling stiffness matrix
$B_i$	= Half the width of strip $i$
$c$	= Neutral axis depth
$CC_i$	= Concrete force in compression zone strip $i$
$CC_{TOT}$	= Total concrete compression force
$CF_i$	= FRP force in compression zone strip $i$
$CF_{TOT}$	= Total FRP compression force
$D$	= FRP tube outside diameter = Average cross-section diameter
$D_{in}$	= Inside diameter of FRP shell
$D_{out}$	= Outside diameter of FRP shell
$[D]$	= Flexural stiffness matrix
$e$	= Column axial load eccentricity
$e'$	= Original applied axial load eccentricity prior to deflection
$E$	= FRP tube elastic modulus
$E_1$	= Lamina elastic modulus in the fibre direction
$E_2$	= Lamina elastic modulus in the direction perpendicular to the fibre direction
$E_c$	= Tangent concrete elastic modulus
$E_c'$	= Secant elastic modulus
$E_{c0}$	= Tangent elastic modulus
$E_f$	= Elastic modulus of the fibres
$(E_{fc})_i$	= Compressive elastic modulus of FRP in strip $i$
$(E_{ft})_i$	= Tensile elastic modulus of FRP in strip $i$
$E_m$	= Elastic modulus of the matrix
$E_{s,hoop}$	= Hoop elastic modulus of FRP shell
$E_{sec}$	= Secant elastic modulus
$E_x$	= Elastic modulus
$E_{x,eff}$	= Effective longitudinal elastic modulus
$E_{y,eff}$	= Effective transverse elastic modulus
$f_c$	= Unconfined concrete stress
$f_{c,int}$	= Intermediate confinement concrete stress
$f_c'$	= 28-day concrete compressive strength



$f_{cc}$	=	Confined concrete stress
$f_{cc}'$	=	Confined peak concrete stress
$(f_{ct})_i$	=	Concrete tensile stress
$f_{cr}$	=	Concrete cracking stress
$(f_{fc})_i$	=	Compressive stress in FRP in strip $i$
$(f_{ft})_i$	=	Tensile stress in FRP in strip $i$
$f_{fu}$	=	FRP tube strength
$f_{ij}$	=	Tsai-Wu failure criterion coefficient
$f_r$	=	Concrete modulus of rupture
$F_{1t}$	=	Lamina tensile strength in the fibre direction
$F_{1c}$	=	Lamina compressive strength in the fibre direction
$F_{2t}$	=	Lamina tensile strength perpendicular to the fibres
$F_{2c}$	=	Lamina compressive strength perpendicular to the fibres
$F_6$	=	Lamina in-plane shear strength
$G_{12}$	=	Lamina longitudinal shear modulus
$G_f$	=	Fibre shear modulus
$G_m$	=	Matrix shear modulus
$G_{xy,eff}$	=	Effective shear modulus
$h$	=	Height of beam-column test specimen
	=	Depth of strip in numerical integration for equilibrium
$h_i$	=	Depth of strip $i$
$h_k$	=	Distance from a mid-height reference plane to the top of lamina $k$
$h_{k-1}$	=	Distance from a mid-height reference plane to the bottom of lamina $k$
$I$	=	Moment of inertia
$k$	=	Column end-support condition factor
	=	Post-peak decay factor
$L$	=	Column length
	=	Beam span
$L_i$	=	Arc length of the circle with diameter $D$ between the top and bottom of strip $i$
$m$	=	Lamina stiffness matrix transformation coefficient
$M$	=	Applied bending moment resolved about the neutral axis
$M_0$	=	Externally applied bending moment at mid-height due to an eccentrically applied axial load
$M_1$	=	Primary moment
$M_2$	=	Secondary moment
$MCC_i$	=	Moment due to compression zone concrete force in strip $i$

$MCC_{TOT}$	= Total moment due to compression in the concrete
$MCF_i$	= Moment due to compression zone FRP force in strip $i$
$MCF_{TOT}$	= Total moment due to compression in the FRP
$M_s$	= Resultant twisting moment
$MTC_i$	= Moment due to tension zone concrete force in strip $i$
$MTC_{TOT}$	= Total moment due to tension in the concrete
$MTF_i$	= Moment due to tension zone FRP force in strip $i$
$MTF_{TOT}$	= Total moment due to tension in the FRP
$M_x$	= Resultant moment in the laminate global y-z plane
$M_y$	= Resultant moment in the laminate global x-y plane
$n$	= Lamina stiffness matrix transformation coefficient
	= Total number of laminas in the laminate
	= Curve fitting factor in Thornfeldt, Tomaszewicz, and Jensen's unconfined concrete stress-strain model
	= Number of strips for equilibrium numerical integration
$N_s$	= Resultant shear force in the laminate global x-y plane
$N_x$	= Resultant force in the laminate global x-direction
	= Compressive axial stress
$N_y$	= Resultant force in the laminate global y-direction
	= Tensile lateral stress
$P$	= Applied axial compressive load
$Q_{11}$	= Component of the lamina stiffness matrix
$Q_{12}$	= Component of the lamina stiffness matrix
$Q_{21}$	= Component of the lamina stiffness matrix
$Q_{22}$	= Component of the lamina stiffness matrix
$Q_{66}$	= Component of the lamina stiffness matrix
$[Q]$	= Intermediate lamina stiffness matrix
$Q_{ss}$	= Component of the transformed lamina stiffness matrix
$Q_{sx}$	= Component of the transformed lamina stiffness matrix
$Q_{sy}$	= Component of the transformed lamina stiffness matrix
$Q_{xs}$	= Component of the transformed lamina stiffness matrix
$Q_{xx}$	= Component of the transformed lamina stiffness matrix
$Q_{xy}$	= Component of the transformed lamina stiffness matrix
$Q_{ys}$	= Component of the transformed lamina stiffness matrix
$Q_{yx}$	= Component of the transformed lamina stiffness matrix
$Q_{yy}$	= Component of the transformed lamina stiffness matrix
$r$	= Radius of gyration

$R$	= Radius of concrete core and FRP shell
$S_{11}$	= Component of the lamina compliance matrix
$S_{12}$	= Component of the lamina compliance matrix
$S_{21}$	= Component of the lamina compliance matrix
$S_{22}$	= Component of the lamina compliance matrix
$S_{66}$	= Component of the lamina compliance matrix
$[S]$	= Lamina compliance matrix
$S_{fk}$	= Tsai-Wu safety factor for layer $k$
$t$	= FRP tube wall thickness
$t_{ss}$	= Effective structural thickness of FRP tube wall
$[T]_k$	= Lamina transformation matrix
$TC_i$	= Concrete force in tension zone strip $i$
$TC_{TOT}$	= Total concrete tensile force
$TF_i$	= FRP force in tension zone strip $i$
$TF_{TOT}$	= Total FRP tensile force
$u_R$	= Radial displacement of concrete core and FRP shell
$z_k$	= Distance from a mid-height reference plane to the middle of lamina $k$
$x$	= Distance between load points in four-point bending test setup
$\alpha_1$	= Factor for bond between the concrete and reinforcement
$\beta_1$	= Concrete stress block calculation factor
$\delta$	= Cross-section deflection from original position
$\varepsilon_1$	= Strain in the fibre direction
$\varepsilon_2$	= Strain in the direction perpendicular to the fibres
$\varepsilon_b$	= Strain at the bottom of the cross-section
$\varepsilon_c$	= Unconfined concrete strain
$\varepsilon_{cc}$	= Confined concrete strain
$\varepsilon_c'$	= Unconfined peak concrete strain
$\varepsilon_{cc}'$	= Peak confined concrete strain
$\varepsilon_{cr}$	= Concrete cracking strain
$\varepsilon_{cu}$	= Concrete crushing strain
$\varepsilon_{fu}$	= FRP tube rupture strain
$\varepsilon_i$	= Input concrete strain
$\varepsilon_t$	= Strain at the top of the cross-section
$\varepsilon_x$	= Strain in the laminate global x-direction
$\varepsilon_x^0$	= Strain component on the reference plane
$\varepsilon_y$	= Strain in the laminate global y-direction

$\varepsilon_y^0$	= Strain component on the reference plane
$\gamma_6$	= In-plane shear strain
$\gamma_s$	= Laminate global x-y plane shear strain
$\gamma_s^0$	= Strain component on the reference plane
$\kappa_s$	= Laminate curvature due to applied moment
$\kappa_x$	= Laminate curvature due to applied moment
$\kappa_y$	= Laminate curvature due to applied moment
$\nu_{12}$	= Lamina major Poisson's ratio
$\nu_{21}$	= Lamina minor Poisson's ratio
$\nu$	= FRP tube Poisson's ratio
$\nu_c$	= Concrete Poisson's ratio
$\nu_{c0}$	= Initial concrete Poisson's ratio
$\nu_f$	= Fibre Poisson's ratio
$\nu_m$	= Matrix Poisson's ratio
$\nu_s$	= FRP shell Poisson's ratio
$\nu_{xy,eff}$	= Effective major Poisson's ratio
$\nu_{yx,eff}$	= Effective minor Poisson's ratio
$\nu_f$	= Fibre volume fraction
$\nu_m$	= Matrix volume fraction
$(\phi_1)_i$	= Angle between a vertical line passing through the centre of the cross-section and the intersection of top of strip $i$ with the circle with diameter $D$
$(\phi_2)_i$	= Angle between a vertical line passing through the centre of the cross-section and the intersection of bottom of strip $i$ with the circle with diameter $D$
$\phi_i$	= Angle between the vertical line passing through the centre of the cross-section and a radial line passing through the centre of the cross-section and the intersection of the middle of strip $i$ with the circle with diameter $D$
$\psi$	= Cross-section curvature
$\rho$	= Concrete filled FRP tube reinforcement ratio
$\rho_{br}$	= Balanced reinforcement ratio
$\sigma_1$	= Stress in the fibre direction
$\sigma_2$	= Stress in the direction perpendicular to the fibres
$\sigma_a$	= Axial compressive stress in FRP shell
$\sigma_h$	= Tensile hoop stress in FRP shell
$\sigma_R$	= Lateral confining pressure
$\sigma_x$	= Stress in the laminate global x-direction

- $\sigma_y$  = Stress in the laminate global y-direction
- $\tau_6$  = In-plane shear stress
- $\tau_s$  = Laminate global x-y plane shear stress
- $\theta$  = Angle between the positive global x-axis and positive lamina 1-axis
- $\theta_k$  = Angle between the positive global x-axis and the positive lamina 1-axis of lamina  $k$

## **Chapter I:**

### **Introduction**

#### **1.1 General**

It is estimated that repair and replacement of deteriorated timber, reinforced concrete, and steel piles costs nearly US\$2-billion each year in the United States alone (Iskander and Hassan, 1998). Steel piles and steel reinforcement in concrete piles corrode in contaminated or high-alkaline soils and in marine regions, causing premature degradation. Waterborne organisms deteriorate timber marine piles, resulting in relatively short service lives. Creosoted timber piles are also harmful to the environment, and are difficult and expensive to dispose of.

Concrete filled fibre reinforced polymer (FRP) tube members provide an excellent alternative to conventional reinforced concrete and steel piles. Steel-free concrete filled FRP tubes are durable, have high strength-to-weight ratios, and can be less expensive to install than conventional piles. Costs are minimized since the shell is the stay-in-place concrete form, therefore reducing transportation costs by allowing for simple on-site fabrication. Costs are reduced

further because the engineered FRP shell is the longitudinal and circumferential reinforcement for the concrete core, eliminating the expense of supplying and placing reinforcing steel cages. The shell also protects the concrete from water intrusion, avoiding damage by freeze-thaw cycling and chloride penetration. Another advantage is that multidirectional fibre orientations in the shell are possible, allowing designs to be optimized for specific loading conditions.

The potential applications of concrete filled FRP tubes are not limited to piles alone. The members can also be used for transmission poles, overhead sign structures on highways, piers and girders in bridges, structural columns in high load or seismic applications, or any other application where high strength and durability are required. Figure 1.1 shows concrete filled FRP tubes used in a marine piling application.

## **1.2 Objective and Scope**

The main objective of this research is to examine the behaviour of concrete filled FRP tubes subjected to axial load, bending moment, or combinations of axial compressive load and bending moment. The behaviour of two types of cross-sections with different FRP shell structures was studied experimentally. An analytical model capable of predicting the behaviour of cylindrical concrete filled FRP tube members subjected to general loads is proposed.

Chapter 2 presents background on FRP materials, including their composition, fabrication, and advantages over traditional construction materials. A brief summary of some of the published research on concrete filled steel tubular members and hybrid FRP/concrete members follows.

Chapter 3 describes the experimental program, including the test specimens, specimen materials, test setups and instrumentation used in pure flexural, pure axial, and combined flexural-axial tests.

Chapter 4 includes the experimental results and discussion. Axial load and moment-deflection behaviour, failure modes, and load and moment-strain behaviour are the primary topics discussed.

Chapter 5 presents the proposed analytical model. Modelling includes determination of FRP laminate effective elastic properties, evaluation of a variable confined concrete stress-strain relationship depending on axial load eccentricity, prediction of FRP laminate failure, a numerical integration approach to evaluate cross-section force and moment equilibrium, and calculation of member deflection.

Chapter 6 provides conclusions and suggested areas for future research on concrete filled FRP tube technology.



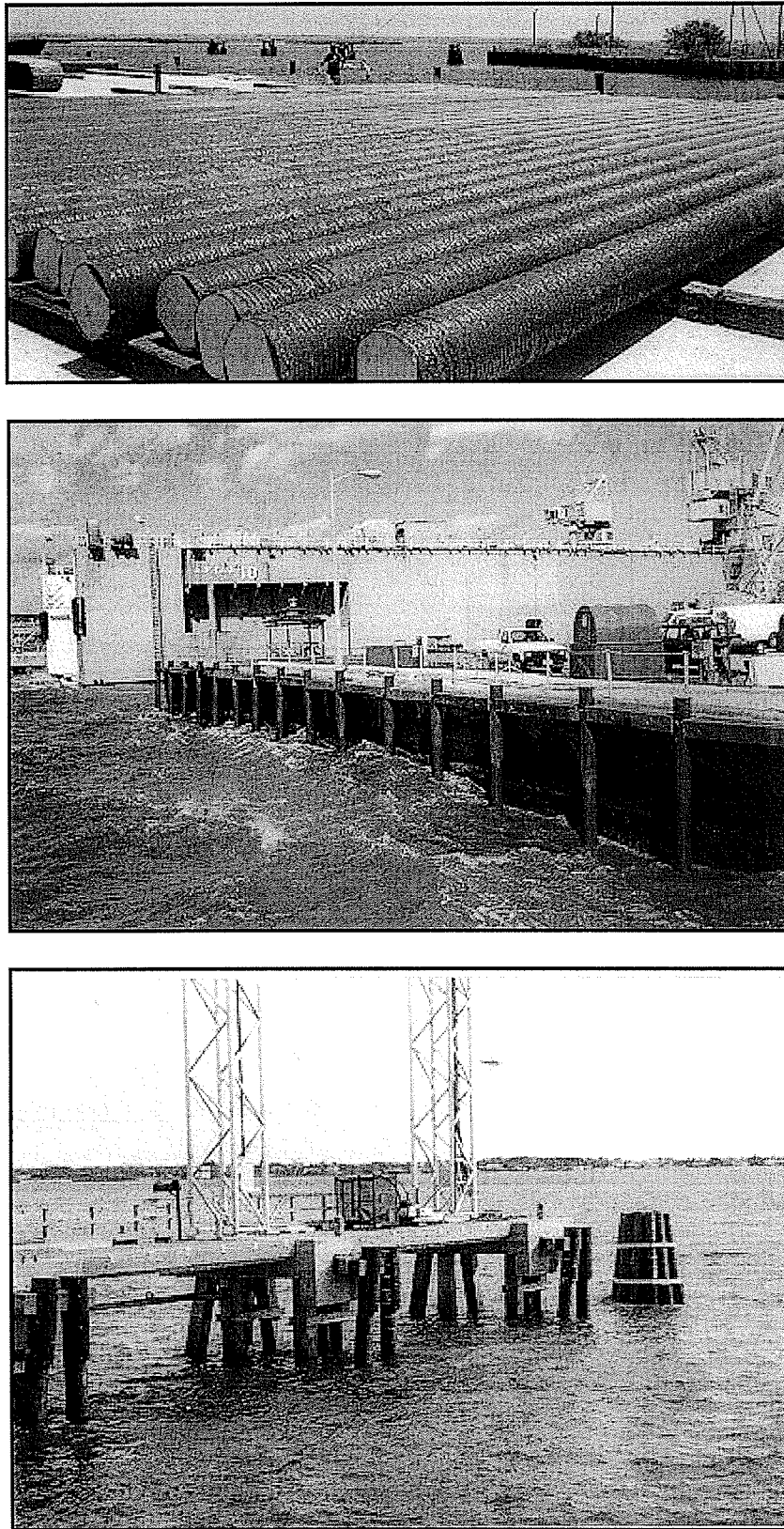
### 1.3 Acknowledgments

I would like to thank Dr. Sami Rizkalla for his support, guidance, and encouragement during the preparation of this thesis.

I would also like to thank:

- Dr. Aftab Mufti, and Dr. Subramaniam Balakrishnan for serving on the examining committee.
- The ISIS Canada Network of Centres of Excellence and the Natural Sciences and Engineering Research Council (NSERC) for their financial support.
- Mr. Bob Greene, Lancaster Composite, for donating the FRP tubes used in the study, and for his collaboration during the research program.
- Laboratory technicians Mr. Moray McVey, Mr. Grant Whiteside, and Mr. Scott Sparrow for their invaluable expertise and assistance during the experimental work.
- Dr. Amir Fam and Dr. Emile Shehata for their technical guidance and support during the research.
- Fellow graduate students Ms. Heather Crocker, Mr. Karim Helmi, Mr. David Schnerch, Ms. Brea Williams, Mr. Guido Camata, Mr. Jon Kell and Mr. Mina Dawood for their assistance with the experimental work.

This thesis is dedicated to my family. Their support made the completion of this work possible.



**Figure 1.1:** Concrete filled FRP tube members in marine piling applications.

## **Chapter II:**

# **Background and Related Research**

## **2.1 Introduction**

The advent of fibre reinforced polymers (FRPs) provided engineers with a new construction material that was lighter and stronger than steel, and more durable due to corrosion resistance. To date, widespread FRP use in civil engineering structures has been limited to rehabilitation and retrofit applications. Externally applied FRP sheets have been used in concrete column strengthening and rehabilitation, timber pile strengthening, concrete beam shear and flexural strengthening, and masonry wall strengthening. Seismic retrofitting of concrete columns with carbon FRP sheets in regions susceptible to earthquakes has demonstrated that FRPs are as effective and more economical than conventional steel jacketing (Seible, 1996). Shallow surface grooving and embedment of FRP rods has also been used to strengthen concrete beams, concrete slabs, and timber beams. Some of the common FRP rehabilitation and retrofitting applications are shown in Figure 2.1.

There is also promise for the use of FRP in new construction. FRP rods and strands have been developed to replace conventional internal steel reinforcing and prestressing strands in concrete members. Another possible application is concrete filled FRP tube members. Research has demonstrated that concrete filled steel tubular (CFST) members have increased strength, stiffness, and ductility over the sum of their individual components, hollow structural steel and concrete. Concrete filled FRP members offer similar enhanced performance characteristics, with the added benefits of durability and low weight. Research on CFST members has been performed since the beginning of the 20<sup>th</sup> century, whereas research on concrete filled FRP members is limited because the concept is relatively new. Because the two systems are similar, it is valuable to study the behaviour of CFST members to gain an understanding of the performance characteristics that can be expected of concrete filled FRP members.

This chapter begins with an overview of FRP materials including their composition, fabrication, and advantages. A summary of some of the published research on CFST members, FRP encased concrete members, concrete filled FRP members, and analytical modelling of FRP confined concrete follows.

## 2.2 Fibre Reinforced Polymers

### 2.2.1 *Composition of Fibre Reinforced Polymers*

FRPs are two-phase composite materials consisting of fibres dispersed through a polymer matrix. The fibres typically have high strengths and moduli and are the primary load-carrying component of the composite. There are a wide variety of fibres available for FRP production including aramid (Kevlar), hemp, boron, carbon (graphite), polyester, nylon, ceramic, quartz, and glass (Daniel and Ishai, 1994; CompositeTek webpage, 2000). Infrastructure engineering FRP applications use carbon and glass fibres almost exclusively. Composite matrices are metallic, ceramic, or, in the case of FRP composites, polymeric. Polymers are chemical compounds consisting of millions of like molecules, bonded into layers or three-dimensional networks. The term “polymer” is derived from “poly”, meaning many, and “mer”, meaning parts. The polymer matrix in an FRP protects the fibres from severe environmental effects like ultraviolet radiation, extreme temperatures, and humidity. The matrix also maintains the orientation of the embedded fibres, giving the composite its shape, transfers stresses between fibres, and provides resistance against buckling when the material is subjected to compressive stress.

#### 2.2.1.1 Polymer Matrices

Completely cured polymer matrices are formed from a combination of materials unique to the polymer type and desired end use. Most polymers consist of a resin and catalyst. Resins are solid or pseudosolid organic materials and catalysts are

materials that initiate the polymerization chemical reaction that causes the matrix to cure. Additives like colorants, fire retardants, electrical conductivity promoters, antistatic agents, and antioxidants can also be included to achieve specific desired properties.

The matrix significantly affects FRP performance. Choosing a matrix with a high tensile modulus can maximize the compressive strength of an FRP. High matrix tensile strength controls cracking between laminas in an FRP laminate. Using a matrix with high toughness can minimize ply delamination and crack propagation. A matrix should also contribute to the durability of FRP by resisting ingress of moisture and solvents like antifreeze, gasoline, and de-icing chemicals (Williams, 2000).

The two major classes of polymers are thermosets and thermoplastics. Thermoset polymers like epoxy, polyimide, vinyl ester, urethane, phenolic and polyester, cure to an irreversible solid state when their molecular structure is cross-linked with strong covalent bonds. Conversely, thermoplastic polymers like poly-ether-ether-ketone (PEEK), polysulfone, polypropylene, polyethylene, polystyrene, acrylonitrile-butadiene-styrene (ABS), nylon, and polyphenylene, have linear molecular structures bonded by weak intermolecular forces. The weak secondary bonds allow thermoplastics to repeatedly revert to their initial liquid state upon reheating to their melt temperature and harden when cooled (Owens Corning webpage, 2000). Historically, FRP composites have been

formed primarily with thermoset polymers, although thermoplastic polymer applications have increased in recent years due to improved mechanical properties and cost effectiveness. Epoxy and polyester thermoset polymers used in the FRP tubes in this study are discussed in more detail in the following two sections.

#### *2.2.1.1.1 Epoxy Polymers*

The epoxy class of polymer matrices, sometimes referred to as epoxide, oxirane, or ethoxyline, are characterized by the epoxide reactive group, consisting of an oxygen atom linked to each of two linked carbon atoms. Epoxies are chemically cross-linked by amines, anhydrides, and acids, usually resulting in a three-dimensional cross-linked structure. There are many possible combinations of resins and curing agents that can form an epoxy, but all classes typically cure with little molecular reorientation and no by-products. Curing results in a tough, relatively strain-free matrix that adheres well to other substances. Additional coupling agents can be included to improve adherence to other substances. Epoxies are common in high performance FRPs because they have excellent mechanical properties, good fatigue behaviour, low moisture absorption, good heat and chemical resistance, and are easy to process.

#### *2.2.1.1.2 Polyester Polymers*

Polyesters account for approximately 75-percent of the thermoset polymers used in the composites industry (SPI, 1995). The term “polyester” is formed from two

other terms, “polymerization”, the process by which small chemical units called monomers are combined to form a polymer, and “esterification”, the combination of carboxylic acid with an alcohol to produce an ester and water. The most common types of esters in the composites industry are unsaturated esters, which contain carbon-to-carbon bond sites that are reactive, ready to attach to other atoms or molecular chains to form cross-linked chains (Richardson, 1987).

Although epoxies are superior to polyesters in their mechanical properties and adherence to other substances, polyesters are commonly chosen over epoxies because they are easier to work with due to lower viscosities, cure more rapidly, and cost less than most epoxies. Unlike epoxies, polyesters typically shrink significantly during curing. This property causes depressions or texturing on the surface of polyester FRPs, while epoxy FRPs typically have smoother surfaces.

#### 2.2.1.2 Embedded Fibres

The fibres are the main load-carrying component in FRP composites. Fibres can be embedded in matrices in many different ways, depending on the application. Continuous fibre composites contain long, continuous fibres that are either oriented parallel (unidirectional continuous fibre composite), at right angles to each other (cross-ply continuous fibre composite), or in several different directions (multidirectional continuous fibre composite). Discontinuous or short-fibre composites contain short fibres oriented parallel to each other or dispersed randomly through the matrix. In general, FRP composites with fibres oriented in one direction have high stiffness and strength in the direction of the fibres and



low stiffness and strength in the direction perpendicular to the fibres. FRP composites with multiple fibre directions or randomly oriented short fibres have similar strengths and stiffness in multiple directions (Daniel and Ishai, 1994). Civil engineering applications typically use unidirectional continuous fibre composites.

High performance FRP composites used in structures typically contain glass or carbon fibres. Some of the advantages of glass fibres include low cost compared to carbon fibres, good chemical resistance, and good insulating properties. Carbon fibres have higher strength-to-weight ratios than glass fibres and good fatigue resistance. Although glass and carbon fibres each have many desirable properties, they also have drawbacks. Glass fibres have lower tensile strengths and moduli than carbon fibres, low fatigue resistance, higher specific gravities than carbon fibres, and are sensitive to abrasion. Carbon fibres are relatively expensive, have low impact resistance, and conduct electric current.

E-glass type fibres are used in the FRP tubes in this study. Glass fibres are also available in S- and R-types that are manufactured with specialized processes to improve tensile strength, tensile modulus, and heat resistance compared to E-glass. E-glass fibres are more common because of their low cost.

Individual glass fibres are gathered into bundled strands called roving during fabrication because it is nearly impossible to transport and work with individual

filaments without breaking them, due to their extreme fragility. Multi-end roving consists of a large number of parallel fibres bundled together without twisting. Multi-end roving is typically used in FRP fabrication processes that require chopped fibres. Single-end roving consists of a large number of fibres wound together helically forming a single rope-like strand. Single-end roving is used in FRP fabrication processes that require unidirectional fibres. Glass fibres are commercially available in spooled unidirectional roving or woven bi-directional mats, as shown in Figure 2.2.

### ***2.2.2 Fibre Reinforced Polymer Fabrication Processes***

There are a wide variety of FRP fabrication processes to select from, depending on the desired end product. The most common processes include hand lay-up, spray-up, compression moulding, pultrusion, injection moulding, and filament winding (SPI, 1995). Filament winding, the process used to manufacture the FRP shells used in this study, is described in detail in section 2.2.2.1. The other FRP fabrication processes listed are described briefly below.

Hand lay-up and spray-up are similar processes popular in fabrication of large FRP products that require high strength. Hand lay-up consists of placing reinforcing fibre mats and liquid polymer against the finished surface of an open mould. Multiple layers of fibres and polymer can be placed and any entrapped air is removed using squeegees or rollers. In spray-up, a specialized gun is used to spray chopped fibres and resin on a mould. The spray gun is designed to chop

fibres from a continuously fed strand, mix the polymer from its constituents, combine the fibres and polymer at a constant ratio, and spray the combination on the surface of a mould. Brushes or rollers are used after application to remove any entrapped air. Typical applications for hand lay-up and spray-up include boat hulls, automotive body parts, pools, tanks, and equipment housings.

Compression moulding is a high volume FRP composite production process. Fibres are laid on matched-metal dies the shape of the desired end product, impregnated with polymer compound, and compressed with hydraulic pressure held until curing is complete. Applications of compression moulding include automotive, appliance, construction, electrical, recreational, and marine parts.

Pultrusion is a process used to form shaped parts like channels, plates, rods, and tubes. Fibre strands are continuously pulled through a polymer bath, drawn through a die to form a constant cross-section, and held in the desired shape until cured. Pultruded products are used in place of traditional steel beams, channels, plates, rods, pipes and other shapes in engineering and construction, especially in marine, water treatment, high saline environment, and industrial applications that require corrosion resistant components.

Injection moulding is used to fabricate specialized parts that require high dimensional accuracy. Chopped fibres and polymer are injected under pressure

into a steel cavity that is shaped exactly like the desired end product. The finished product is removed once curing is complete.

### 2.2.2.1 Filament Winding

Filament winding is the most common FRP fabrication process used to produce hollow tube sections. In filament winding, continuous fibre roving or bands are wrapped around a rotating mandrel. The process is performed at high speed, with precise laydown of strands in predetermined patterns. Filament winding is mainly used to manufacture hollow axisymmetric products like pipes, tanks, rocket motors, and hydro poles (Karbhari, 1996). Advances in filament winding technology and use of Computer Aided Design/Computer Aided Manufacturing (CAD/CAM) also make filament winding of nonsymmetrical parts possible. Filament winding is one of the easiest FRP manufacturing processes to automate, making the process very repeatable and relatively cost effective.

There are two categories of filament winding, wet winding and dry winding. Wet winding occurs when fibre strands fed from a spool are guided through a resin impregnation bath, then wound on a mandrel. The resin content in the wound composite is affected by the resin viscosity, interface pressure at the mandrel surface, winding tension, number of layers per unit length, and mandrel diameter. Prepregs are used in dry filament winding. Prepregs are ready-to-wind roving impregnated with resin and stored for later use. The resin is commonly brought to a "B" stage cure at the time of preimpregnation, and then brought to a "C" stage

cure after winding. B-stage is an intermediate reaction stage in which the material swells when in contact with certain liquids, and softens when heated, but may not entirely dissolve or fuse. C-stage is the final stage of the polymerization reaction in which the material is practically insoluble and infusible. The nature of the preimpregnation process necessitates a resin that cures at elevated temperature or pressure, otherwise it would be difficult to store prepregs for an extended period of time before use without the resin completing the full curing cycle prematurely. In general, wet winding is less expensive than dry winding because it makes use of low cost raw materials, while dry winding with prepregs provides consistent and dependable resin contents that cannot always be assured in wet winding (Composite Solutions webpage, 2000).

#### *2.2.2.1.1 Filament Winding Process*

A typical wet filament winding process is shown in Figure 2.3. A large numbers of strands are pulled from fibre strand creels over a series of guides or scissor bars that maintain the desired strand tension. Strands are pulled through a stainless steel comb or textile thread board to gather them into bundles before entering a resin bath containing the desired resin-catalyst combination and other additives like pigments or UV absorbers. After impregnation in the resin bath, strands are pulled through a wiping apparatus that removes excess resin and ensures that the resin is uniformly spread throughout the bundle, evacuating any air pockets. One type of resin wiping device consists of a set of squeeze rollers with an adjustable top roller to attain the desired resin content and maintain strand

tension. A simple orifice through which a bundle is drawn to scrape away excess resin is another common device. The orifice system is troublesome if filament breakage occurs during the winding process because it is difficult to feed a new filament through the orifice while the process is in motion.

The bundle is drawn into a band by a steel comb, board, or ring, and laid on a rotating mandrel by the carriage after the proper resin content and full impregnation are achieved. The carriage traverses back and forth along the length of the mandrel in helical winding machines. Both the rate of mandrel rotation and carriage transit speed are controlled to achieve the desired wind angle. A crisscross fibre pattern is formed by the back and forth motion of the carriage, creating an interlocking or interweaving effect between the bands of fibres. The product is cured after the desired number of bands is laid on the mandrel to achieve the specified thickness and wind angles. A collapsible mandrel is used if the object is to be removed from the mandrel after curing (Williams, 2000).

Three types of filament winding can be performed to achieve the required winding pattern:

1. Helical winding: The mandrel rotates continuously while the fibre strand feed carriage traverses the length of the mandrel at a speed regulated to provide the desired wind angle.

2. Polar winding: Strands are wound tangentially to one polar opening, down one side of the mandrel, then reverse direction at the other pole and are placed along the other side of the mandrel. A polar arm lays down the strands as it revolves about the mandrel in a circular fashion.
3. Hoop winding: Also referred to as girth, 90-degree, or circumferential winding. It is considered high-angle helical winding approaching 90-degrees. The carriage travel speed is low compared to the rate of mandrel rotation so that each rotation lays down a strand or band of fibres adjacent to the previous band. Hoop winding is seldom used as a stand-alone process. It is typically combined with helical or polar winding to ensure a balanced stress structure in the finished FRP product.

#### *2.2.2.1.2 Advantages of Filament Winding*

Some of the advantages of filament winding over other FRP fabrication processes include:

1. Continuous strands can be used over the entire component area without joints or splices.
2. Fibres can be oriented along load directions easily.
3. Large parts can be produced quickly.
4. High fibre volumes can be achieved.
5. Filament winding is readily automated, reducing labour costs and increasing production speed, efficiency, and quality control.

6. Highly repetitive fibre placement is possible from layer-to-layer and part-to-part.
7. Filament winding tooling costs are low.
8. Custom engineered components can be designed to optimize weight, fatigue strength, ultimate strength, and stiffness by placing fibres exactly where needed within a part to achieve the desired mechanical characteristics (Addax webpage, 2000).

#### *2.2.2.1.3 Quality Control During Filament Winding*

Strand tension and fibre wet out are two of the most important process parameters that must be controlled in filament winding in order to create a high quality product.

Appropriate strand tension is necessary to maintain fibre alignment on the mandrel and control resin content. Inconsistent resin contents from the inside to the outside of the composite, residual stresses after curing, large mandrel deformations, or even fibre breakage can occur if the strand tension is too high. Inadequate strand tension can cause voids and misaligned or wavy fibres on the mandrel.

Appropriate fibre wet out is necessary to ensure no voids are formed within the finished product. The viscosity of the resin should be low enough that a moving strand of fibres is fully impregnated throughout when it passes through the resin



bath, but high enough to ensure that the resin does not run or drip off the strand before it is placed on the mandrel. The higher the number of strands in the bundle, the more difficult it is to achieve a consistent wet out through the bundle. The higher the strand tension, the more likely it is that resin from underlying layers will be squeezed out while laying the new layer. Winding speed should be slow enough, or the resin bath long enough, to ensure that there is enough time to fully impregnate the bundle passing through the bath.

Another common problem is insufficient resin pot life, especially when winding large parts where a significant amount of time may elapse between placing of consecutive layers. Delamination of layers in the completed product may occur if one layer of fibres and resin is already significantly cured prior to placement of the subsequent layer, preventing a good chemical bond to form between the layers.

### ***2.2.3 Fibre Reinforced Polymer Laminates***

Filament winding creates FRP laminates. An FRP laminate consists of two or more individual plies, or laminas with various configurations, stacked and bonded together. A lamina is a plane or curved layer of unidirectional fibers or woven fibres embedded in a matrix. Laminas are considered to have orthotropic material properties along the ply axes shown in Figure 2.4. The 1-axis, referred to as the longitudinal or fibre axis, lies in the direction of the fibres in a unidirectional lamina. The 2-axis and 3-axis are referred to as transverse axes because they lie

perpendicular to the fibre axis (Peters et al, 1991). Each ply in the laminate can have a different composition, thickness, and orientation. The effective elastic properties of a laminate are typically described using a fixed global coordinate system, shown in Figure 2.5, recognizing that fibre directions in each lamina are not necessarily parallel to other laminas. Ply orientations are specified by the angle between the reference x-axis in the global coordinate system and the fibre axis of the lamina, measured counterclockwise on the x-y plane.

Laminate ply composition is termed the lay-up. The exact location, sequence, and orientation of the plies within the laminate are termed the stacking sequence. A laminate is symmetric when each layer on one side of the middle surface has a corresponding layer on the other side of the middle surface the same distance away, with the same composition, thickness, and orientation. A laminate with pairs of lamina with identical thickness and composition but orientations 90-degrees apart is referred to as a balanced laminate. FRP laminates are specifically designed based on the intended use of the product being fabricated because their properties in various directions are highly dependent on the lay-up and stacking sequence.

#### ***2.2.4 Advantages of Fibre Reinforced Polymers***

There are many advantages of using FRP in place of conventional materials in infrastructure, one of the most significant being corrosion resistance. Bridges and roadways are subjected to de-icing salts and other chemicals that cause severe

deterioration of steel members and reinforcement due to corrosion. In recent years, maintenance and new construction budgets are falling well short of the cost of repair and reconstruction of deteriorated structures in many jurisdictions, leading to an ever-increasing infrastructure deficit. Use of FRP materials can alleviate the problem. Corrosion resistance also makes FRP a sensible choice in marine applications where members are constantly attacked by salt water. Use of FRP in rehabilitation and new construction makes structures more durable, increasing their service lives.

Another advantage of FRP is that high strength-to-weight and stiffness-to-weight ratios can be achieved through proper selection of fibres, matrix, and fibre-to-matrix volume ratio. FRP composites can be optimally designed to reach strengths four to five times the yield strength of conventional steel, with comparable moduli, while their specific weights remain about a quarter the specific weight of steel. Lower weights ease handling and construction, allowing rapid installation. Rapid construction and reduced transportation, labour, and heavy equipment costs decrease construction expenses. Lower overall component weight also reduces dead load, permitting higher live loads to be applied, or decreases foundation demands (Black, 2000; Canning et al 1999).

FRPs also provide designers with virtually endless flexibility and adaptability. The large variety of FRP manufacturing processes allow composites to be produced in almost any shape, size, and configuration, for nearly any civil engineering

application imaginable. Other advantages of FRP composites include long fatigue life, good wear resistance, thermal stability, acoustic insulation, electromagnetic neutrality, and pleasing aesthetics.

An apparent drawback of FRPs is their relatively high initial cost compared to conventional construction materials like steel or concrete. However, composites used in infrastructure have service lives up to 10-times longer than conventional materials, drastically reducing maintenance and rehabilitation costs. FRP material costs in new construction or rehabilitation are equivalent to or lower than conventional materials when life cycle costing is applied in infrastructure construction and maintenance planning.

Another common concern expressed by contractors, infrastructure owners, and engineers is that FRP materials cannot be used with confidence because their performance is unproven, especially in the long-term (Williams, 2000). However, composites have been used in boat manufacturing for over 60 years, with the first fibreglass boat produced in 1942 (Martin Marietta Materials, 2000; Daniel and Isaii, 1994). Composites were also used in the aerospace and electrical component fields at that time. There were several advances in composites technology in the following three decades, including the invention of filament winding in the 1950s, the first boron and high-strength carbon fibres in the 1960s, and development of aramid (Kevlar) fibres by Dupont in 1973. FRP composite use expanded widely in the aerospace, automotive, sporting goods, and

biomedical industries by the end of the 1970s (Daniel and Isaii, 1994). Approximately three billion pounds of composite products are manufactured every year in the United States. There are approximately 2000 composites manufacturing plants and materials suppliers across the United States, with greater than 150,000 employees (American Composites Manufacturing Association webpage, 2000). The expertise and confidence in FRPs from these industries can be carried over to civil engineering infrastructure applications. Research on FRPs for civil engineering infrastructure is also common, with many high-profile field demonstration projects proving its viability and effectiveness as a construction material.

## **2.3 Research Related to Hybrid FRP/Concrete Members**

This section briefly summarizes some of the published research related to hybrid FRP/concrete members, beginning with concrete filled steel tubular (CFST) members. CFST members behave similar to and share many of the same benefits as FRP encased concrete members. A summary of some of the research on FRP confined concrete and concrete filled FRP tubes is also included.

### ***2.3.1 Performance of Concrete Filled Steel Tubular Members***

One of the first documented cases of enhanced performance of CFST members was by Sewell in 1901 (Garnder and Jacobson, 1967). Hollow steel columns were filled with concrete to attempt to improve their service lives by protecting

them from internal corrosion. Some of the columns were inadvertently overloaded and Sewell determined that filling the hollow steel columns with concrete had enhanced their stiffness.

Since that time several researchers recognized some of the key advantages of CFST columns over traditional reinforced concrete columns or hollow structural steel columns. One of the advantages is that the steel tube acts as continuous longitudinal, confining, and shear reinforcement for the concrete, decreasing or eliminating the need for internal longitudinal and spiral reinforcing steel and increasing shear capacity (Furlong, 1967; Schneider, 1998; Shams and Saadeghvaziri, 1997). Construction is simplified and accelerated, decreasing costs because less reinforcing steel placement is required. Costs are reduced further because removable forms are eliminated because the shell acts as the stay-in-place concrete pour form (Furlong, 1967; Gardner and Jacobson, 1967; Shams and Saadeghvaziri, 1997).

Another advantage is that the steel tube reinforcing is located at the most effective location, on the periphery of the concrete column, increasing the efficiency of the section. Increased efficiency provides higher capacity than traditional reinforced concrete columns of the same cross-sectional dimensions. Conversely, smaller cross-sections can be used while maintaining equivalent column capacity, increasing available net floor space in buildings. This advantage is prominent in high-rise construction where large reinforced concrete

columns are typically required (Kilpatrick and Rangan, 1999). Costs can also be reduced and quality control improved because CFST members are well suited to precast production (Furlong, 1967).

Experimental testing has shown that axially loaded composite CFST members have higher strengths, stiffness, ductility, energy dissipation, and fatigue performance than the sum of their individual components, concrete and hollow structural steel. These characteristics make CFST members desirable in many engineering applications including piles and piers for bridges and viaducts, columns for offshore structures, columns supporting roofs of storage tanks, and other structural columns, especially in regions susceptible to earthquakes (Shams and Saadeghvaziri, 1997; Schneider, 1998). Steel jacketing of concrete columns has become a common practice to retrofit old structures in seismic regions like California and Japan to bring the structures into compliance with current seismic design codes.

#### 2.3.1.1 Concrete Filled Steel Tubular Columns

Concrete confinement is the primary reason for improved performance of CFST members. Tests on short, circular CFST members where the steel shell and concrete core were loaded simultaneously have shown that the steel shell expands at a higher rate than the concrete core due to Poisson's effect at low axial loads (Gardner and Jacobson, 1967; Okamoto, 1988; Schneider, 1998). The Poisson's ratio of concrete at strain levels below 0.001 is between 0.15 and

0.25, which is lower than the Poisson's ratio of steel, 0.283. The concrete core begins to expand more rapidly at higher loads approaching its peak unconfined strength, reaching Poisson's ratios up to 0.60, while the steel shell continues to expand at a constant rate (Fam, 2000). Concrete expansion "catches up" to the shell and confinement is initiated because the shell begins to exert a radial pressure on the concrete at the interface. The radial confining pressure enhances the strength and ductility of the concrete core by subjecting it to a triaxial state of stress (Gardner and Jacobson, 1967; Shams and Saadeghvaziri, 1997). The concrete core also enhances the performance of the steel shell by laterally supporting it against elastic local buckling to the interior (Prion and Boehme, 1994). The steel shell buckling mode is forced outward, typically occurring well into the yielding stage. Premature buckling of the shell prior to yielding is prevented, increasing the overall strength and ductility of the CFST member (Furlong, 1967; Gardner and Jacobson, 1967; Shams and Saadeghvaziri, 1997; Schneider, 1998)

Several factors affect the level of confinement on the concrete core, including the thickness of the steel tube relative to the cross-sectional dimensions of the column, slenderness ratio of the column, shape of the cross-section, and whether or not the steel shell is loaded simultaneously with the concrete core (Knowles and Park, 1969; Shams and Saadeghvaziri, 1997; Kilpatrick and Rangan, 1999).



The concrete confinement effect is increased with increasing shell thickness-to-column cross-sectional area ratio because the hoop stiffness of the steel shell increases with increasing thickness, allowing higher confining pressures to develop.

Several studies have shown that the concrete confinement effect decreases with increasing column slenderness. Tests demonstrated that long CFST columns tend to exhibit premature buckling failures prior to reaching strains high enough to cause the concrete core to expand sufficiently to initiate confinement. Han (2000) found that even the unconfined concrete strength has little effect on the load bearing capacity of slender CFST columns. Short CFST columns fail by crushing of the concrete and local buckling of the steel shell after yielding, maximizing the axial load by reaching the peak confined concrete strength and shell yield strength simultaneously (Knowles and Park, 1969).

Researchers found that square or rectangular CFST columns did not exhibit appreciable performance enhancement compared to the sum of their individual components. This phenomenon occurs because concrete confining pressure must develop through plate bending of the flat-sided structural steel sections (Furlong, 1967; Tomii et al, 1977). Only relatively small confining pressures develop, even when thick steel shells with respect to column cross-sectional dimensions are used. Circular steel tubes are much more effective because

radial confining pressure is developed through membrane-type hoop stresses (Furlong, 1967; Tomii et al, 1977).

Studies have also been performed to determine if confinement is affected by loading the concrete core and steel shell simultaneously versus loading the concrete core only. Sakino et al (1985) tested three groups of CFST specimens. Each group was identical except for the way the load was applied. Load was applied simultaneously to the steel shell and concrete in the first group and to the concrete core only in the second group. The third group was loaded like the second group except the interior surface of the steel shell was coated with oil prior to casting concrete to minimize the bond between the concrete and steel. Testing showed that concrete confinement did not occur in the group of concrete and steel loaded specimens until yielding of the steel occurred. The other two sets of specimens exhibited concrete confinement prior to yielding. Longitudinal strains were measured in the steel shells of both sets, even though one set of steel tubes had been greased. The axial stiffness of the concrete only loaded specimens was approximately half the stiffness of the concrete and steel loaded specimens, but the ultimate and yield axial loads were greater in the concrete only loaded specimens. It is important to recognize that loads are applied simultaneously to the concrete and steel shell in most CFST member field applications.

A possible explanation for Sakino et al's findings may be Lohr's principle, documented in 1934, to describe the state of stress in the steel shell of an axially loaded CFST member (Knowles and Park, 1969). Lohr stated that the steel shell of a CFST member is subjected to a biaxial state of stress when axial load is applied simultaneously to the shell and concrete core, due to axial stress caused by the applied load and hoop stress due to radial pressure between the concrete and steel once confinement begins. The biaxial state of stress causes a lower steel shell circumferential yield stress than if the shell was subjected to a uniaxial hoop stress only, decreasing the maximum confining pressure on the concrete. This decreases the overall member axial strength compared to a member where the steel shell is subjected to hoop stress only, even though the shell resists some of the axial load on the member. Lohr suggested that the phenomenon always occurs, even if load is applied to the concrete only and measures are taken to eliminate bond between the concrete and steel. Some bond will always occur, especially when a high radial confining pressure is exerted on the concrete, increasing the friction between the concrete and steel. The effect of bond strength on the flexural capacity of CFST columns has been studied. Okamoto (1988) found that bond strength does not have a significant effect on the flexural capacity of CFST columns.

#### 2.3.1.2 Concrete Filled Steel Tubular Beams and Beam-columns

Barber et al (1987) tested CFST members in flexure. Their specimens included hollow steel tubes, concrete filled steel tubes with welded end plates to prevent

concrete core slippage, concrete filled steel tubes without end plates, and concrete filled tubes without end plates, internally greased prior to casting concrete. They studied the effect of bond between the concrete and steel on the flexural behaviour of CFST members. Test results showed that concrete filled tubes had 25-percent higher strengths and 22-percent higher stiffness than hollow steel tubes. Increased strength was due to delayed onset of local buckling of the steel shell in the compression zone, accompanied by contribution of the concrete in the compression zone to the internal moment (Barber et al, 1987). The researchers also concluded that slip was negligible and a positive form of shear transfer between the steel tube and concrete was not required because each of the concrete filled specimens behaved similarly. The concrete filled tubes failed in tension because compression side local buckling of the steel shell was delayed by the lateral support provided by the concrete core. Barber et al observed that the neutral axis depth rose with increasing moment, as is expected due to the non-linear response of concrete in compression.

Kilpatrick and Rangan (1999) tested CFST columns subjected to a variety of short-term eccentric loads, including unequal eccentricities at each end causing single-curvature bending and double-curvature bending. They found that single-curvature columns decreased in strength with increasing slenderness and increasing eccentricity. Decreasing strength with increasing slenderness can be attributed to premature column buckling prior to full initiation of concrete confinement. Increasing eccentricity causes decreasing strength because non-

uniform axial stress is applied to the concrete causing decreased non-uniform radial expansion and lower concrete confining pressure. Once maximum column strength was achieved, the rate of loss of residual strength decreased with increasing eccentricity and slenderness. Kilpatrick and Rangan also found that subjecting CFST columns to double-curvature enhances their strength and flexural stiffness, similar to conventional reinforced concrete columns.

Rangan and Joyce (1992) presented a proposed analysis procedure to predict the strength of eccentrically loaded CFST members. A neutral axis depth is assumed in the procedure, followed by calculation of internal forces and moments, and determination of whether or not cross-section force and moment equilibrium is satisfied. A new iteration with a revised neutral axis depth is performed if equilibrium is not satisfied. Rangan and Joyce demonstrated that the analysis procedure predicted their and other researchers' experimental results reasonably well. Furlong (1967) applied a similar approach to accurately estimate CFST beam-column strengths by treating the members as conventional reinforced concrete sections with reinforcement on the periphery.

Although there are many advantages to using CFST members, there are some drawbacks to using steel shells. Steel is susceptible to corrosion, especially in applications like marine piling and bridge piers where it is subjected to chemical attack from saltwater and de-icing chemicals. Large steel cross-sections and wall thickness are expensive and difficult to handle due to their weight. Potential

performance is also restricted because there is a limit to the concrete confining pressure available for a given steel tube size and thickness because of yielding. In addition, a steel shell's resistance in the axial and hoop directions cannot be uncoupled or optimized because steel is isotropic (Mirmiran and Shahawy, 1997).

### ***2.3.2 Performance of Fibre Reinforced Polymer Encased Concrete Members***

Studies on glass FRP box sections by Deskovic and Triantafillou (1995) and on glass FRP bridge deck sections by Williams (2000) showed that glass FRP alone is effective in flexure, but members are typically not very stiff due to the material's low elastic modulus. Therefore, design is governed by stiffness and the full strength potential of FRP materials is not realized. Deskovic and Triantafillou suggested that composite concrete FRP members could be developed for beam, column, and beam-column applications with the durability and tensile strength advantages of FRP combined with the stiffness and high compressive load capacity of concrete. This section summarizes some of the published research on hybrid FRP/concrete members, including FRP wrapped concrete members, concrete filled FRP tubular members, and FRP confined concrete.

Research on CFST members, described in section 2.3.1, has clearly demonstrated the advantages of jacketing concrete to attain a synergistic effect that improves member performance over the sum of its individual components. Composite members with FRP shells in place of steel shells have similar

enhanced performance characteristics, but overcome some of the drawbacks of steel shells.

Potential advantages of encasing concrete in FRP instead of steel jackets include:

1. Steel is susceptible to corrosion, especially in applications like marine piling and bridge piers where it is subjected to chemical attack from saltwater and de-icing chemicals, whereas FRPs are corrosion resistant. Corrosion resistance extends member service life, reducing life-cycle maintenance, rehabilitation, and reconstruction costs.
2. FRP shells are much lighter and easier to handle than large steel tubes, reducing transportation and construction costs.
3. Designers are not restricted by inherent, isotropic, unchangeable mechanical properties like those of steel when they use FRP shells. The longitudinal and hoop resistances can be uncoupled and changed when FRP laminates are used, allowing for optimization for each specific application. The Poisson's ratios of FRP tubes can also be designed lower than steel tubes, causing initiation of concrete confinement at lower loads, well below the maximum capacity of the member.
4. FRPs generally behave linearly elastic until failure, allowing a member's maximum performance potential to be realized because concrete confinement increases until failure. Steel shells produce a constant, limited confining pressure when they begin to yield.

### 2.3.2.1 Fibre Reinforced Polymer Wrapped Concrete Members

Fardis and Khalili (1981) reported one of the first attempts to use FRP composites to confine concrete. They tested circular concrete cylinders wrapped with several different types of polyester resin impregnated glass fibre cloths. The cloths consisted of fibres oriented longitudinally and circumferentially with respect to the axis of the cylinders. The researchers recognized that longitudinal and circumferential fibres are required in FRP encased compression members because the circumferential fibres confine the concrete and the longitudinal fibres resist any tension caused by bending and improve the buckling capacity by increasing member flexural rigidity. Fardis and Khalili found that the FRP wraps increased the compressive strength and ductility of the concrete cylinders. They observed that failure occurred when the lateral strain of the concrete under the combined effect of applied axial load and radial confining pressure reached the failure strain of the FRP in the circumferential direction. FRP fracture and concrete crushing occurred essentially simultaneously. The FRP used consisted of equal volumes of fibres and polyester matrix, a 50-percent fibre volume fraction. Fardis and Khalili suggested that a fabrication process like filament winding could be used to premanufacture the FRP shells in order to better control the matrix content, increasing the fibre volume fraction to the order of 80-percent. They rationalized that premanufactured FRP tubes would increase the confinement effect due to higher fibre contents and provide the added benefit of stay-in-place forms.



Purba and Mufti (1998) tested concrete columns wrapped with carbon FRP sheets applied after concrete casting. The orientation and number of sheets was varied between specimens. Some specimens were subjected to concentric axial loads while others were subjected to axial loads at small eccentricities compared to the depth of the cross-section. Purba and Mufti observed that concrete compressive strength, column strength, and column ductility significantly increased by using circumferentially oriented FRP sheets in both the concentric and eccentric load cases, but that minor increases occurred when the sheets were oriented longitudinally. Small increases in column compressive strength occurred when FRP sheets were oriented longitudinally because the sheets resisted some of the axial load through composite action with the concrete. No conclusions on flexural behaviour were made because all specimens failed in compression modes. Purba and Mufti suggested further research on flexural behaviour by increasing axial load eccentricities.

Picher et al (1996) studied short rectangular and square columns wrapped with different numbers of layers of carbon FRP sheets after concrete casting. Corner radii were also varied. They found that ductility was increased by the FRP, but strength gains were minimal or did not occur at all. They concluded that square columns were not confined nearly as well as circular columns, but confinement improved with increasing corner radius.

Fardis and Khalili (1981) tested concrete box beams encased in polyester impregnated glass fibre mats. They theorized that the FRP would carry tensile force in the tension zone, provide partial confinement of the concrete in the compression zone, increasing the strength and ductility of the beam, and partially resist beam shear on the vertical faces. The authors noted that other researchers including Izbal and Hatcher (1977) and Iyengar et al (1971) showed that confining concrete in the compression zone increased the ductility and strength of concrete beams. Tests on five beams with varying numbers of unidirectional glass fibre layers along the tension face showed that the strength of FRP encased concrete beams exceeded the strength of typical conventional steel under-reinforced concrete beams with the same dimensions. The FRP encased beams demonstrated excellent ductility, returning to their original positions when they were loaded to near failure and subsequently unloaded.

#### 2.3.2.2 Axially Loaded Concrete Filled Fibre Reinforced Polymer Members

A study on using non-metallic materials to confine concrete was reported by Kurt in 1978. He tested commercially available PVC (polyvinyl chloride) and ABS (acrylonitrile-butadiene-styrene) plastic pipes filled with concrete. Kurt found that concrete strength and ductility were enhanced, even though the plastic pipes used were neither strong nor stiff.

Kanathrana and Lu (1998) tested axially loaded concrete filled pultruded FRP tubes. The specimens failed by longitudinal splitting of the tubes almost

immediately upon high lateral expansion of the concrete core at the peak unconfined strength. Marginal increase in concrete strength and ductility due to confinement was realized. Kanathrana and Lu attributed the failure to the lack of circumferential strength and stiffness of pultruded FRP tubes and concluded that filament winding could create much more effective confinement because fibres could be placed circumferentially.

Mirmiran and Shahawy (1997) tested concrete filled filament wound glass FRP tubes with different numbers of FRP layers yielding shell thickness of 1.45, 2.21, and 2.97-millimetres. All specimens were 305-millimetres high and 152.5-millimetres in diameter. The fibres were oriented nearly circumferentially at  $\pm 75$ -degrees. Circumferential grooves were cut in the shells near the top and bottom of each cylinder to avoid axially loading the shells with their concrete cores, limiting biaxial stress effect. Mirmiran and Shahawy found that concrete compressive strength and ductility were significantly enhanced by confinement, increasing with increasing shell thickness. Failure was initiated by shell rupture near mid-height.

The behaviour of square concrete filled glass FRP tubes was studied in a subsequent research program (Mirmiran et al, 1998). Specimens were 152.5-millimetres square and 305-millimetres high, with 6.35-millimetre corner radii. The number of  $\pm 75$ -degree FRP layers was varied, similar to the cylinder tests. No increase in strength due to confinement was observed, although some

increase in ductility occurred. The load dropped significantly after the peak unconfined concrete strength and specimens eventually failed due to local stress concentrations at the corners of the tube. Behaviour was not affected appreciably by changing the shell thickness. The researchers concluded that cylindrical FRP shells enhanced concrete compressive performance much more effectively than square FRP shells and that shell thickness did not affect the performance of concrete filled square FRP shell members.

Mirmiran et al's findings corroborated Rochette's (1996) findings. Rochette performed a similar study on circular, rectangular, and square aramid and carbon FRP jackets with various concrete strengths, number of FRP layers, and tube corner radii. Rochette determined that circular sections were much more effective than square or rectangular ones, but that the confinement effectiveness of non-circular tubes was dependent on the corner radius and cross-section dimensions. Confinement effectiveness increased with increased corner radius and decreased with increased average cross-section depth.

Mirmiran and Shahawy (1998) reported the results of tests on the effect of length on the capacity of concrete filled glass FRP axial members. The specimens used were similar to the ones used in the cylinder tests by Mirmiran and Shahawy (1997) described previously, except that four different lengths were used. The height-to-diameter ratios of the specimens used were 2:1, 3:1, 4:1, and 5:1. The researchers observed that there was no effect on the performance or axial load

capacity of the members due to length for the range of lengths tested. They predicted that load carrying capacities would decrease if more slender members were tested.

### 2.3.2.3 Concrete Filled Fibre Reinforced Polymer Beams and Beam-columns

Seible (1996) proposed use of concrete filled carbon FRP tubes for columns and beams in bridges. A series of circular and square beams 1.83-metres long were tested in four-point flexure with 0.71-metre long shear spans. Tubes were 152-millimetres in inside diameter, or 152-millimetres high and 152-millimetres wide internally in the case of the square specimens. The filament wound tubes consisted of 80-percent longitudinal fibres oriented at  $\pm 10$ -degrees and 20-percent circumferential fibres oriented at 90-degrees. The tubes were either 2.3 or 4.6-millimetres thick. Corner radii of the square tubes were one-third the depth of the section. The researchers observed that the square beams achieved 25-percent higher bending capacities and 50-percent higher stiffness than the circular beams. This occurred because the square beams had much larger concrete cross-sectional areas in the compression zone and larger FRP cross-sectional areas in compression and tension contributing to the internal moment couple. Applications of the beams in composite girder-concrete deck slab and girder-glass FRP deck slab systems were proposed.

Mirmiran and Shahawy (2000) tested 348-millimetre and 369-millimetre diameter concrete filled FRP tubular members subjected to combined axial loads and

bending moments. The 348-millimetre diameter tubes were spin-cast, a process where dry FRP fabric is laid inside a rotating mould subsequently injected with resin. The centrifugal force from rotation drives the resin into the fabric, forming the wall of the tube. The group of spin-cast tubes had 14-millimetre thick walls, consisting of a non-structural inner resin layer 4.6-millimetres thick, a 0.5-millimetre thick gel exterior coating, and 40 laminas at 0 and +/- 45-degrees forming a symmetric structural laminate. The 369-millimetre diameter tubes were filament wound with 6.6-millimetre thick walls composed of 17 layers of +/- 55-degree laminas. The tubes' reinforcement ratios,  $\rho$ , were 15.44 and 7.03-percent respectively, calculated using:

$$\rho = \frac{4t(D+t)}{D^4} \quad [\text{Eq. 2.1}]$$

where  $t$  = *shell thickness*  
 $D$  = *shell outside diameter*

The 348-millimetre and 369-millimetre diameter tubes were classified as under-reinforced and over-reinforced, respectively, by comparing their reinforcement ratios to the balanced reinforcement ratio,  $\rho_{br}$ , for FRP reinforced concrete proposed by ACI Committee 440 in their "State-of-the-art Report on Fibre Reinforced Plastic Reinforcement for Concrete Structures" (ACI 440R, 1996), expressed:

$$\rho_{br} = 0.85\beta_1 \frac{f'_c}{f_{fu}} \frac{\varepsilon_{cu}}{\varepsilon_{cu} + \varepsilon_{fu}} \quad [\text{Eq. 2.2}]$$

where  $\beta_1$  = concrete stress block calculation factor

$f'_c$  = 28-day concrete compressive strength

$f_{fu}$  = FRP tube axial tensile strength

$\varepsilon_{cu}$  = concrete crushing strain

$\varepsilon_{fu}$  = FRP tube axial tensile rupture strain

An FRP reinforced concrete member is considered under-reinforced when its reinforcement ratio is below the balanced reinforcement ratio and over-reinforced when its reinforcement ratio is above the balanced reinforcement ratio.

2590-millimetre long specimens were tested by applying a constant axial load between 0 and 2792-kN and subjecting the members to increasing bending moment. Mirmiran and Shahawy found that the ultimate deflections of the over-reinforced specimens were 0.50 to 0.75 those of the under-reinforced specimens and the over-reinforced specimens reached 1.25 to 4 times the ultimate strengths of the under-reinforced specimens. The under-reinforced specimens demonstrated a plastic hinging phenomenon that caused increased mid-span deflection without significant increase in applied lateral loads. Secondary moment effects were observed in both cases due to the low stiffness of the members, but were less significant in the over-reinforced specimens due to smaller lateral deflections. Mirmiran et al (2000) concluded that bond between the concrete and

FRP shell is not a factor in beam-columns because the shell is loaded with the concrete core and composite action is not required to transfer compressive and tensile forces to the shell. They suggested that a positive means of shear transfer such as internal ribs should be provided between the FRP shell and concrete core in beam applications to increase the strength and stiffness.

#### 2.3.2.4 Other Hybrid Fibre Reinforced Polymer/Concrete Members

Deskovic and Triantafillou (1995) proposed a glass FRP box beam with a cast-in-place layer of concrete on top of the compression flange, cast between extensions of the webs, and carbon FRP sheets or strips applied to bottom of the tension flange. The concept was designed to take advantage of the desirable properties of each material. Concrete was placed in the compression region because it has high compressive strength, is stiff in compression, and is inexpensive. Carbon FRP was selected for the tension region because it has high stiffness, enhancing the rigidity of the member, high tensile strength, and good fatigue resistance. Carbon FRP also fails at a lower strain than glass FRP, causing it to be the first element of the member to fail in tension, resulting in pseudoductile behaviour that indicates imminent member failure. 3.0-metre span beam specimens 300-millimetres deep and 180-millimetres wide were fabricated and tested. Deskovic and Triantafillou observed that the carbon FRP in the tension zone failed first as designed, resulting in a drop in load, followed by further load increase and member deflection, until overall member failure occurred due to crushing of the concrete in the compression zone. The observed



behaviour demonstrated the pseudoductility desired. The researchers noted that member dimensions, concrete thickness and strength, and quantity of carbon FRP tensile reinforcing could be designed based on the desired span and applied loads in specific applications.

Canning et al (1999) developed a very similar hybrid flexural member concept. Their box-shaped section consisted of a concrete layer in the compression zone cast in-situ between extensions from the webs, rigid foam cored glass FRP laminates for the webs, and bottom flange formed with carbon FRP sheets embedded between layers of glass FRP continuous with the webs. The beams fabricated for flexural testing were 75-millimetres wide and 170-millimetres high, with 1.5-metre spans. Canning et al observed concrete crushing failure in the compression zone, followed by shear failure of the webs. They reported that the hybrid beam had an ultimate bending capacity equivalent to a singly reinforced concrete beam with the same concrete dimensions, reinforced with a two-percent area of steel, while reducing the weight by approximately 75-percent. The hybrid beam's flexural rigidity was half the rigidity of the comparable reinforced concrete beam, resulting in a deflection-to-span ratio of 1/150.

Parvathaneni et al (1996) proposed prestressing concrete filled filament wound glass FRP tubes to take advantage of the concrete confinement effect while reducing or eliminating internal tensile stresses due to applied loads. The members were developed for offshore piles subjected to axial compression,

combined axial compression and lateral bending, and tensile loads. Parvatheneni et al suggested that prestressing could increase the confined concrete compressive strength to six to eight times the unconfined strength, depending on tube thickness, diameter, laminate structure, and unconfined concrete compressive strength used. 6.35-millimetre thick E-glass fibre and vinyl ester resin FRP tubes filled with 35-MPa concrete were fabricated. The tubes were prestressed with three 35-mm diameter high-strength Dywidag prestressing bars, followed by concrete casting and curing and release of the prestressing, resulting 31-MPa compressive stress in the concrete. A 13.72-metre long pile was constructed from three segments spliced with steel bars. The pile was driven 7.62-metres into a riverbed using a conventional diesel hammer. An 8.9-kN lateral test load was applied at the top of the pile, causing only 34-millimetres of deflection due to the pile's high stiffness. Parvathaneni et al concluded that prestressing concrete filled FRP tubular members was a promising technology requiring further study.

### ***2.3.3 Analytical Modelling of FRP Confined Concrete Behaviour***

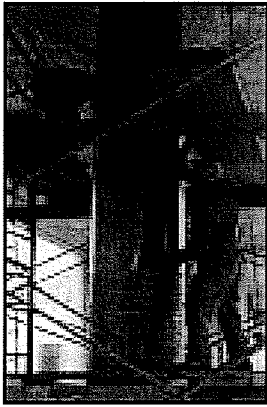
Attempts to accurately model the behaviour of FRP confined concrete have been made by several researchers. Some of these are based on Mander et al's (1988) unified model describing the stress-strain behaviour of concrete subjected to uniaxial compressive stress, confined by transverse steel reinforcement. The model accounts for any general steel confining reinforcement including spirals, circular hoops, and rectangular hoops with or without crossties. It also accounts

for cyclic loading and effects of strain rate. The basic formulation of Mander et al's model is described in section 5.2.2.3.2.

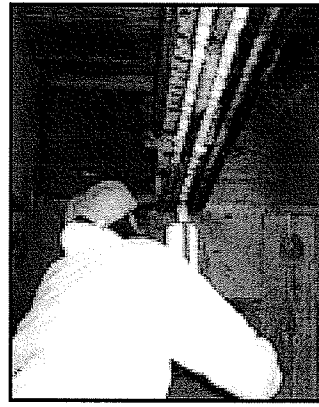
The main challenge in developing a similar model to describe FRP confined concrete stress-strain behaviour is that the confining pressure is variable due to the elastic nature of FRP, not constant as with a yielded steel jacket (Spoelstra and Monti, 1999; Fam, 2000). Fam (2000) compared the behaviour of glass FRP and steel confined concrete. He noted that if axial load is applied to the concrete only, steel begins to confine concrete at small strains because it has a high elastic modulus. Glass FRP confined concrete behaves similar to unconfined concrete at low strain levels because glass FRP typically has a low hoop elastic modulus and is therefore insensitive to small concrete lateral expansion. High concrete lateral expansion occurs as the applied stress approaches the peak unconfined concrete compressive strength, causing activation of concrete confinement by the glass FRP jacket. The confining pressure increases continuously because FRP is elastic, until the shell ruptures and concrete fails when the circumferential stress reaches the hoop strength of the FRP. Steel confined concrete behaves differently because circumferential yielding of the jacket at low axial strains causes constant confining pressure on the concrete core, independent of the concrete lateral expansion (Fam, 2000). Several researchers have proposed FRP confinement models including Parent and Labossiere (1997), Becque (1998), Samaan et al (1998), and Spoelstra and Monti (1999). Some of the available models do not accurately predict the ultimate

confined concrete failure strain. Others are only applicable to high confinement cases because they cannot model the post-peak softening behaviour in low confinement cases observed in several studies (Fam, 2000).

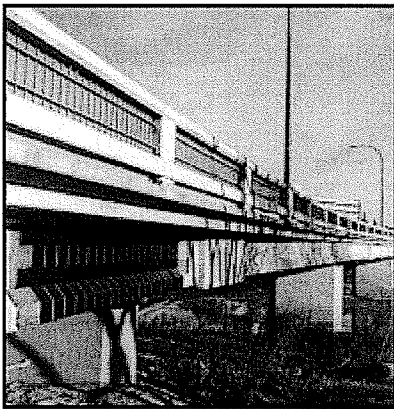
Fam and Rizkalla (2001) proposed a modified Mander's model for FRP confinement based on radial displacement compatibility between the concrete core and FRP shell. The model is applicable to concrete-filled FRP tubes and FRP wrapped concrete, with or without voided cores, uniaxially loaded in compression. The model accounts for axial loading on the shell if desired and predicts post-peak softening behaviour in low confinement cases. Fam and Rizkalla demonstrated the accuracy and wide-ranging applicability of the model by comparing its predictions to his experimental results and the results of many other researchers (Fam and Rizkalla, 2001). Fam and Rizkalla's model is described in more detail in section 5.2.2.3.2.



(a) Concrete column retrofit (FRP sheets)



(b) Timber beam flexural strengthening (embedded FRP rods)

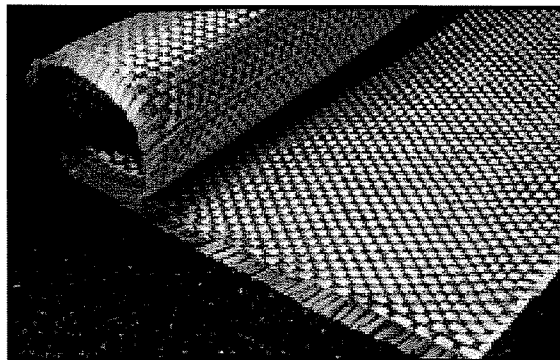


(c) Beam shear strengthening (FRP sheets)

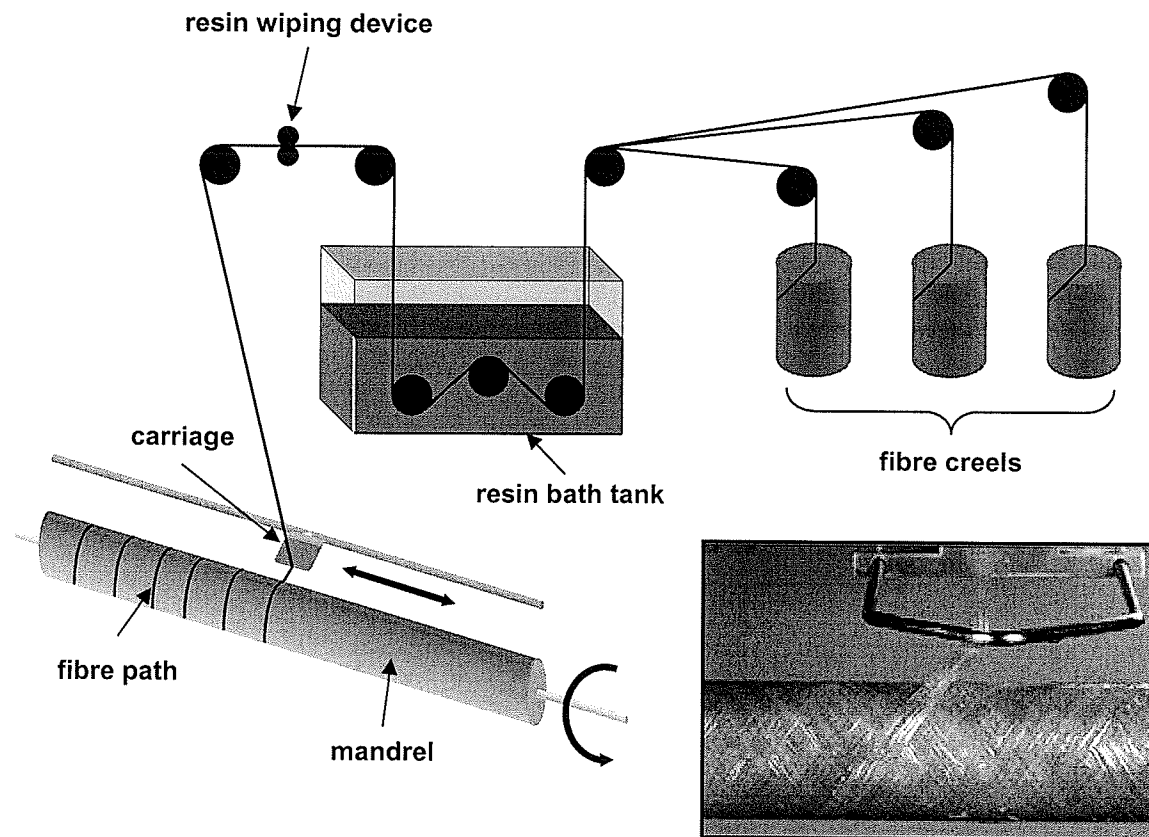


(d) Precast double-“Tee” flexural strengthening (FRP strips)

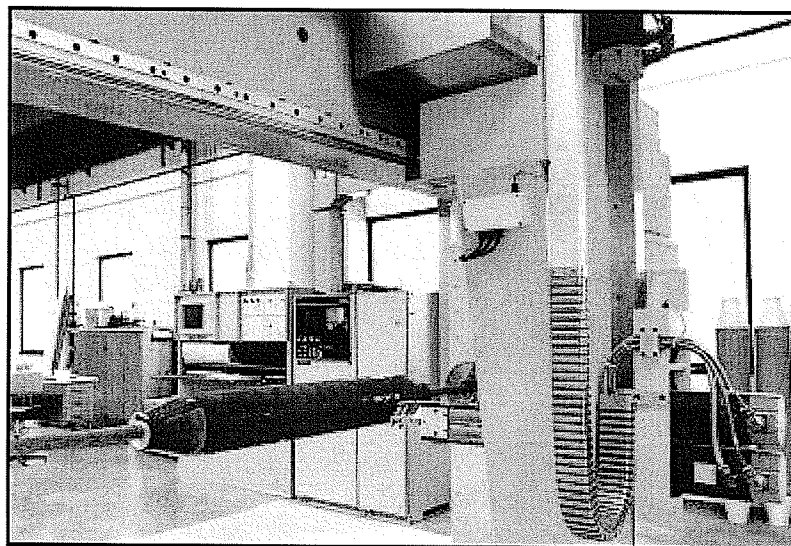
**Figure 2.1:** Fibre reinforced polymer retrofitting and rehabilitation applications (ISIS Canada webpage, 2004).



**Figure 2.2:** Glass fibre bi-directional woven mats and unidirectional spooled roving (Owens Corning webpage, 2004).

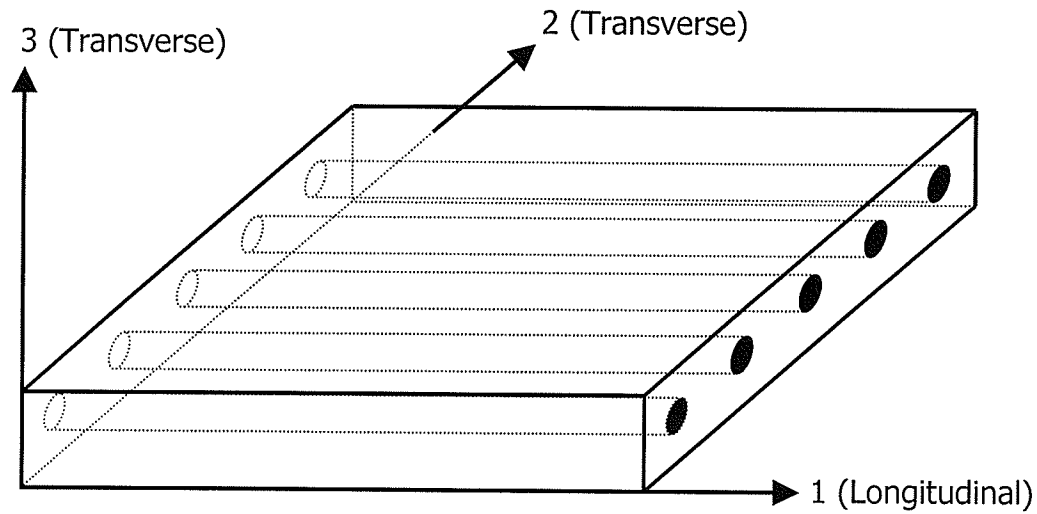


(a) filament winding process schematic and photo (Mallick, 1994; Owens Corning webpage, 2004).

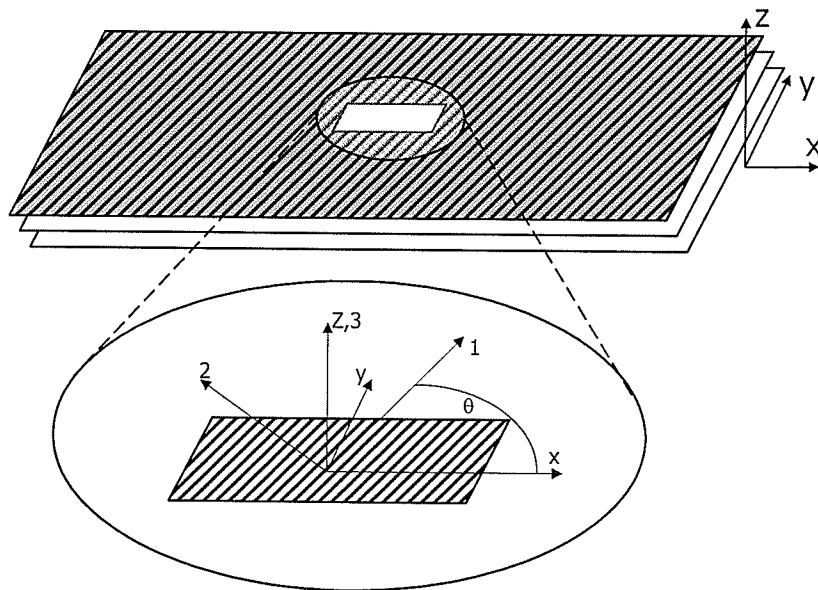


(b) typical filament winding machine (Trival Kompoziti webpage, 2004).

**Figure 2.3:** The FRP filament winding process.



**Figure 2.4:** Orientation of lamina principal material coordinate axes.



**Figure 2.5:** Orientation of laminate global coordinate axes with respect to lamina principal material axes.

## Chapter III:

# Experimental Program

### 3.1 Introduction

The objective of the experimental program was to study the structural behaviour of concrete filled FRP tube members subjected to bending moment only, axial load only, and combined axial loads and bending moments. The load conditions simulated those that can be expected in field applications of concrete filled FRP tube members, including marine piling systems and overhead sign structures.

The experimental program was divided into three phases. The first phase included large-scale beam tests to study flexural behaviour. A total of four specimens were tested in Phase I, using a four-point bending configuration. Combined bending moment and axial load behaviour was studied in the second phase. Nine short-column specimens were tested in Phase II. Phase III included pure axial load testing of two specimens.

The specimens in Phase I of the experimental program were instrumented to measure applied load, deflection at mid-span, and longitudinal and lateral strains



within the constant moment region, across the depth of the section. The specimens in Phase II were instrumented to measure applied load, lateral deflection at mid-height, lateral deflection at the ends, and longitudinal and lateral strains at mid-height across the depth of the section. The specimens in Phase III were instrumented to measure applied axial load and longitudinal and lateral strains at mid-height at several locations around the circumference of the specimens.

### **3.2 Materials Used to Fabricate the Test Specimens**

Specimens for the experimental program were fabricated from two distinct materials, a premanufactured fibre reinforced polymer shell approximately one-foot in diameter and a concrete core cast utilizing the shell as the pour form.

#### ***3.2.1 Fibre Reinforced Polymer Tubes***

The FRP tubes used to fabricate the test specimens were manufactured using a continuous filament winding process by Ameron International Fibreglass Pipe Group in Burkburnett, Texas, and donated by Lancaster Composite, Columbia, Pennsylvania. The tubes were filament wound using standard E-glass roving produced by Owens Corning, Toledo, Ohio, or PPG Industries Incorporated, Pittsburgh, Pennsylvania. The roving was packaged in long lengths, wound on 76-millimetre diameter spools. Long roving was used because the filament winding machine at Ameron International is capable of forming cylinders of continuous lengths, to maximum lengths governed only by the length of the

roving. Each cylindrical shell is rotated on a mandrel while the machine moves from front to back, allowing fibre orientations very close to circumferential and longitudinal. Fibres are wrapped under controlled tension to prevent loose or wavy fibres in the finished product. Winding is performed in alternating layers, continuing until the desired number of layers and wall thickness are achieved. Some of the shells were manufactured with Epon 828 epoxy from Shell Chemical Company, Houston, Texas, or DER 331 epoxy from Dow Chemical Company, Midland, Michigan, and others with polyester resin.

Two unique types of FRP tubes were used. One type consisted of E-glass roving and epoxy resin, with an outside diameter of 326-millimetres. These tubes were delivered in 6.1-metre lengths. The other type consisted of E-glass roving and polyester resin, with an outside diameter of 319-millimetres. These tubes were delivered in lengths between 5.5 and 5.8-metres. Figure 3.1 shows the two types of FRP tubes used in the experimental program, prior to casting of the concrete core. The figure emphasizes another distinguishing feature between the tubes. The E-glass/epoxy tubes are maroon in colour, while the E-glass/polyester tubes are grey.

In addition to the principal structure of the walls of the tubes, consisting of layers of glass fibres, both tubes had an inner liner layer intended to facilitate removal from the mandrel after fabrication. The functional thicknesses in terms of structural performance were slightly smaller than the measured thicknesses due

to the inner liner layer. The laminate structure and composition of each tube are described in Tables 3.1 and 3.2, including diameters, measured wall thicknesses, structural wall thicknesses, and fibre layer angles and thicknesses.

#### 3.2.1.1 Effective Elastic Properties of FRP Laminates

Effective elastic properties in the longitudinal and circumferential directions of the tubes for the two laminates used in the experimental program were determined by experimental testing. Experimental results were compared to the results from the laminated plate theory (LPT) and data supplied by the manufacturer. The LPT is described in detail in section 5.2.2.1.

Ideally, the entire cylindrical section of an FRP tube is tested to find its effective elastic properties, avoiding any edge effects that may affect the results. However, it proved difficult to devise a gripping system to perform longitudinal tension tests on a complete cylinder due to the large size of the tubes used in the experimental program. Longitudinal tension tests were performed on 25-millimetre wide strips cut from the shells. Each end of the 762-millimetre long coupons was embedded within a 305-millimetre long hollow steel tube with epoxy to ensure that the coupons would not fail prematurely due to stress concentrations caused by the testing machine's gripping system. The testing machine gripping system was applied to the steel tubes. Each coupon was instrumented with electrical strain gauges to measure longitudinal and lateral strains. Figure 3.2 schematically shows a typical tension coupon. Tensile load was applied to each coupon

monotonically at a constant rate until destructive failure. Figure 3.3 shows typical tension coupons after failure.

Two compression tests were performed on complete cylindrical sections cut from the FRP tubes used in the experimental program. Full cylindrical sections were used because no gripping system was required to apply compressive force to the coupons. Two-to-one height-to-diameter ratios were used. The E-glass/epoxy coupon was 652-millimetres high and 326-millimetres in diameter and the E-glass/polyester coupon was 638-millimetres high and 319-millimetres in diameter. A lathe was used to precisely cut the coupons to the desired length while ensuring that the cut surfaces were perpendicular to the longitudinal axis of the tubes. Each specimen was instrumented with four longitudinally oriented PI-gauge type displacement transducers and two laterally oriented electrical strain gauges at mid-height, as shown in Figure 3.4. Local bearing failure at the interface between the tube and the machine loading plate occurred in both tests, as shown in Figure 3.5. Therefore the test results did not provide accurate laminate compressive strengths, but provided compressive elastic moduli and Poisson's ratios.

### **3.2.2 Concrete Core**

The concrete mix used in the test specimens was designed to ensure that no separation between the concrete core and the fibre reinforced polymer tube would occur due to shrinkage of the concrete during curing. An expansive agent

commercially known as Conex was included as an admixture to overcome shrinkage, causing a pressure fit of the concrete core within the shell. The concrete mix design included the following materials per cubic metre: 360-kg of type 10 cement, 89-kg of Conex, 803-kg of fine aggregate, 998-kg of 3/8-inch (9.5-millimetre) coarse aggregate, 154-kg of water, 4.8-kg of high and mid-range water reducers, and air entrainer to provide five percent total air content. The designed slump of the concrete was 200-millimetres, ensuring adequate workability for casting. A similar mix design is commonly used in field applications for concrete filled FRP tubes in marine piling systems.

### 3.3 Fabrication of Test Specimens

All the test specimens were cast at local precast concrete supplier Lafarge Canada Incorporated, Winnipeg, Canada, due to their large size. Hollow FRP tubes were placed on a steel framework constructed to hold them in an inclined position during casting. Wooden plugs were placed over the ends of the tubes to cap and seal them, and concrete was pumped from a ready mix truck into the tubes through openings in the upper plugs. A vibrator was connected to the supporting steel frame to externally vibrate the concrete during casting, in order to avoid the formation of air voids within the specimens. Figure 3.6 shows the casting setup and process used to fabricate the test specimens. The specimens were laid horizontally and left to cure after casting was completed. They were transported to the Structures Laboratory at the University of Manitoba after curing for at least 28-days. Concrete cylinders prepared at the time of casting of the

tubes were tested according to ASTM standard C39, using a 0.1-millimetres/minute rate of loading. Three truckloads of concrete were necessary due to the large volume of concrete required to cast all of the specimens. 28-day concrete compressive strengths varied between 47 and 62-MPa. Core samples were taken from some specimens to determine concrete compressive strengths at the time of testing because most of the specimens were tested over one and a half years after casting. Concrete compressive strengths at the time of testing varied between 60 and 85-MPa.

### **3.4 Experimental Phase I – Beam Tests**

The objective of the first phase of the experimental program was to study the flexural behaviour of the two types of concrete filled FRP tube members.

#### ***3.4.1 Beam Test Specimens***

Four beam specimens were tested. Table 3.3 describes the specimens tested, including the span, spacing between loads, type of FRP shell, and concrete compressive strength at the time of testing. The study compared beams of similar cross-sectional dimensions and reinforcement ratio, but with different shell compositions and fibre winding configurations. The wooden plugs located at the ends of the tubes used during casting of the specimens were removed prior to testing to ensure that no interference to possible slip of the concrete core in the tube during testing would occur.

### ***3.4.2 Instrumentation of Beam Specimens***

The beams were instrumented within the constant moment region to provide strain and deflection measurements and at the ends to measure any slip between the concrete core and the outer FRP shell during testing. Figure 3.7 shows a schematic of the instrumentation used. The electrical strain gauges in the axial and circumferential directions were type FLA-6-11-5L with resistances of 120-ohms, supplied by Tokyo Sokki Kenkyujo Co. Ltd., Japan. The gauges were affixed to the beam surface using M-Bond 200 two-part adhesive, after the surface was prepared with sandpaper and cleaned. The spacing between each set of circumferential and longitudinal gauges was selected to be  $1/3$  the depth of the beam, to provide strain profiles across the depth of the section. PI-gauge type displacement transducers were also placed in the longitudinal direction along the top and bottom of the beam to measure average strains over their 200-millimetre gauge lengths, for comparison to strain gauge readings. Deflection measurements were taken at mid-span by a linear motion transducer (LMT). Mechanical dial gauges were mounted at the ends of the beam to measure slip between the concrete core and the FRP shell during loading.

### ***3.4.3 Beam Test Setup***

All of the beam specimens were tested using a four-point bending apparatus to provide a region of constant moment and no shear force between the applied point loads. The beams were simply supported at their ends.

Figure 3.8 shows one end of a test specimen resting on a roller support. Steel angle sections were welded to the top plate of the roller support heel up to prevent the round beams from rolling off the supports during testing. Layers of plastic bags filled with plaster of Paris were also placed between the top plate of the roller support, the steel angle sections, and the beam to fill in the voids and provide a large surface area to transfer the load reaction in the beam to the support. The steel roller supports were fixed to stiff, massive, concrete blocks placed on the structural floor of the laboratory.

Load from the testing machine was applied to the beams with a steel spreader beam. Another set of rollers similar to the ones used for the end supports were used at the contact points between the spreader beam and the specimen. Plaster bags were also placed at the load points, between the rollers and the specimen, to provide a large surface area and even contact to transfer the applied loads to the specimen.

The beams were loaded under displacement control using a closed-loop Materials Testing Systems (MTS) 5000-kN (one million pound) testing machine, at 0.5 to 1.5-millimetres/minute rates of loading. Machine load, machine stroke, and all instruments excluding mechanical dial gauges were linked to a 32-channel data acquisition system with LabTech Notebook software. Readings were recorded at a frequency of 1-Hz. Figure 3.9 shows the beam specimen test setup.



### **3.5 Experimental Phase II – Beam-column Tests**

The objective of the second phase of the experimental program was to study the effects of combined axial loads and bending moments on the behaviour of two types of concrete filled FRP tube members. This phase of the study was performed to simulate typical loading conditions concrete filled FRP tube members experience in field applications like marine piling and overhead sign structures on highways.

#### ***3.5.1 Beam-column Test Specimens***

A total of nine beam-column specimens were tested to failure by applying axial loads at various eccentricities to cause coupled axial loads and bending moments on the specimens. The beam-column specimens were oriented vertically in the testing machine. Table 3.4 describes the specimens tested, including applied eccentricities, type of FRP shell, height, and concrete compressive strength at the time of testing. The beam-columns tested had similar cross-sectional dimensions, reinforcement ratios, and heights, but had different FRP shell compositions and fibre winding configurations. Concrete strengths also varied because the specimens were originally cut from original full-length FRP members cast with three separate loads of concrete, as described in section 3.3.

### 3.5.2 Fabrication of Beam-column Test Specimens

The lengths of the beam-columns were selected to minimize potential slenderness effects. The ACI concrete design code recommends accounting for slenderness effects on reinforced concrete columns when the slenderness ratio  $kL/r$  exceeds 22, where  $k$  is a factor that depends on the end support conditions (1.0 for pin-ended columns),  $L$  is the column length, and  $r$  is the cross-section's radius of gyration, expressed:

$$r = \sqrt{\frac{I}{A}} \quad [\text{Eq. 3.1}]$$

where  $I = \text{moment of inertia}$

$$= \frac{\pi D^4}{64} \quad (\text{for a circular cross-section}) \quad [\text{Eq. 3.2}]$$

$A = \text{cross-sectional area}$

$$= \frac{\pi D^2}{4} \quad (\text{for a circular cross-section}) \quad [\text{Eq. 3.3}]$$

$D = \text{cross-section diameter}$

The ACI code suggests use of the geometric moment of inertia, neglecting the transformed area of reinforcement. Combining equation 3.1 to equation 3.3, the radius of gyration of a circular cross-section is  $D/4$ . The maximum length of the beam-column specimens was selected to meet the short-column upper bound slenderness ratio of 22. The lengths of the two types of specimens were slightly

different because of their unequal diameters. E-glass/polyester specimens were 1.75-metres long and E-glass/epoxy specimens were 1.80-metres long.

The beam-column specimens were cut from full-length concrete filled FRP tubes cast using the process described in section 3.3, after concrete cured for at least 28-days. The specimens were cut by a local contractor using a diamond tipped saw, as shown in Figure 3.10. Care was taken to ensure that the cut surfaces were flat and perpendicular to the longitudinal axes of the specimens.

### ***3.5.3 Instrumentation of Beam-column Specimens***

The beam-column specimens were instrumented at mid-height to measure longitudinal and lateral (circumferential) strains. The nature of the eccentric loading apparatus, described in section 3.5.4, caused lateral deflection at the ends of the specimens with respect to the loading axis, in addition to lateral deflection at mid-height, during load application. Therefore, deflection measurements were taken at mid-height and at the ends of the specimens.

Electrical strain gauges were placed in the axial and circumferential directions at mid-height. The gauges used were type FLA-6-11-5L with 120-ohm resistances, supplied by Tokyo Sokki Kenkyujo Co. Ltd., Japan. The gauges were attached to the surface of the beam-columns using M-bond 200 two-part adhesive, after preparation and cleaning of the specimen surface. PI-gauge type displacement transducers were placed on the extreme compression and tension faces of each

beam-column to measure average strains over their 200-millimetre gauge length, for comparison with strain gauge measurements. Lateral deflection measurements at the top, bottom, and mid-height of the beam-column were taken using linear variable displacement transducers (LVDT). Figure 3.11 shows a schematic of the instrumentation used in the beam-column tests.

#### ***3.5.4 Beam-column Test Setup***

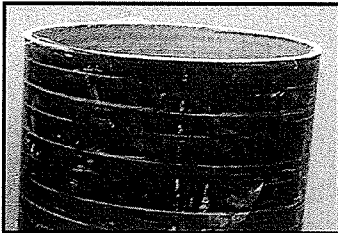
The beam-column specimens were tested using a specially designed eccentric loading apparatus that applied a coupled axial load and bending moment. The apparatus consisted of several key components. 325-millimetre diameter high-strength steel end caps were placed over the ends of the beam-column. The caps were made up of two separate semicircular sections with outward radiating flanges welded to the ends of the semicircles. The two sections were placed over the end of a beam-column and clamped together with  $\frac{3}{4}$ -inch bolts between the flanges. Figures 3.12 and 3.13 show the configuration and dimensions of the eccentric loading caps. Half-cylinder steel pins were welded to the top surface of the upper cap, and the bottom surface of the lower cap at the desired eccentricity from the centreline of the beam-column. The pins fit into grooved plates aligned with the centre of the testing machine, one at the top fixed to the machine crosshead and another at the bottom fixed to the base of the machine. The grooves and pins were greased to minimize friction during rotation of a specimen's ends during testing.

The beam-columns were loaded under axial displacement control using a closed-loop Materials Testing Systems (MTS) 5000-kN (one million pound) testing machine, with a rate of loading between 0.5 and 1.5-millimetres/minute. All test measurements including machine load, machine stroke, strains, and deflections were recorded with a 96-channel data acquisition system with LabView software, at a frequency of 1-Hz. Figure 3.14 shows the beam-column specimen test setup.


### **3.6 Experimental Phase III – Pure Axial Load Tests**

The objective of the third phase of the experimental program was to study the effects of pure axial load on two types of concrete filled FRP tube members. Two specimens were tested, one for each type of FRP shell described in section 3.2.1. The specimens were cut from full-length concrete filled tubes, with care taken to ensure that the cut surfaces were flat and perpendicular to the longitudinal axes of each specimen. The concrete compressive strengths were 60 and 67-MPa for the E-glass/epoxy and E-glass/polyester shell type specimens, respectively. The length of each specimen was selected to yield three-to-one height-to-diameter ratios. Instrumentation on each cylinder consisted of three PI-gauge type displacement transducers and six electrical strain gauges. PI-gauges were oriented longitudinally, placed at 120-degree intervals around the specimen's circumference to measure average axial strain in the FRP shell. Three strain gauges were oriented longitudinally, also placed at 120-degree intervals but staggered midway between the PI-gauge locations. The

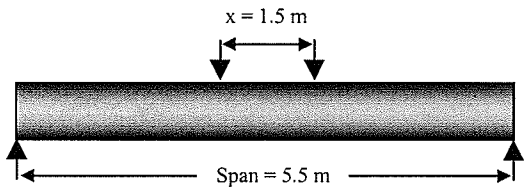
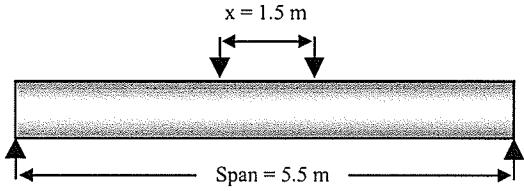
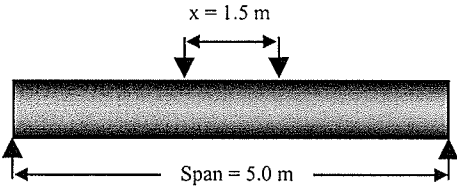
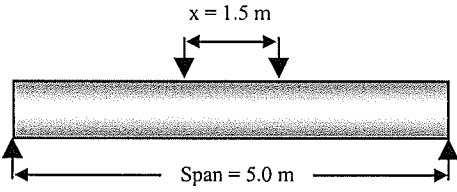
remaining three strain gauges were oriented laterally and placed at the longitudinal strain gauge locations to measure hoop strain in the FRP shell. The axial load test setup and instrumentation are shown in figure 3.15.

E-glass/epoxy laminate tube		
<b>Characteristics</b>		
<i>outside diameter</i>	326-mm	
<i>total thickness (wall)</i>	7.05-mm	
<i>structural thickness (wall)</i>	6.4-mm	
<i>number of wound layers</i>	10	
<i>fibre volume fraction</i>	51%	
<b>Laminate Structure and Stacking Sequence</b>		
<i>Layer</i>	<i>Thickness (mm)</i>	<i>Fibre Angle (degrees)</i>
1	0.56	-88
2	0.43	3
3	0.56	-88
4	0.56	-88
5	0.89	3
6	0.56	-88
7	0.86	3
8	0.56	-88
9	0.86	3
10	0.56	-88

**Table 3.1:** Laminate structure and characteristics of E-glass/epoxy laminate tubes used in the experimental program.

E-glass/polyester laminate tube		
<b>Characteristics</b>		
<i>outside diameter</i>	319-mm	
<i>total thickness (wall)</i>	7.22-mm	
<i>structural thickness (wall)</i>	5.96-mm	
<i>number of wound layers</i>	5	
<i>fibre volume fraction</i>	47%	
<b>Laminate Structure and Stacking Sequence</b>		
<i>Layer</i>	<i>Thickness (mm)</i>	<i>Fibre Angle (degrees)</i>
1	1.04	34
2	1.04	-34
3	1.80	80
4	1.04	34
5	1.04	-34

**Table 3.2:** Laminate structure and characteristics of E-glass/polyester laminate tubes used in the experimental program.

<i>Beam Specimen</i>	<i>Bending Test Configuration*</i>	<i>Shell Type</i>	<i>Concrete Strength** (MPa)</i>
BM-E-1		E-glass/epoxy	60
BM-P-1		E-glass/polyester	62
BM-E-2		E-glass/epoxy	85
BM-P-2		E-glass/polyester	67

\* x is the distance between load points in the four-point bending test setup

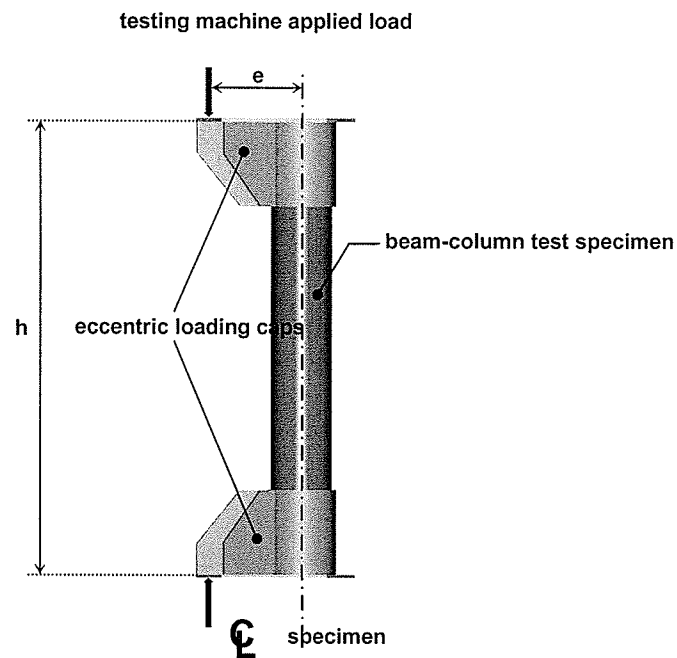
\*\* concrete compressive strength at time of testing

**Table 3.3:** Beam specimens tested in Phase I of the experimental program.

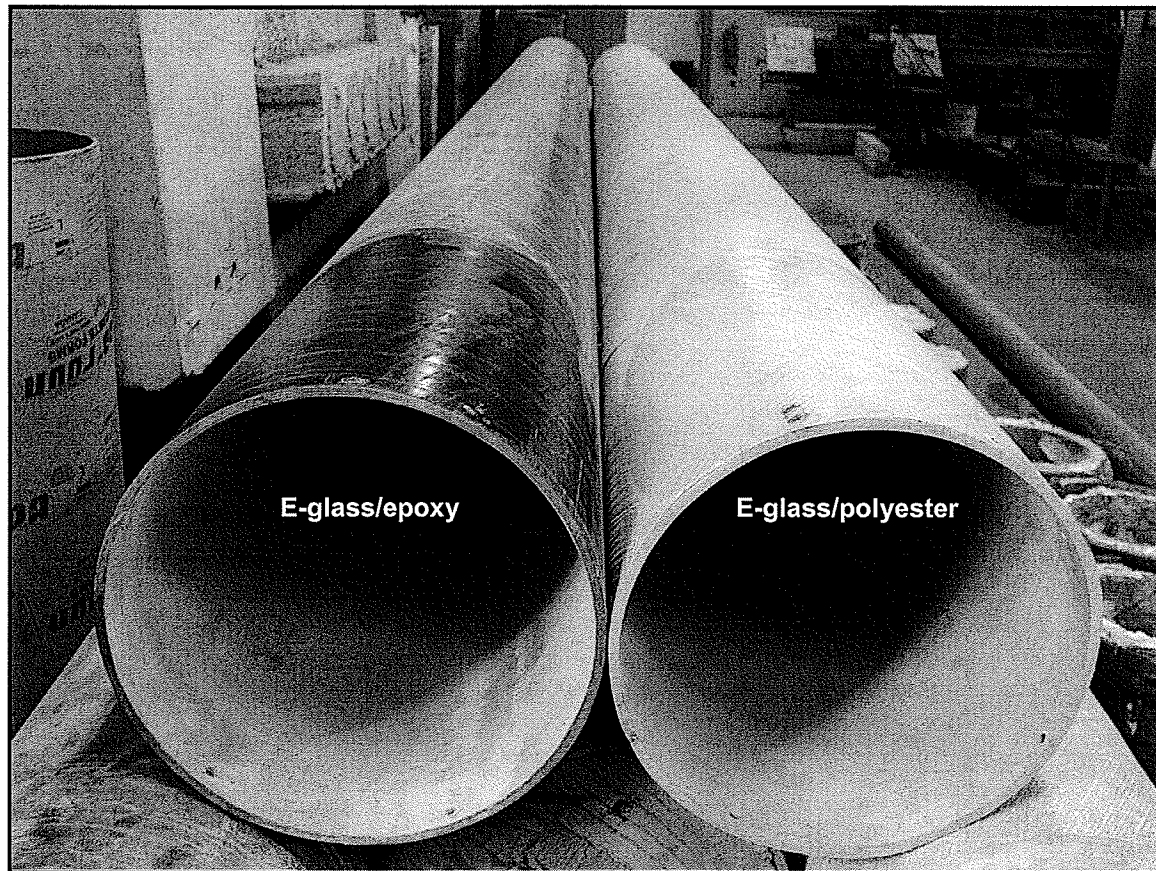


<i>Beam-column Specimen</i>	<i>Eccentricity, e (mm)</i>	<i>Height, h (m)</i>	<i>Shell Type</i>	<i>Concrete Strength* (MPa)</i>
BC-P-e10	10	1.75	E-glass/polyester	77
BC-P-e30	30	1.75	E-glass/polyester	77
BC-P-e100	100	1.75	E-glass/polyester	77
BC-P-e200	200	1.75	E-glass/polyester	77
BC-P-e300	300	1.75	E-glass/polyester	77
BC-E-e30	30	1.80	E-glass/epoxy	60
BC-E-e100	100	1.80	E-glass/epoxy	60
BC-E-e200	200	1.80	E-glass/epoxy	60
BC-E-e300	300	1.80	E-glass/epoxy	60

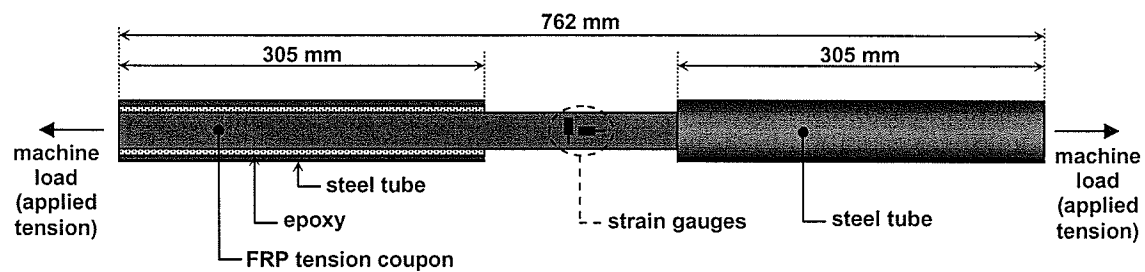
\* concrete compressive strength at time of testing



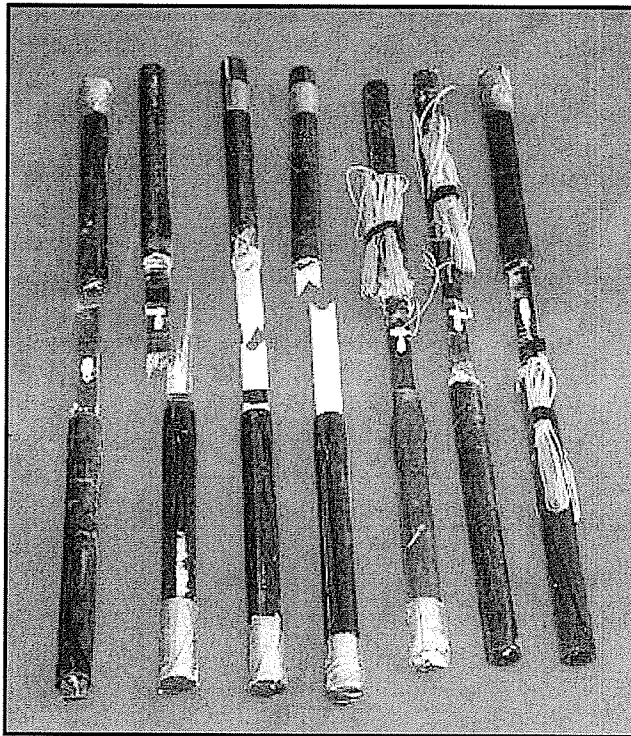
**Table 3.4:** Beam-column specimens tested in Phase II of the experimental program.



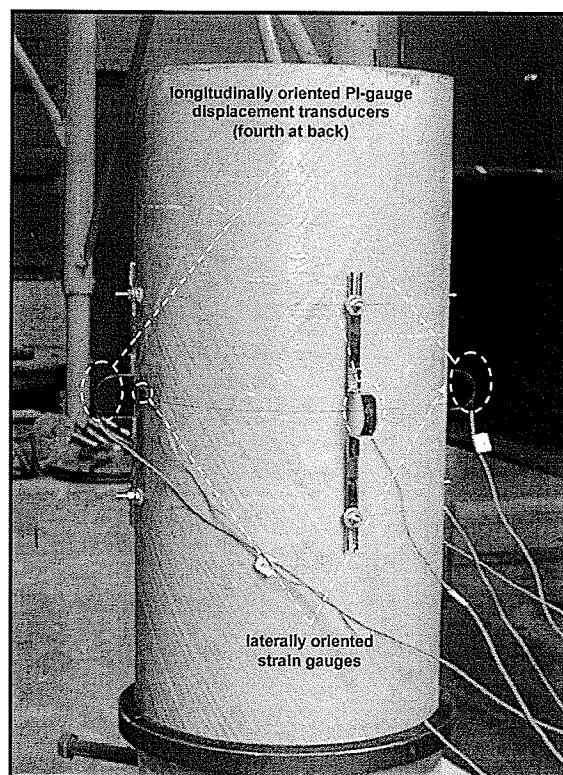
**Figure 3.1:** The two types of FRP shells used to fabricate the test specimens.



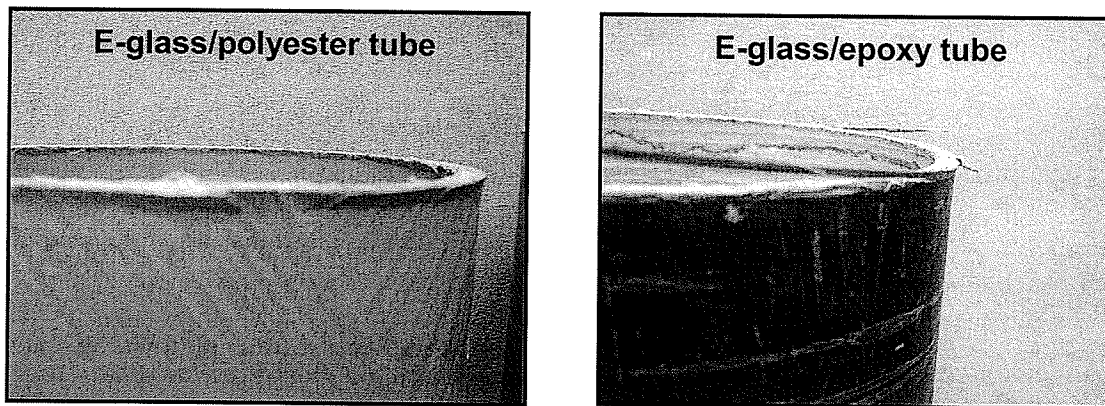
**Figure 3.2:** Longitudinal tension coupon.



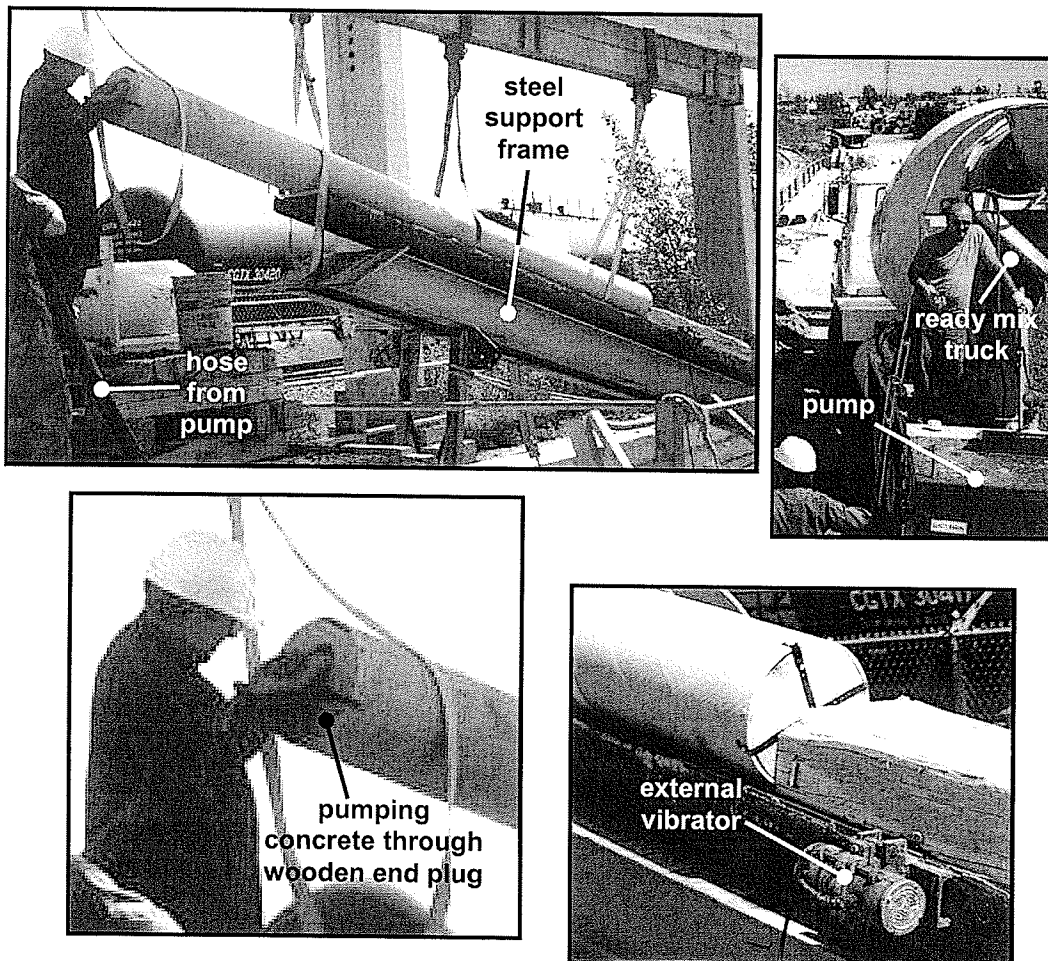
**Figure 3.3:** Typical longitudinal tension coupons after failure.



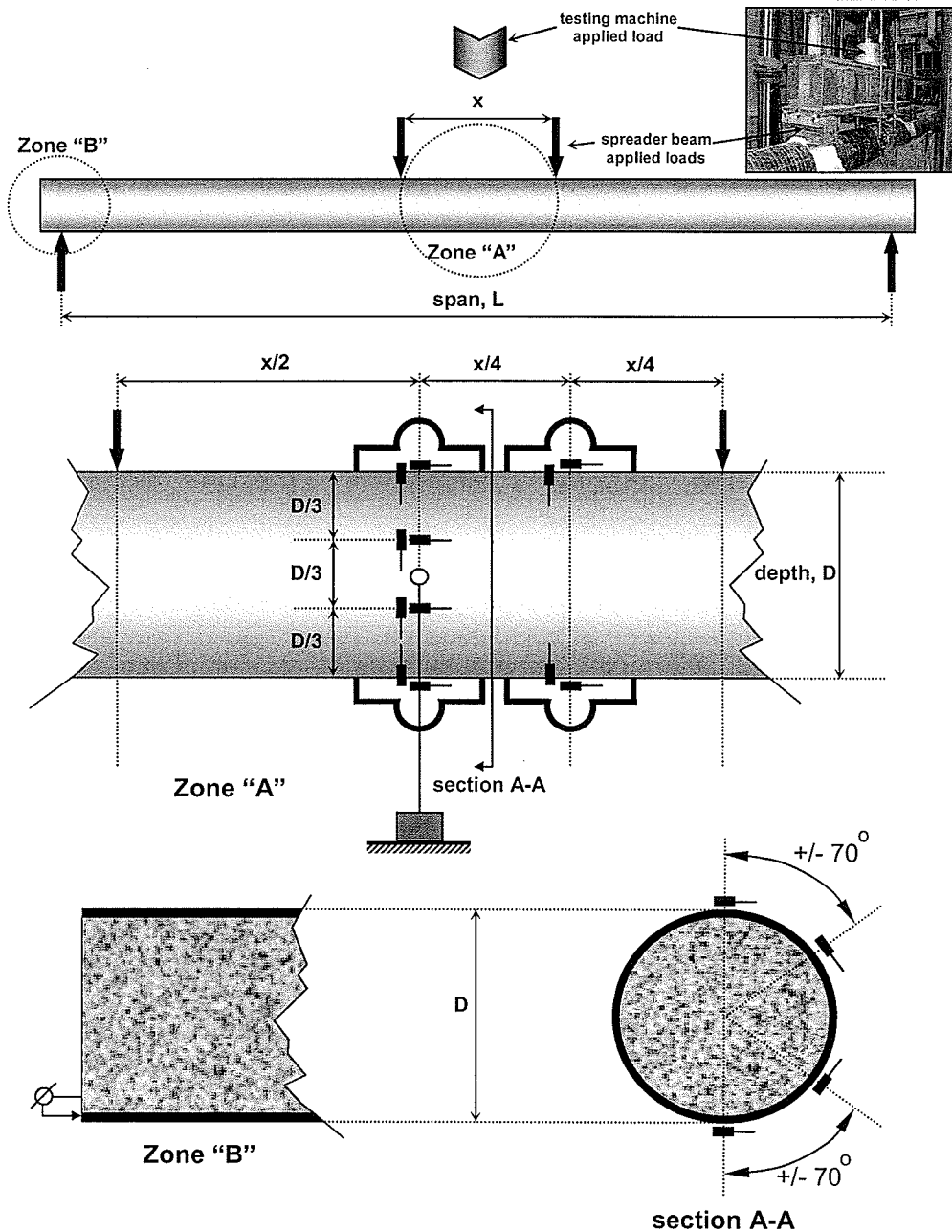
**Figure 3.4:** Longitudinal compression coupon instrumentation.



**Figure 3.5:** Local bearing failures at the top of the compression coupons.



**Figure 3.6:** Concrete casting setup and procedure used to fabricate test specimens for the experimental program.







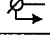

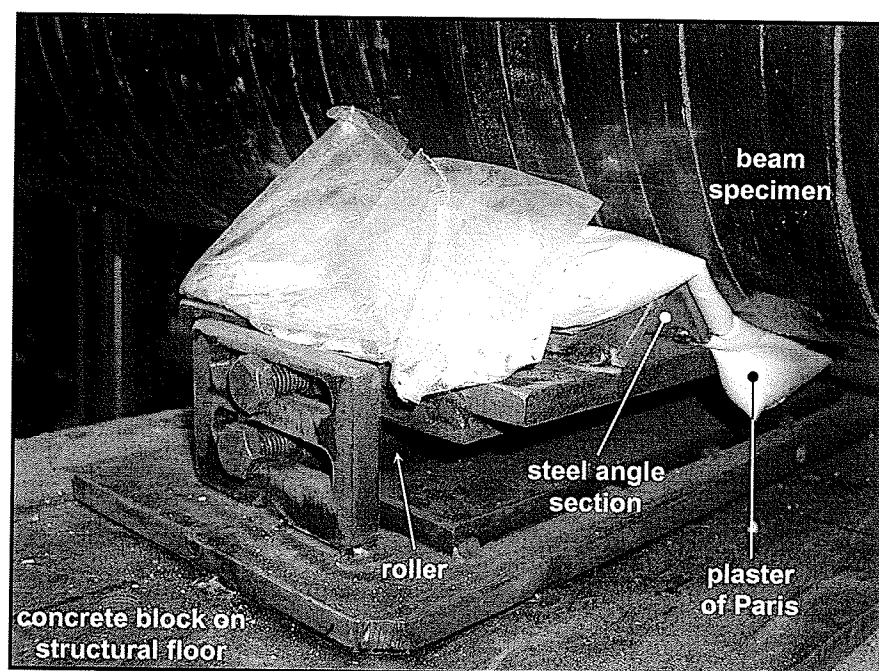
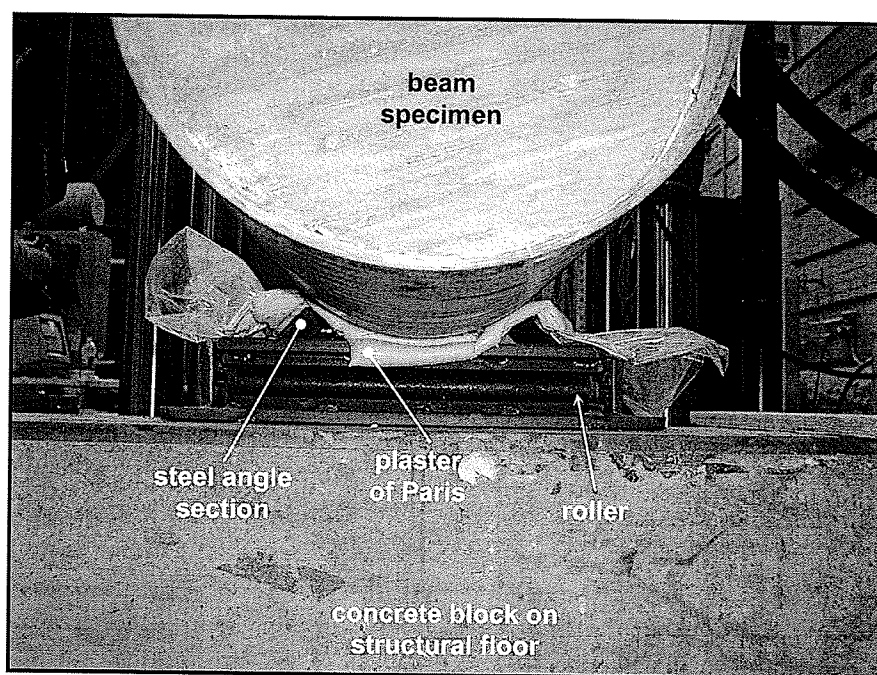
Symbol	Gauge Type		Output
	strain gauge oriented in longitudinal direction	FLA-6-11-5L (120-ohm resistance) type, produced by Tokyo Sokki Kenkyujo Co. Ltd., Japan	strain in direction of orientation
	strain gauge oriented in circumferential (transverse) direction		
	PI-gauge type displacement transducer		average strain over 200-mm gauge length, in direction of orientation
	linear motion transducer		mid-span deflection
	Mechanical dial gauge		relative slip between FRP shell and concrete core
	closed-loop 5000-kN MTS testing machine load cell		applied load (displacement controlled)

Figure 3.7: Instrumentation for beam specimen tests.



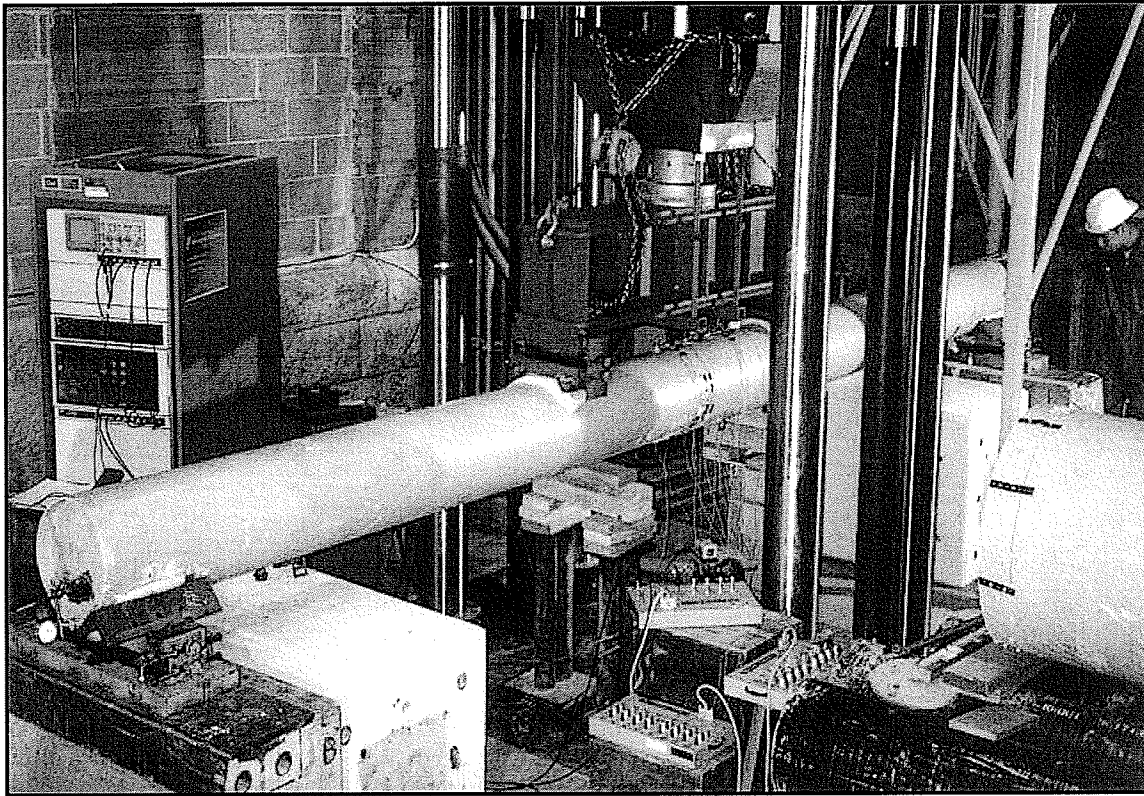


(a) Side view of roller support.

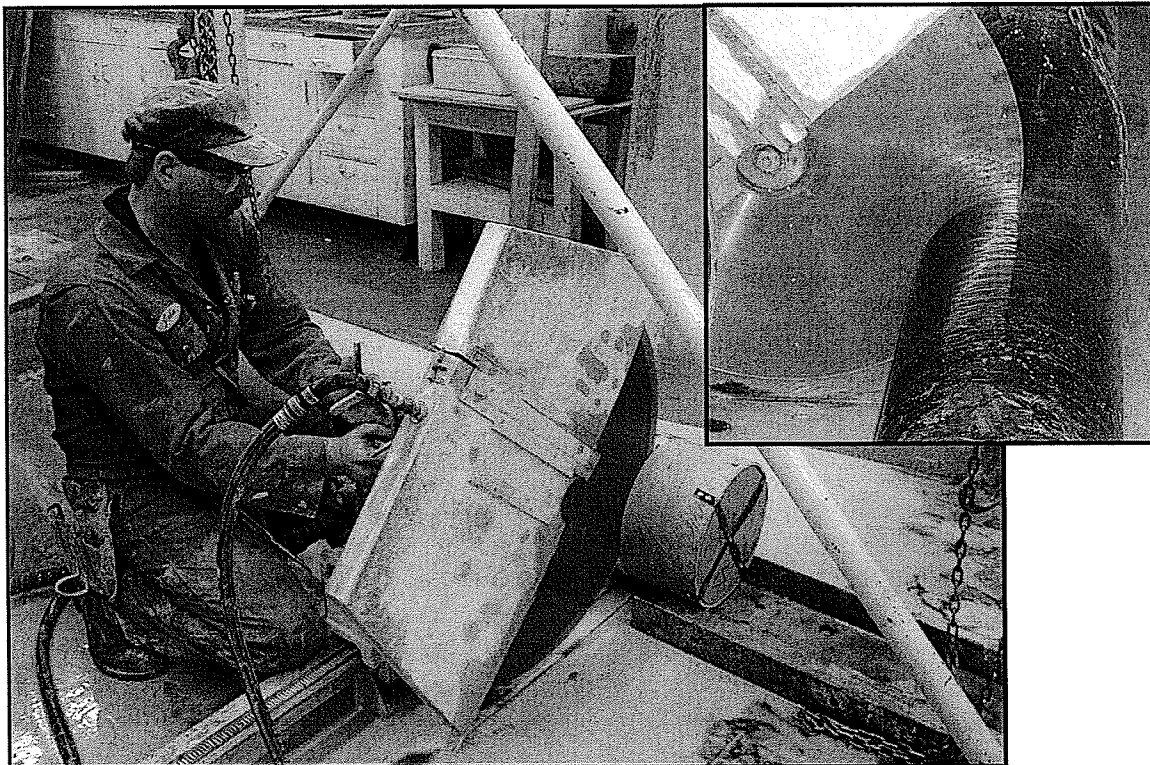


(b) End view of roller support.

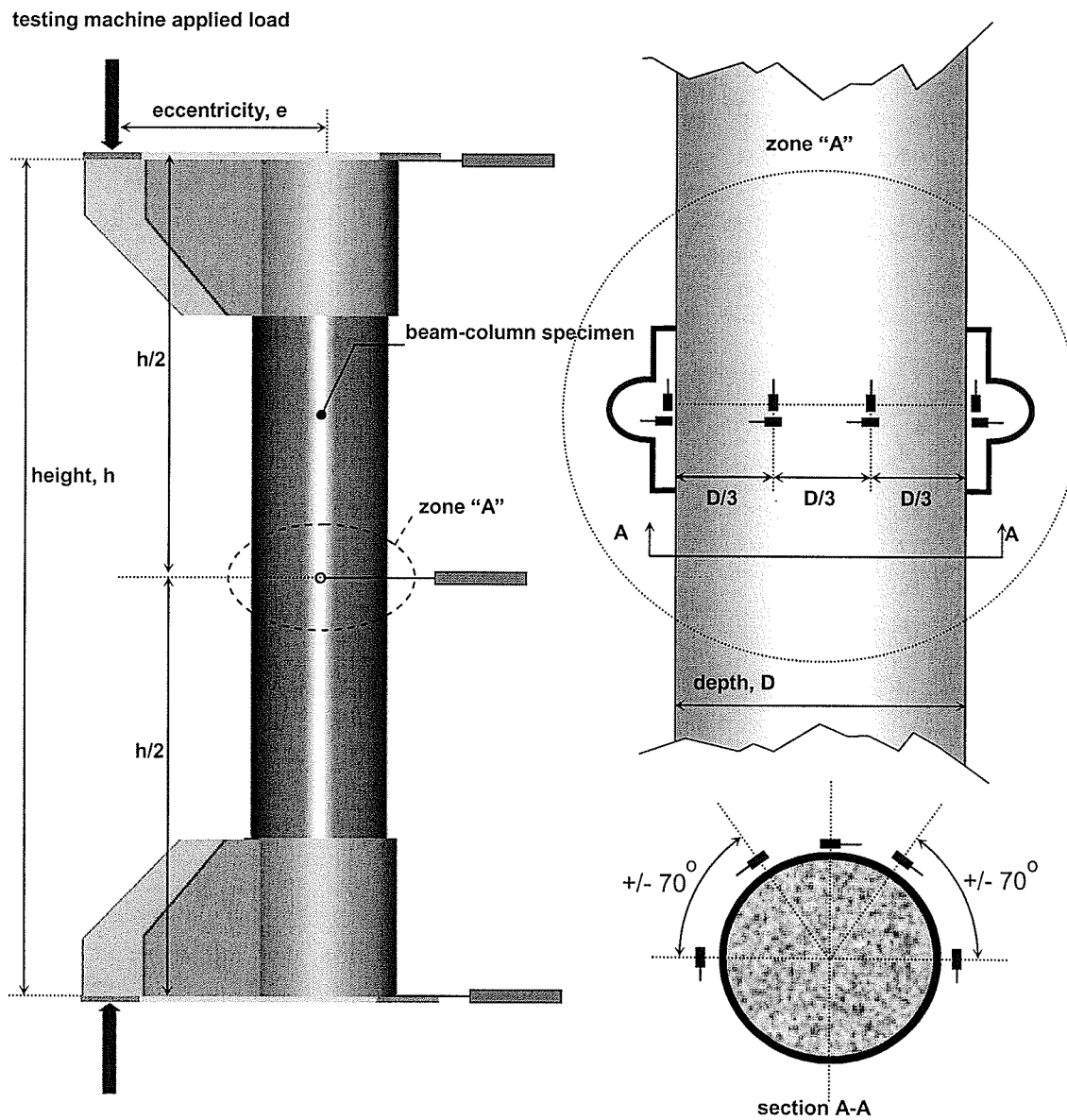
**Figure 3.8:** Roller support used in the beam specimen test setup.








**Figure 3.9:** Beam specimen test setup.



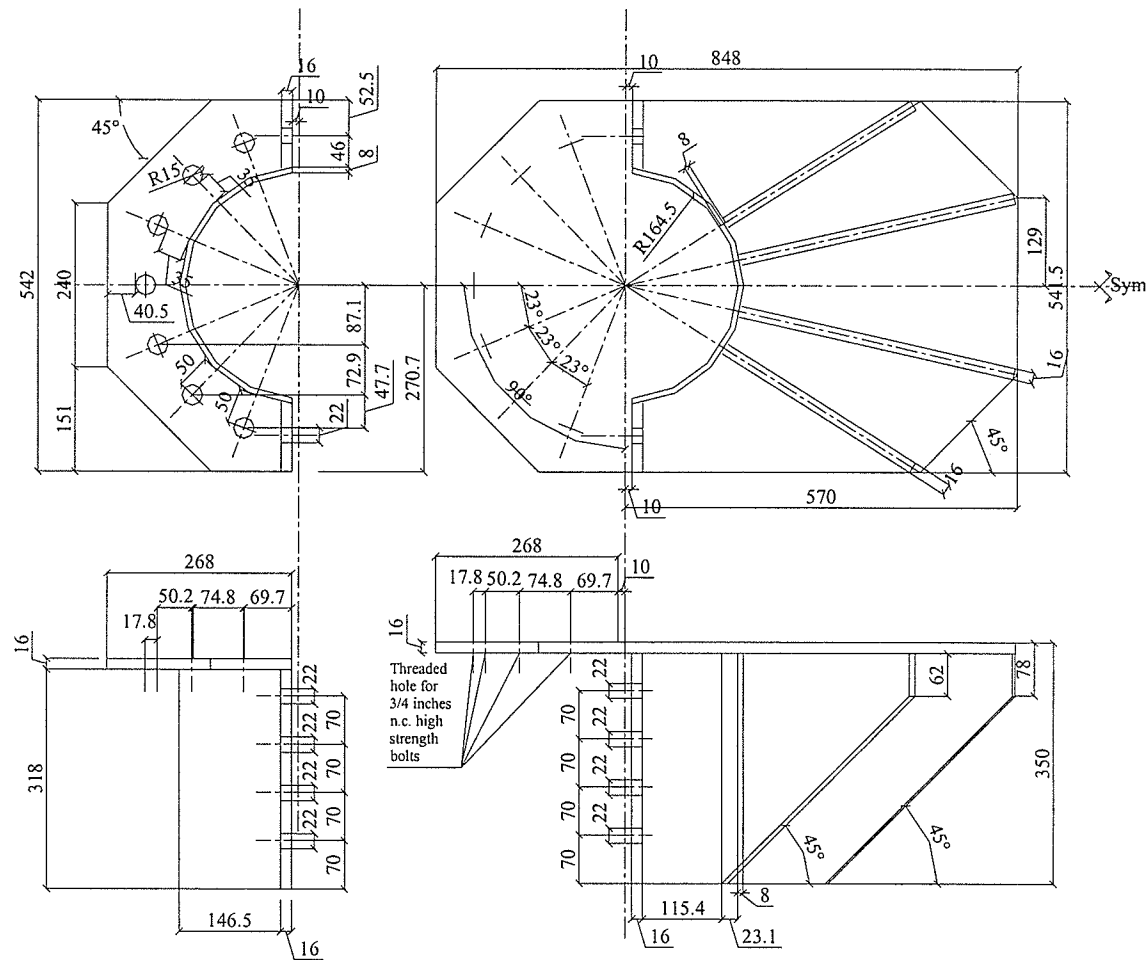
**Figure 3.10:** Cutting beam-column specimens from full-length members.



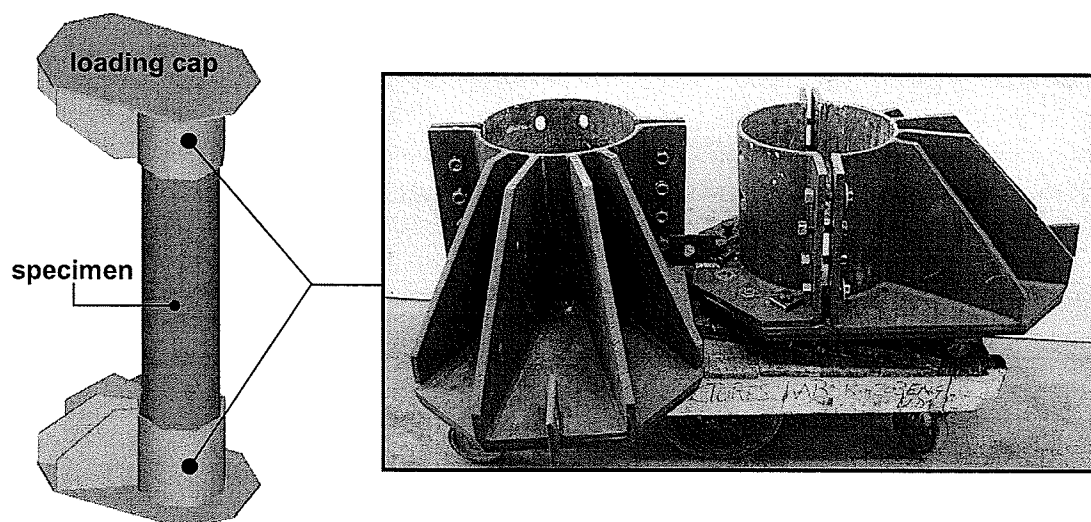
Symbol	Gauge Type		Output
	strain gauge oriented in longitudinal direction	FLA-6-11-5L (120-ohm resistance) type, produced by Tokyo Sokki Kenkyujo Co. Ltd., Japan	strain in direction of orientation
	strain gauge oriented in circumferential (transverse) direction		
	PI-gauge type displacement transducer		average strain over 200-mm gauge length, in direction of orientation
	linear variable displacement transducer (LVDT)		lateral deflection
	closed-loop 5000-kN MTS testing machine load cell		applied load (displacement controlled)

**Figure 3.11:** Instrumentation for beam-column specimen tests.





**Figure 3.12:** Configuration and dimensions of eccentric loading caps used in beam-column tests.



**Figure 3.13:** Eccentric loading caps used in beam-column tests.

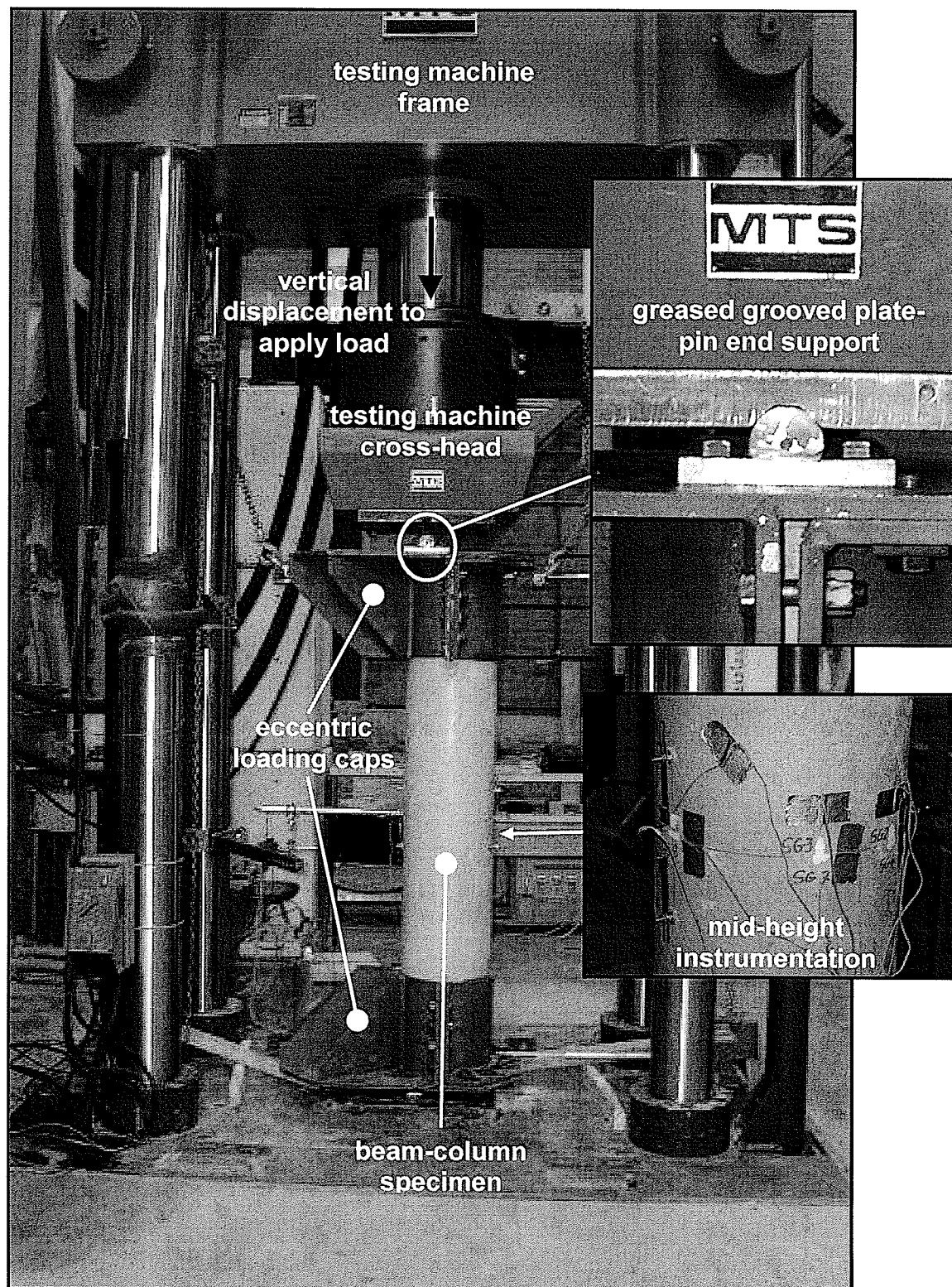


Figure 3.14: Beam-column specimen test setup.



**Figure 3.15:** Pure axial load specimen test setup and instrumentation.

## **Chapter IV:**

# **Experimental Results and Discussion**

### **4.1 Introduction**

The experimental program consisted of three main phases and a total of fifteen large scale test specimens. Phase I included testing of four beam specimens to study flexural behaviour of concrete filled FRP tubes. Combined bending moment and axial load behaviour was studied in Phase II by testing nine beam-column specimens. Two pure axial load specimens were tested in Phase III. This chapter summarizes the results from the three experimental phases, including the results of coupon tests performed to determine the properties of the FRP shells used in the experimental program. Descriptions of the specimens and testing methods are provided in Chapter 3.

### **4.2 Material Properties**

#### ***4.2.1 Effective Elastic Properties of Fibre Reinforced Polymer Shells***

Coupon tests were performed to determine the axial tensile strength and compressive strength, elastic moduli, and failure strains of the FRP laminates used in the experimental program. Section 3.2.1.1 describes the procedure used

to perform the tests. Figures 4.1 and 4.2 show the measured tensile stress-strain relationships and tensile Poisson's ratios of the E-glass/epoxy and E-glass/polyester shells. The behaviour is approximately linear up to failure, which occurred by sudden rupture of the coupons. Figure 3.3 in Chapter 3 shows typical tension coupons after failure. Figures 4.3 and 4.4 show the compressive stress-strain relationships and corresponding Poisson's ratios from the compression tests on the two types of shells. As described in section 3.2.1.1, both compression coupons failed prematurely due to local crushing of the FRP at the contact between the testing machine loading plate and the tube. Therefore, the compressive strength and failure strain from the tests may not be considered in the analysis due to the observed localized failure mode. However, the measured elastic moduli and Poisson's ratios in compression prior to failure are valid.

The effective elastic properties and strengths of the FRP tubes in the axial and hoop directions were also calculated using the laminated plate theory and Tsai-Wu failure criterion described in Chapter 5. In addition, some limited data was obtained from the manufacturer of the tubes. Table 4.1 summarizes the effective elastic properties and strengths of the FRP tubes based on the experimental results, calculations, and manufacturer's data. The manufacturer's data and calculated properties are also plotted in Figures 4.1 to 4.4.

### 4.2.2 Unconfined Concrete Compressive Strengths

As described in Chapter 3, some of the test specimens were tested over one and a half years after concrete casting. Although concrete cylinders cast at the time of fabrication were tested at 28-days to determine concrete compressive strengths, core samples were taken and tested to ascertain the concrete compressive strengths near the time of testing. These strengths are summarized in Tables 3.3 and 3.4.

### 4.2.3 Specimen Classification Based on Reinforcement Ratio

The test specimens in the experimental program are classified as either under-reinforced or over-reinforced by comparing their reinforcement ratios,  $\rho$ , to the balanced reinforcement ratio,  $\rho_{br}$ . The reinforcement ratio is defined as the area of the reinforcement divided by the area of the concrete core. For the case of circular concrete filled FRP tube members, the reinforcement ratio can be expressed:

$$\rho = \frac{D_{out}^2 - (D_{out} - 2t_{ss})^2}{D_{in}^2} \quad [\text{Eq. 4.1}]$$

where  $D_{out}$  = outside diameter of FRP shell

$D_{in}$  = inside diameter of FRP shell

$t_{ss}$  = effective structural thickness of tube wall

The balanced reinforcement ratio for FRP reinforced concrete is defined by the ACI's Committee 440 "State-of-the-art Report on Fibre Reinforced Plastic Reinforcement for Concrete Structures" as (ACI 440R, 1996):

$$\rho_{br} = 0.85 \beta_1 \frac{f'_c}{f_{fu}} \frac{\varepsilon_{cu}}{\varepsilon_{cu} + \varepsilon_{fu}} \quad [\text{Eq. 4.2}]$$

where  $\beta_1$  = concrete stress block calculation factor from clause 10.2.7.3 of the ACI Building Code Requirements for Structural Concrete (ACI 318M-02, 2002)

$$= 0.85 \text{ for } f'_c \leq 30 \text{ (MPa)} \quad [\text{Eq. 4.3a}]$$

$$= 0.85 - 0.05 \left( \frac{f'_c - 30}{7} \right) \text{ for } 30 < f'_c < 58 \text{ (MPa)} \quad [\text{Eq. 4.3b}]$$

$$= 0.65 \text{ for } f'_c \geq 58 \text{ (Mpa)} \quad [\text{Eq. 4.3c}]$$

$$f'_c = \text{concrete compressive strength}$$

$$f_{fu} = \text{FRP tube axial tensile strength}$$

$$\varepsilon_{cu} = \text{concrete crushing strain}$$

$$\varepsilon_{fu} = \text{FRP tube axial tensile rupture strain}$$

A reinforcement ratio lower than the balanced reinforcement ratio indicates an under-reinforced flexural member. Failure is sudden, but is typically accompanied by excessive concrete cracking at the tension side and member deformation, if a sufficiently low reinforcement ratio is selected. A member is considered over-reinforced when the reinforcement ratio is higher than the balanced reinforcement ratio. Failure of over-reinforced flexural members also occurs

suddenly, but without significant visible warning signs like large member deformations or extensive concrete cracking.

The balanced reinforcement ratios of the specimens in the experimental program are calculated using the unconfined concrete compressive strengths of their concrete cores and the tensile properties of the FRP shells. The concrete cores' compressive failure strains were not available from cylinder testing. They are calculated using equations 5.54b and 5.55 to 5.57 in Chapter 5. Two balanced reinforcement ratios are calculated for each specimen, one using the experimental tensile strengths and failure strains from the FRP axial tension coupon tests, and the other using failure stress and strain predictions from the laminated plate theory and Tsai-Wu FRP failure criterion.

Table 4.2 presents the results of the calculations. The reinforcement ratios of the E-glass/epoxy and E-glass/polyester specimens are 8.41 and 8.05-percent respectively. These are higher than each of the calculated balanced reinforcement ratios using the experimental and calculated tube properties, therefore all specimens are classified as over-reinforced.

### **4.3 Experimental Phase I: Flexural Tests**

Four beam specimens were tested in the first phase of the experimental program. Two of the beams were fabricated using E-glass/epoxy FRP shells and the other two using E-glass/polyester FRP shells. Specimens were simply



supported at the ends and tested in flexure by applying two equivalent point loads positioned symmetrically with respect to the span. One of each type of specimen was tested with a 5.5-metre span, and the other with a 5.0-metre span. Chapter 3 describes the laminate structures of the FRP tubes, specimen fabrication process, specimen dimensions, specimen instrumentation, and details of the testing method and apparatus. The beam test experimental results are discussed in the following sections.

#### ***4.3.1 Strengths and Failure Modes***

Each beam specimen was loaded until failure. The ultimate applied loads and corresponding bending moment capacities were 149-kN and 149-kNm for specimen BM-E-1, 177-kN and 155-kNm for specimen BM-E-2, 120-kN and 120-kNm for specimen BM-P-1, and 143-kN and 125-kNm for specimen BM-P-2. The applied loads, which are the sums of the two equivalent applied point loads in the four-point bending apparatus, varied between similarly composed specimens because of different spans, whereas calculated moments were similar because the ability of a particular cross-section to sustain bending moment is independent of the span.

All the specimens failed in tension within the maximum moment region between the applied point loads. In each case, several snapping sounds were heard as the fibres began to rupture, followed immediately by sudden, catastrophic failure. Figure 4.5 shows a typical BM-E-1 and BM-E-2 specimen failure. The specimens

failed by rupture of the longitudinally oriented fibres in tension, accompanied by splitting of the circumferential laminas. The maximum strains measured at the extreme tension faces of specimens BM-E-1 and BM-E-2 were 19.9 and 19.2-millistrain respectively, immediately prior to failure. Figure 4.6 shows the failures of specimens BM-P-1 and BM-P-2. Failure was initiated by rupture of a 34-degree lamina in the shell, accompanied by a rapid release of energy that caused strips of the outer layers of fibres on the shell to peel away from the underlying layers, causing the frayed appearance shown in the figure. The maximum strains measured at the extreme tension faces of specimens BM-P-1 and BM-P-2 were 15.8 and 16.1-millistrain respectively, immediately prior to failure. It is unclear why the maximum tensile strains in each beam test were higher than those presented in Table 4.1 from the tension coupons, calculations using laminated plate theory and the Tsai-Wu failure criterion, and manufacturer's data.

It was observed that flexural capacity was not significantly affected by the concrete compressive strength. Although the concrete strength of BM-E-2 was 42-percent higher than the concrete strength of BM-E-1, the flexural capacity was only 4.03-percent higher. Similarly, the flexural capacity of BM-P-2 was only 4.17-percent higher than BM-P-1, although the concrete strength was 12-percent higher. The full capacity of the concrete in compression was not realized because failure was governed by the tensile strengths of the FRP shells. Specimen failure would have occurred due to crushing of the concrete in the

compression zone if the full capacity of the concrete was reached. The E-glass/epoxy FRP shells had higher tensile strengths than the E-glass/polyester shells, causing specimens BM-E-1 and BM-E-2 to have 24-percent higher flexural capacities than specimens BM-P-1 and BM-P-2.

### ***4.3.2 Deflections and Concrete Cracking***

Figure 4.7(a) compares the load-deflection behaviour of the two 5.5-metre span beams, BM-E-1 and BM-P-1. The sum of the two equal point loads applied to the member is plotted on the load axis and the resultant mid-span deflection of the member is plotted on the deflection axis. In general, the slope of the load-deflection curve of beam BM-E-1 is slightly larger than the slope of specimen BM-P-1's load-deflection curve at a given deflection, indicating that BM-E-1 had a higher flexural stiffness. The specimens had similar cross-section dimensions and concrete strengths, therefore specimen BM-E-1's higher flexural stiffness is attributed to its higher FRP shell tensile and compressive elastic moduli compared to specimen BM-P-1. Figure 4.7(b) shows that specimen BM-E-2 had a higher flexural stiffness than specimen BM-P-1. In this case a portion of the effect can be attributed to a significantly higher concrete compressive strength and resulting higher concrete elastic modulus, in addition to the difference in FRP shell stiffness.

The effect of concrete compressive elastic modulus on stiffness is illustrated in Figure 4.8. Moment-deflection behaviour is plotted to compare specimens with

the same FRP shell but different spans, eliminating span as a variable. In each case the specimen with a higher concrete elastic modulus, indicated by a larger concrete compressive strength, has a higher flexural stiffness than its otherwise similar counterpart.

There are several sudden drops in load and moment on the load and moment-deflection curves of each beam specimen. The load and moment prior to each drop are subsequently recovered with increased deflection, followed by continuing increase in load, moment, and deflection, until the next drop. Drops in load occurred because the tests were performed under displacement control. Sudden increases in deflection resulting in horizontal shifts in the moment and load-deflection curves would have occurred if the tests had been load controlled.

The first drop in each case is attributed to initial cracking of the concrete core. As expected, the stiffness of each beam decreased significantly as it passed from uncracked to cracked section behaviour. Subsequent drops indicate further cracking or slip of the concrete core with respect to the FRP shell, accompanied by slight decreases in flexural stiffness in each case. Specimens BM-P-1 and BM-P-2 exhibited a larger number of significant load drops than specimens BM-E-1 and BM-E-2. In all cases the drops in load were accompanied by loud sounds and slip of the concrete core relative to the FRP shell in the longitudinal direction. Relative slips between the concrete core and FRP shell were measured on specimens BM-E-1 and BM-P-1 only and are presented in Figure

4.9. The total slips measured at each end of specimens BM-P-1 and BM-E-1 were approximately 2.17 and 1.00-mm respectively.

Specimens BM-P-1 and BM-E-1 had identical spans and were nearly the same dimensions, therefore the higher slips measured in specimen BM-P-1 are attributed to lower mechanical bond strength between the concrete core and interior surface of the FRP shell. Figure 4.10 shows that the interior surface of the E-glass/polyester tubes was much smoother than the E-glass/epoxy tubes, which had a shallow ridged profile from the manufacturing process. The step-like pattern in the load-slip behavior of specimen BM-P-1 may have been caused by sudden release of accumulated energy during concrete cracking due to the low bond strength between the shell and concrete core. The load-slip behaviour of specimen BM-E-1 was more gradual because strain energy was dispersed more effectively along the member through better bond between the concrete core and FRP shell, avoiding sudden, large releases of energy during concrete cracking.

The FRP shell was removed from one-half of specimen BM-P-2 after testing to examine the concrete core. Figure 4.11 shows the exposed concrete core. Seven discrete, widely spaced cracks were observed, spaced at 150, 150, 230, 275, 385, and 300-mm from the beam failure location out towards the support location. The wide crack spacing observed is another indication of the low bond strength between the concrete core and FRP shell. No other damage to the concrete core was observed between the cracks. Although the other beam specimens were not cut open to examine their concrete cores, it is assumed that

they had similar crack patterns due to poor bond between the shell and concrete core. Specimens BM-E-1 and BM-E-2 may have contained more cracks due to the slightly better bond between their FRP shells and concrete cores.

### ***4.3.3 Axial Strains and Neutral Axis Depths***

Figures 4.12 and 4.13 show the moment-axial strain relationships measured during the beam tests. The strains were measured in the longitudinal direction at the extreme tensile and compressive faces of the beams. As described in section 4.3.1, the moment capacities and maximum tensile strains of each pair of similarly composed beams were nearly the same. The maximum compressive strains were 7.4, 6.8, 5.9, and 7.1-millistrain for specimens BM-E-1, BM-E-2, BM-P-1, and BM-P-2 respectively, well below the compressive failure strains of the FRP tubes shown in Table 4.1.

The load drops during testing were accompanied by small, temporary decreases in tensile and compressive strains in beams BM-P-1 and BM-P-2. This phenomenon is attributed to an impact effect caused by the sudden release of energy during concrete cracking and slip described in section 4.3.2. The moments and axial strains in specimens BM-E-1 and BM-E-2 increased more gradually because a smaller number and lower magnitude of load drops occurred.

Figures 4.14 and 4.15 show the neutral axis depth-moment relationships in each beam test, calculated using the axial compressive and tensile strains from gauges mounted on the outer surface of the beams. Neutral axis depth calculations below 25-kNm moment are not plotted because noise caused by significant fluctuations in gauge outputs at low strains rendered them invalid. It is expected that the neutral axis depth would be slightly above mid-height prior to initial concrete cracking because the FRP shells have higher stiffness in compression than tension. Once the concrete cracks the neutral axis shifts up in order to balance the forces in the cross-section.

Neutral axis depths were also measured after failure by visually identifying the concrete compression zone on the failed beam's cross-sections, as shown in Figure 4.16. The measurements were taken for all beams except BM-P-1. The measured values were 95, 92, and 75-mm for beams BM-E-1, BM-E-2, and BM-P-2 respectively. The measured depths agreed reasonably well with those calculated with strain measurements for specimens BM-E-1 and BM-E-2. However, the neutral axis depth measured on failed specimen BM-P-2 was significantly lower than the value calculated from the strain measurements. In this case, increasing slip of the concrete core with respect to the FRP shell caused increasing loss in composite action between the shell and concrete, decreasing the concrete contribution to cross-section equilibrium. The member behaved gradually more like an empty FRP shell where the neutral axis depth would be near mid-height. The calculated neutral axis depth increases with increasing

applied load, reflecting the loss of composite action because it is calculated from strain measurements on the surface of the FRP shell. The measured depth on the failed cross-section was the neutral axis depth at an early load stage when the beam behaved compositely. Nearly full composite action occurred throughout loading of specimens BM-E-1 and BM-E-2, until shortly before failure. Figures 4.17 to 4.20 show the axial strain distributions across the depth of each beam at mid-span for moments up to failure, measured by surface mounted strain gauges at the top, one-third the depth, two-thirds the depth, and bottom of each cross-section. The axial strain distributions in the FRP shell remained linear throughout loading in each case.

#### ***4.3.4 Circumferential Strains and Concrete Confinement***

Figures 4.21 to 4.24 show the circumferential-axial strain relationships measured by orthogonally oriented strain gauges at the top, one-third the depth, two-thirds the depth, and bottom of each beam specimen at mid-span. The data shows that hoop stresses developed in the FRP shells independent of flexural stresses in the beams. This is immediately evident by examining the data from the gauges located at one-third the depth of the section. It is expected that axial tensile strains would be accompanied by circumferential compressive strains due to Poisson's effect, because the gauges at one-third the depth were located below the calculated neutral axis depth in all the beams. Because tensile strains were measured in both the axial and circumferential directions, it is concluded that tensile hoop stresses not directly associated with longitudinal stresses from



beam flexure occurred. The additional hoop stresses are likely due to concrete expansion in the compression zone. Hoop tensile stresses develop in the FRP shell from radial confining pressure at the interface between the shell and concrete core, as the shell resists concrete radial expansion caused by internal compressive stresses. The concrete confinement effect is described in detail in section 5.2.2.3.

The expected relationships between axial and circumferential strains, based on the FRP shell Poisson's ratios determined in coupon testing, are superimposed on the beam test data in Figures 4.21 to 4.24. In Figure 4.21, the beam test data from the top of beam BM-E-1 diverges from the Poisson's ratio line, with higher circumferential tensile strains at given axial compressive strains, indicating tensile hoop straining not attributed to the flexural axial strain in the shell.

Although the additional hoop stress and strain are caused by expansion of the concrete in the compression zone, hoop tensile stresses must also occur in the tension zone to maintain force equilibrium in the shell, assuming the effect of friction between the concrete and FRP is negligible. Comparing the test data from the bottom of beam BM-E-1 to the Poisson's ratio line demonstrates that hoop tensile stresses in the tension zone occur, because measured circumferential compressive strains at given axial tensile strains are lower than the Poisson's ratio prediction. Data from beam specimens BM-P-1 and BM-P-2 shown in Figures 4.22 and 4.24, respectively, indicates similar behaviour. The strain gauge readings at two-thirds the depth and bottom of beam BM-E-2,

shown in Figure 4.23, are disregarded because it is assumed that they were affected by a concrete crack at the gauge location.

#### **4.4 Experimental Phase II: Combined Axial Load and Bending Moment Tests**

A total of nine beam-column specimens were tested in the second phase of the experimental program. Four specimens were fabricated using E-glass/epoxy FRP shells and the other five with E-glass/polyester FRP shells. The specimens were tested vertically in a specially designed loading apparatus that applied a coupled axial load and bending moment on the specimen by applying the axial load at an imposed eccentricity. The composition and configuration of the specimens, and a description of the testing apparatus, instrumentation, and method are included in Chapter 3. The beam-column experimental results are discussed in the following sections.

##### **4.4.1 Specimen BC-P-e10**

Figures 4.25 and 4.26 show the load-deflection and moment-deflection behaviours of specimen BC-P-e10. The axial load and moment initially increased rapidly with very little lateral deflection. The total moment in this stage was mainly due to primary moment caused by increasing axial load at the original 10-millimetre eccentricity. It is believed that the peak unconfined concrete stress in the core was reached, causing a reduction in concrete and member stiffness and subsequent increase in lateral deflection just before the initial peak axial load. The peak in axial load coincided with the beginning of failure of the FRP shell

near the top of the specimen. The outer laminas delaminated and buckled outward in the extreme compression zone, as shown in Figure 4.27. The axial load dropped from a peak of approximately 4200-kN when failure of the shell began, but the specimen continued to sustain significant axial load. A horizontal shift in the moment-deflection relationship occurred when the axial load dropped. Lateral deflection increased due to the sudden loss in stiffness, but total moment did not change because the decrease in primary moment from the loss of axial load was overcome by an increase in secondary moment from the larger lateral deflection, as shown in the axial load-moment relationship in Figure 4.28.

Figure 4.29 shows the moment-axial strain behaviour of the specimen. The maximum and minimum axial compressive strains increased in magnitude prior to the initial FRP shell failure. A decrease in compressive strain due to axial load occurred when the shell began to fail, accompanied by increasing flexural strains due to increasing moment, causing the total compressive strain in the minimum compression zone to begin decreasing. The minimum compressive strain did not become tensile before failure, indicating that the neutral axis depth remained outside the cross-section throughout the test, as shown in Figure 4.30.

Further axial load drops occurred as the test continued, caused by sudden propagation of the damage in the shell from the original failure location. Initially, some axial load recovery occurred after each drop, but the axial load decreased after the drops near the end of the test. While the axial load generally decreased

to failure, the total moment increased due to gradually increasing secondary moment with increasing lateral deflection, as shown in Figure 4.28. Specimen failure occurred when the FRP shell split diagonally in several places, parallel to the lamina directions, and the shell crushed on the opposite half of the specimen from the original delamination and buckling location. The specimen did not resist significant axial load past this point. The failure region is shown in Figure 4.31. The ultimate axial load and moment at mid-height at failure were 3322-kN and 70-kNm respectively. The maximum compressive strain measured at mid-height at failure was 6.5-millistrain. However, the measured strain in this case likely does not reflect the true failure strain of the laminate due to the localized failure mode.

The top of the specimen was examined after the eccentric loading cap was removed. Deformation of the concrete, shown in Figure 4.32, was observed on the extreme compression half of the cross-section. It is assumed that this deformation occurred due to softening of the concrete in the extreme compression region at the height of the initial lamina buckling location. The initial delamination and buckling of the shell near the top of the specimen may have caused a localized reduction in stiffness, forcing the concrete to resist most of the load in the region. This may have led to a large deformation of the concrete without any confinement by the shell because it was already severely damaged. Further damage to the shell occurred during the deformation, causing the localized failure observed.

Figure 4.33 shows the circumferential-axial strain behaviour of specimen BC-P-e10. The behaviour suggests that some concrete confinement may have developed near the end of the test at mid-height. Confinement occurs when a concrete core dilates radially at a higher rate than the FRP shell, forcing the shell to resist the radial expansion. A confining pressure develops at the interface between the concrete core and FRP shell, inducing tensile hoop stresses in the shell that cause tensile hoop strains. If no concrete confinement occurred in the test, it would be expected that the circumferential-axial strain relationship in the maximum compression zone would follow the predicted response from the compressive Poisson's ratio. However, if confinement occurred, the slope of the relationship would be higher than predicted by Poisson's ratio because an additional hoop tensile strain would be imposed by the confinement effect.

Initially, the hoop-axial strain relationship in the maximum axial compressive strain zone of the specimen followed the predicted response from the Poisson's ratio determined in coupon testing, indicating that no additional hoop stresses due to confinement were present. The slope increased at 6.4-millistrain compressive strain, indicating the initiation of confinement. However, this occurred very near failure, and the strain measurements were taken at mid-height, not near the failure location. It is unlikely that any confinement developed near the failure region due to the severe damage to the shell at that location by this point in the test. Therefore, the localized failure prevented the specimen from

reaching its full, potential capacity if confinement occurred effectively to enhance the performance.

#### **4.4.2 Specimen BC-P-e30**

Beam-column specimen BC-P-e30 exhibited behaviour similar to specimen BC-P-e10. Figures 4.25 and 4.26 show the axial-deflection and moment-deflection behaviours of the specimen. Axial load and moment initially increased with no lateral deflection in the expected direction, although a negative deflection less than 0.5-millimetres was measured prior to the peak axial load. The negative deflection reading may have been caused by some initial out-of-straightness of the specimen or seating in the testing apparatus under load. Initiation of failure of the FRP shell suddenly occurred by delamination and outward buckling of the outer lamina in a small area slightly above mid-height, in the maximum compression zone. A drop in axial load from a peak of approximately 3550-kN and an increase in lateral deflection accompanied the failure. However, the secondary moment did not increase enough to overcome the loss in primary moment, causing the total moment to drop, as shown in the axial load-moment behaviour in Figure 4.28. It is believed that the peak unconfined concrete stress was not reached in this case because the peak axial load did not occur after some lateral deflection as with specimen BC-P-e10, indicating that softening of the concrete likely did not occur. Significant lateral deflection only began after the initial failure of the FRP shell.

Similar to specimen BC-P-e10, the axial load generally decreased after initiation of failure in the shell. The total moment remained almost constant at the level after the initial drop due to increasing secondary moment. A pattern of incremental further propagation of the damage in the shell and corresponding axial load drops continued until a final large drop in load occurred. The specimen no longer resisted significant axial load after this point. The compression failure region is shown in Figures 4.34 and 4.35. Although some splitting of the FRP shell along the lamina directions occurred, no crushing of the fibres or differential deformation of the concrete core were observed as with specimen BC-P-e10. The axial load and moment at mid-height at failure were 2925-kN and 101-kNm. The maximum compressive strain measured at mid-height was 9.9-millistrain.

Figure 4.29 shows the moment-axial strain behaviour of the specimen. The beginning of shell failure occurred when the maximum compressive strain reached 3.7-millistrain at a moment of 106-kNm. Unlike specimen BC-P-e10, the minimum compressive strain did not initially increase rapidly, reaching only 0.2-millistrain compression at 80-kNm moment. This indicates that tensile strain due to flexure was almost equivalent to compressive strain due to axial load to this point. The strain began to return to zero above 80-kNm moment, becoming tensile just before the shell began to fail. The transition to tension caused the neutral axis depth, shown in Figure 4.30, to move from outside the cross-section to within the cross section. The axial strain reversed direction again past the load drop. Because the axial load did not increase and the moment either remained

constant or increased, the axial strain should only have increased in tensile magnitude if no other effects were present. However, the axial strain actually decreased, indicating that a hoop tensile strain in the shell must have occurred, causing a superimposed compressive strain in the axial direction due to Poisson's effect. The hoop strain was likely caused by radial confining pressure developed at the interface between the concrete core and FRP shell. The neutral axis depth in Figure 4.30 increased when this occurred because it was calculated based on the measured extreme compressive and tensile axial strains. Because it only reflects the actual depth of uncracked concrete core when the measured axial strains are caused by flexural deformation only, and no loss in strain compatibility between the shell and concrete core has occurred, the neutral axis depth is disregarded past the axial load drop.

The circumferential-axial strain behaviour plotted in Figure 4.36 supports the assertion that concrete confinement occurred. The circumferential-axial strain relationship at the maximum axial compression zone is distinctly bi-linear. The initial slope prior to the transition point is close to the expected slope predicted with the experimentally determined compressive Poisson's ratio, indicating no confinement. The transition point coincides with first failure of the FRP shell. A sudden increase in slope occurs past the transition point, indicating the presence of a superimposed hoop tensile strain in addition to the strain from Poisson's effect. It is believed that a sudden loss in shell stiffness due to initiation of shell failure caused the concrete to sustain a larger proportion of the applied load,



increasing the lateral strain in the concrete enough to initiate confinement by contact with the shell. The circumferential-axial strain relationship at the opposite side of the shell also demonstrates onset of confinement. If confinement did not occur, it would be expected that the hoop strain at this location after the shell failure began would increase in compression due to Poisson's effect because the axial strain was tensile. However, an increasing tensile hoop strain was actually measured, indicating tensile hoop stress due to confinement. The tensile axial strain also began moving towards compression due to the increasing tensile hoop strain and Poisson's effect.

#### **4.4.3 Specimen BC-P-e100**

The axial load-deflection and moment-deflection behaviours of specimen BC-P-e100 are shown in Figures 4.25 and 4.37. The axial load, deflection, and moment increased continuously until delamination and buckling of the FRP shell occurred in a small area in the maximum compression zone slightly below mid-height, at approximately 1715-kN axial load, accompanied by drops in the axial load and moment. Axial load and moment subsequently increased to failure, as shown in Figure 4.28, with one small drop. The moment at failure was higher than the initial peak moment, but the initial peak axial load was not recovered. The failure region is shown in Figure 4.38. No other significant damage to the shell occurred outside the region shown in the figure because the initial failure in the shell did not propagate significantly. The axial load and moment at mid-height at failure

were 1664-kN and 200-kNm. The maximum compressive strain measured at mid-height was 12.2-millistrain.

The first sign of FRP shell failure occurred when the maximum compressive and tensile strains were 4.2 and 4.0-millistrain respectively, as shown in the moment-axial strain relationship in Figure 4.39. The sudden loss in shell stiffness caused the concrete core to resist more of the applied load, causing increased radial displacement of the concrete and initiation of confinement. The presence of confinement is demonstrated in the circumferential-axial strain relationship in Figure 4.40 by a change in slope at the maximum axial compression and tension zones. The initial slopes agree well with the predictions using Poisson's ratio determined in coupon testing. Once the initial axial load drop occurred, the slopes changed, indicating hoop tensile strain from concrete confinement.

The neutral axis depth-moment behaviour is shown in Figure 4.30. The neutral axis depth decreased slightly throughout the test, but remained just below the mid-height of the cross-section. The portion of the behaviour past the initial peak moment of 187-kNm is disregarded because it is calculated based on axial strains in the FRP shell, which were affected by compressive failure of the shell and the confinement effect above 187-kNm moment.

#### 4.4.4 Specimen BC-P-e200

The axial load-deflection, moment-deflection, and axial load-moment behaviours of specimen BC-P-e200 are shown in Figures 4.25, 4.37, and 4.41. The axial load, lateral deflection and moment gradually increased until failure, with one small load and moment drop likely caused by concrete cracking. Although some sounds were heard during the test, there were no visible signs of impending failure on the surface of the FRP shell, like those observed during testing of specimens BC-P-e10, BC-P-e30, and BC-P-e100. The specimen failed suddenly in the maximum tension zone at mid-height. As shown in Figure 4.42, failure was characterized by tensile rupture of shell laminas parallel to the fibre directions. The axial load and bending moment at mid-height at failure were 878-kN and 203-kNm. The maximum tensile strain measured at mid-height was 17.1-millistrain.

Figure 4.39 shows the specimen's moment-axial strain behaviour. A small dip in the moment occurred at 158-kN axial load, coinciding with the onset of confinement demonstrated in the circumferential-axial strain behaviour shown in Figure 4.43. The change in slope of the circumferential-axial strain relationship at the maximum compressive axial strain location is not as pronounced as with specimens BC-P-e30 and BC-P-e100, indicating a lower level of confinement. This likely occurred because the neutral axis depth was much smaller in specimen BC-P-e200 than specimens BC-P-e30 and BC-P-e100 because of a higher moment. A smaller area of concrete was in compression, decreasing the

amount of hoop stress developed in the shell because a smaller shell interior surface area had to resist radial expansion of the concrete.

The neutral axis depth-moment relationship is shown in Figure 4.30. The neutral axis depth decreased slightly with increasing moment, remaining above the mid-height of the cross-section. Similar to specimen BC-E-e100, the data is disregarded after concrete cracking occurred and confinement began at 158-kNm moment.

#### **4.4.5 Specimen BC-P-e300**

Figures 4.25, 4.37, and 4.41 show the axial load-deflection, moment-deflection, and axial load-moment behaviours of specimen BC-P-e300. A sharp drop in moment and axial load occurred at 22-kNm moment, accompanied by a horizontal shift in the moment-deflection curve. This likely occurred due to first cracking of the concrete core in tension. The axial load, deflection, and moment subsequently increased continuously until failure, with no further load or moment drops. As with specimen BC-P-e200, there were no visible signs of impending failure on the FRP shell. The specimen failed suddenly in the maximum tension zone below the upper eccentric loading cap. Figure 4.44 shows the failure region. The axial load and moment at mid-height at failure were 524-kN and 172-kNm. The maximum tensile strain measured at mid-height was 17.1-millistrain.

A change in slope of the circumferential-axial strain relationship in the maximum compression zone occurred at 5-millistrain axial compressive strain, as shown in Figure 4.45. As with specimen BC-P-e200, the slope change was very small, and no transition point was observed in the circumferential-axial strain relationship at the other side of the cross-section, indicating that very little confinement occurred.

The neutral axis depth-moment relationship is shown in Figure 4.30. Although unexpected, the relationship demonstrates a small increase in neutral axis depth with increasing moment near the end of the test. This may be due to the phenomenon described in section 4.3.3. Some loss of strain compatibility between the shell and concrete core may have occurred after concrete cracking, causing a loss in flexural stiffness that made the specimen behave progressively more like an empty FRP shell, where the neutral axis depth would be near the cross-section's mid-height. The neutral axis depth appears to increase because the axial strains used to calculate it were measured on the surface of the FRP shell.

Specimens BC-P-e200 and BC-P-e300 did not carry further loads after failure of their FRP shells because the tensile failure mode was catastrophic, not progressive like the compression failure modes of specimens BC-P-e10, BC-P-e30, and BC-P-e100.

#### 4.4.6 Specimen BC-E-e30

Figures 4.46 and 4.47 show the axial load-deflection and moment-deflection behaviours of specimen BC-E-e30. The axial load and moment increased continuously to a peak at approximately 3905-kN axial load, decreased slightly, and then increased again until failure. The axial load increased very little after the drop, and did not reach the initial peak value before failure. The total moment increased above the initial peak due to a significant contribution from secondary moment, as shown in the axial load-moment behaviour in Figure 4.48. No FRP shell damage or sharp drops in axial load were observed during the transition from peak axial load to post-peak behaviour. The specimen failed suddenly in the maximum compression zone, approximately one-third the height from the bottom of the specimen. It is believed that radial concrete confining pressure coupled with the applied axial load and moment induced a biaxial state of stress in the FRP shell that caused rupture of the fibres in the hoop direction, accompanied by crushing of the shell in the axial direction. Distinct hoop tensile rupture of the shell and crushing in the axial direction were observed in the failure region, shown in Figures 4.49 and 4.50. Sounds were heard and the colour of the shell gradually lightened at the failure location shortly before failure. The colour change of the shell is attributed to yielding of the polymer matrix in the laminate. Other signs of impending failure like the progressive lamina buckling observed in the low eccentricity E-glass/polyester shell specimens did not occur. The axial load and bending moment at mid-height prior at failure were 4010-kN and 217-

kNm. The maximum compressive strain measured at mid-height was 16.7-millistrain.

The moment-axial strain relationship shown in Figure 4.51 indicates that the specimen was originally entirely in compression because flexural tensile strains at the minimum compression zone were not large enough to overcome the compressive strain from the axial load. The minimum compression side of the cross-section eventually went into tension, just before the moment reached the original peak. The peak occurred when the maximum compressive and tensile strains were 6.3 and 0.5-millistrain respectively. The circumferential-axial strain relationship in Figure 4.52 suggests that confinement of the concrete began prior to the initial peak load and moment, at approximately 3.6-millistrain maximum compressive strain and 0.5-millistrain compressive strain at the opposite side of the cross-section. The shape of the moment-axial strain curve after the initiation of confinement indicates that the confined concrete reached a peak stress coinciding with the initial peak moment and load, the concrete stress decreased slightly causing the decrease in axial load and moment, and then began increasing again, causing increasing axial load and moment until failure. The gradually decreasing slope of the circumferential-axial strain relationship at the maximum compression zone towards the end of the test suggests that confinement decreased as the specimen approached failure.

Figure 4.53 shows the neutral axis depth-moment behaviour. The neutral axis depth decreased with increasing moment, dropping suddenly at the initial peak moment. It is important to note that the neutral axis depth may not reflect the true depth of uncracked concrete past the peak because the axial strains measured on the surface of the FRP shell, used to calculate the neutral axis depth plotted, are affected by circumferential strains from confinement.

#### **4.4.7 Specimen BC-E-e100**

Figures 4.46 and 4.47 show the axial-load deflection and moment-deflection behaviours of specimen BC-E-e100. The axial load and moment increased continuously at first. A sudden drop occurred after the axial load reached a peak at 1725-kN, accompanied by a sound, likely caused by concrete cracking. As shown in the axial load-moment behaviour in Figure 4.48, the total moment continued to increase after the crack due to increasing secondary moment, with several drops caused by further cracking, while the axial load did not increase significantly between the subsequent cracks. The specimen failed suddenly at the maximum tension side, slightly below mid-height, as shown in Figures 4.54 and 4.55. The FRP shell failed by horizontal splitting of the outer hoop lamina and tensile rupture of the longitudinal fibres in the underlying lamina. Like specimen BC-E-e30, discolouration of the shell at the failure location occurred before failure.



Considerable damage to the shell also occurred in the maximum compression region, slightly above the tension failure location. Figure 4.56 shows the damage on the compression side, which resembled the shell crushing observed in the compression failure region of specimen BC-E-e30. However, the distinct hoop tensile rupture of the shell below the crushed region on specimen BC-E-e30 did not occur on specimen BC-E-e100, indicating that the crushed region observed on specimen BC-E-e100 was likely not the primary failure location, but rather a secondary effect that followed tensile failure of the shell on the opposite side. The axial load and bending moment at mid-height at failure were 1790-kN and 260-kNm. The maximum tensile strain measured at mid-height was 16.7-millistrain.

The circumferential-axial strain relationship in Figure 4.57 indicates that concrete confinement developed gradually, as there is a smooth increase in slope of the data from the maximum axial compression zone. The data also shows that confinement was likely affected by concrete cracking because there are shifts in the curve at axial strains corresponding to the drops on the moment-axial strain behaviour shown in Figure 4.51. The circumferential strain at the maximum axial compression zone continued to increase after each crack, at a higher rate than predicted by the Poisson's ratio, indicating that confinement continued after cracking. This is also demonstrated by the circumferential-axial strain relationship at the maximum tension side. Although the curve is discontinuous due to the effects of cracking, it indicates a superimposed tensile hoop stress as the

magnitude of the circumferential compressive strain decreases with increasing axial tensile strain, especially near the end of the test when a tensile circumferential strain rapidly develops.

The neutral axis depth decreased with increasing moment as shown in Figure 4.53, but remained below the cross-section's mid-height before the first drop in axial load and moment. Again, the data past the drop does not reliably represent the true depth of uncracked concrete because it is based on axial strain measurements on the surface of the FRP shell. The accuracy of the calculated neutral axis depth prior to the drop in moment may also be affected by hoop strains in the shell from confinement.

#### **4.4.8 Specimen BC-E-e200**

Specimen BC-E-e200 exhibited a more gradual increase in axial load and moment than specimen BC-E-e100. Three significant axial load and moment drops occurred, one near the beginning of loading at 23-kNm moment, another at 157-kNm moment, and a third at 179-kNm moment, as shown in the axial load-deflection and moment-deflection relationships in Figures 4.46 and 4.47. Each drop was accompanied by a sound, likely caused by concrete cracking. The circumferential-axial strain behaviour is shown in Figure 4.58. Although the circumferential-axial strain relationship at the maximum compression side of the cross-section indicates that some concrete confinement occurred prior to cracking at 157-kNm moment, the effect was small because it did not affect the

hoop strain at the other side of the cross-section. The slope of the circumferential-axial curve at the maximum tension zone followed the tensile Poisson's ratio line until the next crack at 179-kNm moment, which occurred at maximum compressive and tensile strains of 7.3 and 12.2-millistrain, as shown in the moment-axial strain relationship in Figure 4.59. A larger confinement effect was initiated at this point, indicated by an immediate reversal of the hoop strain at the tension side towards the tension-tension quadrant of the circumferential-axial strain plot in Figure 4.58. The slope of the circumferential-axial relationship at the extreme compressive side also began to increase past the second crack, indicating increasing confinement. The third crack did not have a significant effect on the circumferential-axial strain behaviour.

The axial load reached a plateau toward the end of the test, while the total moment continued to increase due to increased secondary moment effect with increasing lateral deflection, as shown in the axial load-moment relationship in Figure 4.60. The specimen failed in the maximum tension zone. In this case the failure occurred near the bottom of the specimen, just above the top of the eccentric loading cap, as shown in Figure 4.61. Failure occurred by horizontal splitting of the outer hoop lamina and tensile rupture of the longitudinal fibres. Secondary crushing of the FRP shell at the compression side near the height of the tension failure occurred, although it was not as substantial as on specimen BC-E-e100. The shell colour lightened in the eventual failure region shortly before failure. The specimen did not exhibit a bi-linear load-deflection response

similar to specimens BC-E-e30 and BC-E-e100, but rather a gradual increase in axial load and deflection with decreasing slope prior to failure, as shown in Figure 4.46. The axial load and bending moment at mid-height at failure were 863-kN and 215-kNm. The maximum tensile strain measured at mid-height was 17.8-millistrain.

The neutral axis depth-moment relationship is shown in Figure 4.53. The neutral axis depth remained relatively constant above the mid-height of the cross-section with increasing moment, prior to the moment drops.

#### **4.4.9 Specimen BC-E-e300**

Specimen BC-E-e300 behaved similar to beam-column BC-E-e200. The axial load-deflection relationship in Figure 4.46 demonstrates that axial load increased smoothly after two small drops near the beginning of the test, peaked, and then decreased continuously until failure. The moment-deflection relationship in Figure 4.47 shows that total moment increased smoothly after two drops coinciding with the drops in axial load, and remained relatively constant prior to failure. The plateau in total moment was caused by increasing secondary moment with increasing deflection, although the primary moment decreased towards the end of the test due to decreasing axial load, as shown in Figure 4.60.

The two drops in moment and axial load near the beginning of the test were accompanied by sounds, likely caused by concrete core cracking. As shown in

the moment-axial strain relationship in Figure 4.59, the second crack occurred at tensile and compressive axial strains of 2 and 1-millistrain at 47-kNm moment, initiating confinement. The circumferential-axial strain behaviour is shown in Figure 4.62. The circumferential-axial strain curve at the maximum tension side initially followed the tensile Poisson's ratio line, then suddenly changed directions and began approaching the tension-tension quadrant of the plot when the crack at 47-kNm moment occurred. The slope of the circumferential-axial strain relationship in the maximum compression zone also began to increase after the crack, indicating increasing confinement.

The specimen failed in the maximum tension zone just below mid-height. The failure region is shown in Figure 4.63. As with specimens BC-E-e30, BC-E-e100, and BC-E-e200, the shell colour lightened in the failure region prior to failure. Failure occurred by tensile rupture of the longitudinal fibres accompanied by horizontal splitting of the hoop laminas. Very little crushing of the shell occurred on the compression side opposite the tension failure region. The bending moment at mid-height and axial load at failure were 171-kNm and 489-kN respectively. The maximum tensile strain measured at mid-height was 14-millistrain.

The neutral axis depth-moment relationship is shown in Figure 4.53. The calculated neutral axis depth shifted at the two drops in moment near the beginning of the test, and then remained relatively constant, increasing slightly

near the end of the test. Similar to specimen BC-P-e300, the apparent increase in neutral axis depth may have been caused by some loss of strain compatibility between the shell and concrete core.

#### 4.5 Experimental Phase III: Axial Compression Tests

Two pure axial load specimens were tested in the last phase of the experimental program, one with an E-glass/epoxy shell, and the other with an E-glass/polyester shell. The composition of each specimen, and a description of the testing apparatus, instrumentation, and method are included in Chapter 3.

The axial load-axial strain and circumferential-axial strain behaviours of the E-glass/epoxy shell specimen are shown in Figures 4.64 and 4.65. Predicted axial force in the concrete based on a calculated unconfined concrete stress-strain relationship is plotted with the axial load-axial strain behaviour. Load and axial strain increased until the FRP shell began to crush and rupture in tension near the top of the specimen, as shown in Figure 4.66, causing the axial load to drop from a peak of approximately 5540-kN. The load increased again until hoop tensile rupture of the shell began near the bottom of the specimen, and another load drop occurred. The rupture at the bottom of the specimen quickly propagated up the shell causing a final large drop in axial load. The specimen no longer sustained a significant axial load after this point. The failure at the bottom of the specimen is shown in Figure 4.67.

Although the calculated unconfined concrete stress-strain relationship suggests that the peak concrete stress would occur at 2.3-millistrain, the actual true peak unconfined stress in the specimen's concrete core likely occurred slightly earlier. The concrete began to soften after reaching its peak unconfined stress, initiating confinement. The circumferential-axial strain relationship in Figure 4.65 indicates that concrete confinement began when the axial strain reached 2-millistrain because the rate of increase of tensile hoop strain suddenly increased after originally following the tensile Poisson's ratio line. Softening of the concrete likely caused the initial crushing failure in the shell observed at the top of the specimen. The confinement effect did not cause a significant increase in axial load capacity, but enhanced the ductility of the specimen. The hoop tensile rupture failure mode at the end of the test likely occurred due to a biaxial state of stress in the shell from the axial load and confining pressure, combined with local bearing effects at the interface between the specimen and loading plate.

The axial load-axial strain behaviour of the E-glass/polyester shell specimen is shown in Figure 4.69, along with a predicted concrete force-strain relationship based on a calculated unconfined concrete stress-strain curve. In this case some internal cracking was heard prior to the peak axial load, causing a shift in the axial load-axial strain relationship. A crack was heard at the peak axial load of approximately 5660-kN, followed by a large decrease in the load. Subsequent drops in load occurred as the concrete continued to crack, and the FRP shell began to fail. Failure occurred by splitting of an exterior lamina parallel to the

fibre direction and tensile rupture of the underlying lamina along its fibre direction, beginning at the top of the specimen and propagating down the shell. The failure region is shown in Figure 4.69. The circumferential-axial strain relationship shown in Figure 4.70 indicates a sudden increase in circumferential strain when the axial load dropped from the peak, suggesting that concrete confinement was initiated after significant cracking of the concrete core. However, the confinement effect did not improve the axial load carrying capacity or ductility of the specimen, likely because the concrete was already near or at failure when confinement began. Complete failure of the concrete was delayed until the shell began to rupture due to a combination of biaxial stresses and local effects at the top of the specimen.

The pure axial load tests indicate that neither type of FRP shell provided significant confinement. Although the E-glass/epoxy type shell seemed to increase the ductility of the concrete, it did not increase the compressive strength. The E-glass/polyester type shell did not appear to provide any benefit aside from holding the fractured concrete core together before rupturing. Major factors causing the lack of significant confinement are the shells' low hoop stiffnesses. In addition, the E-glass/polyester shell had a large compressive Poisson's ratio that delayed the onset of confinement because the concrete had to dilate significantly to overcome the radial expansion of the shell. It is expected that shells with higher hoop stiffness and lower axial Poisson's ratios would be



more effective in confining concrete, increasing both the strength and ductility of the concrete compared to unconfined behaviour.

			E-glass/epoxy Shell	E-glass/polyester Shell
Axial Tensile Properties	experimental	$f_{tu}$ (MPa)	237	175
		$\varepsilon_{tu}$ (ms)	15.4	13.5
		$E$ (MPa)	16059	14690
		$\nu$	0.11	0.58
	calculated	$f_{tu}$ (MPa)	258	163
		$\varepsilon_{tu}$ (ms)	15.0	13.3
		$E$ (MPa)	* 22900, 18912, 18013, 17493, 17176	* 16591, 12216
		$\nu$	* 0.12, 0.19, 0.24, 0.28, 0.29	* 0.34, 0.62
	manufacturer's	$f_{tu}$ (MPa)	345	207
		$\varepsilon_{tu}$ (ms)	16.7	13.6
		$E$ (MPa)	20700	15200
		$\nu$	-	-
Axial Compressive Properties	experimental	$f_{tu}$ (MPa)	-	-
		$\varepsilon_{tu}$ (ms)	-	-
		$E$ (MPa)	20656	19070
		$\nu$	0.13	0.50
	calculated	$f_{tu}$ (MPa)	261	213
		$\varepsilon_{tu}$ (ms)	11.4	12.8
		$E$ (MPa)	22900	16591
		$\nu$	0.12	0.34
	manufacturer's	$f_{tu}$ (MPa)	276	-
		$\varepsilon_{tu}$ (ms)	13.3	-
		$E$ (MPa)	20700	15200
		$\nu$	-	-
** Hoop Tensile Properties	calculated	$f_{tu}$ (MPa)	328	140
		$\varepsilon_{tu}$ (ms)	16.8	14.7
		$E$ (MPa)	* 24535, 21325, 20064, 19598	* 17144, 10012, 9483

\* calculations predict multilinear response

\*\* only calculated predictions were available for hoop tensile properties

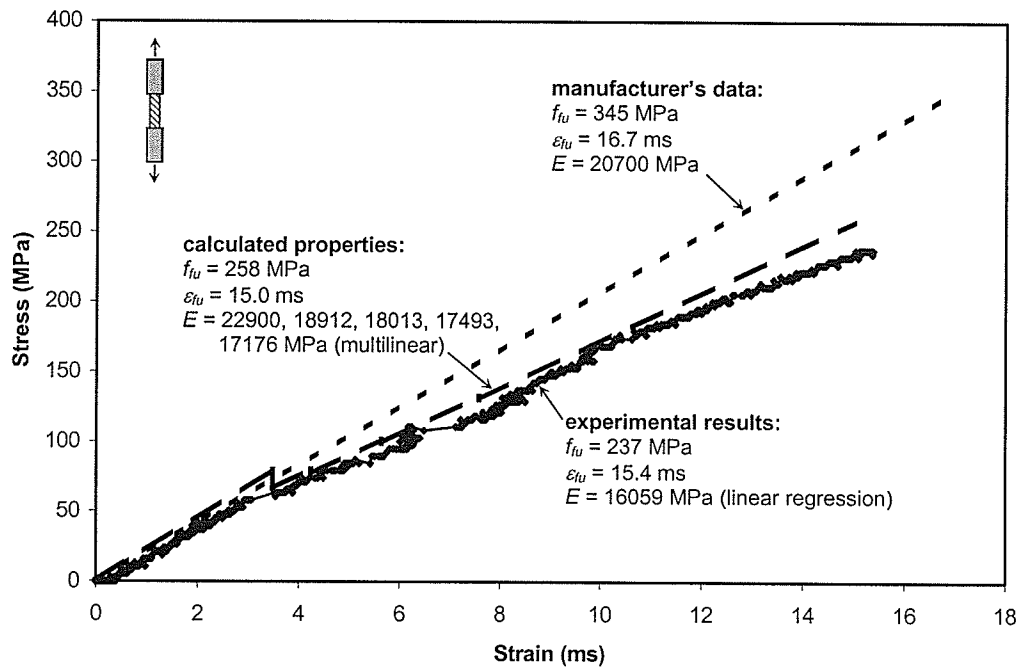
**Table 4.1:** Effective elastic properties of the FRP tubes used in the experimental program.

Specimen ID	Shell Outside Diameter (mm)	Shell Total Thickness (mm)	Shell Structural Thickness (mm)	$\rho$	$f_c'$ (MPa)	$\epsilon_c'$	Experimental $f_{fu}$	Experimental $\epsilon_{fu}$	$\rho_{br}^*$	Calculated $f_{fu}$	Calculated $\epsilon_{fu}$	$\rho_{br}^{**}$
BM-E-1	326	7.05	6.40	8.41%	60	0.2392%	237	1.540%	2.37%	258	1.500%	2.23%
BM-P-1	319	7.22	5.96	8.05%	62	0.2421%	175	1.350%	3.73%	163	1.330%	4.07%
BM-E-2	326	7.05	6.40	8.41%	85	0.2738%	237	1.540%	3.49%	258	1.500%	3.28%
BM-P-2	319	7.22	5.96	8.05%	67	0.2492%	175	1.350%	4.07%	163	1.330%	4.44%
BC-P-e10	319	7.22	5.96	8.05%	77	0.2631%	175	1.350%	4.74%	163	1.330%	5.17%
BC-P-e30	319	7.22	5.96	8.05%	77	0.2631%	175	1.350%	4.74%	163	1.330%	5.17%
BC-P-e100	319	7.22	5.96	8.05%	77	0.2631%	175	1.350%	4.74%	163	1.330%	5.17%
BC-P-e200	319	7.22	5.96	8.05%	77	0.2631%	175	1.350%	4.74%	163	1.330%	5.17%
BC-P-e300	319	7.22	5.96	8.05%	77	0.2631%	175	1.350%	4.74%	163	1.330%	5.17%
BC-E-e30	326	7.05	6.40	8.41%	60	0.2392%	237	1.540%	2.37%	258	1.500%	2.23%
BC-E-e100	326	7.05	6.40	8.41%	60	0.2392%	237	1.540%	2.37%	258	1.500%	2.23%
BC-E-e200	326	7.05	6.40	8.41%	60	0.2392%	237	1.540%	2.37%	258	1.500%	2.23%
BC-E-e300	326	7.05	6.40	8.41%	60	0.2392%	237	1.540%	2.37%	258	1.500%	2.23%

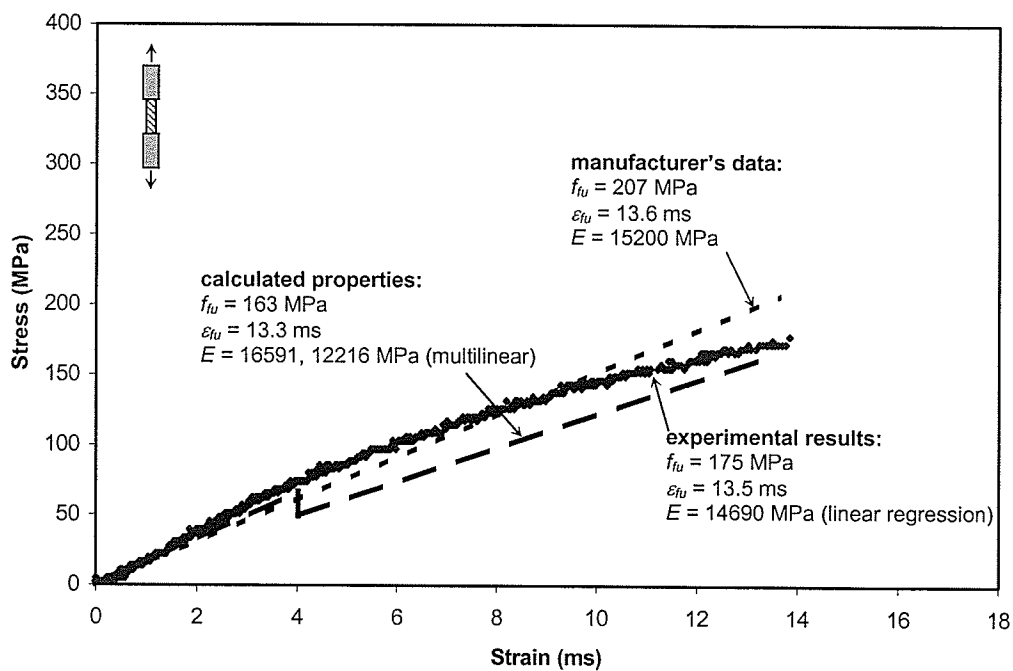
\* balanced reinforcement ratio calculated with experimental FRP tube properties from tension coupon tests

\*\* balanced reinforcement ratio calculated with FRP tube properties calculated using laminated plate theory (Chapter 5)

**Table 4.2:** Calculated reinforcement ratios and balanced reinforcement ratios for each specimen tested in the experimental program.

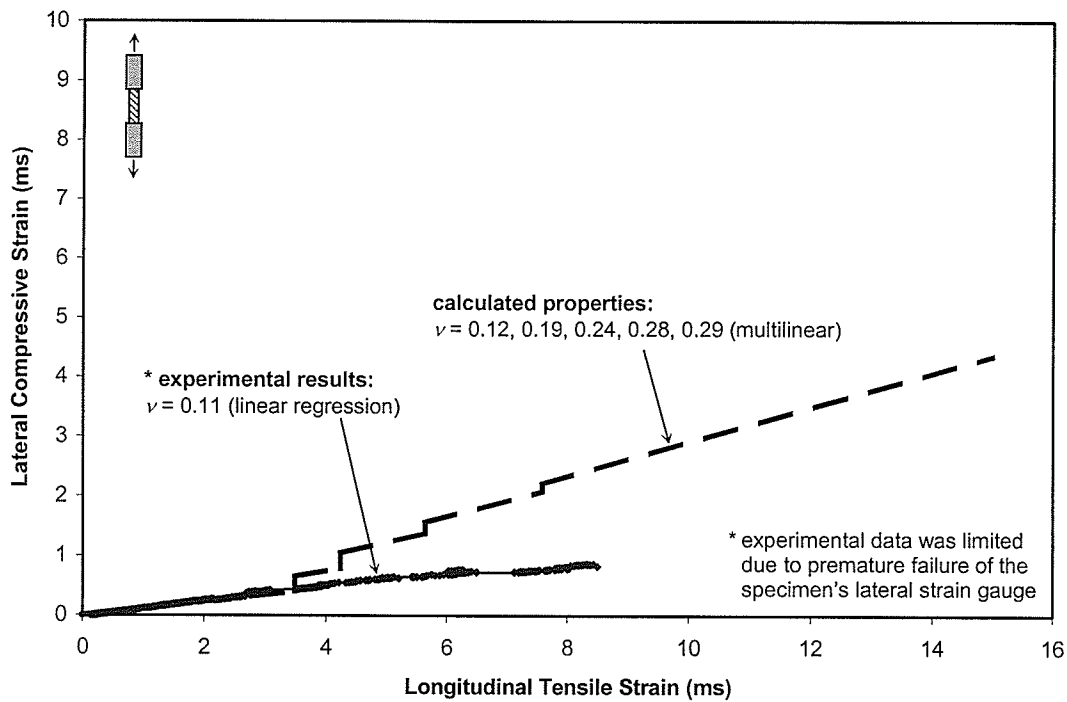


(a) E-glass/epoxy FRP shell.

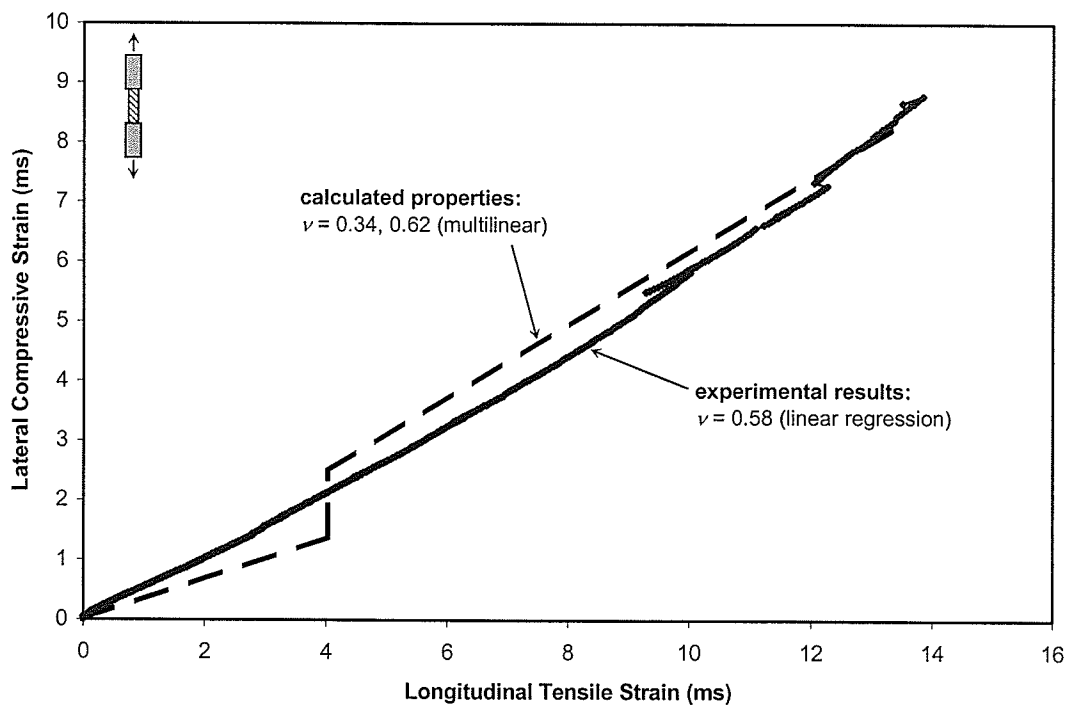


(b) E-glass/polyester FRP shell.

**Figure 4.1:** Axial tensile properties of the FRP shells used in the experimental program.

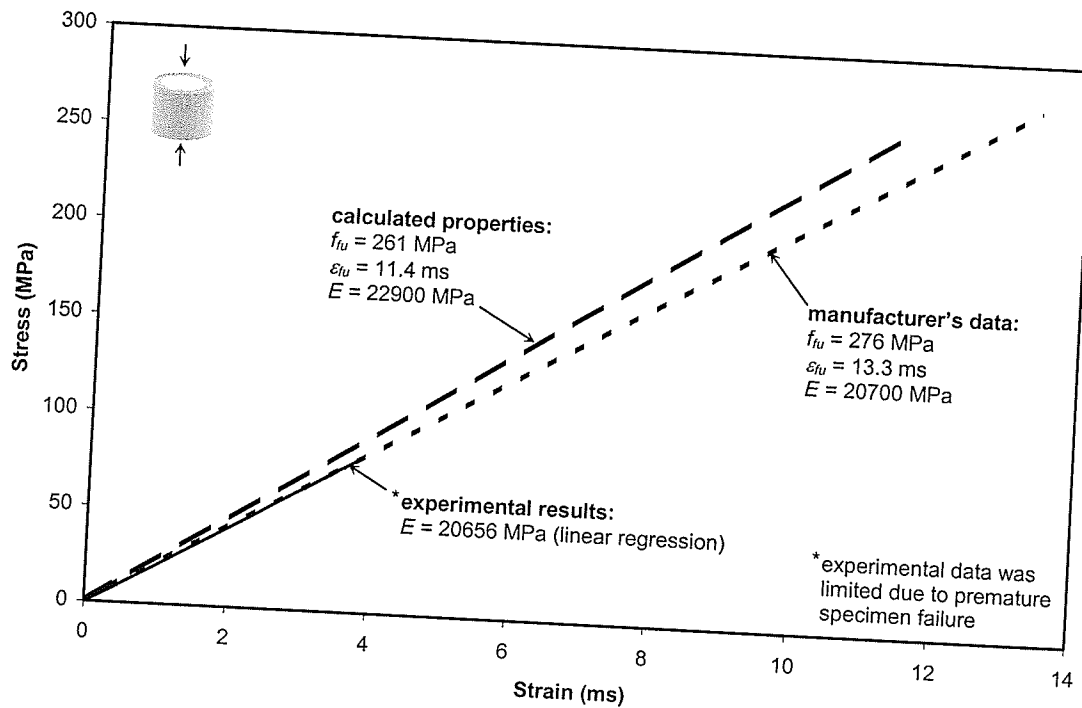


(a) E-glass/epoxy FRP shell.

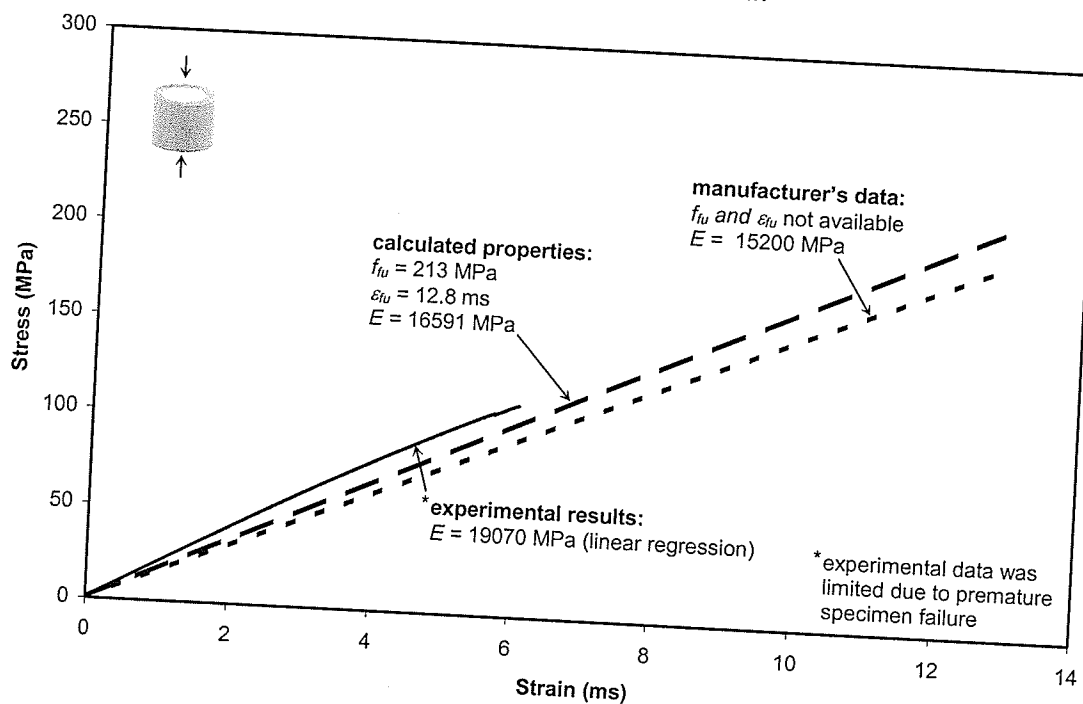


(b) E-glass/polyester shell

**Figure 4.2:** Axial tensile Poisson's ratios of the FRP shells used in the experimental program.

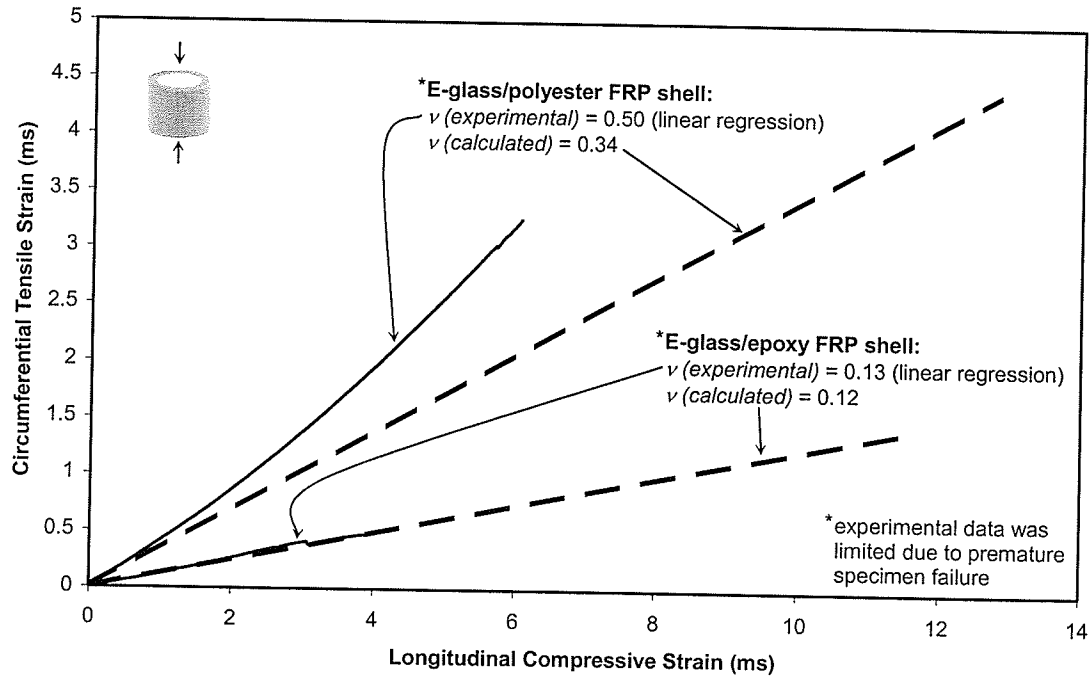


(a) E-glass/epoxy FRP shell.

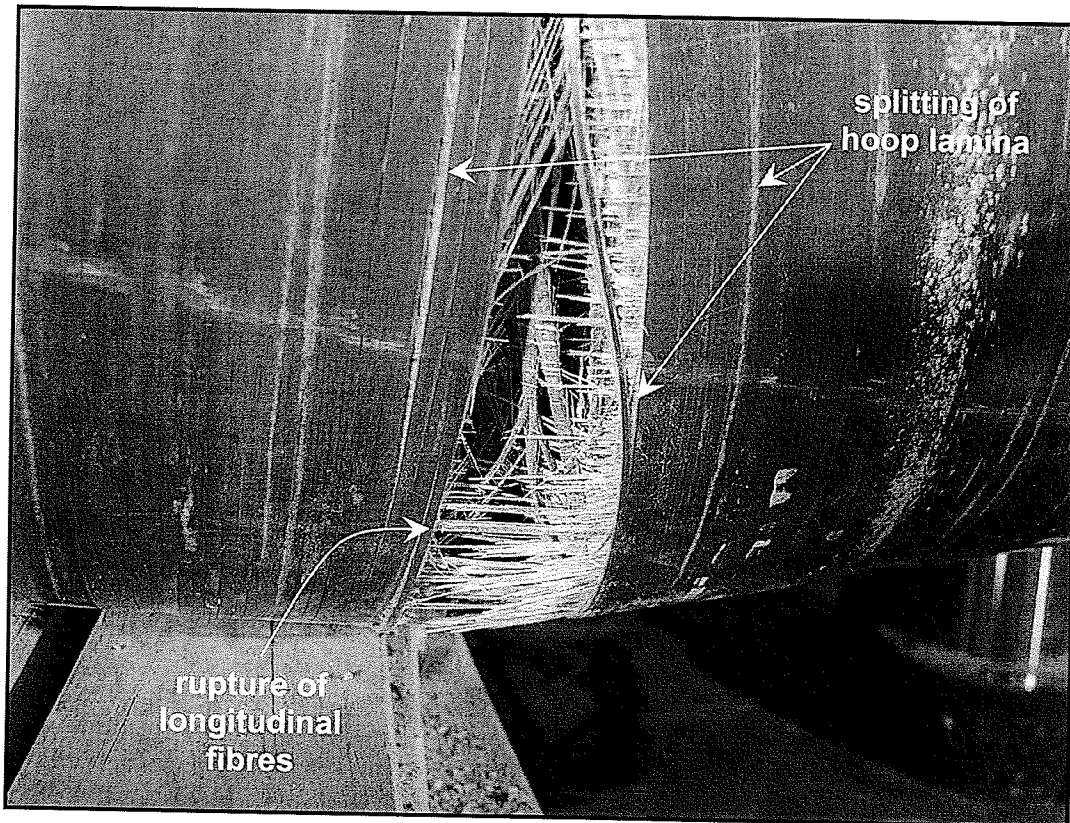


(a) E-glass/polyester FRP shell.

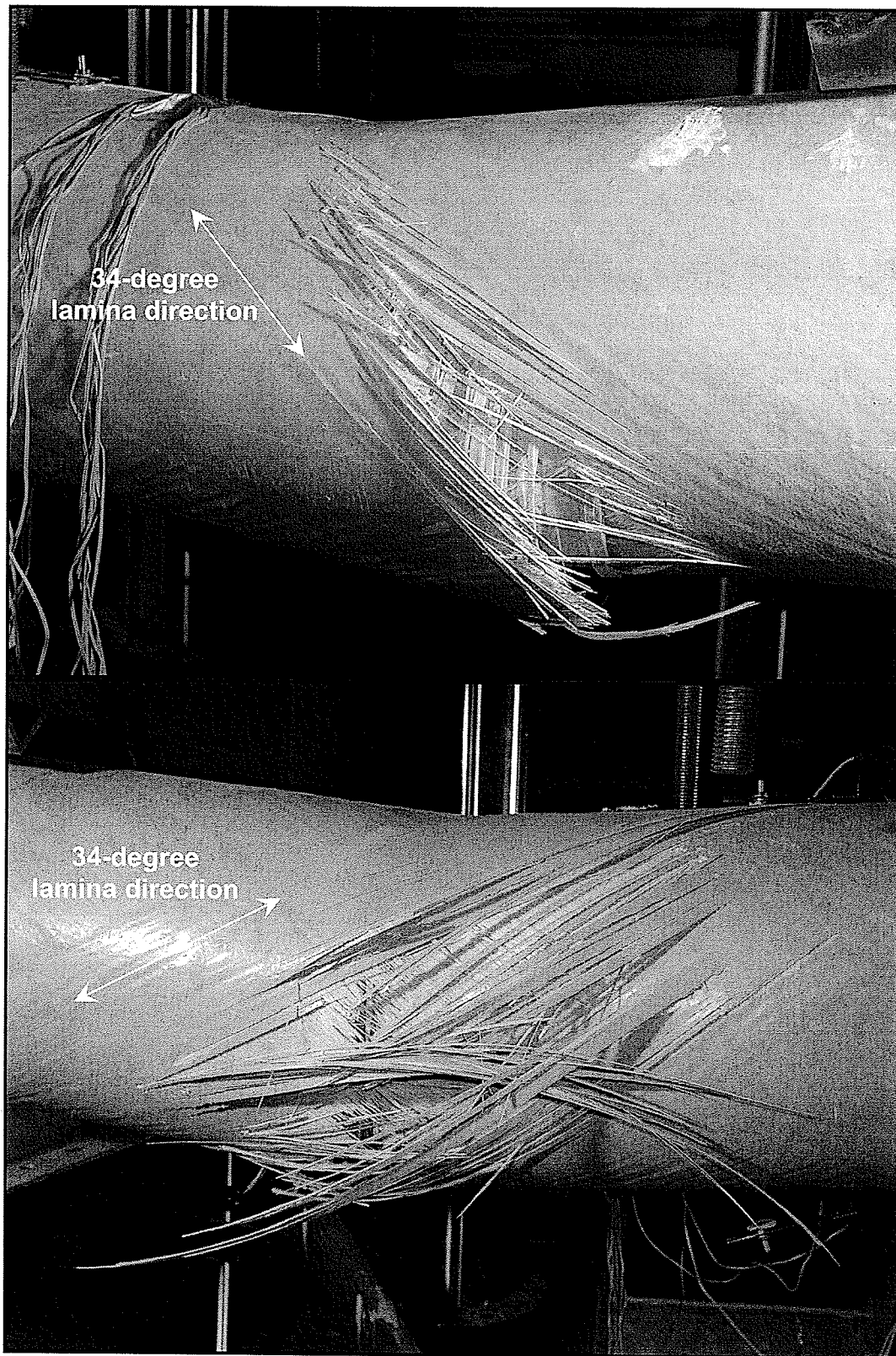
Figure 4.3: Axial compressive properties of the FRP shells used in the experimental program.



**Figure 4.4:** Axial compressive Poisson's ratios of the FRP shells used in the experimental program.

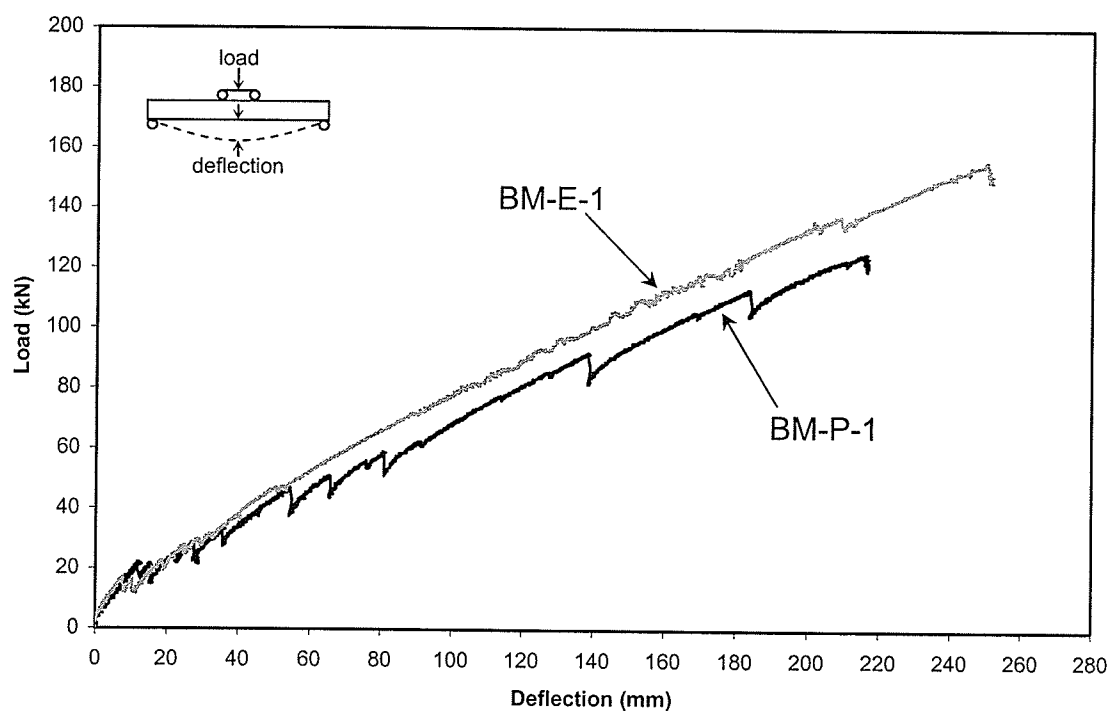


**Figure 4.5:** Typical tensile failure of beam specimens BM-E-1 and BM-E-2.

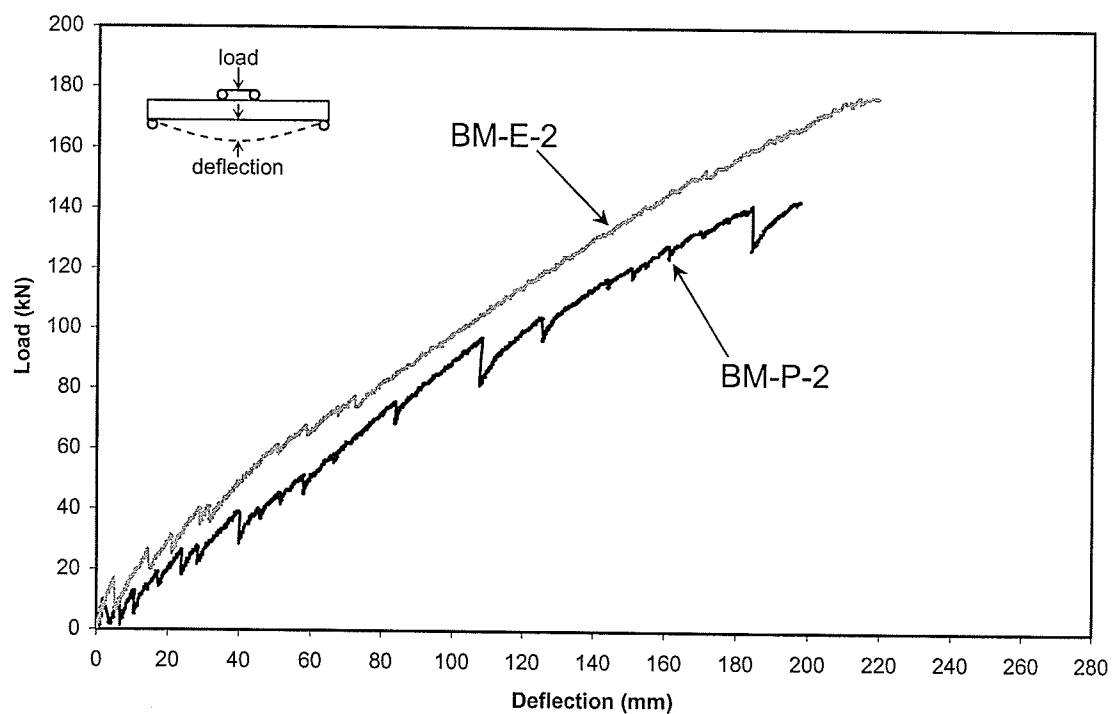


**Figure 4.6:** Specimens BM-P-1 and BM-P-2 failures by rupture of the FRP shell in tension.



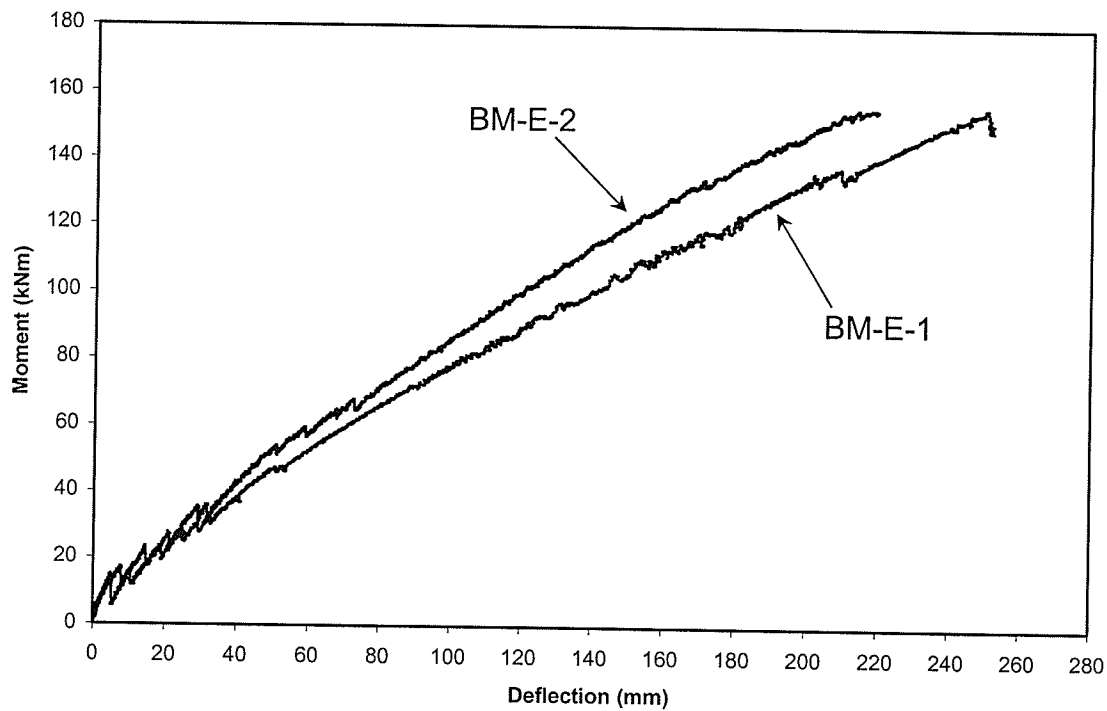


(a) 5.5-metre span beams specimens BM-E-1 and BM P-1.

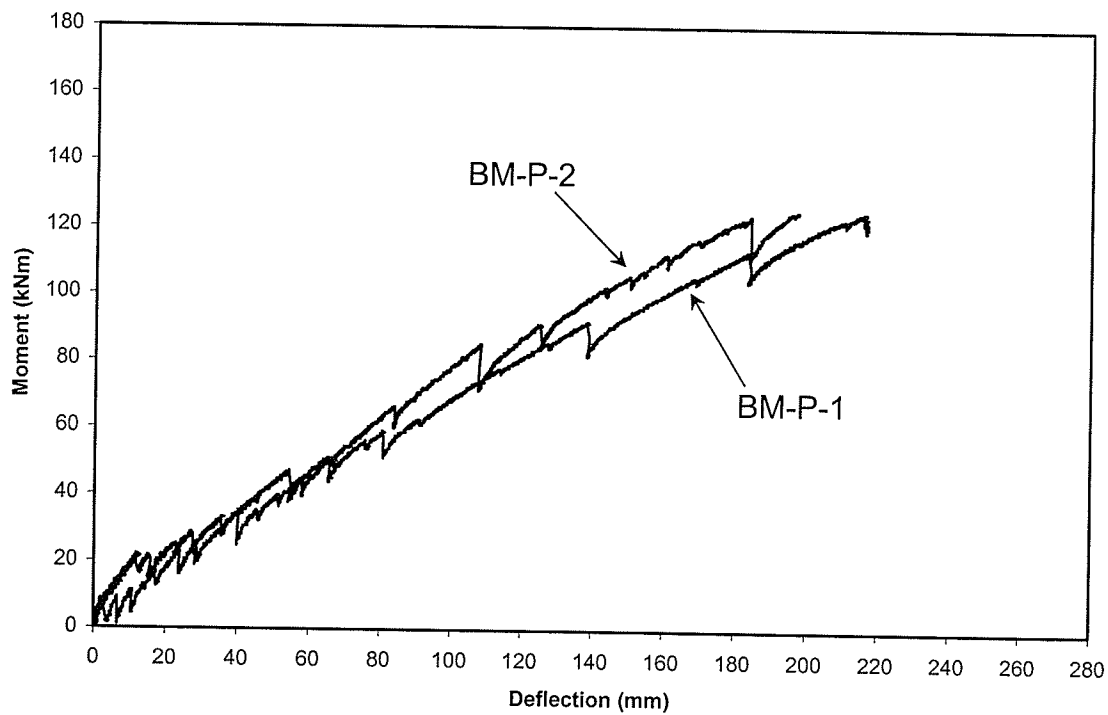


(b) 5.0-metre span beam specimens BM-E-2 and BM-P-2.

**Figure 4.7:** Load-deflection behaviours of the beam specimens.

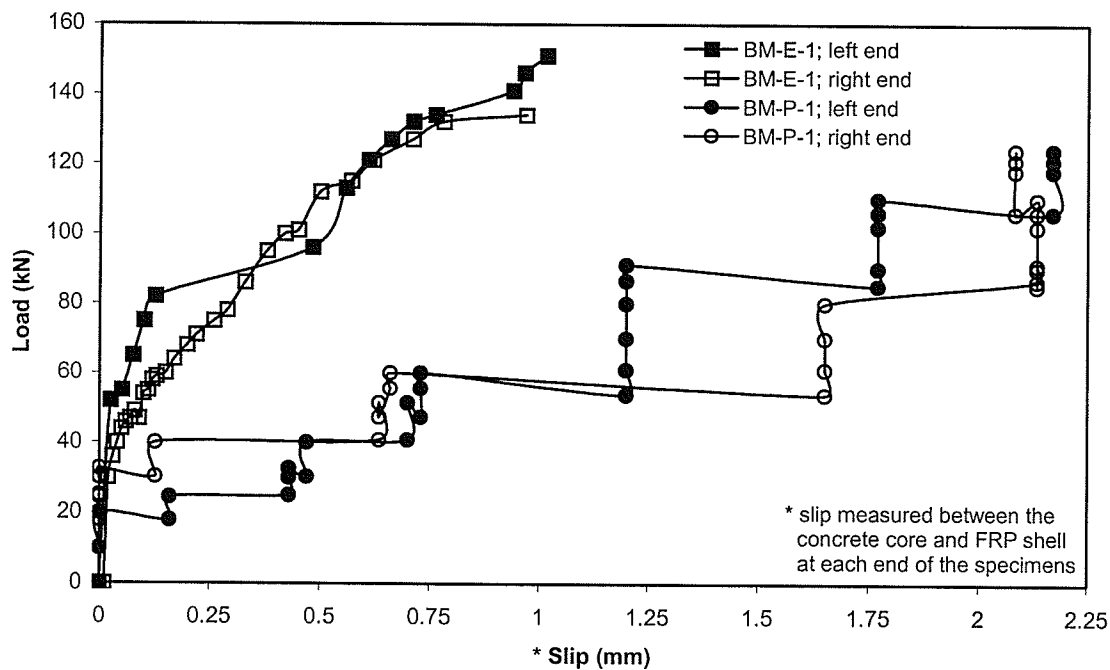


(a) E-glass/epoxy FRP tube specimens BM-E-1 and BM-E-2.

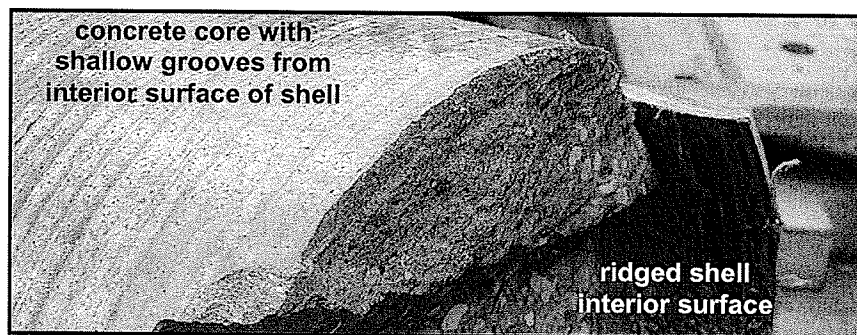


(b) E-glass/polyester FRP tube specimens BM-P-1 and BM-P-2.

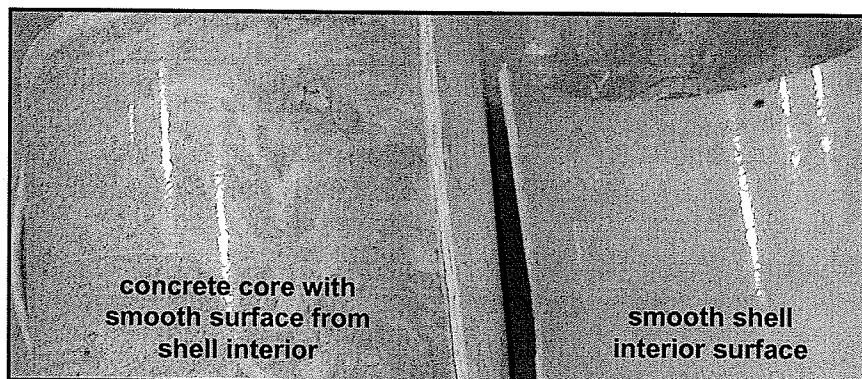
**Figure 4.8:** Moment-deflection behaviours of the beam specimens.



**Figure 4.9:** Load-slip behaviours of beam specimens BM-E-1 and BM-P-1.

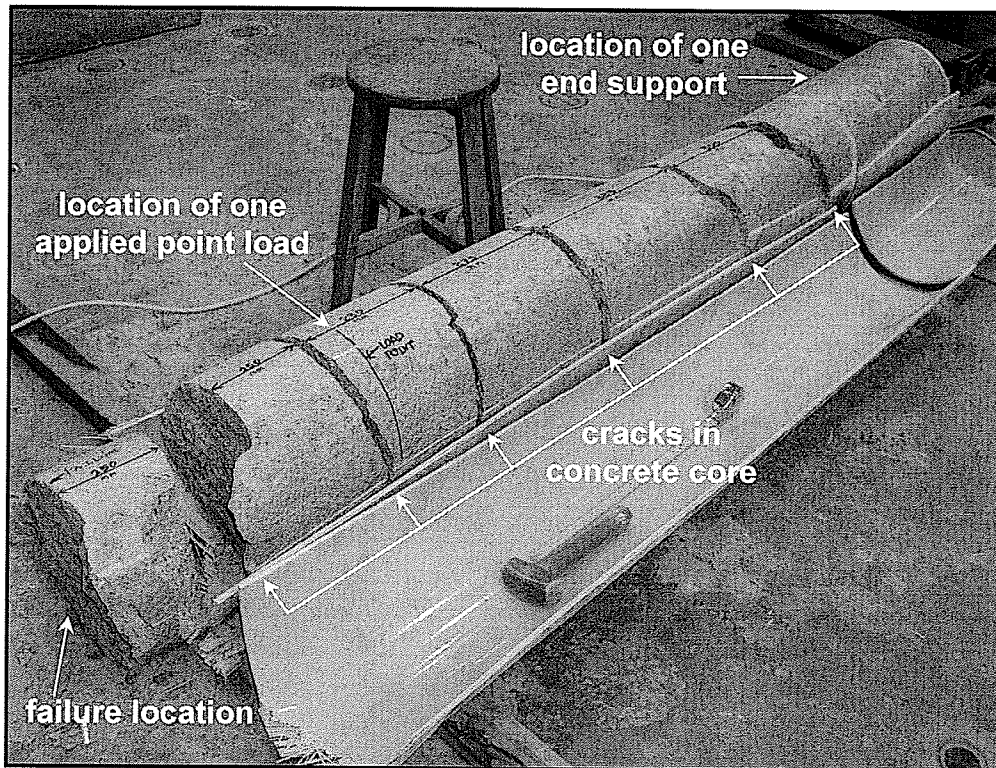


**(a)** Ridged E-glass/epoxy shell and resulting grooved concrete core.

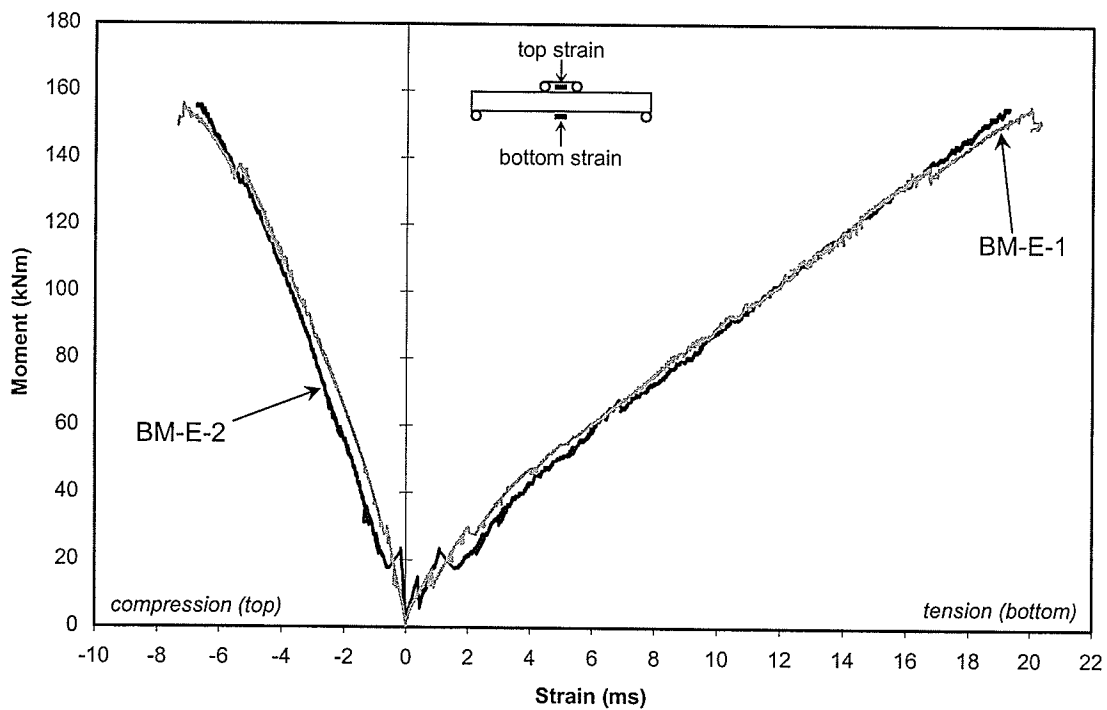


**(b)** Smooth E-glass/polyester shell and resulting smooth concrete core.

**Figure 4.10:** Specimens with FRP shells removed to demonstrate the difference in shell interior surface profiles.



**Figure 4.11:** FRP shell removed from half of specimen BM-P-2 to show the crack pattern in the concrete core.



**Figure 4.12:** Moment-axial strain relationships of beams BM-E-1 and BM-E-2.

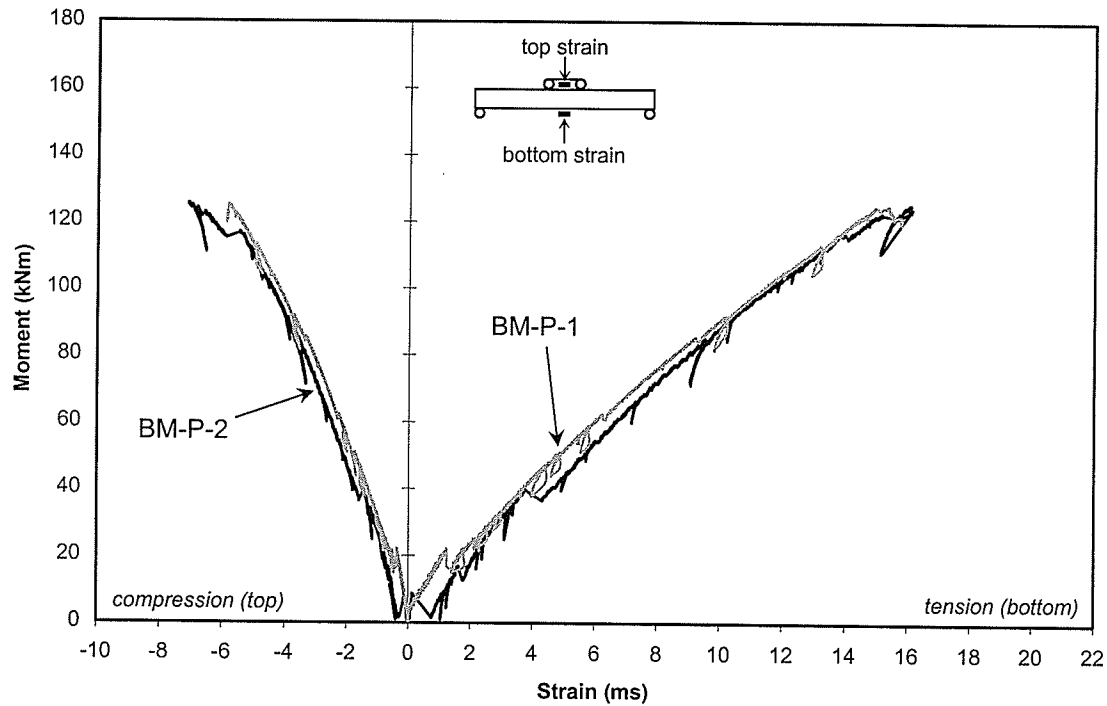


Figure 4.13: Moment-axial strain behaviours of beams BM-P-1 and BM-P-2.

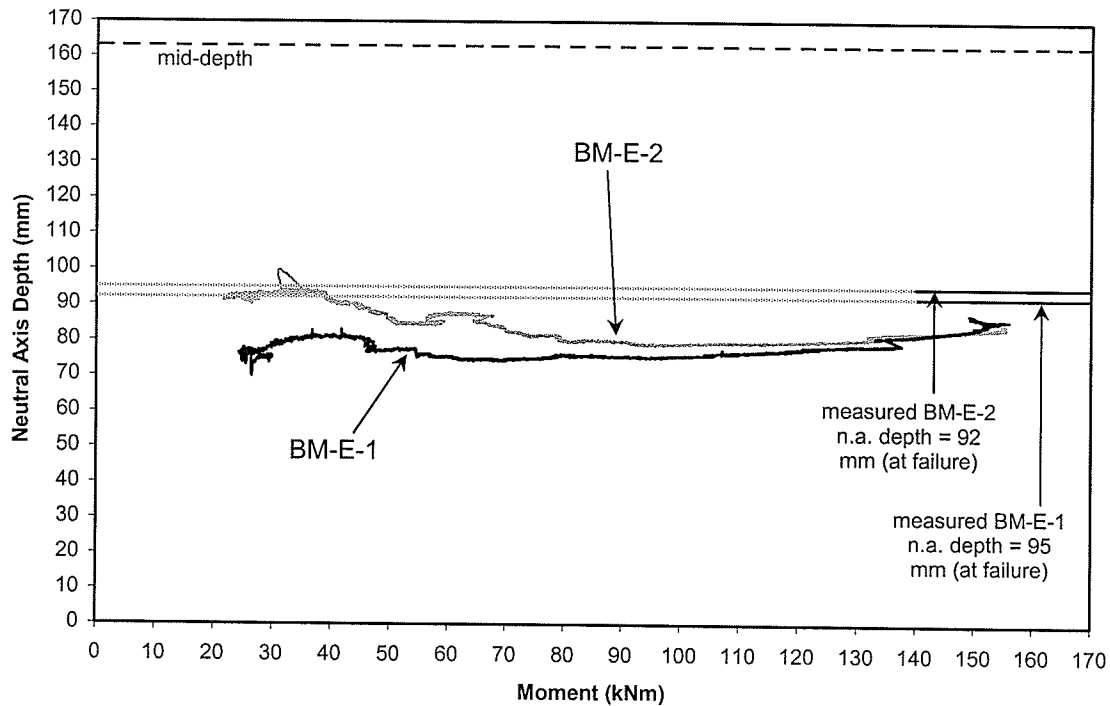
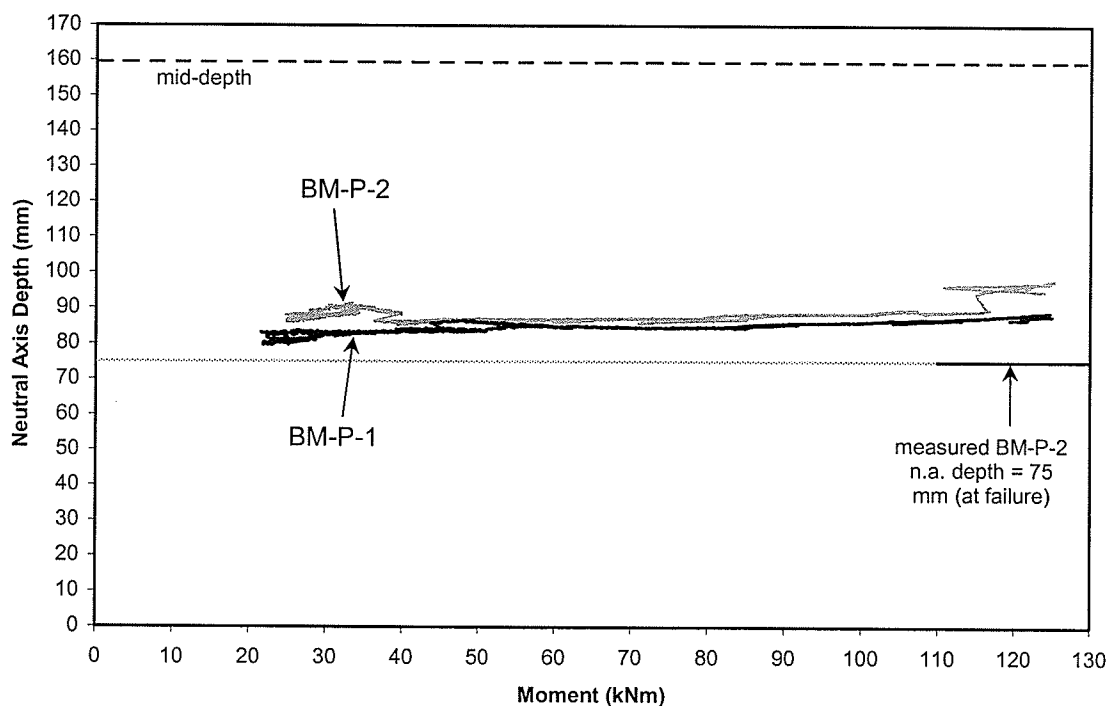
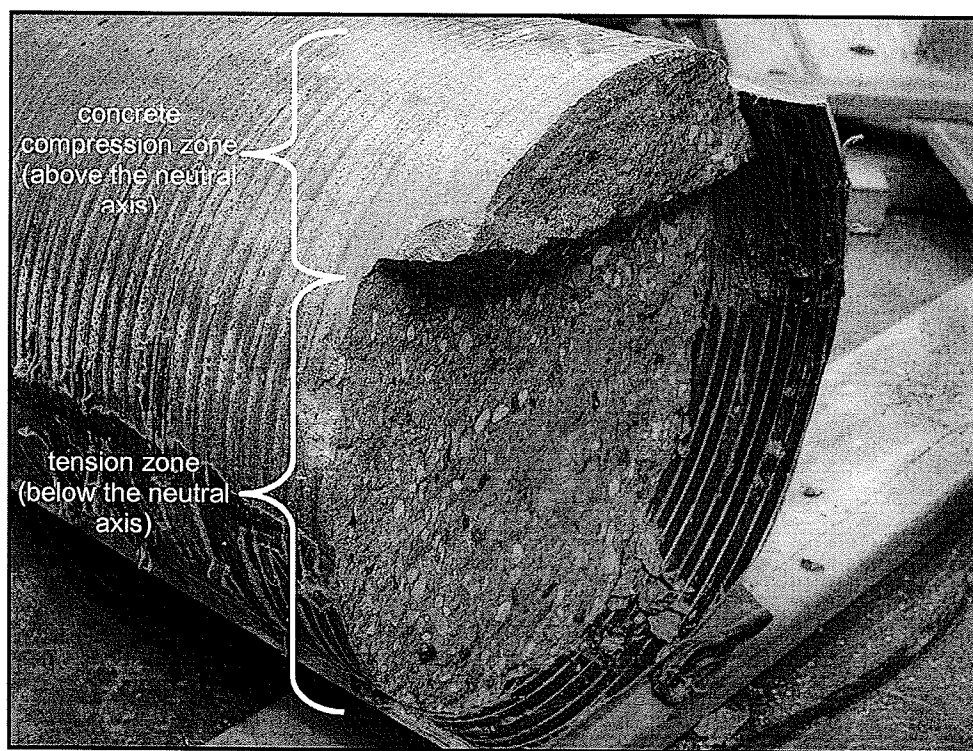


Figure 4.14: Neutral axis depth-moment relationships of specimens BM-E-1 and BM-E-2, calculated from axial strains on the surface of the beams.



**Figure 4.15:** Neutral axis depth-moment relationships of specimens BM-P-1 and BM-P-2, calculated from axial strains on the surface of the beams.



**Figure 4.16:** Beam specimen concrete core appearance after failure, enabling visual determination of the neutral axis depth.

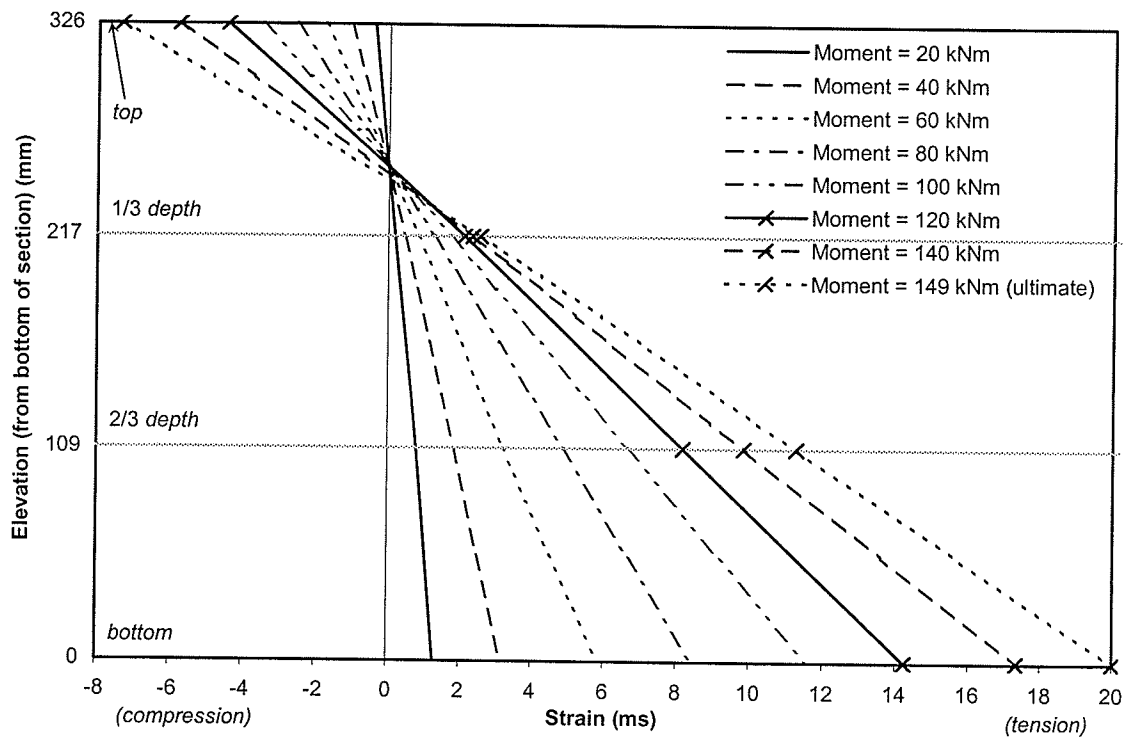


Figure 4.17: Axial strain distributions across section depth at mid-span of specimen BM-E-1.

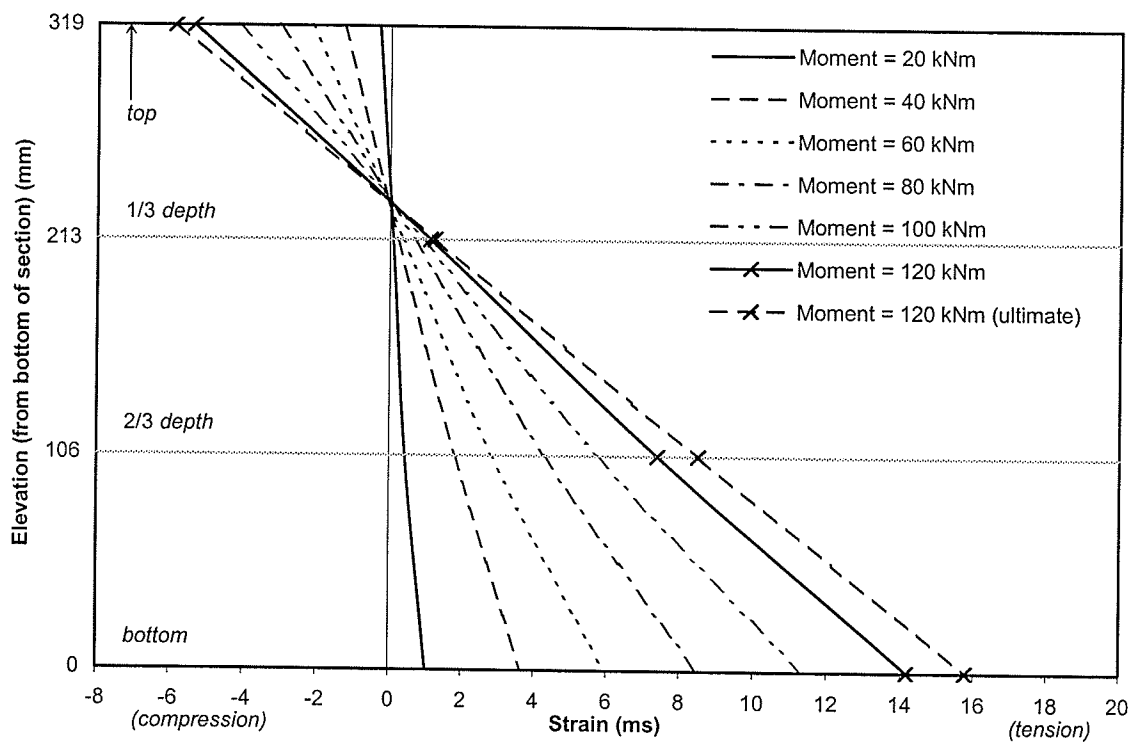
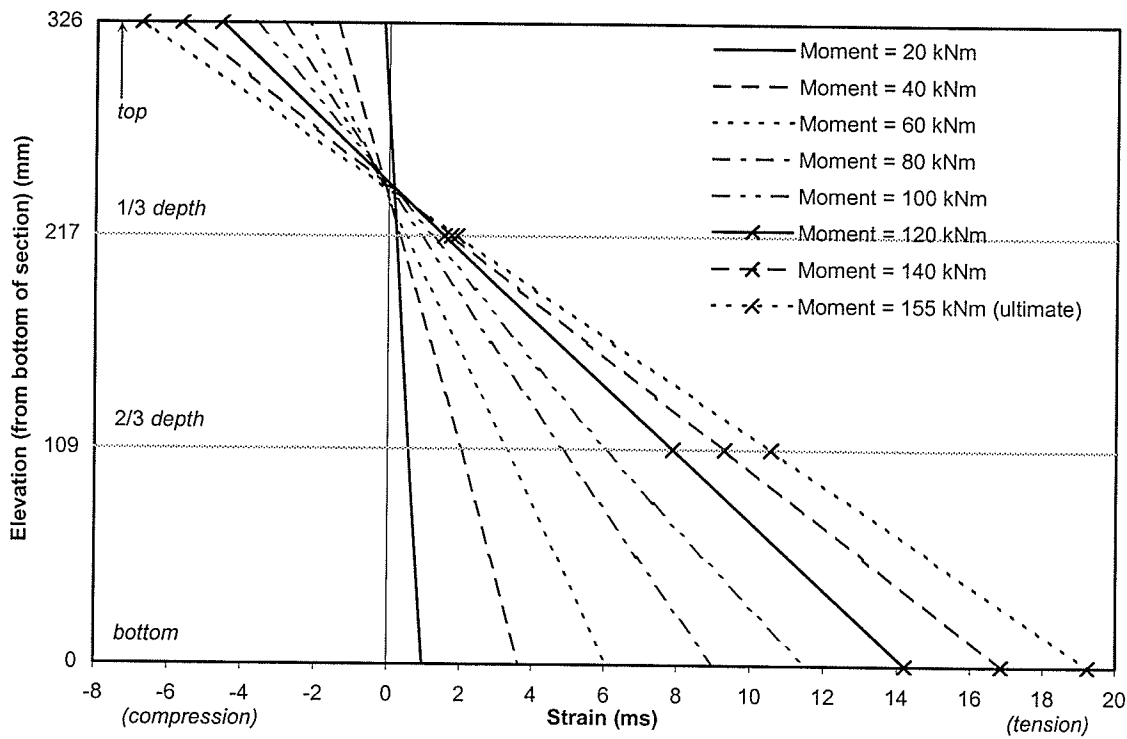
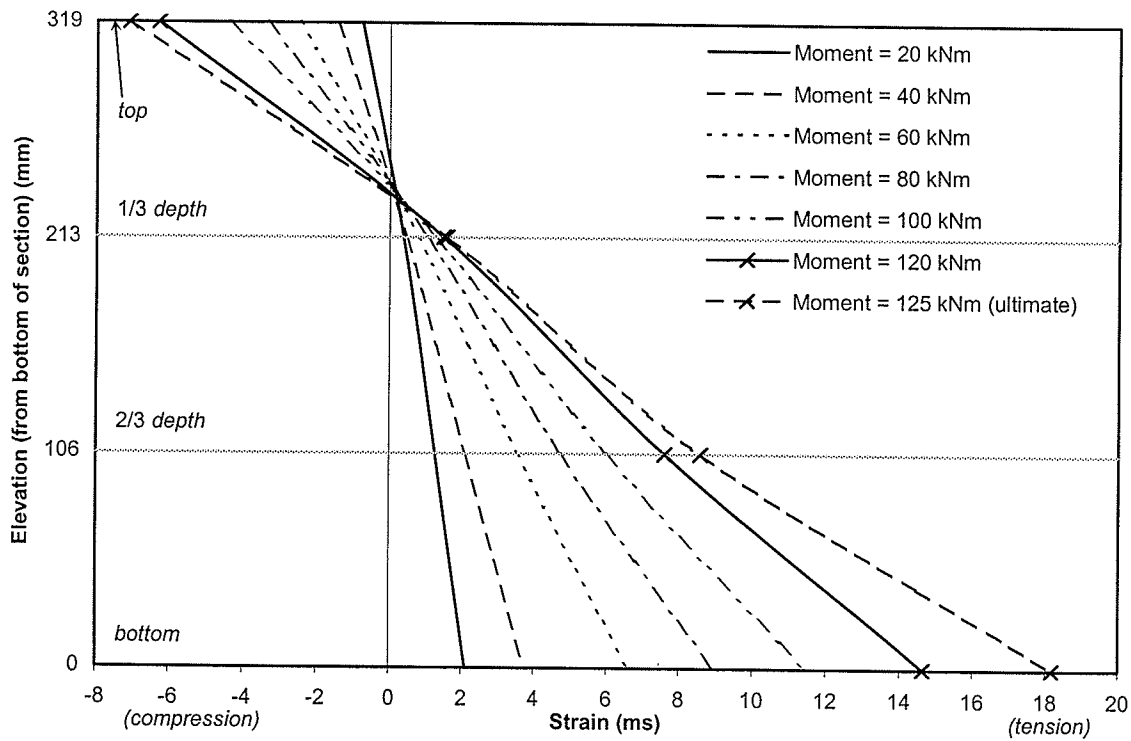


Figure 4.18: Axial strain distributions across section depth at mid-span of specimen BM-P-1.



**Figure 4.19:** Axial strain distributions across section depth at mid-span of specimen BM-E-2.



**Figure 4.20:** Axial strain distributions across section depth at mid-span of specimen BM-P-2.



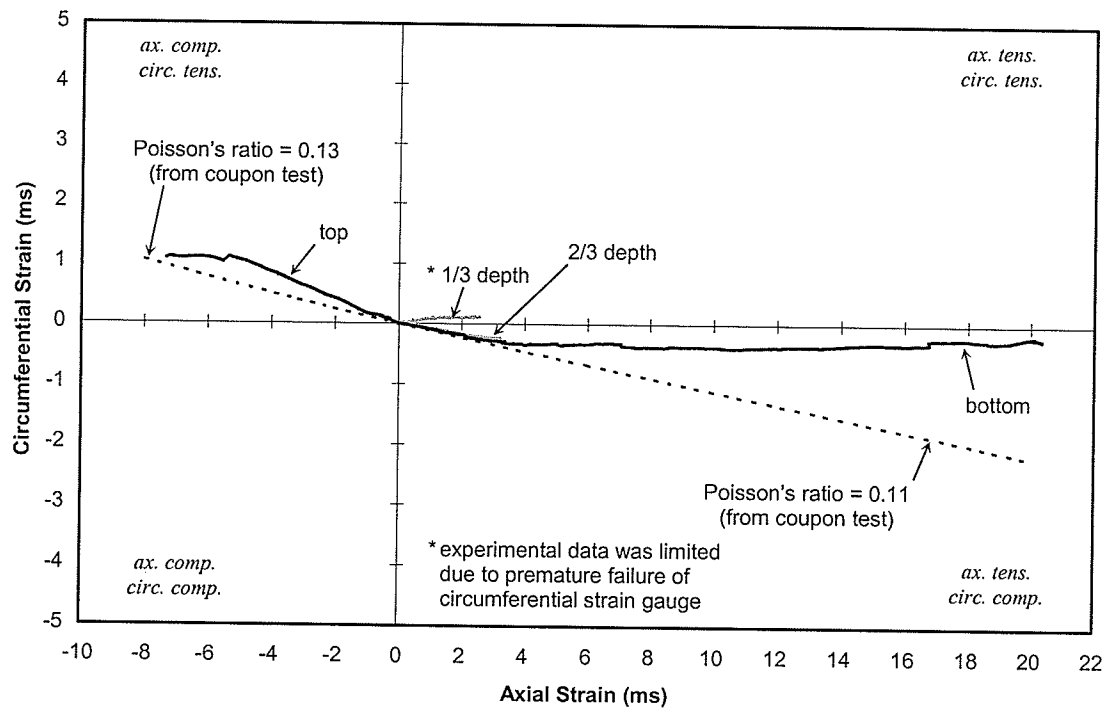


Figure 4.21: Circumferential-axial strain behaviour of specimen BM-E-1.

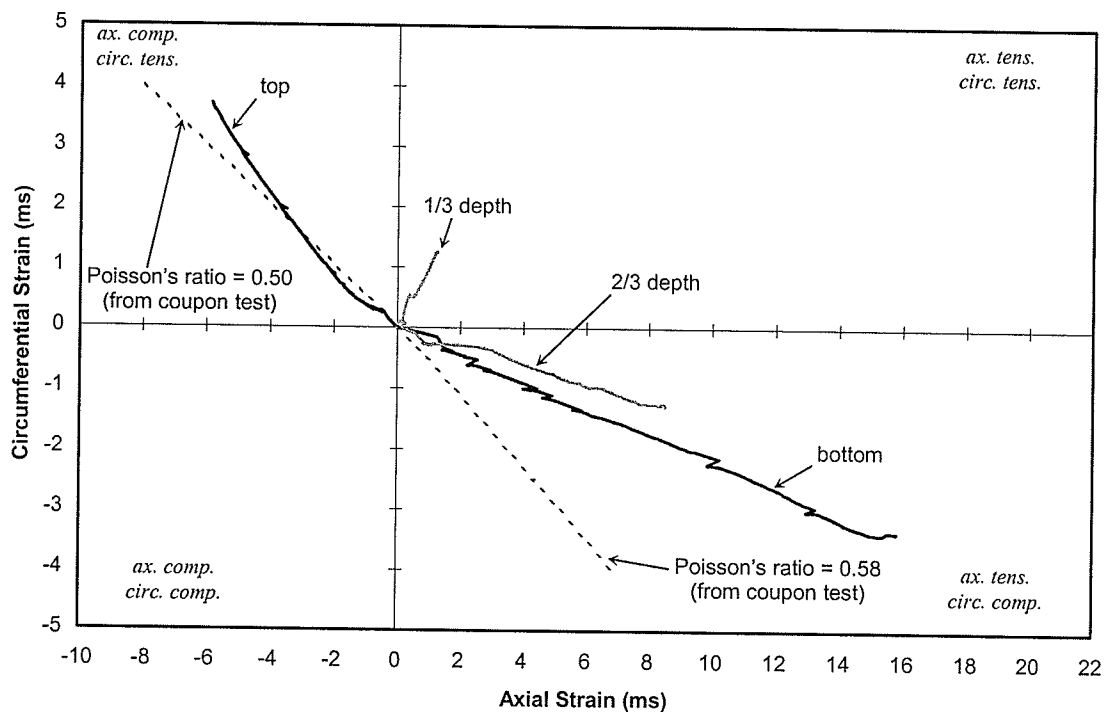


Figure 4.22: Circumferential-axial strain behaviour of specimen BM-P-1.

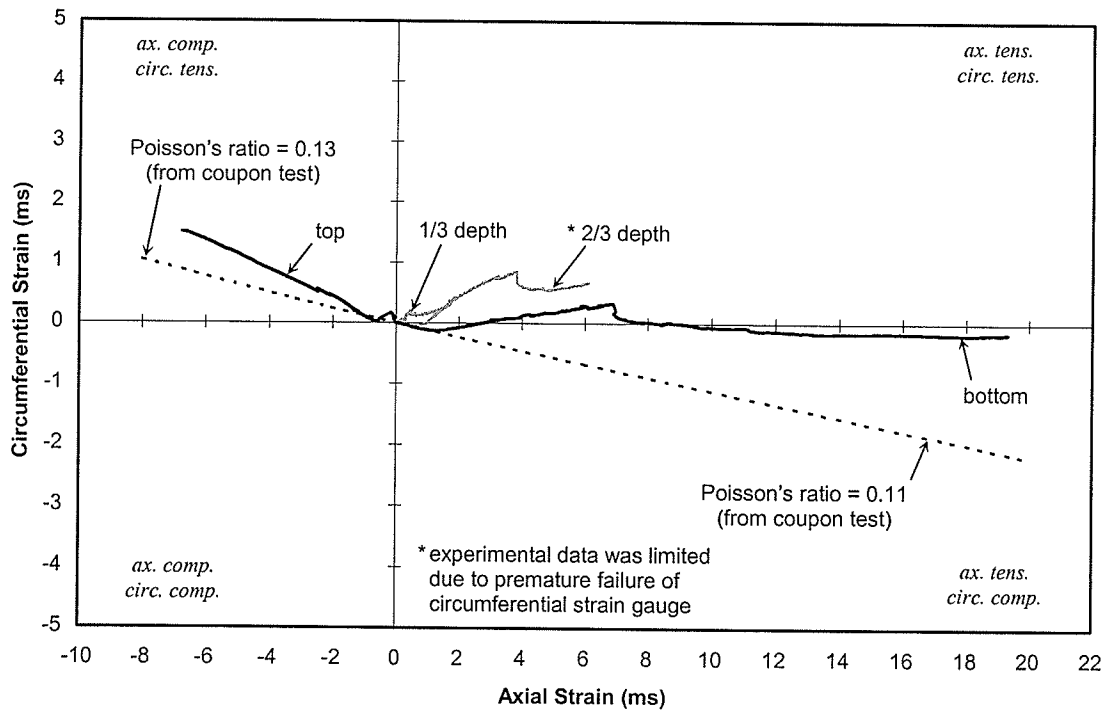


Figure 4.23: Circumferential-axial strain behaviour of specimen BM-E-2.

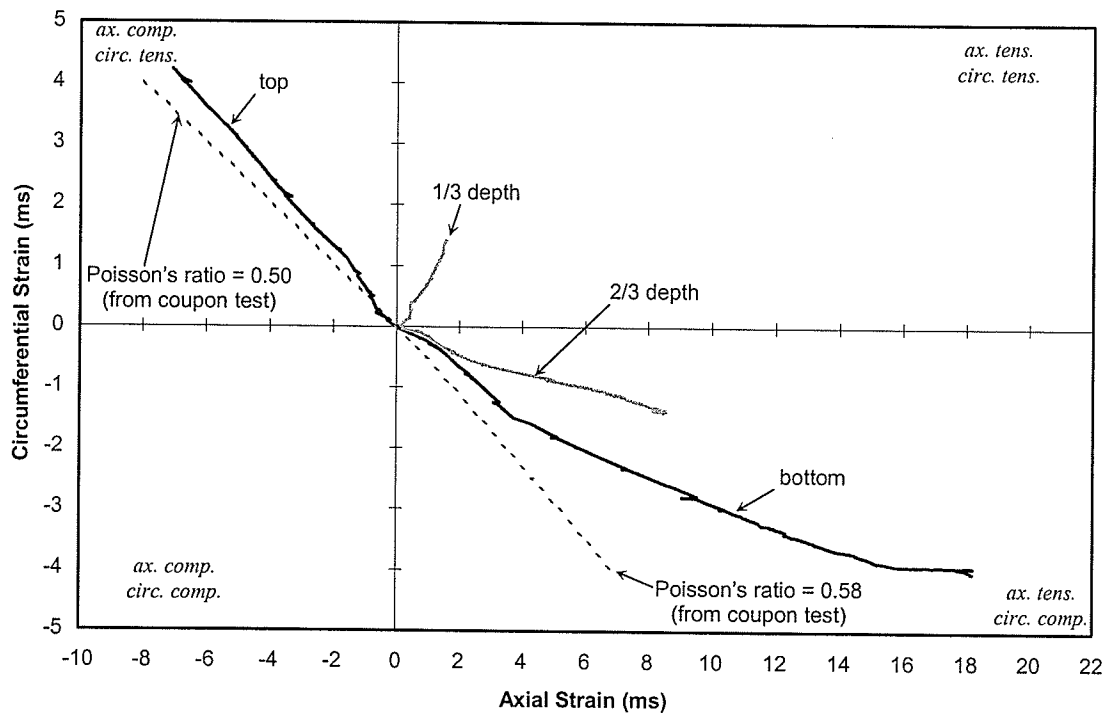
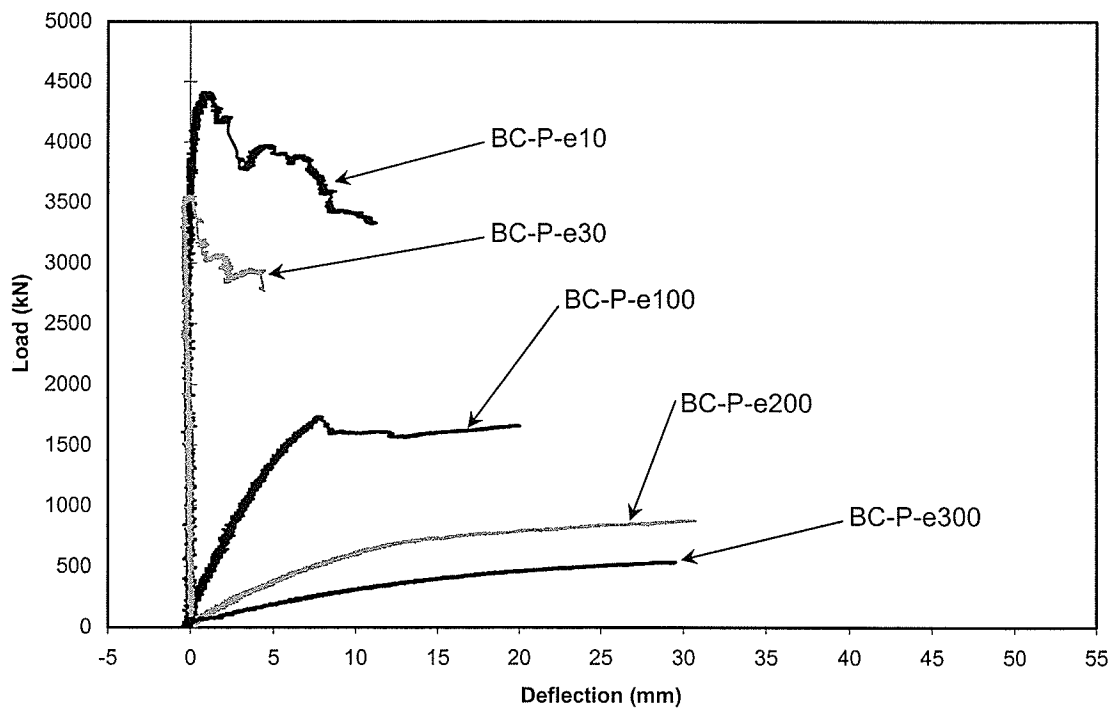
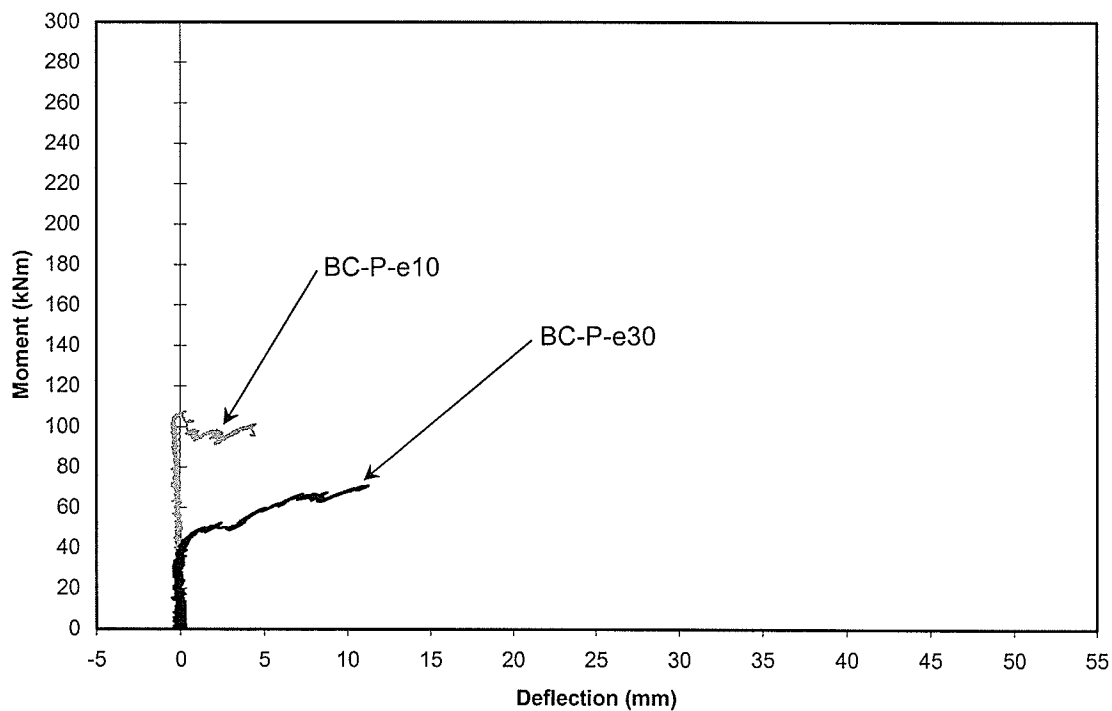


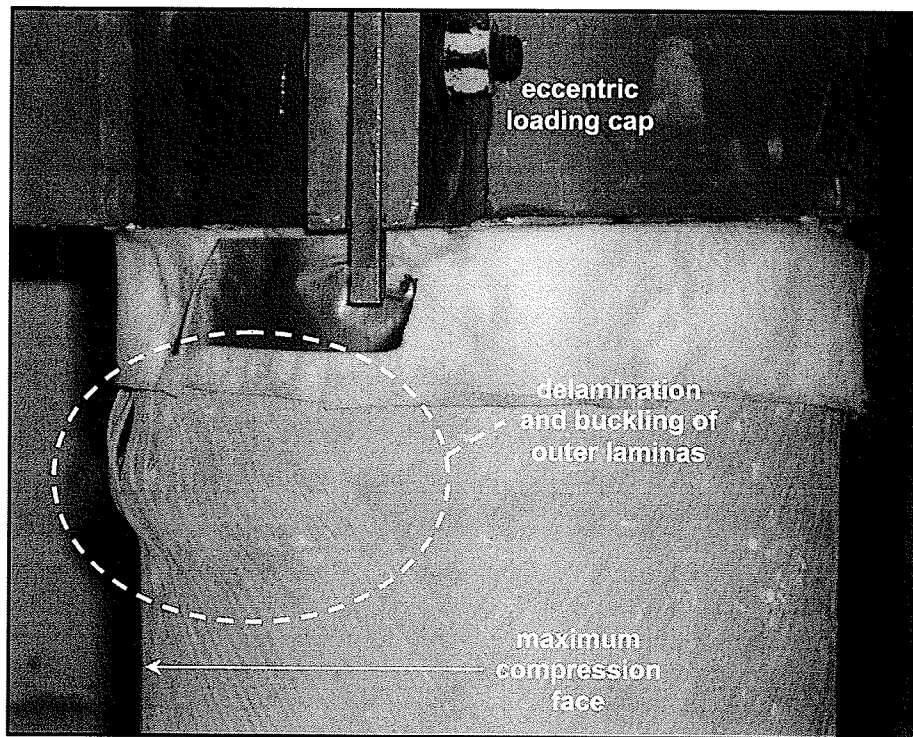
Figure 4.24: Circumferential-axial strain behaviour of specimen BM-P-2.



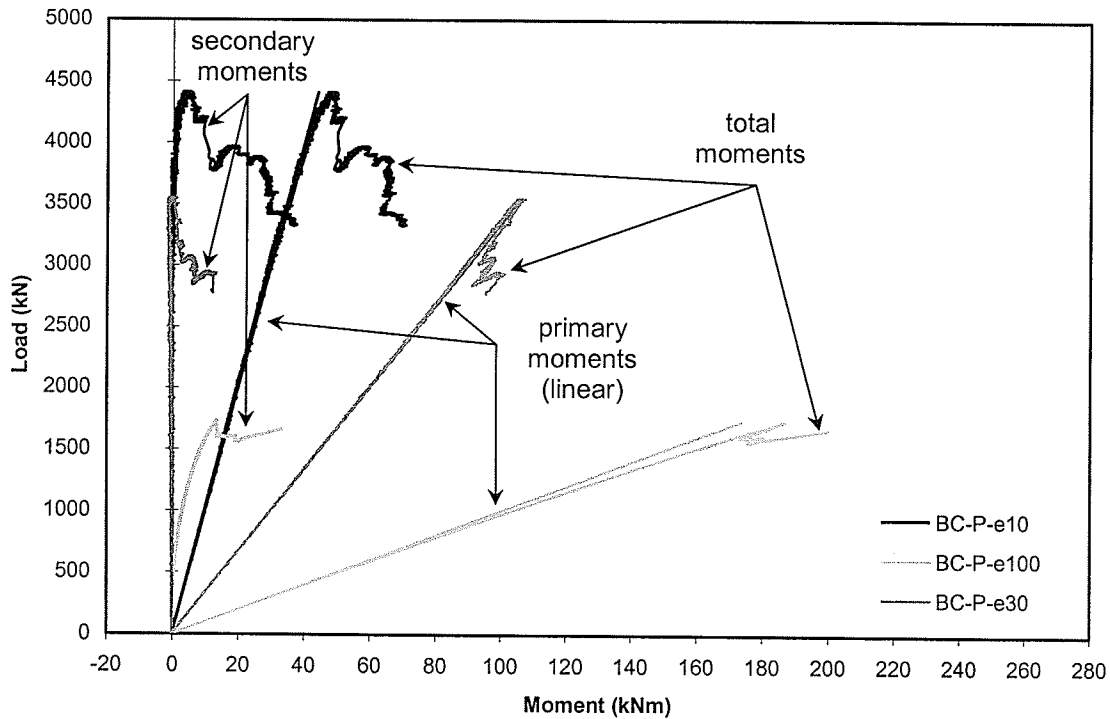
**Figure 4.25:** Axial load-deflection behaviours of beam-column specimens BC-P-e10, BC-P-e30, BC-P-e100, BC-P-e200, and BC-P-e300.



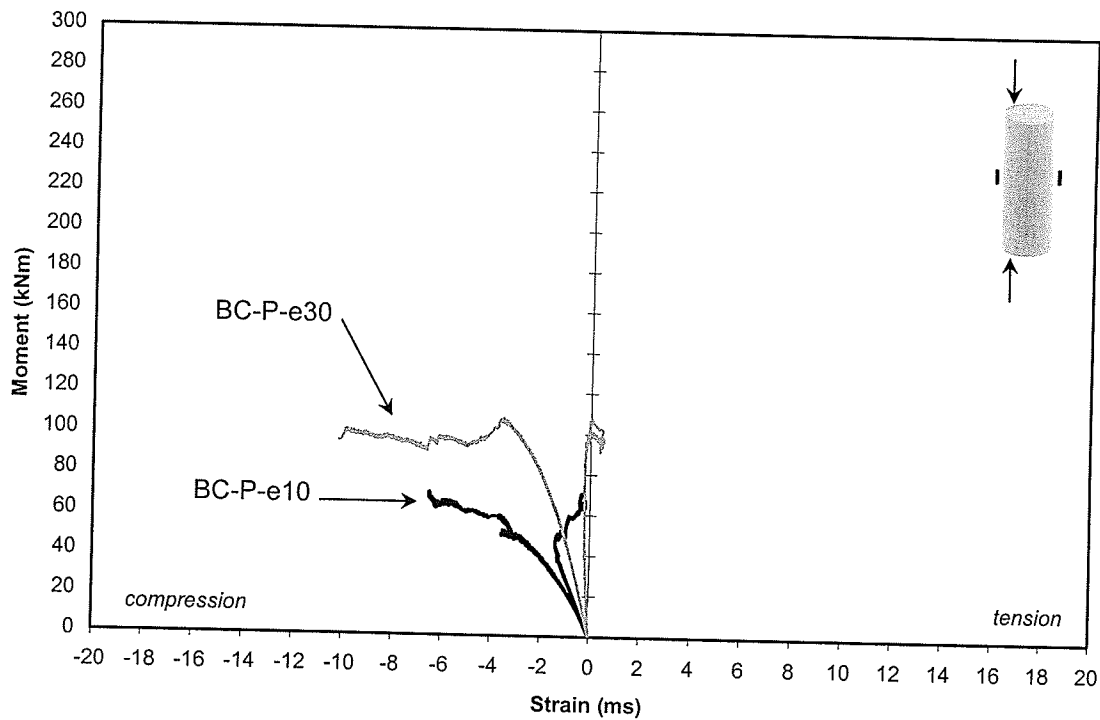
**Figure 4.26:** Moment-deflection behaviours of beam-column specimens BC-P-e10 and BC-P-e30.



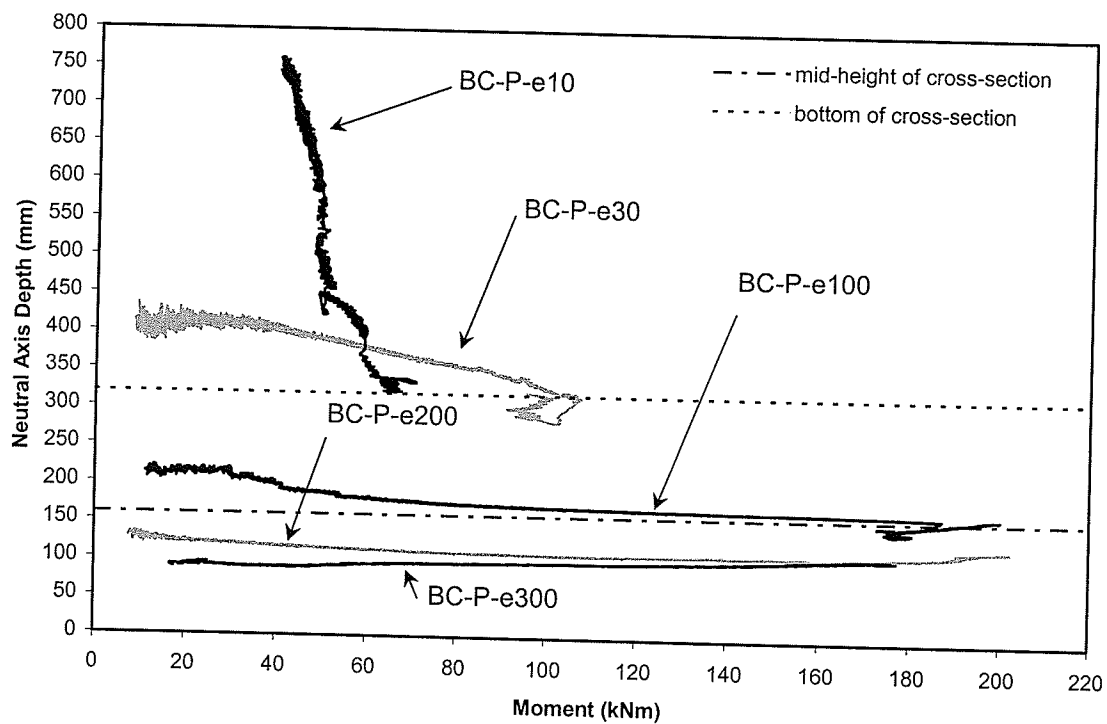
**Figure 4.27:** Initial delamination and buckling of FRP shell laminas in the maximum compression zone of specimen BC-P-e10.



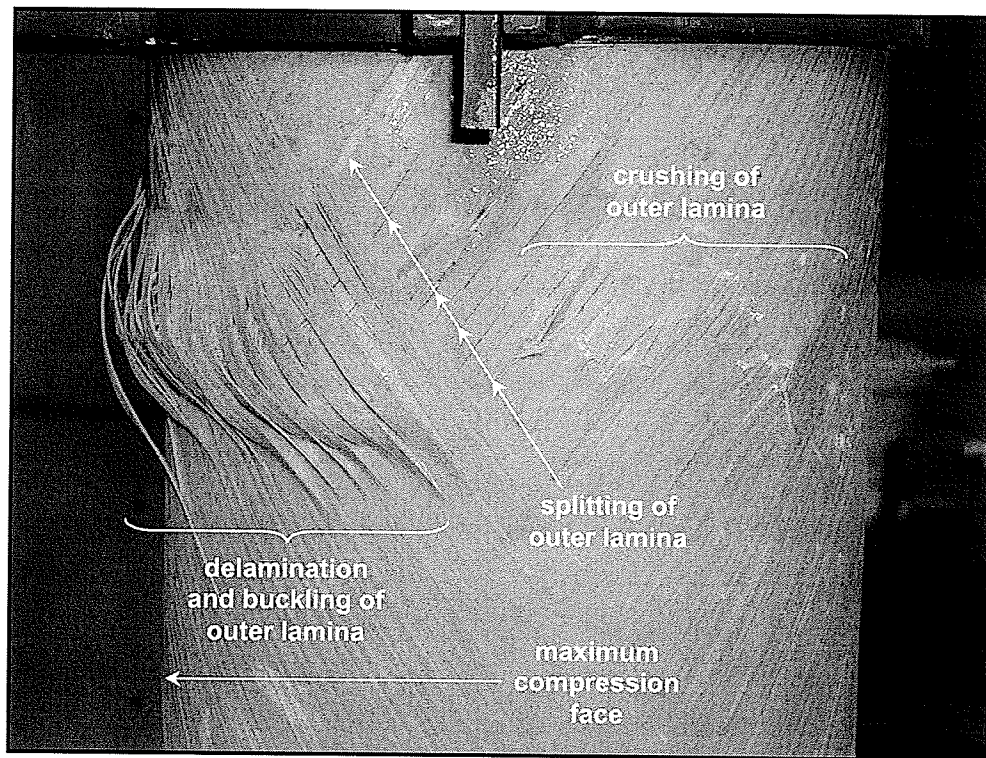
**Figure 4.28:** Axial load-moment behaviours of beam-columns BC-P-e10, BC-P-e30, and BC-P-e100.



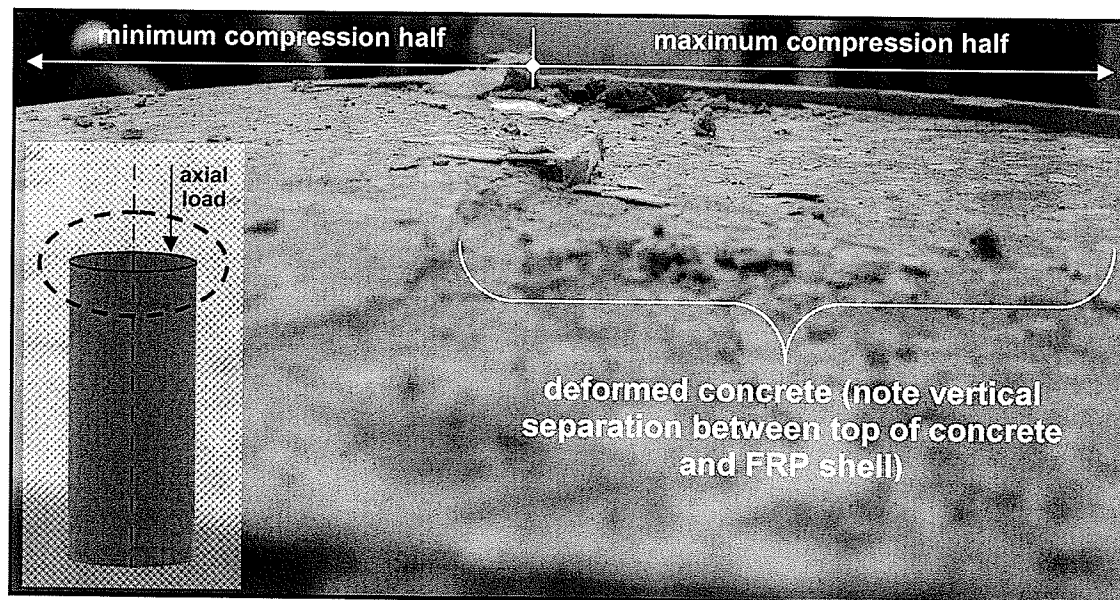
**Figure 4.29:** Moment-axial strain behaviours of beam-columns BC-P-e10 and BC-P-e30.



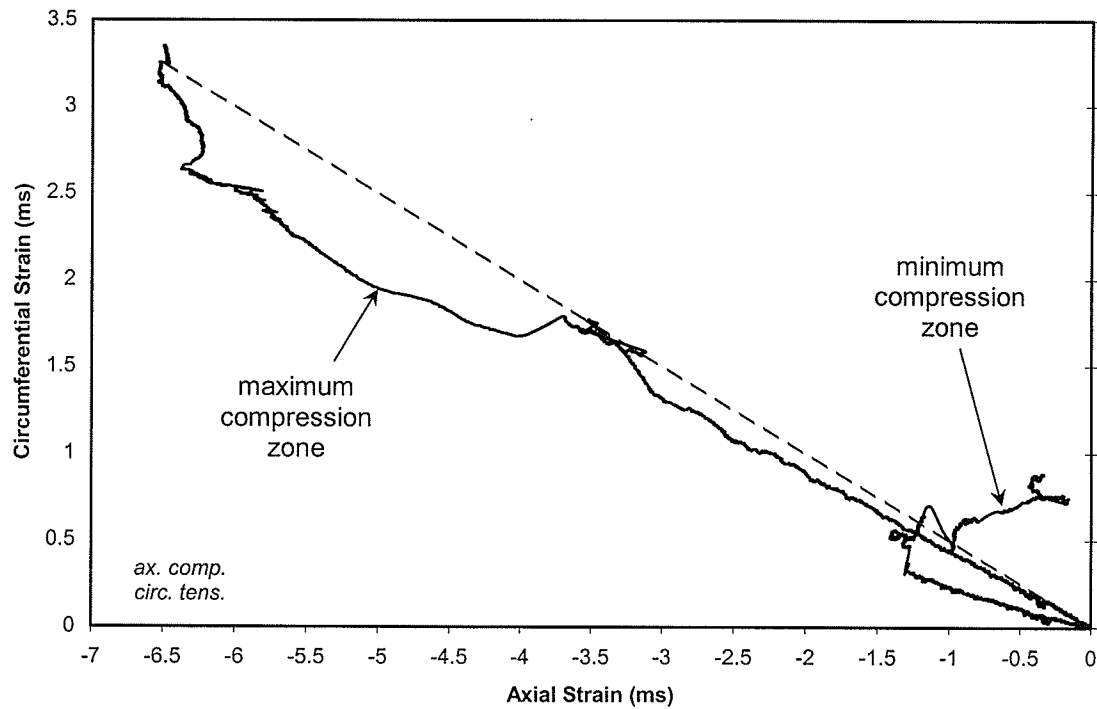
**Figure 4.30:** Neutral axis depth-moment behaviours of beam-columns BC-P-e10, BC-P-e30, BC-P-e100, BC-P-e200, and BC-P-e300.



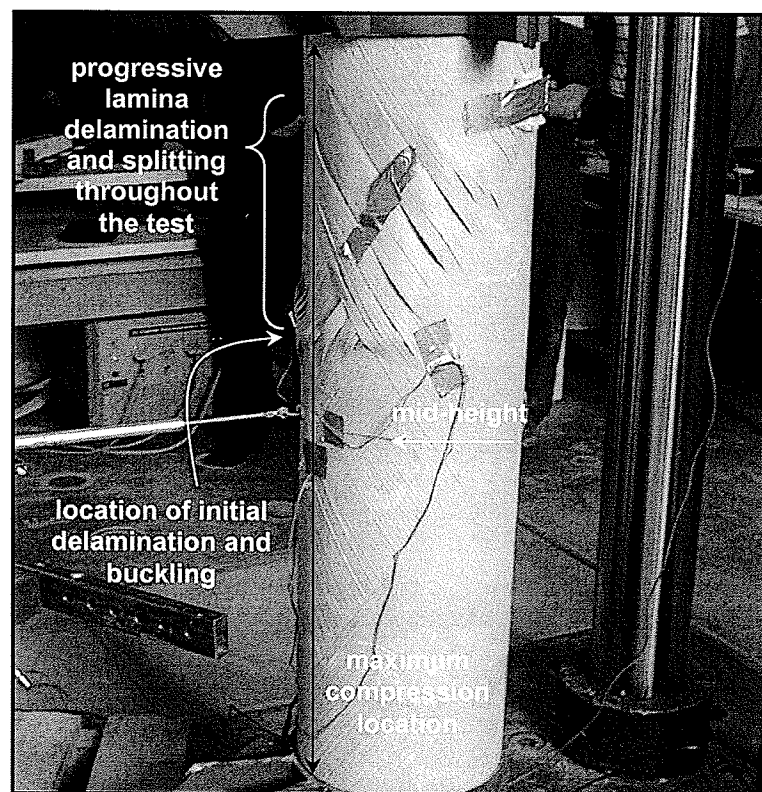
**Figure 4.31:** Overall failure of specimen BC-P-e10 by propagation of delamination and buckling, splitting, and crushing of shell laminas.



**Figure 4.32:** Deformation of concrete core in the maximum compression region of specimen BC-P-e10.



**Figure 4.33:** Circumferential-axial strain behaviour of beam-column specimen BC-P-e10.



**Figure 4.34:** Failure of outer laminas of specimen BC-P-e30.

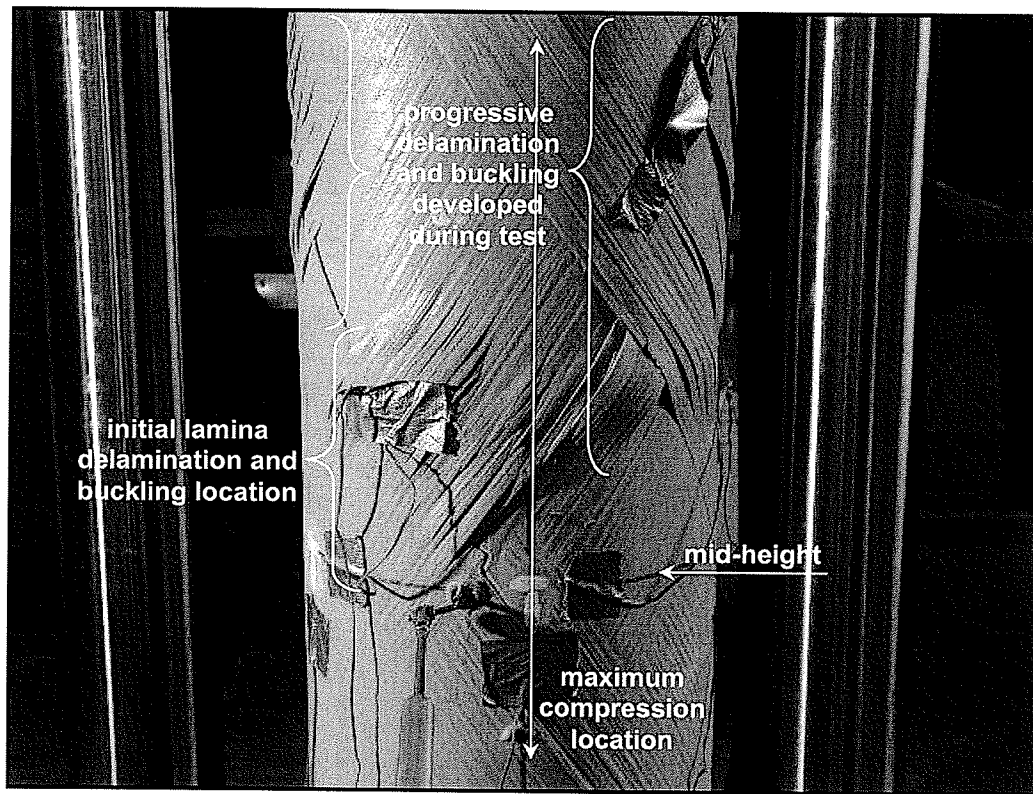


Figure 4.35: Maximum compression face of specimen BC-P-e30 at failure.

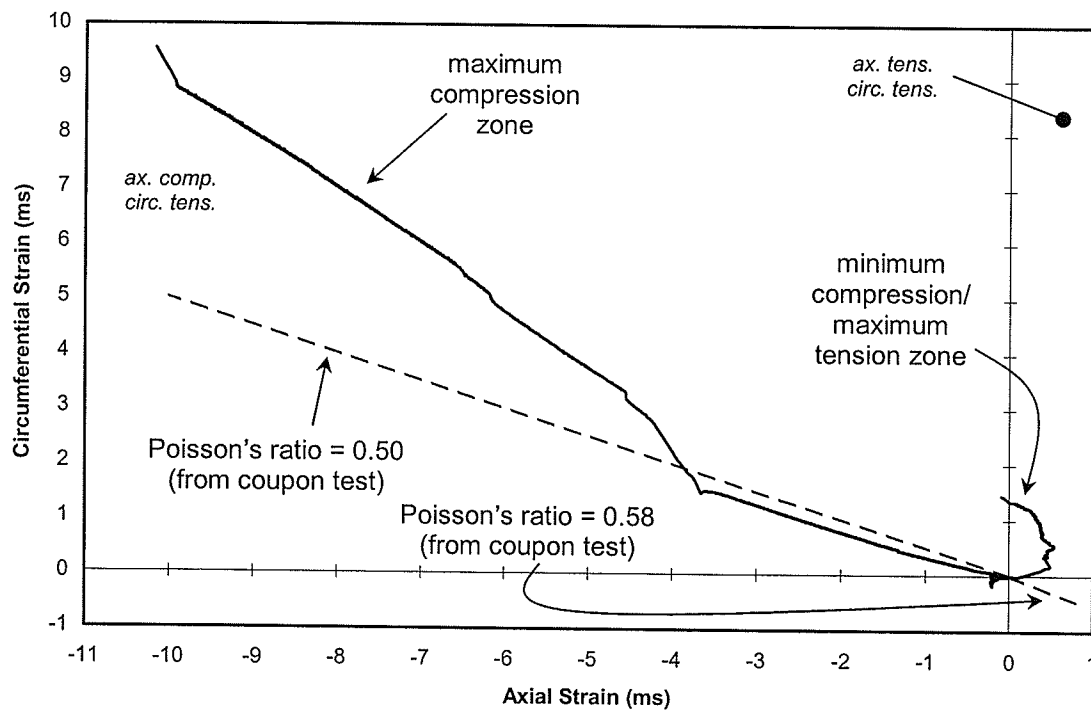
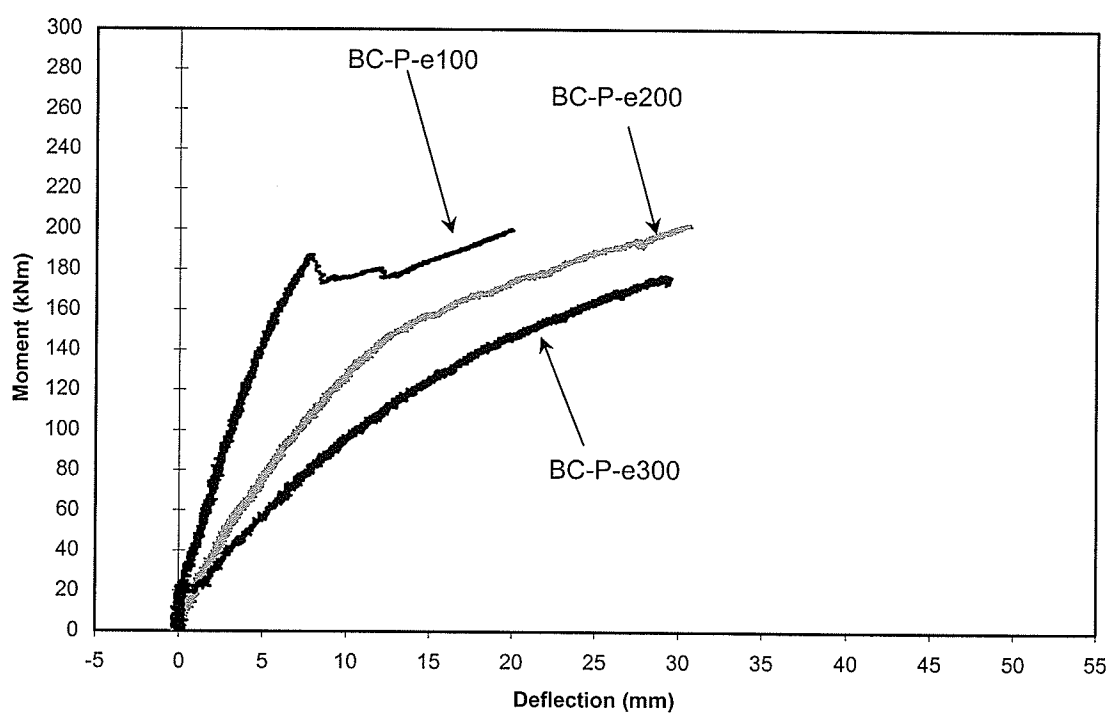
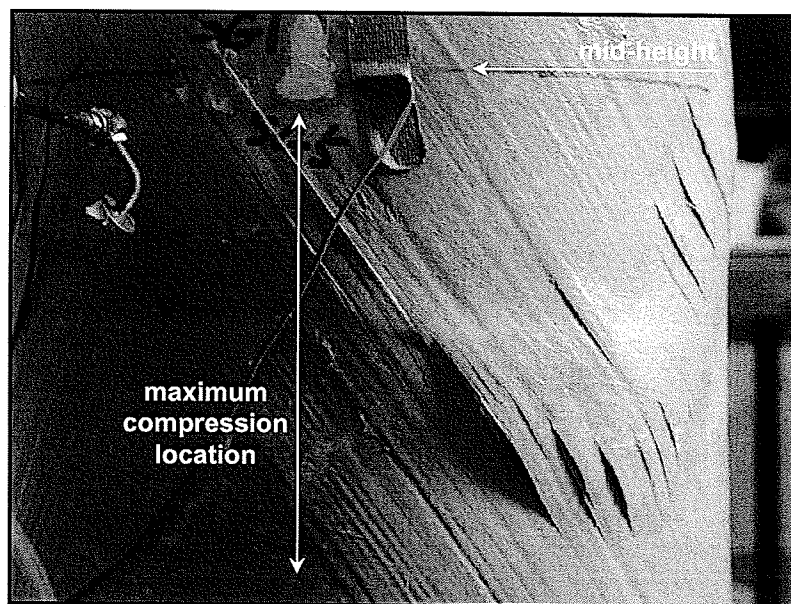


Figure 4.36: Circumferential-axial strain behaviour of beam-column specimen BC-P-e30.

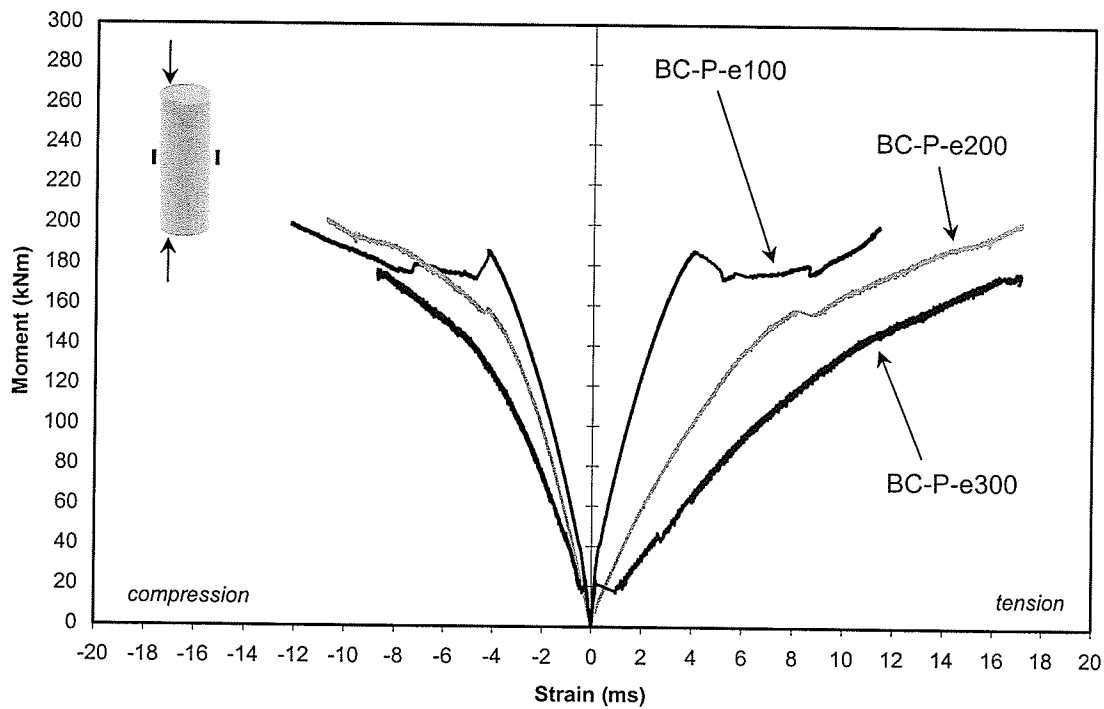




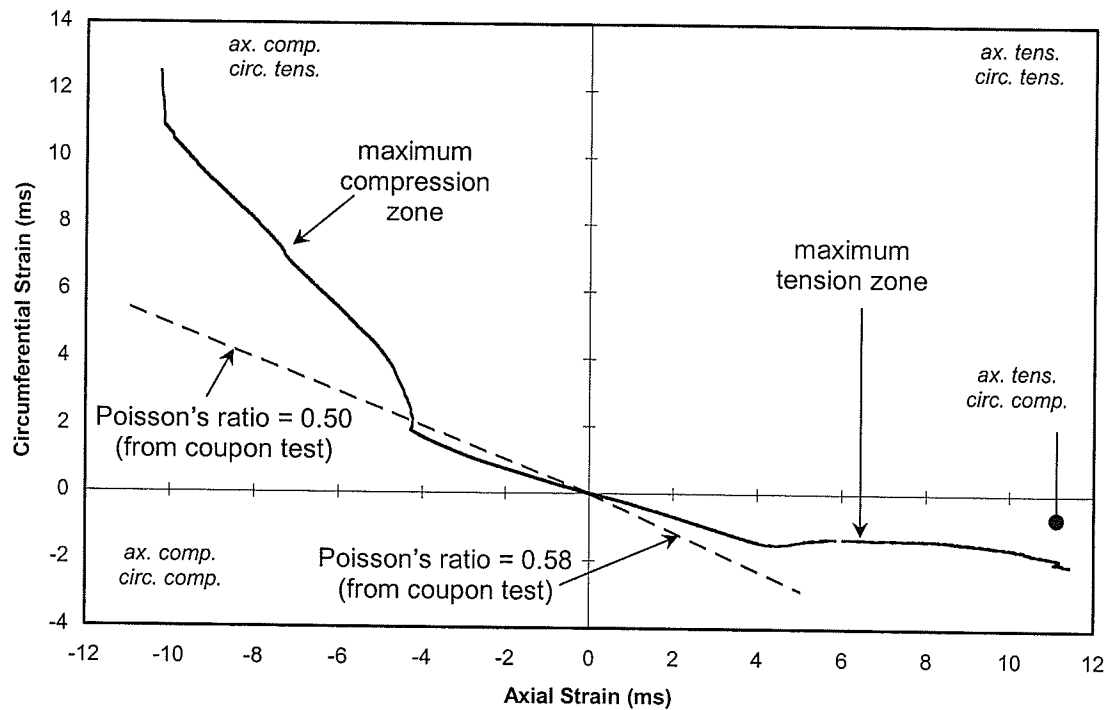
**Figure 4.37:** Moment-deflection behaviours of beam-column specimens BC-P-e100, BC-P-e200, and BC-P-e300.



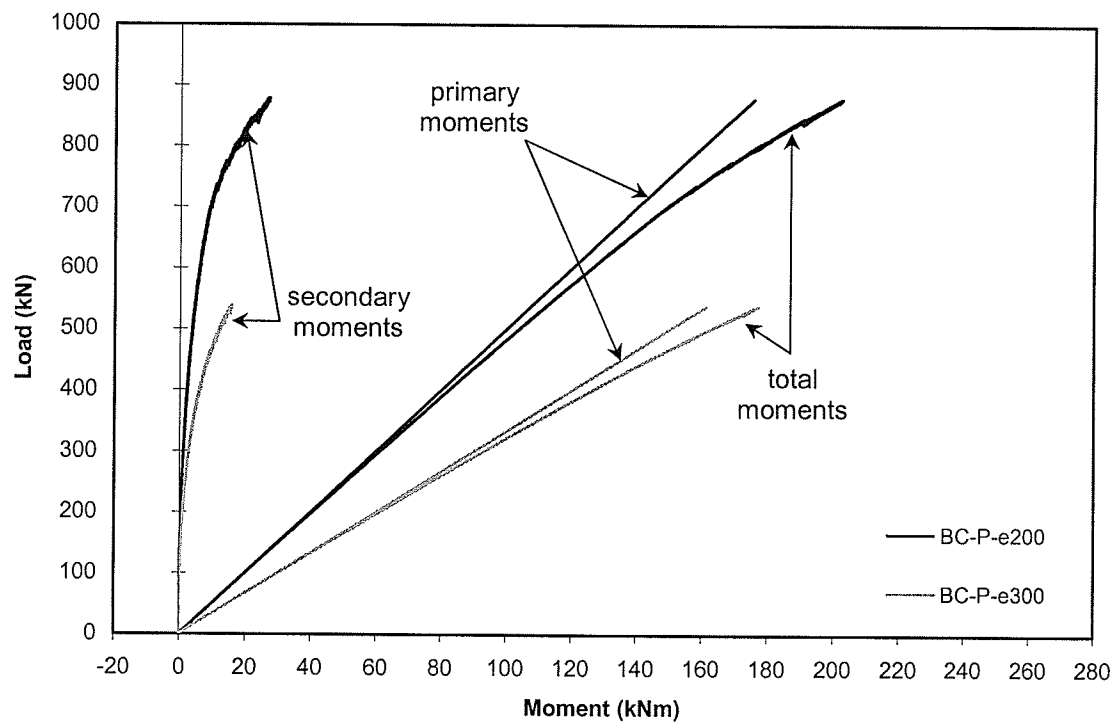
**Figure 4.38:** Failure region at the maximum compression face of specimen BC-P-e100.



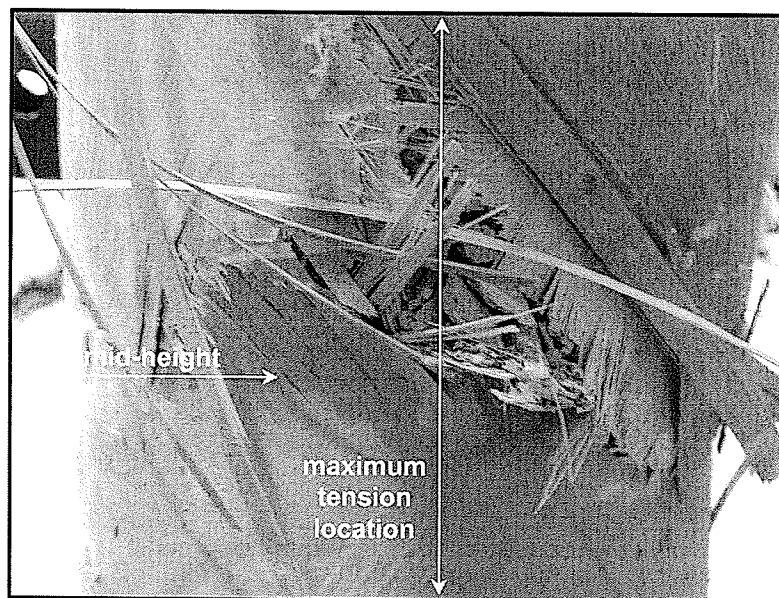
**Figure 4.39:** Moment-axial strain behaviours of beam-column specimens BC-P-e100, BC-P-e200, and BC-P-e300.



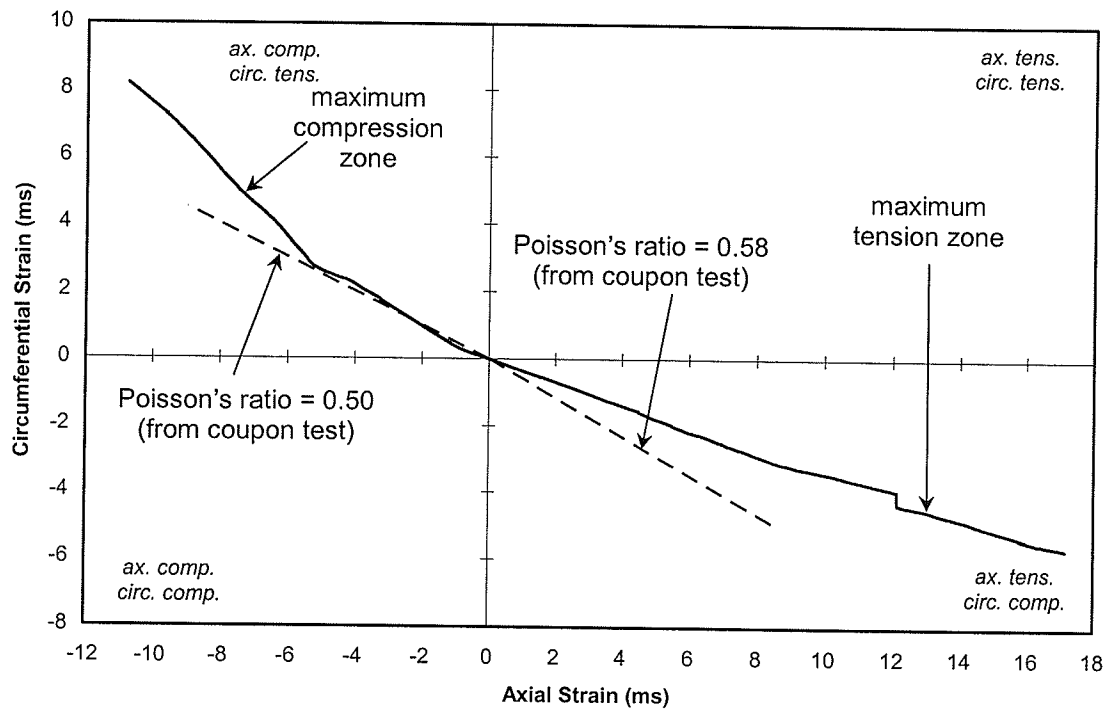
**Figure 4.40:** Circumferential-axial strain behaviour of beam-column specimen BC-P-e100.



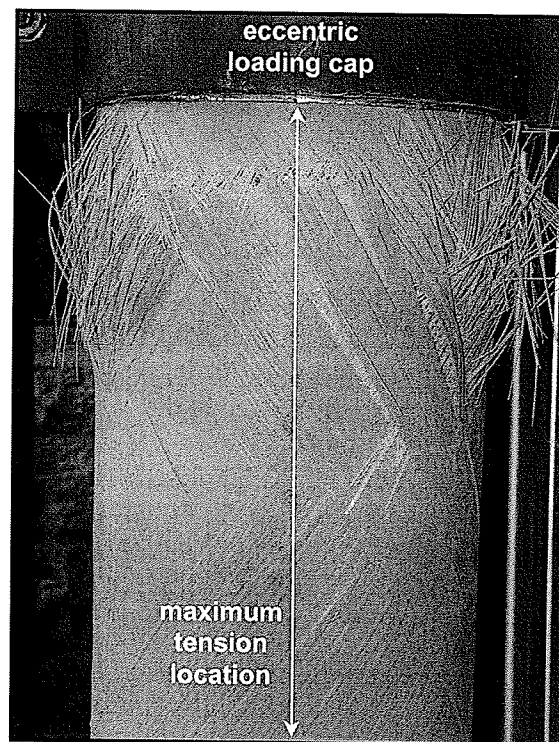
**Figure 4.41:** Axial load-moment behaviours of beam-column specimens BC-P-e200 and BC-P-e300.



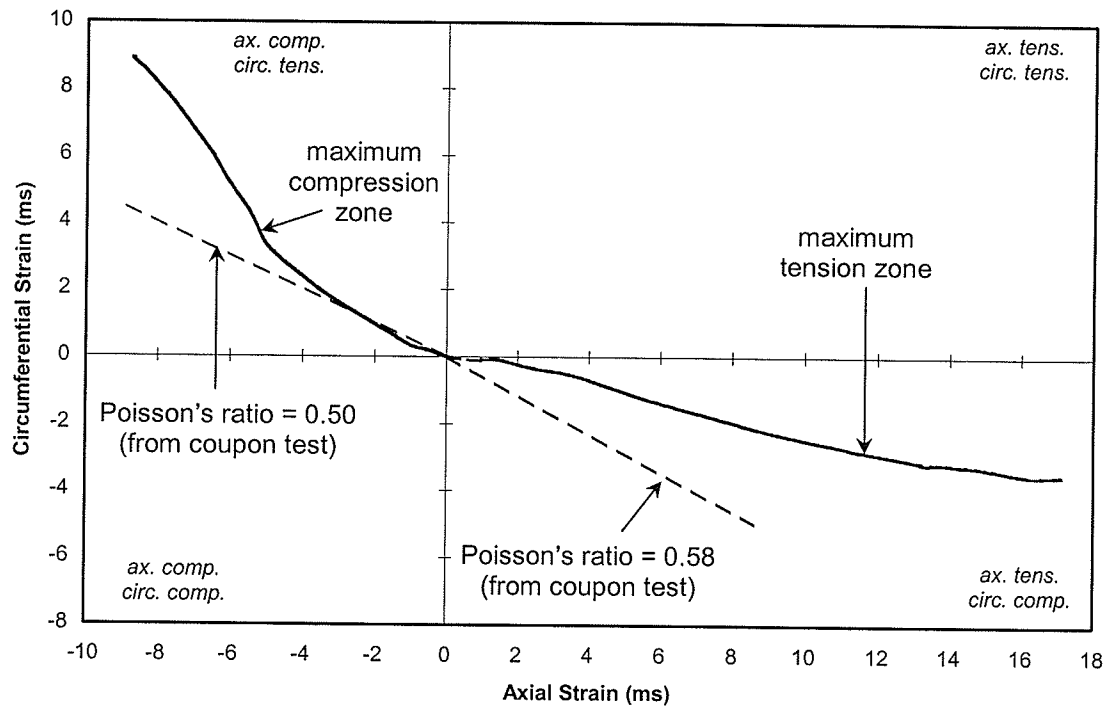
**Figure 4.42:** Tension failure of specimen BC-P-e200.



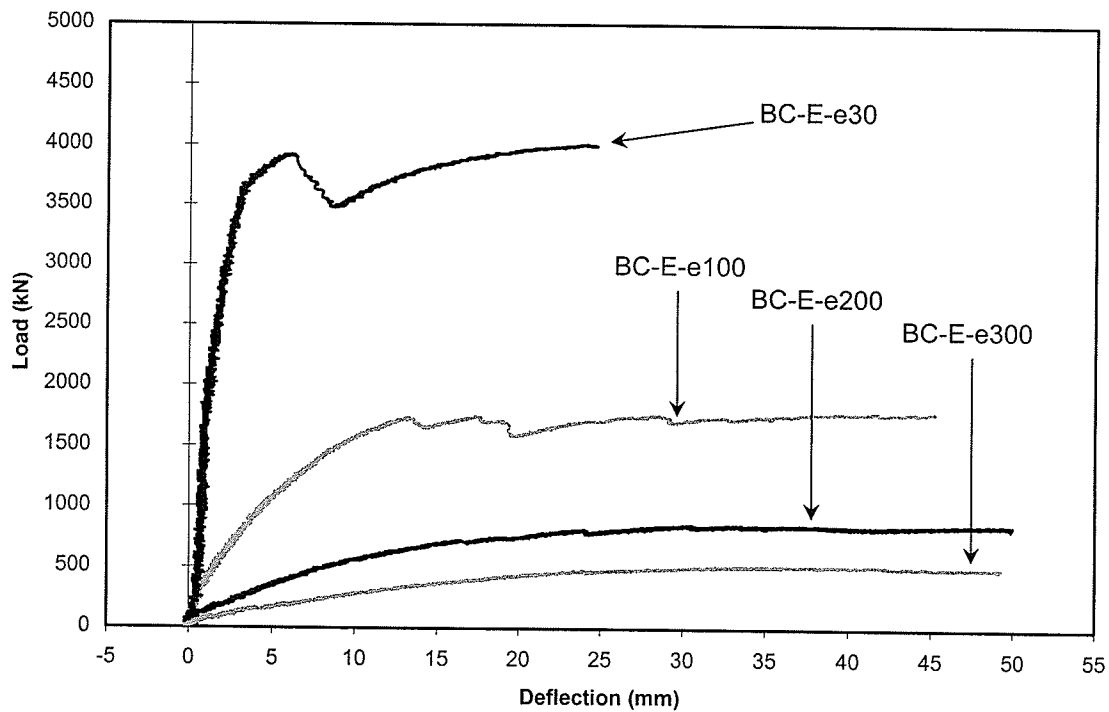
**Figure 4.43:** Circumferential-axial strain behaviour of beam-column specimen BC-P-e200.



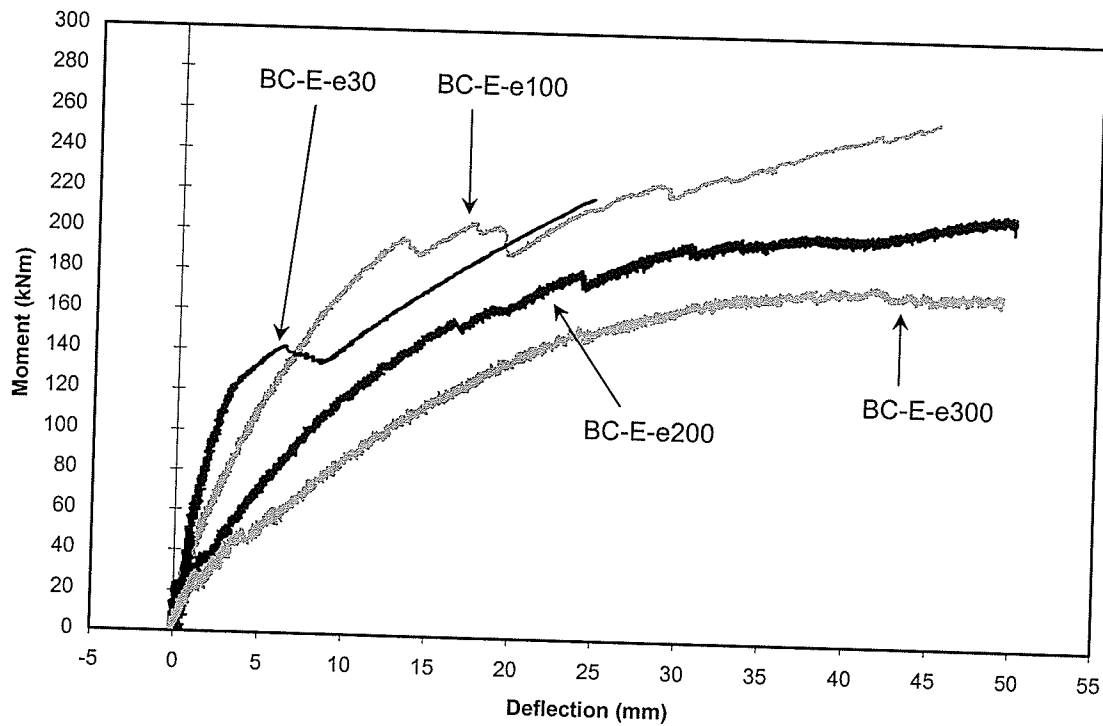
**Figure 4.44:** Tension failure of specimen BC-P-e300 near the top eccentric loading cap.



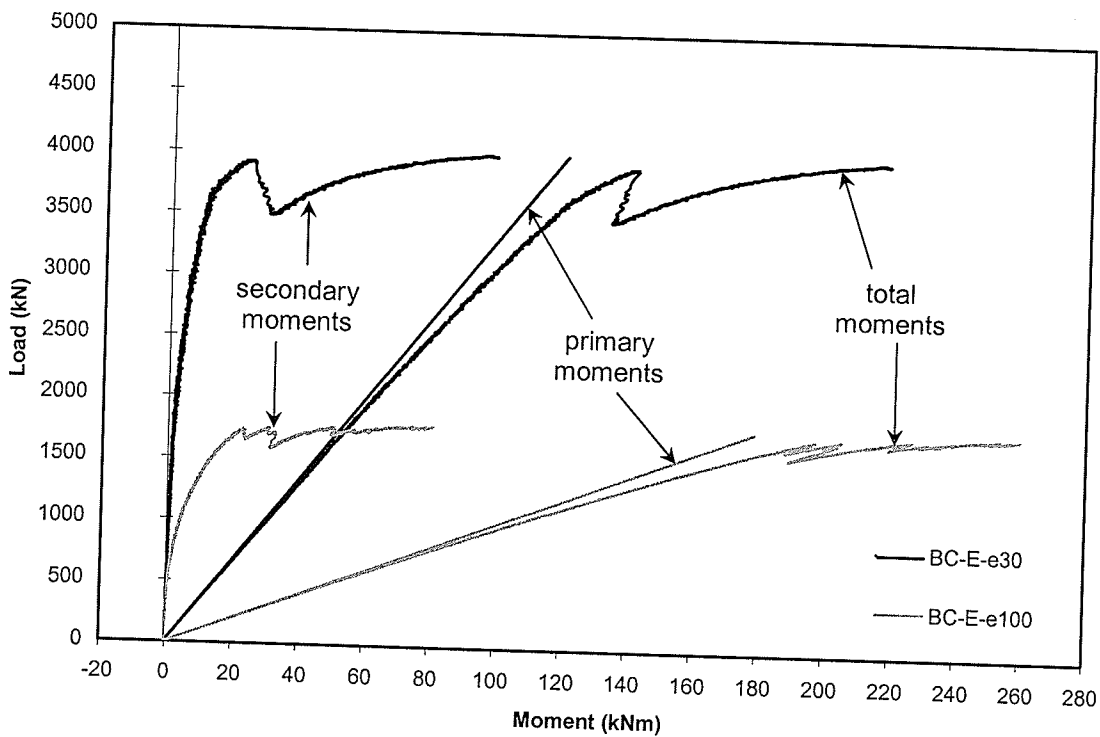
**Figure 4.45:** Circumferential-axial strain behaviour of beam-column specimen BC-P-e300.



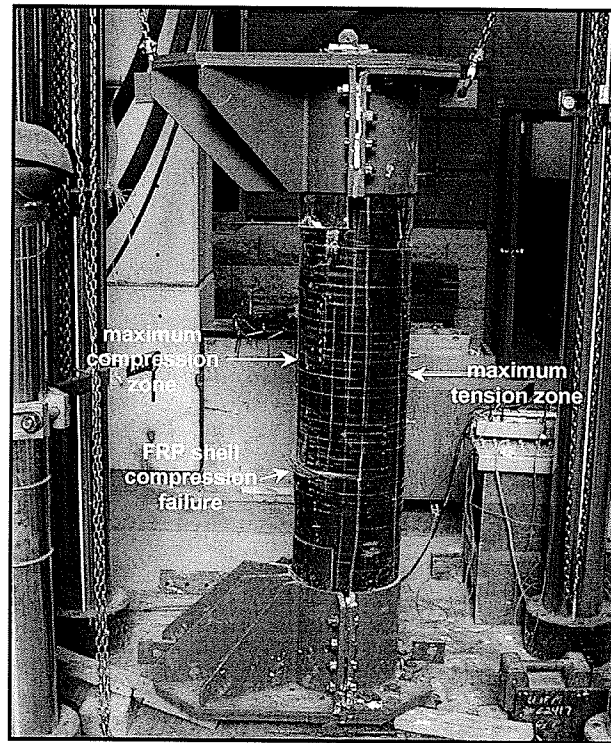
**Figure 4.46:** Axial load-deflection behaviours of beam-column specimens BC-E-e30, BC-E-e100, BC-E-e200, and BC-E-e300.



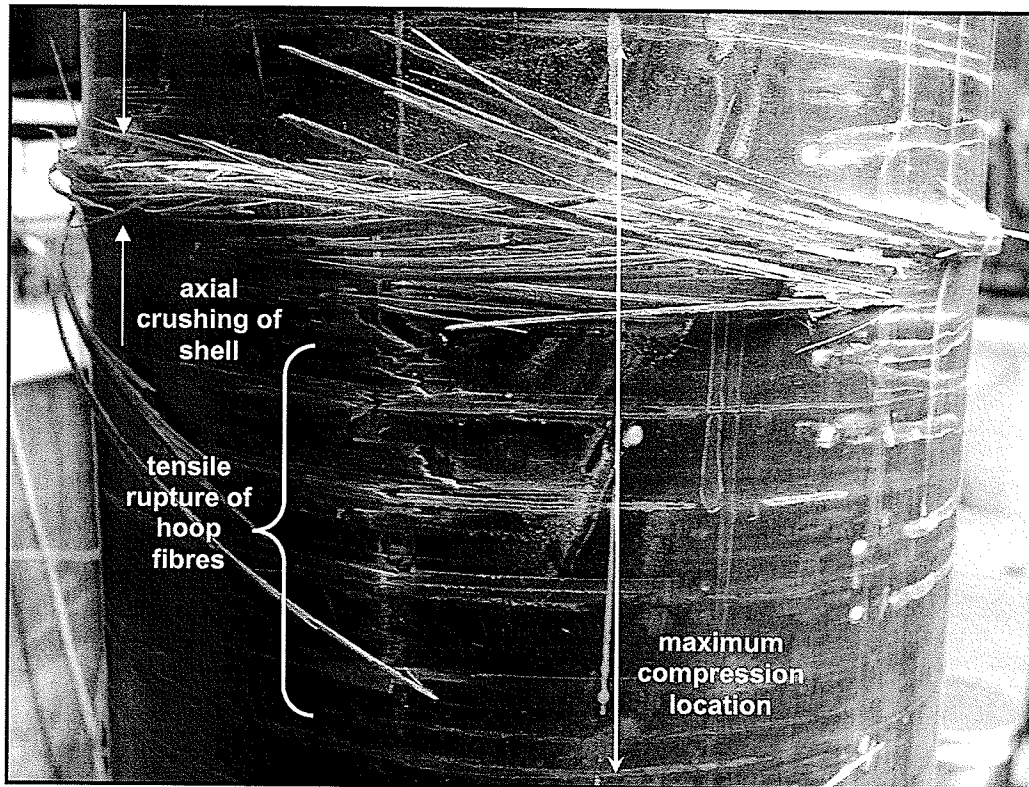
**Figure 4.47:** Moment-deflection behaviours of beam-column specimens BC-E-e30, BC-E-e100, BC-E-e200, and BC-E-e300.



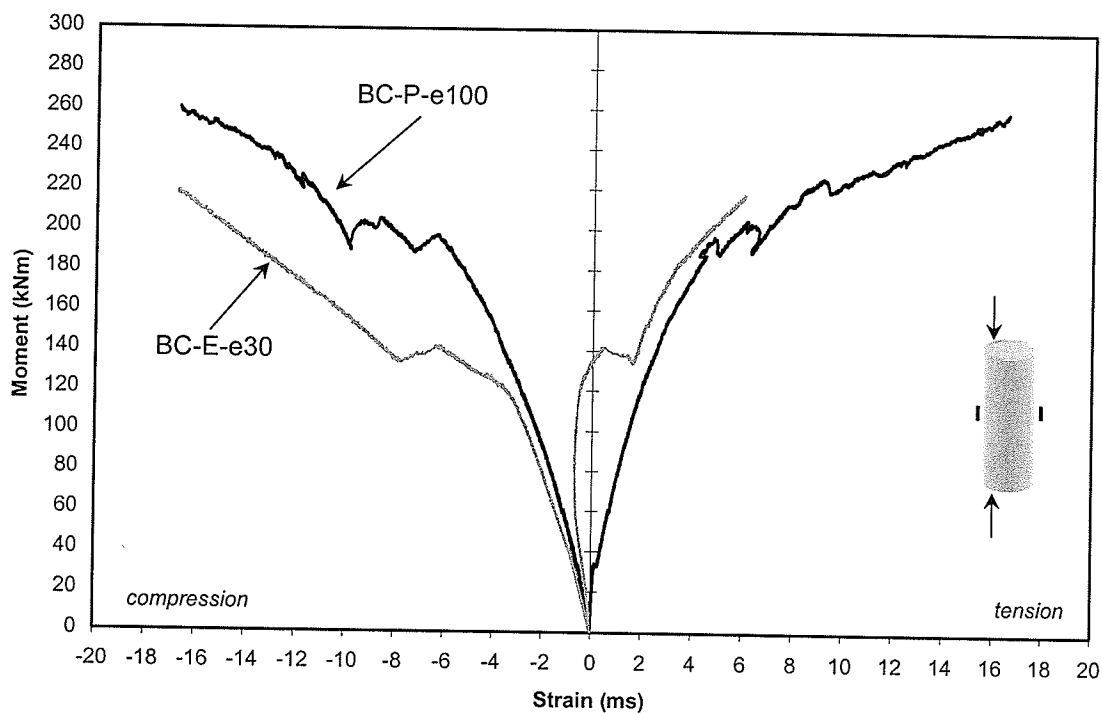
**Figure 4.48:** Axial load-moment behaviours of beam-column specimens BC-E-e30 and BC-E-e100.



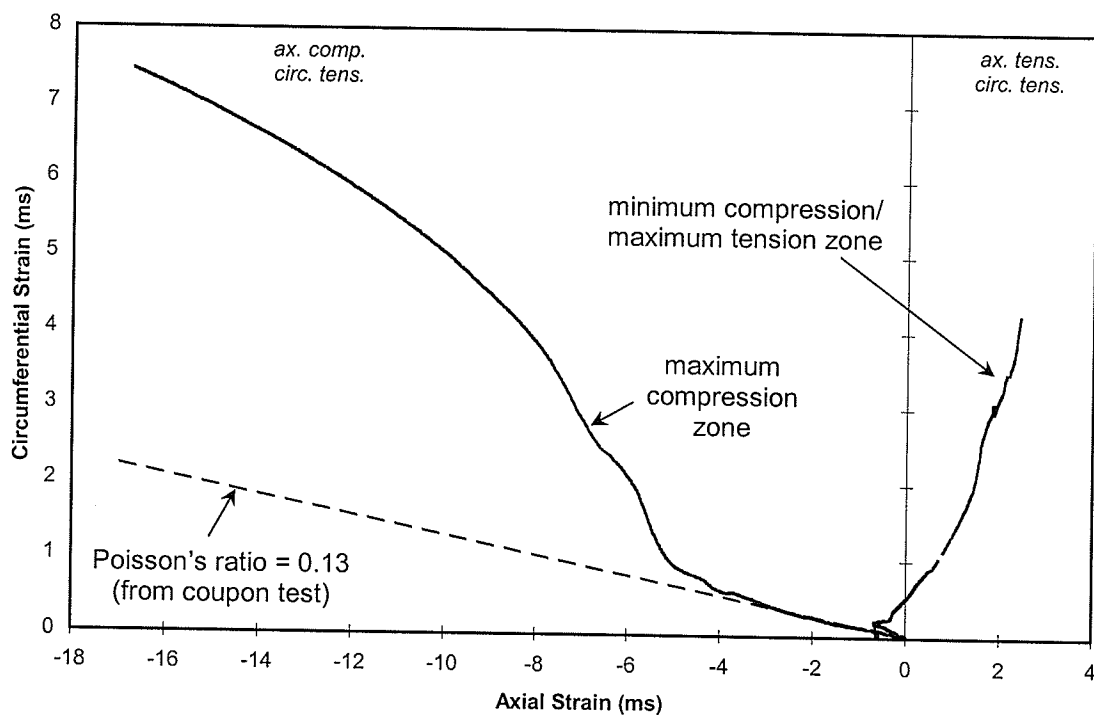
**Figure 4.49:** Failure location on specimen BC-E-e30.



**Figure 4.50:** FRP shell compression failure on specimen BC-E-e30.

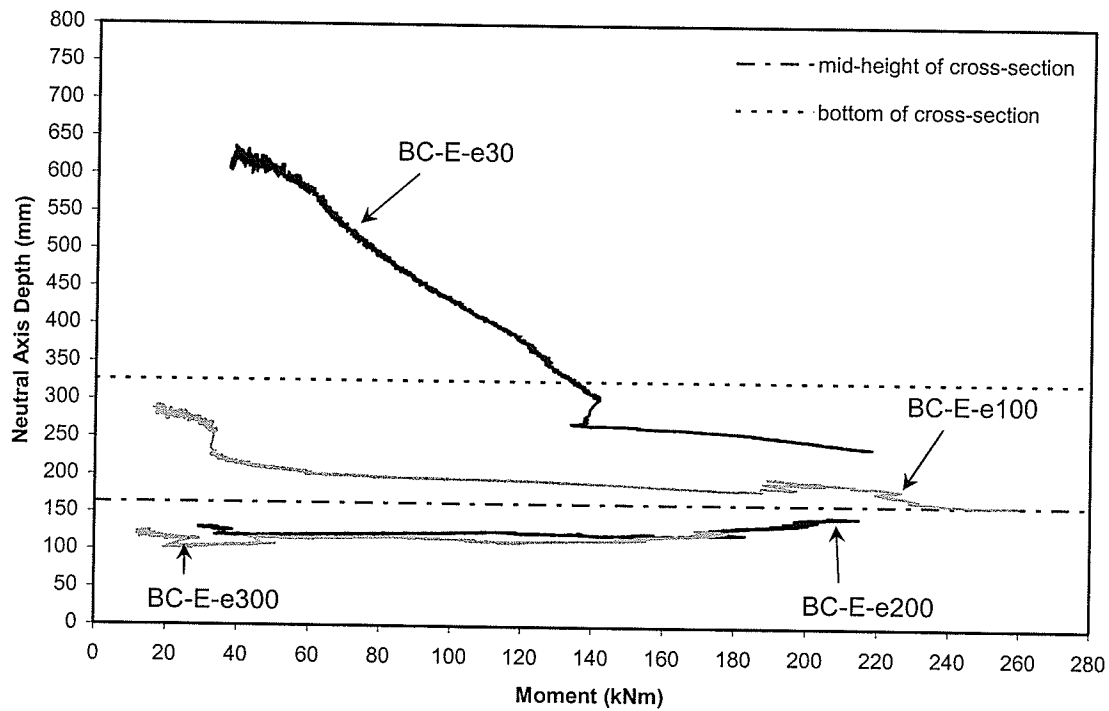


**Figure 4.51:** Moment-axial strain behaviours of beam-column specimens BC-E-e30 and BC-E-e100.

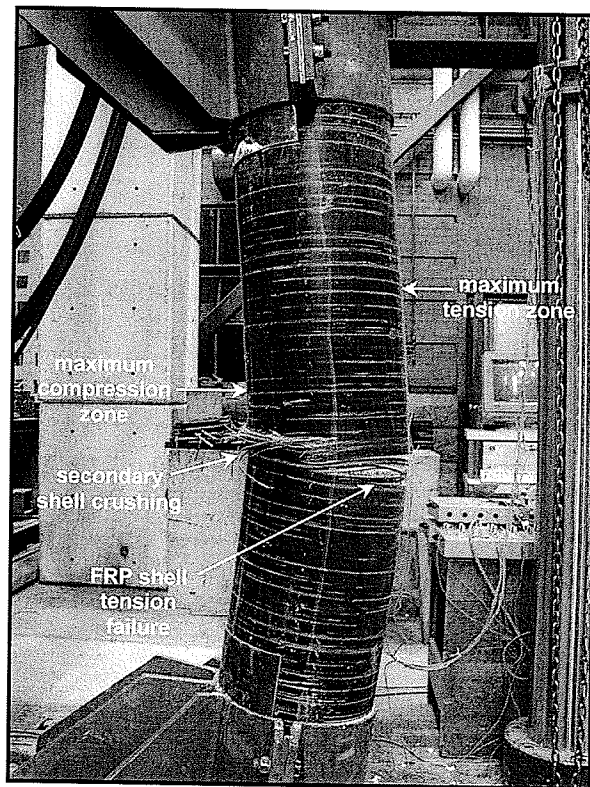


**Figure 4.52:** Circumferential-axial strain behaviour of beam-column specimen BC-E-e30.





**Figure 4.53:** Neutral axis depth-moment behaviours of beam-column specimens BC-E-e30, BC-E-e100, BC-E-e200, and BC-E-e300.



**Figure 4.54:** Failure location on specimen BC-E-e100.

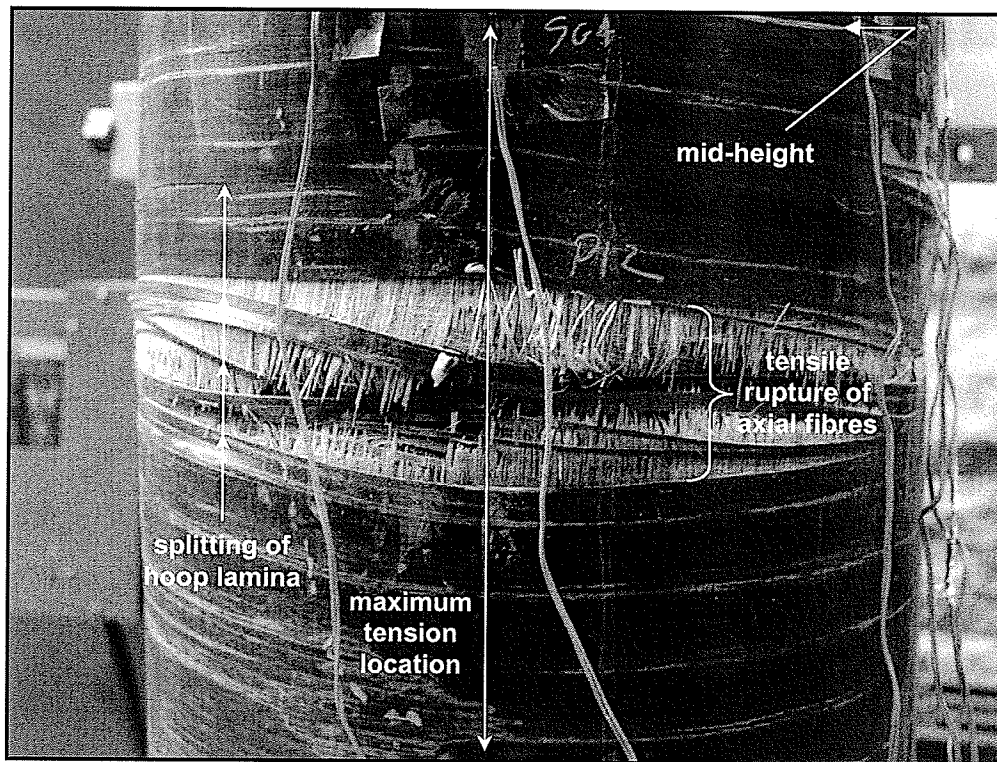


Figure 4.55: FRP shell tension failure on specimen BC-E-e100.

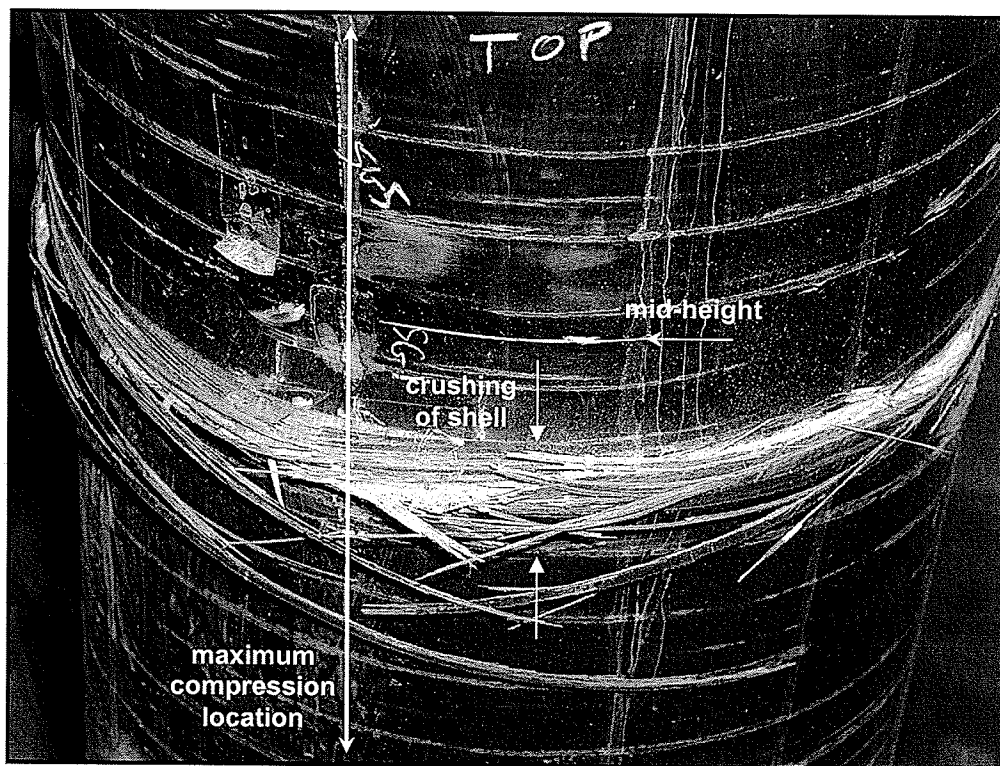
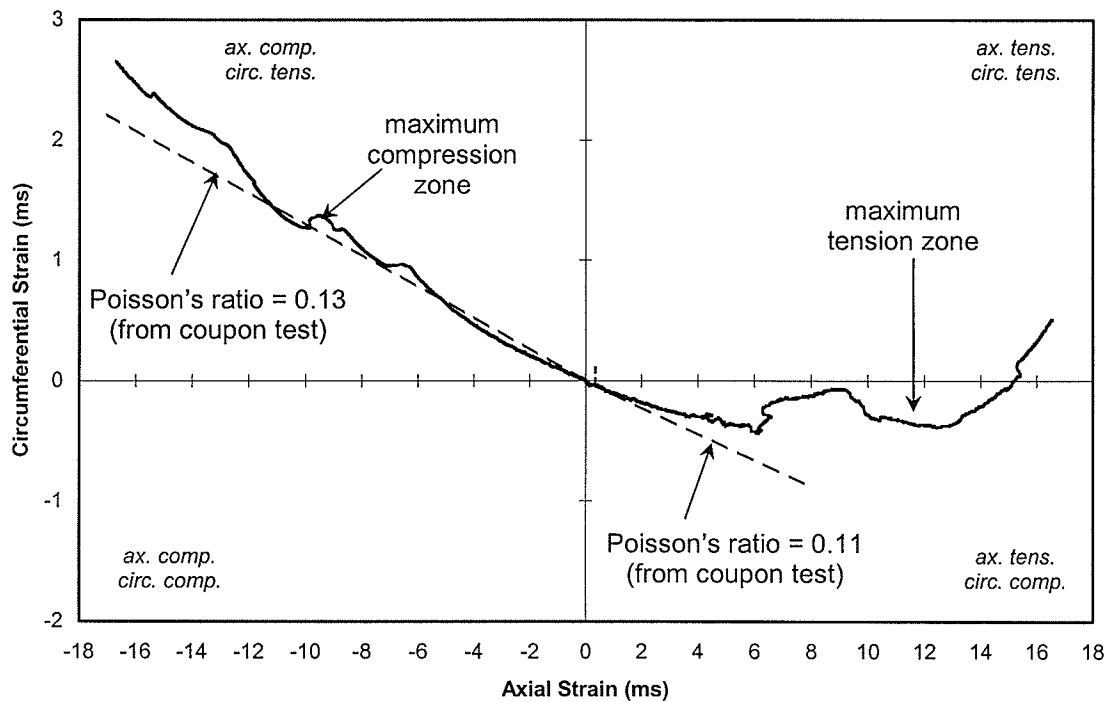
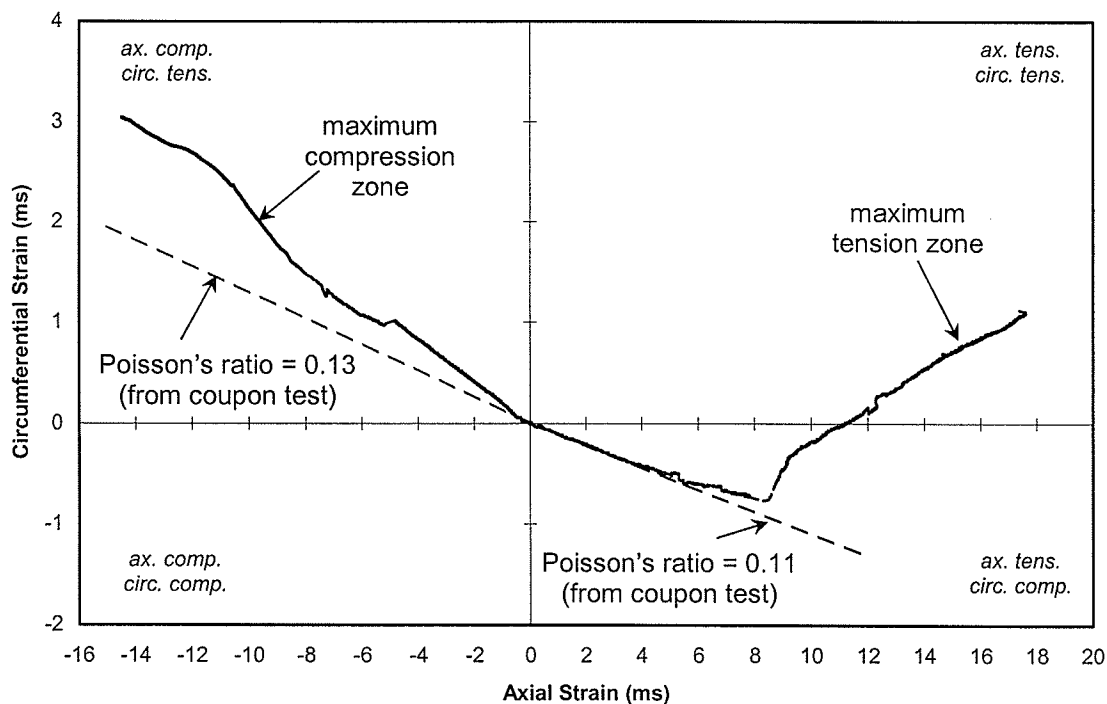


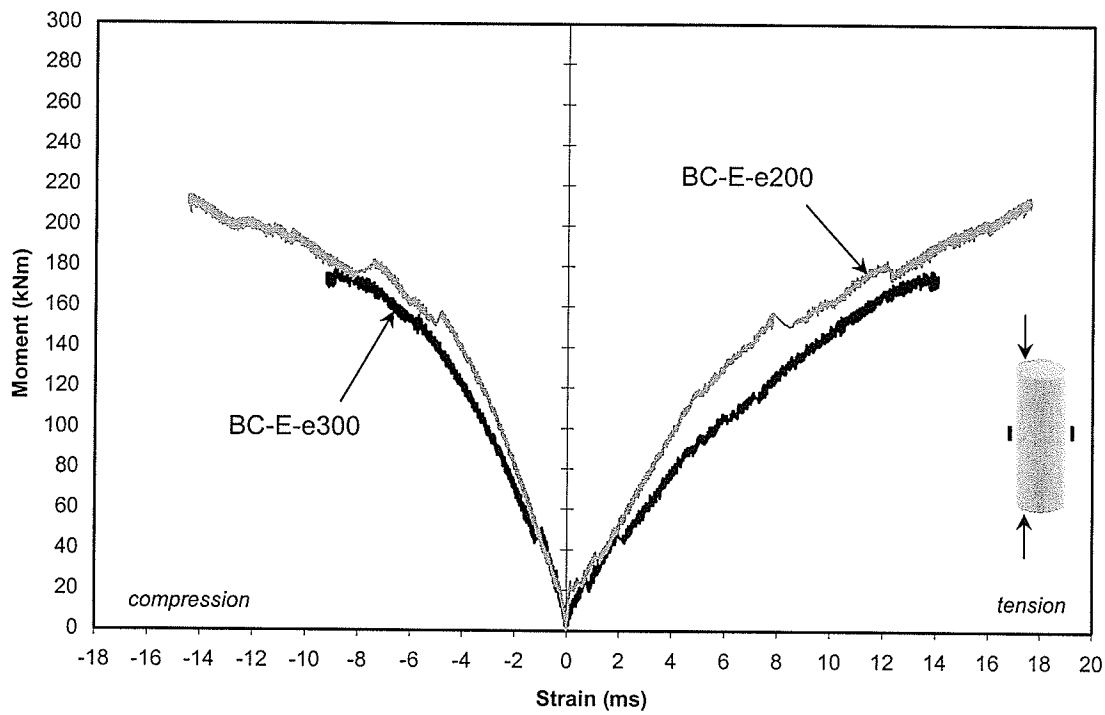
Figure 4.56: Compression side of specimen BC-E-e100 after failure.



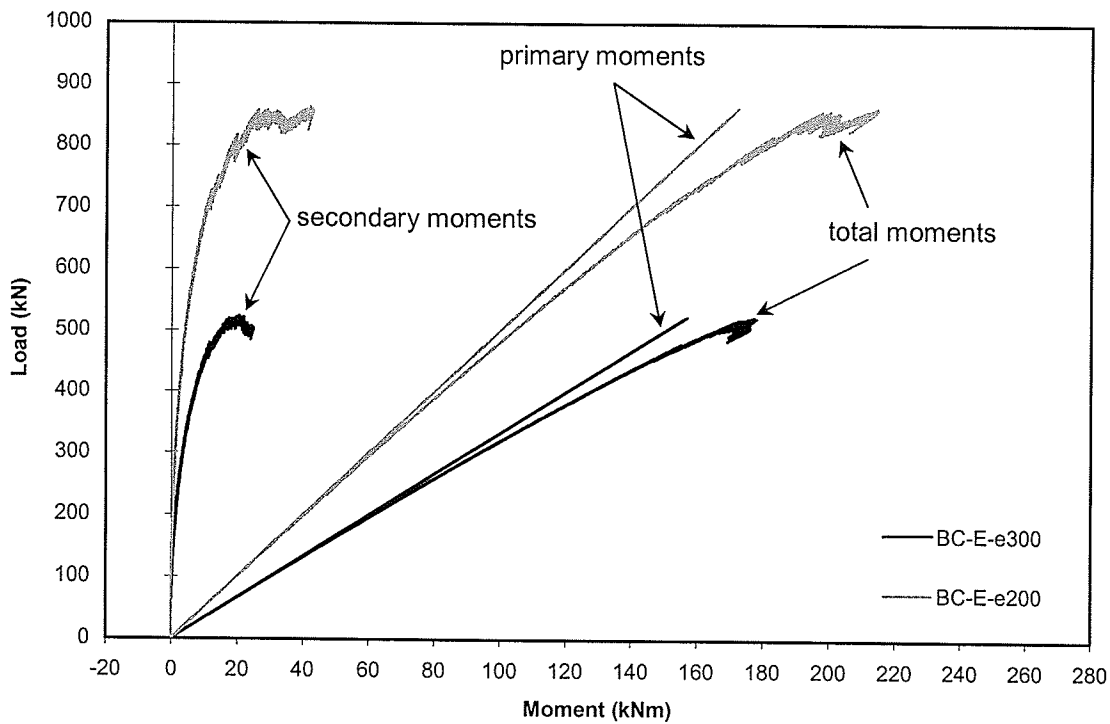
**Figure 4.57:** Circumferential-axial strain behaviour of beam-column specimen BC-E-e100.



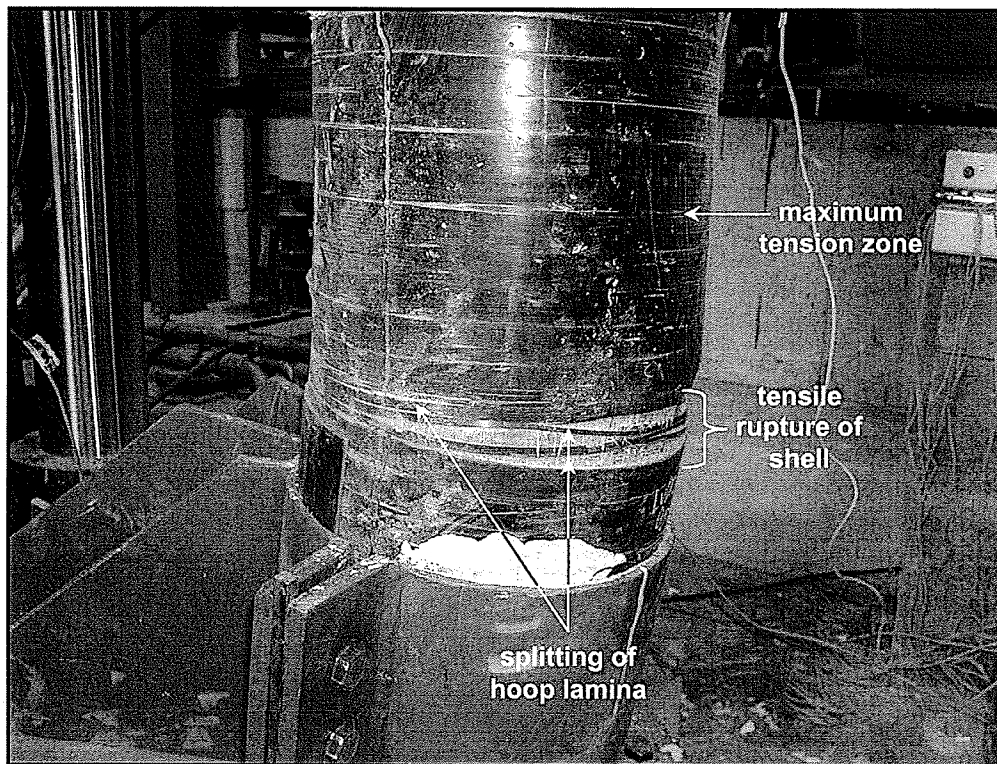
**Figure 4.58:** Circumferential-axial strain behaviour of beam-column specimen BC-E-e200.



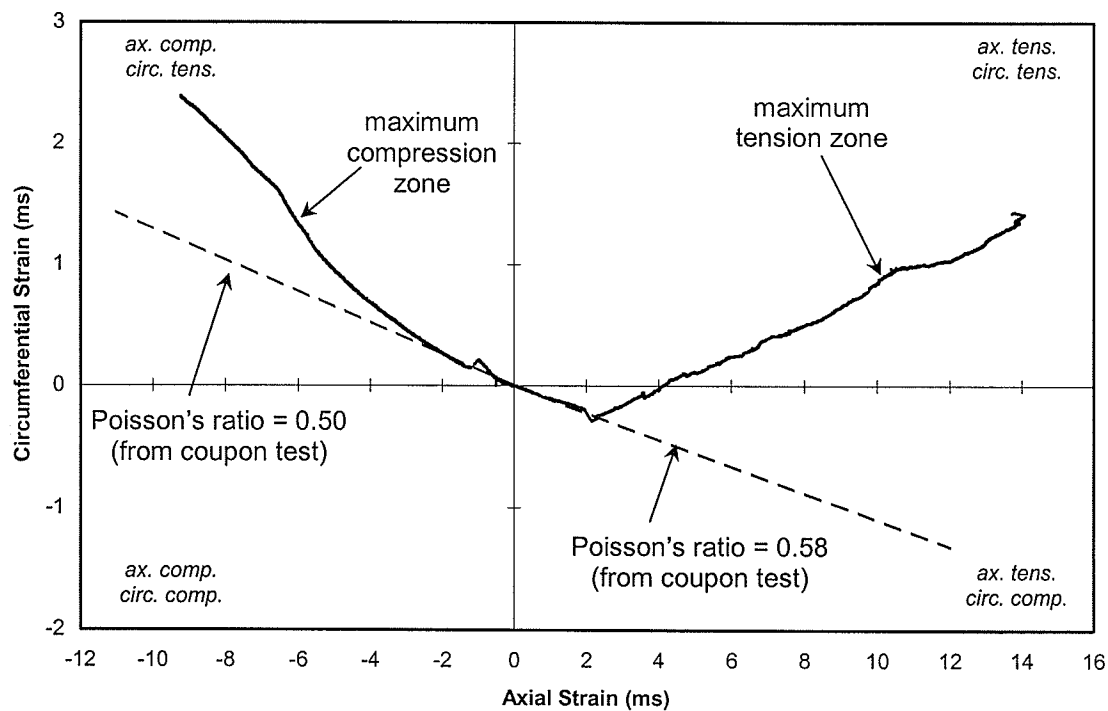
**Figure 4.59:** Moment-axial strain behaviours of beam-column specimens BC-E-e200 and BC-E-e300.



**Figure 4.60:** Axial load-moment behaviours of beam-column specimens BC-E-e200 and BC-E-e300.



**Figure 4.61:** FRP shell tension failure of specimen BC-E-e200.



**Figure 4.62:** Circumferential-axial strain behaviour of beam-column specimen BC-E-e300.

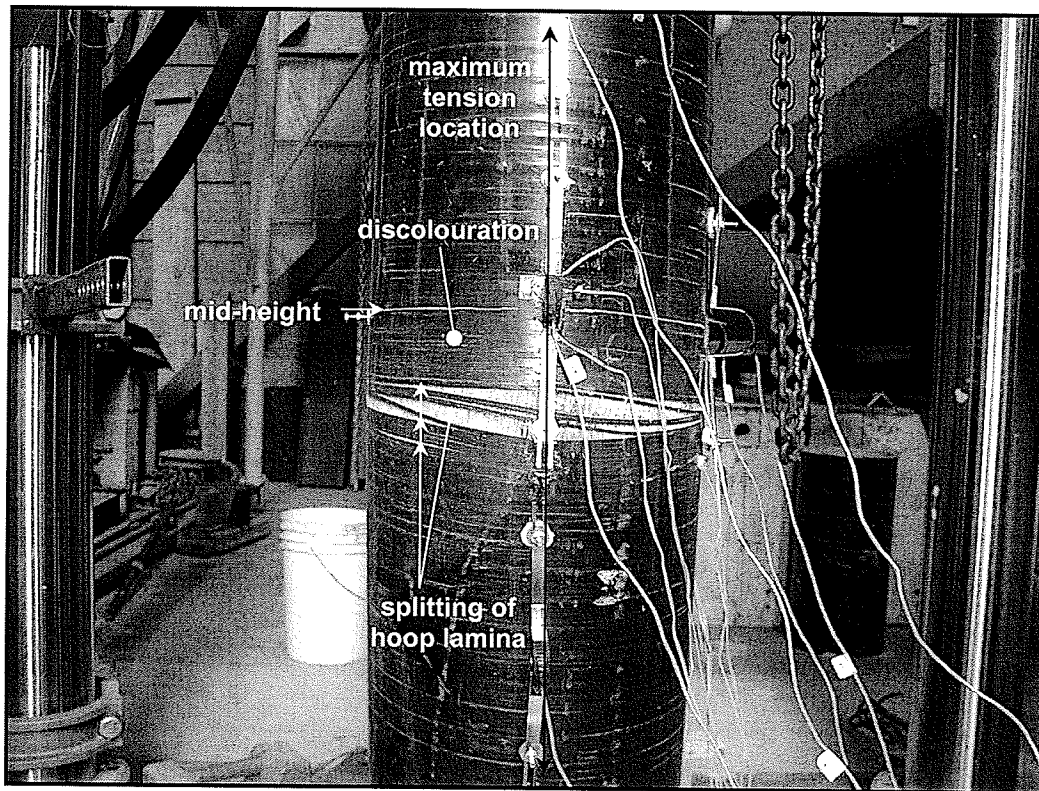


Figure 4.63: FRP shell tension failure of specimen BC-E-e300.

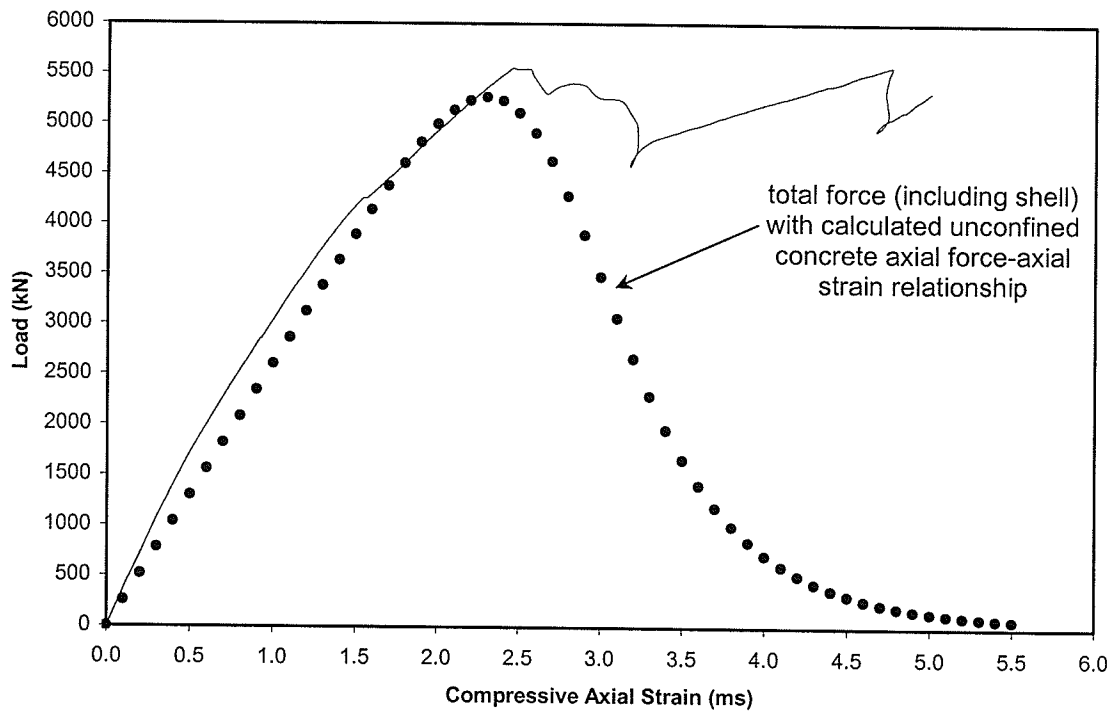
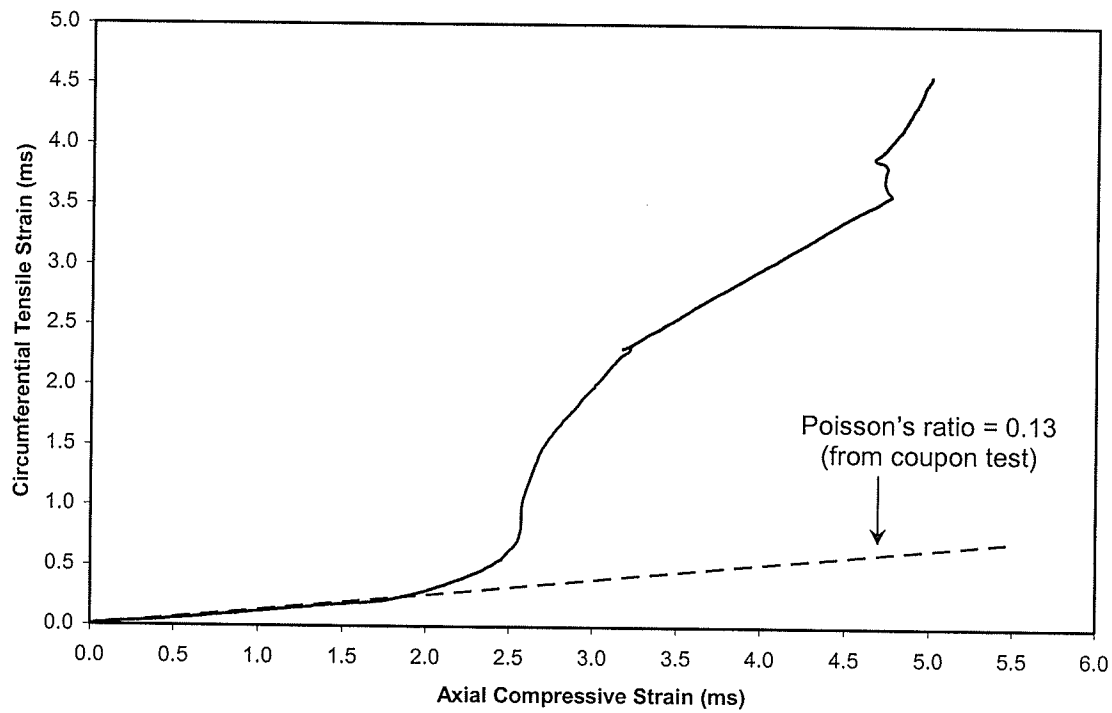
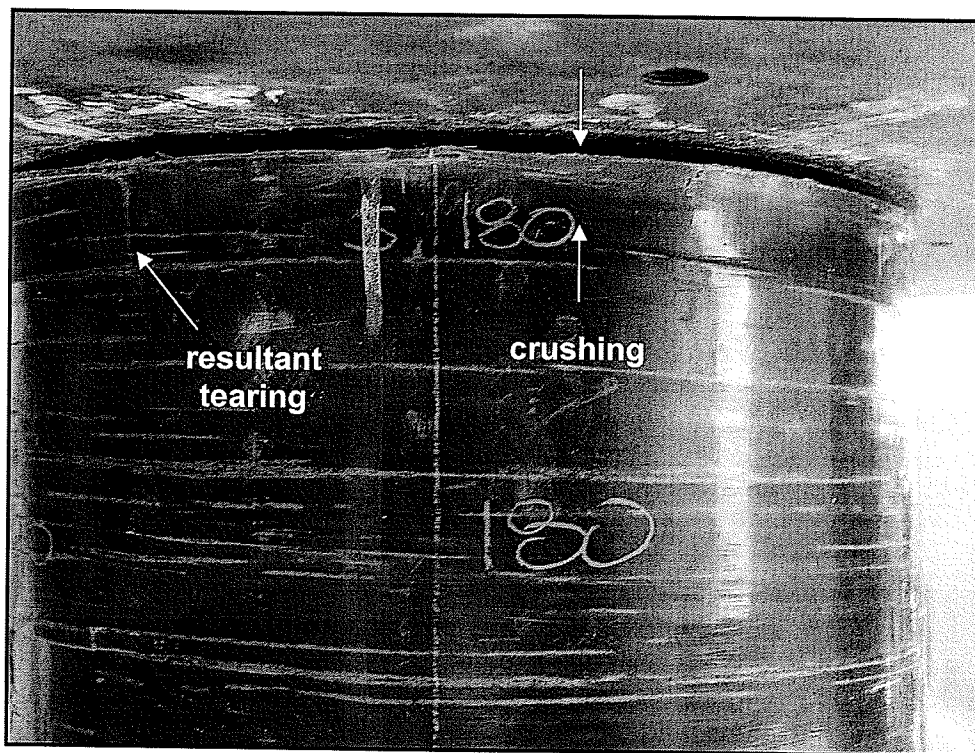


Figure 4.64: Load-axial strain behaviour of the E-glass/epoxy shell pure axial load specimen.

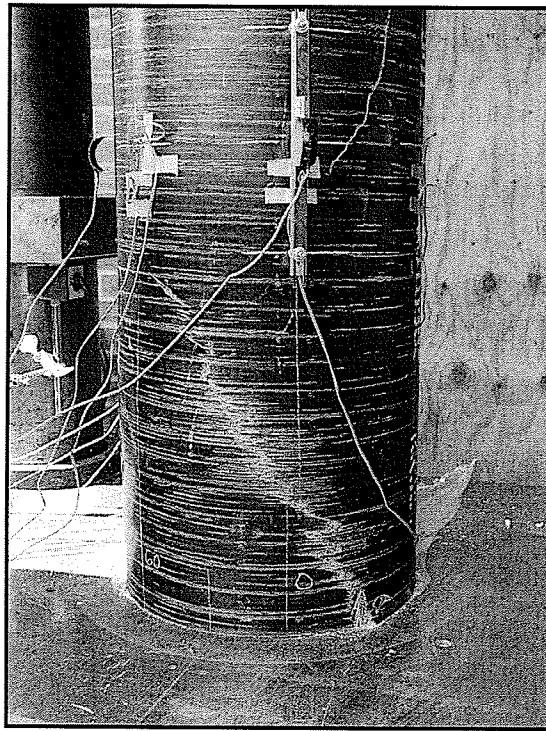


**Figure 4.65:** Circumferential-axial strain behaviour of the E-glass/epoxy shell pure axial load specimen.

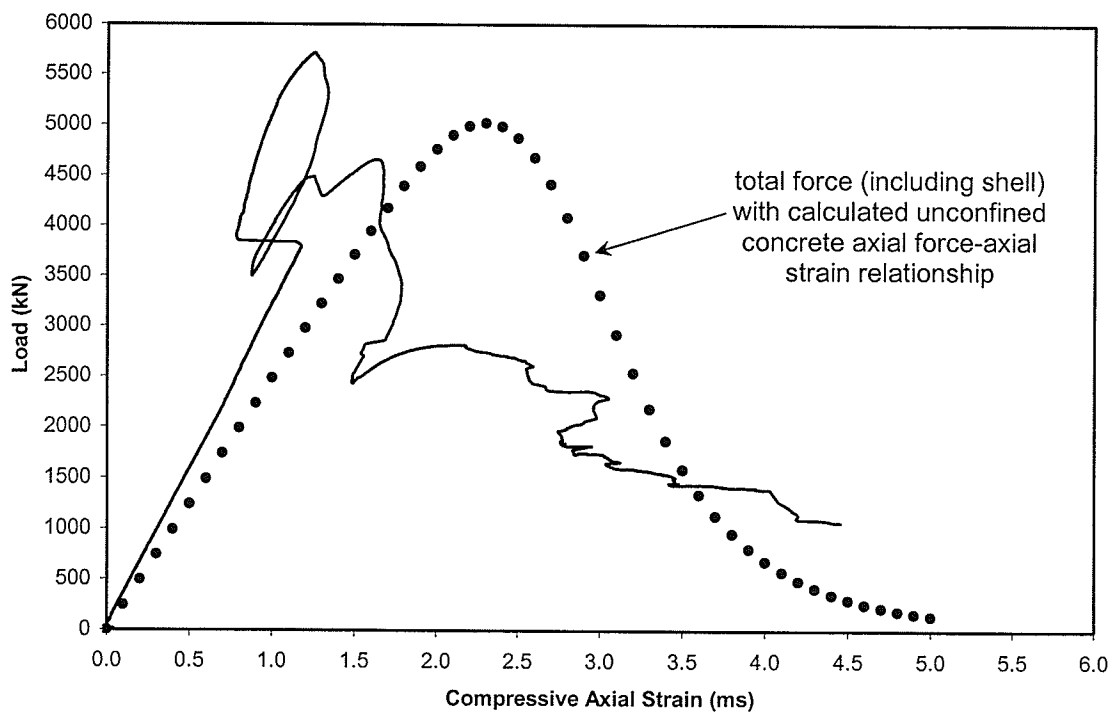


**Figure 4.66:** Crushing of FRP shell near the top of the E-glass/epoxy shell pure axial load specimen.



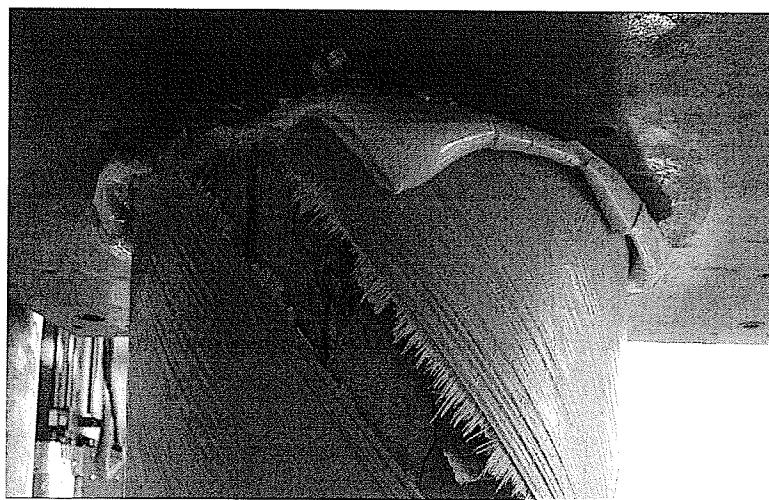


**Figure 4.67:** Failure of the FRP shell near the bottom of the E-glass/epoxy shell pure axial load specimen.

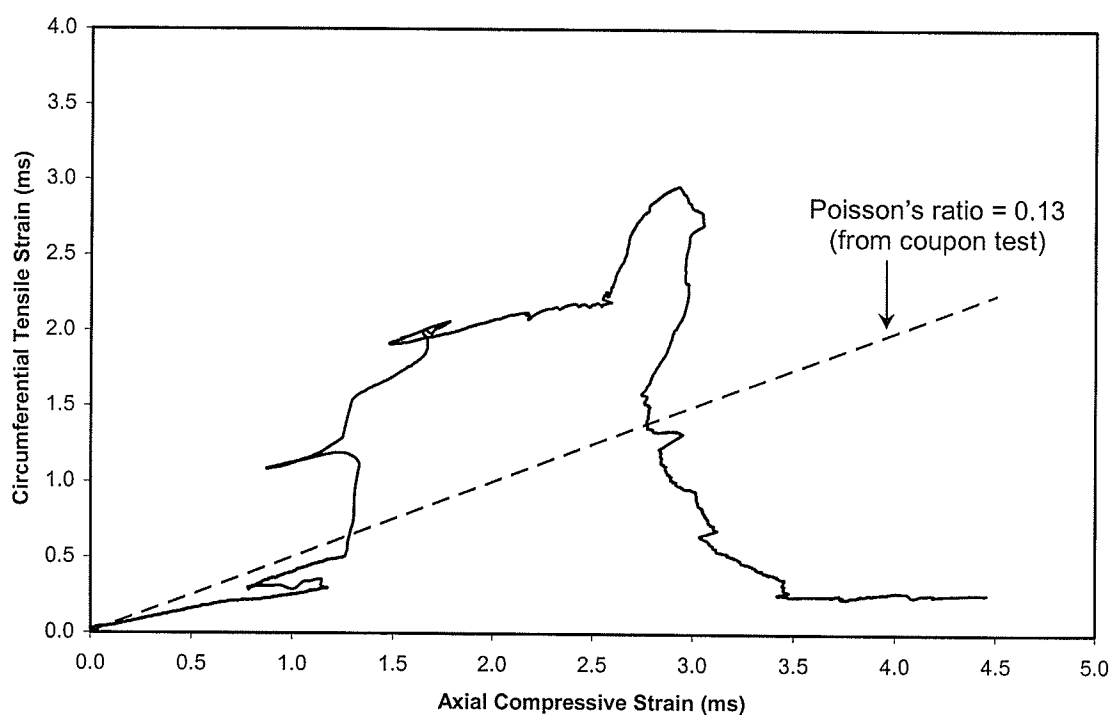


**Figure 4.68:** Load-axial strain behaviour of the E-glass/polyester shell pure axial load specimen.





**Figure 4.69:** FRP shell rupture on the E-glass/polyester shell pure axial load specimen.



**Figure 4.70:** Circumferential-axial strain behaviour of the E-glass/polyester shell pure axial load specimen.

## **Chapter V:**

# **Analytical Model and Verification With Experimental Results**

## **5.1 Introduction**

Structural engineers typically require verification of the behaviour and strength of newly developed technologies before they will specify them for use in their structural designs. Laboratory experimental testing is one tool that can be used to study the behaviour of structural members. Although laboratory testing of scaled or full-scale members is effective in determining how a member will react to applied loads in the field, time required and cost of the testing program can become prohibitive when a complex system is being studied and a number of variables could be changed.

In the case of concrete filled FRP tube members, some of the variables that can be changed include concrete strength, FRP laminate composition, FRP laminate stacking sequence, FRP laminate thickness, diameter of the member, length of the member, combination of axial load and bending moment applied to the

member, and nature of load application. A time consuming and costly experimental program would have to be performed to optimize all variables for a particular application, possibly causing an engineer to decide to use a more traditional structural system for the application in lieu of using the new technology.

Analytical modelling is another effective tool used to study the behaviour of structural members. A verifiable analytical model can be used to study the effect of changing multiple variables in the system in a time and cost efficient manner. Analytical modeling is particularly useful in optimizing a system to perform its function in the simplest and safest way, while reducing material and construction costs.

An analytical model was developed to describe the behaviour of concrete filled FRP tube members subjected to axial load, bending moment, and combined axial loads and bending moments. The model consists of individual models used to determine laminate effective elastic properties, variable concrete confinement, cross-section equilibrium, deflection, and ultimate failure. A Microsoft Visual Basic for Applications version 6.0 software program, providing a simple user interface, was created to automate the extensive calculations required to apply the model. The proposed analytical model was verified using experimental results.

## 5.2 Analytical Model

### 5.2.1 Overview

The proposed analytical model consists of several individual parts used to model FRP laminate effective elastic properties, laminate strengths, and concrete stress-strain relationships. The model is applied using a step-by-step analysis approach involving numerical integration to evaluate cross-section equilibrium and deflection. The following sections describe each component of the proposed analytical model in detail, concluding with step-by-step procedures to apply the model for three unique load cases, axial load only, bending moment only, and combined axial load and bending moment.

### 5.2.2 Modelling FRP Laminate and Concrete Material Properties

#### 5.2.2.1 Laminate Stiffness Model

The shells of concrete filled FRP tube members consist of several FRP laminas of various thicknesses stacked together to form a laminate. Each lamina is a continuous fibre composite, made up of long, continuous, parallel fibres embedded in a polymer matrix. The laminate is called a multidirectional laminate because the individual laminas are stacked such that the fibre direction in one lamina is not necessarily parallel to the fibre direction in other laminas.

The elastic properties of each lamina are typically known or can be calculated using elastic properties of the matrix and fibres and the fibre-to-matrix volume ratio. The laminated plate theory (LPT) is used to calculate the effective elastic

properties of the complete laminate. LPT accounts for individual lamina elastic properties, locations of each lamina in the laminate relative to other laminas, and orientation of the fibres in each lamina with respect to the other laminas in the laminate.

Two sets of coordinate axes are used in LPT. Figure 2.4 shows the orientation of the principal material coordinate axes used when referring to individual laminas. The 1-axis is oriented parallel to the direction of the fibres in a lamina. The 2-axis lies in the plane of a lamina, perpendicular to the 1-axis, transverse to the direction of the fibres. The 3-axis is perpendicular to the plane of a lamina, therefore perpendicular to the plane formed by the 1- and 2-axes. Nonparallel laminas in a laminate each have unique sets of 1- and 2-axes, but share a common 3-axis. Figure 2.5 shows the orientation of laminate global coordinate axes used to describe the direction of applied loads and resultant strains on the entire laminate. The z-axis is perpendicular to the plane of the laminate, parallel to lamina 3-axes in the principle material coordinate system. X and y-axes lie in the plane of the laminate and are not necessarily parallel to lamina 1- and 2-axes in the principle material coordinate system.

Fibre directions in individual laminas are designated by the angle  $\theta$  between the positive x-axis in the laminate global coordinate system and positive 1-axis in the lamina principal material coordinate system, as shown in Figure 2.5. As shown in Figure 5.1, the laminate global x-direction will refer to the direction parallel to a

member's longitudinal axis, the laminate global y-direction will refer to the hoop direction circumferential to a member, and the laminate global z-axis will refer to the direction radial from the centre of a member's cross-section in further discussion on the analytical model.

Several assumptions are made in order to apply LPT, including:

1. Each lamina is homogenous and orthotropic on a macroscopic scale.
2. The laminate is very thin relative to its width.
3. The laminate behaves linearly elastic.
4. Displacements are continuous throughout the laminate.
5. The strain distribution through the laminate thickness is linear.

Application of LPT begins by establishing elastic properties of each lamina in a laminate. If unknown, a lamina's elastic properties are calculated from matrix and fibre elastic properties as follows:

$$E_1 = E_f \nu_f + E_m \nu_m \quad [\text{Eq. 5.1}]$$

$$E_2 = \frac{E_f E_m}{E_f - \sqrt{\nu_f} (E_f - E_m)} \quad [\text{Eq. 5.2}]$$

$$\nu_{12} = \nu_f \nu_f + \nu_m \nu_m \quad [\text{Eq. 5.3}]$$

$$\nu_{21} = \frac{E_2}{E_1} \nu_{12} \quad [\text{Eq. 5.4}]$$

$$G_{12} = \frac{G_f G_m}{G_f - \sqrt{\nu_f} (G_f - G_m)} \quad [\text{Eq. 5.5}]$$

where  $E_1, E_2, E_f, E_m$  = elastic modulus of the lamina in the fibre direction, elastic modulus of the lamina in the direction transverse to the fibres, elastic modulus of the fibres, and elastic modulus of the matrix

$\nu_{12}, \nu_{21}, \nu_f, \nu_m$  = major Poisson's ratio, minor Poisson's ratio, Poisson's ratio of the fibres, and Poisson's ratio of the matrix

$\nu_f, \nu_m$  = ratio of fibre volume to total volume (matrix and fibres), and ratio of matrix volume to total volume (matrix and fibres)

$G_{12}, G_f, G_m$  = lamina longitudinal shear modulus, shear modulus of the fibres, and shear modulus of the matrix

In-plane strains are related to in-plane stresses in a single lamina by the following relationship, derived from mechanics of elastic materials:

$$\begin{bmatrix} \varepsilon_1 \\ \varepsilon_2 \\ \gamma_6 \end{bmatrix} = \begin{bmatrix} S_{11} & S_{12} & 0 \\ S_{21} & S_{22} & 0 \\ 0 & 0 & S_{66} \end{bmatrix} \begin{bmatrix} \sigma_1 \\ \sigma_2 \\ \tau_6 \end{bmatrix} \quad [\text{Eq. 5.6}]$$

where  $\varepsilon_1, \varepsilon_2, \gamma_6$  = strain in the fibre direction, strain in the direction transverse to the fibres, and in-plane shear strain

$\sigma_1, \sigma_2, \tau_6$  = stress in the fibre direction, stress in the direction transverse to the fibres, and in-plane shear stress

$[S]$  = lamina compliance matrix

$$S_{11} = \frac{1}{E_1} \quad [\text{Eq. 5.7}]$$

$$S_{22} = \frac{1}{E_2} \quad [\text{Eq. 5.8}]$$

$$S_{12} = -\frac{\nu_{12}}{E_1} \quad [\text{Eq. 5.9a}]$$

$$= -\frac{\nu_{21}}{E_2} \quad [\text{Eq. 5.9b}]$$

$$S_{66} = G_{12} \quad [\text{Eq. 5.10}]$$

Solving equation 5.6 for lamina stresses:

$$\begin{bmatrix} \sigma_1 \\ \sigma_2 \\ \tau_6 \end{bmatrix} = \begin{bmatrix} Q_{11} & Q_{12} & 0 \\ Q_{21} & Q_{22} & 0 \\ 0 & 0 & Q_{66} \end{bmatrix} \begin{bmatrix} \varepsilon_1 \\ \varepsilon_2 \\ \gamma_6 \end{bmatrix} \quad [\text{Eq. 5.11}]$$

where  $[Q] = \text{intermediate lamina stiffness matrix}$   
 $= [S]^{-1} \quad [\text{Eq. 5.12}]$

$$Q_{11} = \frac{E_1}{1 - \nu_{12}\nu_{21}} \quad [\text{Eq. 5.13}]$$

$$Q_{22} = \frac{E_2}{1 - \nu_{12}\nu_{21}} \quad [\text{Eq. 5.14}]$$

$$Q_{12} = Q_{21} \quad [\text{Eq. 5.15a}]$$

$$= \frac{\nu_{21}E_1}{1 - \nu_{12}\nu_{21}} \quad [\text{Eq. 5.15b}]$$

$$= \frac{\nu_{12}E_2}{1 - \nu_{12}\nu_{21}} \quad [\text{Eq. 5.15c}]$$

$$Q_{66} = G_{12} \quad [\text{Eq. 5.16}]$$



The intermediate lamina stiffness matrix is symmetric. Equation 5.11 describes lamina behaviour when stresses are applied in lamina principal material coordinate directions. A transformed lamina stiffness matrix is established to describe lamina behaviour when stresses are applied in laminate global coordinate directions, which may lie at an angle to a lamina's principal material coordinate directions. The stress-strain relationship in the laminate global coordinate system for a generally oriented lamina is expressed:

$$\begin{bmatrix} \sigma_x \\ \sigma_y \\ \tau_s \end{bmatrix} = \begin{bmatrix} Q_{xx} & Q_{xy} & Q_{xs} \\ Q_{yx} & Q_{yy} & Q_{ys} \\ Q_{sx} & Q_{sy} & Q_{ss} \end{bmatrix} \begin{bmatrix} \varepsilon_x \\ \varepsilon_y \\ \gamma_s \end{bmatrix} \quad [\text{Eq. 5.17}]$$

where  $\sigma_x, \sigma_y, \tau_s$  = stress in the laminate global x-direction, stress in the laminate global y-direction, and laminate global x-y plane shear stress

$\varepsilon_x, \varepsilon_y, \gamma_s$  = strain in the laminate global x-direction, strain in the laminate global y-direction, and laminate global x-y plane shear strain

$$Q_{xx} = m^4 Q_{11} + n^4 Q_{22} + 2m^2 n^2 Q_{12} + 4m^2 n^2 Q_{66} \quad [\text{Eq. 5.18}]$$

$$Q_{yy} = n^4 Q_{11} + m^4 Q_{22} + 2m^2 n^2 Q_{12} + 4m^2 n^2 Q_{66} \quad [\text{Eq. 5.19}]$$

$$Q_{xy} = m^2 n^2 Q_{11} + m^2 n^2 Q_{22} + (m^4 + n^4) Q_{12} - 4m^2 n^2 Q_{66} \quad [\text{Eq. 5.20}]$$

$$Q_{xs} = m^3 n Q_{11} - mn^3 Q_{22} + (mn^3 - m^3 n) Q_{12} + 2(mn^3 - m^3 n) Q_{66} \quad [\text{Eq. 5.21}]$$

$$Q_{ys} = mn^3 Q_{11} - m^3 n Q_{22} + (m^3 n - mn^3) Q_{12} + 2(m^3 n - mn^3) Q_{66} \quad [\text{Eq. 5.22}]$$

$$Q_{ss} = m^2 n^2 Q_{11} + m^2 n^2 Q_{22} - 2m^2 n^2 Q_{12} + (m^2 - n^2)^2 Q_{66} \quad [\text{Eq. 5.23}]$$

where  $m = \cos \theta$  [Eq. 5.24]

$$n = \sin \theta \quad [\text{Eq. 5.25}]$$

Similar to the intermediate lamina stiffness matrix, the transformed lamina stiffness matrix is symmetric, therefore  $Q_{yx} = Q_{xy}$ ,  $Q_{sx} = Q_{xs}$ , and  $Q_{sy} = Q_{ys}$ . The transformed lamina stiffness matrix reduces to the intermediate lamina stiffness matrix when the lamina principal material coordinate system 1-axis is parallel to the laminate global coordinate system x-axis. A transformed lamina stiffness matrix is calculated for each lamina  $k$  in the laminate.

Stacking all lamina in the laminate together and integrating applied stresses over the laminate thickness, the following relationship is established:

$$\begin{bmatrix} N_x \\ N_y \\ N_s \\ M_x \\ M_y \\ M_s \end{bmatrix} = \begin{bmatrix} A_{xx} & A_{xy} & A_{xs} & B_{xx} & B_{xy} & B_{xs} \\ A_{yx} & A_{yy} & A_{ys} & B_{yx} & B_{yy} & B_{ys} \\ A_{sx} & A_{sy} & A_{ss} & B_{sx} & B_{sy} & B_{ss} \\ B_{xx} & B_{xy} & B_{xs} & D_{xx} & D_{xy} & D_{xs} \\ B_{yx} & B_{yy} & B_{ys} & D_{yx} & D_{yy} & D_{ys} \\ B_{sx} & B_{sy} & B_{ss} & D_{sx} & D_{sy} & D_{ss} \end{bmatrix} \begin{bmatrix} \epsilon_x^0 \\ \epsilon_y^0 \\ \gamma_s^0 \\ \kappa_x \\ \kappa_y \\ \kappa_s \end{bmatrix} \quad [\text{Eq. 5.26a}]$$

$$= \begin{bmatrix} [A] & [B] \\ [B] & [D] \end{bmatrix} \begin{bmatrix} \epsilon_x^0 \\ \epsilon_y^0 \\ \gamma_s^0 \\ \kappa_x \\ \kappa_y \\ \kappa_s \end{bmatrix} \quad [\text{Eq. 5.26b}]$$

where  $N_x, N_y, N_s$  = resultant force in the laminate global x-direction,  
resultant force in the laminate global y-direction, and  
resultant shear force in the laminate global x-y plane,  
per unit width

$M_x, M_y, M_s$  = resultant moment in the laminate global y-z plane,  
resultant moment in the laminate global x-y plane, and  
resultant twisting moment, per unit width

$\varepsilon_x^0, \varepsilon_y^0, \gamma_s^0$  = strain components on a reference plane equidistant  
from the top and bottom of the laminate, in the  
laminate global coordinate system

$\kappa_x, \kappa_y, \kappa_s$  = laminate curvatures due to applied moments  
 $M_x, M_y, M_s$

$[A]$  = extensional stiffness matrix, relating in-plane loads to  
in-plane strains

$[B]$  = coupling stiffness matrix, relating in-plane loads to  
curvatures and moments to in-plane strains

$[D]$  = flexural stiffness matrix, relating moments and  
curvatures

$$A_{ij} = \sum_{k=1}^n Q_{ij}^k (h_k - h_{k-1}) \quad [\text{Eq. 5.27}]$$

$$B_{ij} = \frac{1}{2} \sum_{k=1}^n Q_{ij}^k (h_k^2 - h_{k-1}^2) \quad [\text{Eq. 5.28}]$$

$$D_{ij} = \frac{1}{3} \sum_{k=1}^n Q_{ij}^k (h_k^3 - h_{k-1}^3) \quad [\text{Eq. 5.29}]$$

$Q_{ij}^k$  = element of the transformed lamina stiffness matrix in  
equation 5.17 for lamina  $k$

$n$  = total number of laminas in the laminate

$h_k$  = distance from a mid-height reference plane to the top  
of lamina  $k$  (see Figure 5.2)

$h_{k-1}$  = distance from the mid-height reference plane to the  
bottom of lamina  $k$  (see Figure 5.2)

The extensional, coupling, and flexural stiffness matrices are symmetric, together forming an unsymmetric laminate stiffness matrix. Equation 5.26b is used to calculate laminate effective elastic properties. The solution for a laminate effective longitudinal elastic modulus  $E_{x,eff}$  will be used to illustrate the procedure. A unit load is applied to the laminate in the x-direction in the laminate global coordinate system, while all other loads are set equal to zero. The load is applied in the form of a stress  $\sigma_x$  per unit width, multiplied by the overall thickness  $h$  of the laminate. Equation 5.26b is solved for the strains and curvatures term and the applied unit load is substituted to give:

$$\begin{bmatrix} \varepsilon_x \\ \varepsilon_y \\ \gamma_s \\ \kappa_x \\ \kappa_y \\ \kappa_s \end{bmatrix} = \begin{bmatrix} [A] & [B] \\ [B] & [D] \end{bmatrix}^{-1} \begin{bmatrix} \sigma_x h \\ 0 \\ 0 \\ 0 \\ 0 \\ 0 \end{bmatrix} \quad [\text{Eq. 5.30}]$$

Simplifying equation 5.30 yields:

$$\varepsilon_x = (A_{11})^{-1} \sigma_x h \quad [\text{Eq. 5.31}]$$

It is known from mechanics of elastic materials that the strain and stress in an elastic material are related in the following way:

$$\sigma_x = E_x \varepsilon_x \quad [\text{Eq. 5.32}]$$

The laminate effective elastic modulus in the x-direction is determined by substituting equation 5.32 into equation 5.31 and isolating the elastic modulus term:

$$E_{x,eff} = \frac{1}{(A_{11})^{-1} h} \quad [\text{Eq. 5.33}]$$

Similar procedures are applied to yield the remainder of the laminate effective elastic properties shown below:

$$E_{y,eff} = \frac{1}{(A_{22})^{-1} h} \quad [\text{Eq. 5.34}]$$

$$G_{xy,eff} = \frac{1}{(A_{33})^{-1} h} \quad [\text{Eq. 5.35}]$$

$$\nu_{xy,eff} = -\frac{(A_{21})^{-1}}{(A_{11})^{-1}} \quad [\text{Eq. 5.36}]$$

$$\nu_{yx,eff} = -\frac{(A_{12})^{-1}}{(A_{22})^{-1}} \quad [\text{Eq. 5.37}]$$

The proposed concrete filled FRP tube member analytical model utilizes the preceding procedure to calculate laminate effective elastic properties for specific laminate compositions and configurations.

### 5.2.2.2 Modelling Lamina and Overall Laminate Strengths

The proposed analytical model requires a method to detect individual lamina failures when a laminate is subjected to varying states of stress. The Interactive Tensor Polynomial (Tsai-Wu) Theory developed by Tsai and Wu is used to model progressive laminate failure, lamina by lamina, when a laminate is subjected to uniaxial or biaxial states of stress. The laminate stiffness model described in section 5.2.2.1 is applied to calculate revised laminate effective elastic properties as each lamina fails.

The Tsai-Wu theory is applied by subjecting a laminate to a set of forces and moments in the laminate global coordinate system and determining whether or not a lamina in the laminate fails due to the combined effect of the applied loads. First, equation 5.26a is solved for the strains and curvatures term by multiplying both sides of the equation by the inverse of the laminate stiffness matrix:

$$\begin{bmatrix} \varepsilon_x^0 \\ \varepsilon_y^0 \\ \gamma_s^0 \\ \kappa_x \\ \kappa_y \\ \kappa_s \end{bmatrix} = \begin{bmatrix} [A] & [B] \\ [B] & [D] \end{bmatrix}^{-1} \begin{bmatrix} N_x \\ N_y \\ N_s \\ M_x \\ M_y \\ M_s \end{bmatrix} \quad [\text{Eq. 5.38}]$$

Applied forces and moments are input to calculate resultant reference plane strains and laminate curvatures. The calculated reference plane strains and

laminate curvatures are converted to strains in the global coordinate system for lamina  $k$  in the laminate using:

$$\begin{bmatrix} \varepsilon_x \\ \varepsilon_y \\ \gamma_s \end{bmatrix}_k = \begin{bmatrix} \varepsilon_x^0 \\ \varepsilon_y^0 \\ \gamma_s^0 \end{bmatrix} + z_k \begin{bmatrix} \kappa_x \\ \kappa_y \\ \kappa_s \end{bmatrix} \quad [\text{Eq. 5.39}]$$

where  $z_k$  = distance from a mid-height reference plane to the middle of lamina  $k$

The calculated strains in the global coordinate system for lamina  $k$  are transformed to strains in the lamina principal material coordinate system based on the angle  $\theta_k$  between the lamina principal material 1-axis and the laminate global x-axis, as follows:

$$\begin{bmatrix} \varepsilon_1 \\ \varepsilon_2 \\ \frac{1}{2}\gamma_6 \end{bmatrix} = [T]_k \begin{bmatrix} \varepsilon_x \\ \varepsilon_y \\ \frac{1}{2}\gamma_s \end{bmatrix}_k \quad [\text{Eq. 5.40}]$$

where  $[T]_k$  = lamina transformation matrix

$$= \begin{bmatrix} m^2 & n^2 & 2mn \\ n^2 & m^2 & -2mn \\ -mn & mn & m^2 - n^2 \end{bmatrix}_k \quad [\text{Eq. 5.41}]$$

Stresses in lamina  $k$  corresponding to the strains from equation 5.40 are calculated with equation 5.11. The Tsai-Wu failure criterion is then applied to lamina  $k$ . The Tsai-Wu failure criterion is expressed in the following form:

$$1 = f_1 S_{fk} (\sigma_1)_k + f_2 S_{fk} (\sigma_2)_k + f_{11} S_{fk}^2 (\sigma_1)_k^2 + f_{22} S_{fk}^2 (\sigma_2)_k^2 + f_{66} S_{fk}^2 (\tau_6)_k^2 + 2 f_{12} S_{fk}^2 (\sigma_1)_k (\sigma_2)_k \quad [\text{Eq. 5.42}]$$

where  $S_{fk}$  = safety factor for layer  $k$  subjected to applied stresses

$$f_1 = \frac{1}{F_{1t}} - \frac{1}{F_{1c}} \quad [\text{Eq. 5.43}]$$

$$f_{11} = \frac{1}{F_{1t} F_{1c}} \quad [\text{Eq. 5.44}]$$

$$f_2 = \frac{1}{F_{2t}} - \frac{1}{F_{2c}} \quad [\text{Eq. 5.45}]$$

$$f_{22} = \frac{1}{F_{2t} F_{2c}} \quad [\text{Eq. 5.46}]$$

$$f_{66} = \frac{1}{F_6^2} \quad [\text{Eq. 5.47}]$$

$$f_{12} \cong -\frac{1}{2} (f_{11} f_{22})^{1/2} \quad [\text{Eq. 5.48}]$$

$F_{1t}$  = lamina tensile strength in the fibre direction

$F_{1c}$  = lamina compressive strength in the fibre direction

$F_{2t}$  = lamina tensile strength perpendicular to the fibres

$F_{2c}$  = lamina compressive strength perpendicular to the fibres



$$F_6 = \text{lamina in-plane shear strength}$$

As expressed in equations 5.43 to equation 5.48, the  $f$  terms in equation 5.42 are coefficients related to lamina strength properties. Lamina strength properties  $F$  are usually known for a given lamina composition. Equation 5.42 is expressed in simplified terms as:

$$0 = aS_{fk}^2 + bS_{fk} - 1 \quad [\text{Eq. 5.49}]$$

$$\text{where} \quad a = f_{11}(\sigma_1)_k^2 + f_{22}(\sigma_2)_k^2 + f_{66}(\tau_6)_k^2 + 2f_{12}(\sigma_1)_k(\sigma_2)_k \quad [\text{Eq. 5.50}]$$

$$b = f_1(\sigma_1)_k + f_2(\sigma_2)_k \quad [\text{Eq. 5.51}]$$

Quadratic equation 5.49 is solved for safety factor  $S_{fk}$ , yielding the following positive solution:

$$S_{fk} = \frac{-b + \sqrt{b^2 + 4a}}{2a} \quad [\text{Eq. 5.52}]$$

Equation 5.52 provides the factor of safety against failure for lamina  $k$  when the laminate is subjected to a general state of stress caused by applied loads and moments in the laminate global coordinate directions. A lamina is capable of resisting a given state of stress if the calculated safety factor is greater than or equal to 1. The lamina fails when the safety factor falls below 1.

Laminate failure analysis for two specific states of stress is required when modelling concrete filled FRP tube members. The states of stress of interest are described in the following two sections.

#### *5.2.2.2.1 Modelling Lamina and Overall Laminate Uniaxial Tensile Strengths*

It is assumed that the FRP shell of a concrete filled FRP tube member is subjected to uniaxial tensile stress in the global x-direction in the tension zone when pure bending moment or combined bending moment and axial load are applied to the member, as shown in Figure 5.3 for a pure bending moment.

A stress-strain relationship to failure for uniaxial tensile stress on a lamina in the global x-direction is established using the following procedure:

1. Set the applied axial load in the global x-direction,  $N_x$ , in equation 5.38 equal to an arbitrary positive value. Set all other load and moment terms equal to zero.
2. Calculate safety factors  $S_{fk}$  for each lamina in the laminate using equation 5.52.
3. Vary  $N_x$  until the minimum calculated lamina safety factor in step 2 is 1.

A lamina safety factor of 1 indicates that the applied stress, equivalent to applied load  $N_x$  divided by laminate thickness  $h$ , has reached the failure strength of the lamina.

4. Calculate the strain in the global x-direction corresponding to the calculated lamina failure load with equation 5.38, using the current inverted laminate stiffness matrix.
5. Calculate a revised inverted laminate stiffness matrix and revised laminate effective elastic properties using the procedure described in section 5.2.2.1, discounting the failed lamina's stiffness but maintaining the original relative positions of other laminas and original overall laminate thickness.
6. Recalculate safety factors for remaining intact laminas using equation 5.38, without changing  $N_x$ . If failure of a lamina causes other lamina safety factors to fall below 1, the other laminas also fail at the current load and corresponding strain.
7. Once the minimum safety factor for remaining intact laminas calculated in step 6 is greater than 1, increase  $N_x$  to detect the next lamina failure.
8. Repeat step 4 to step 7 until all lamina have failed. Failure of the last lamina signifies ultimate laminate failure.

A similar procedure can be applied to establish laminate stress-strain relationships for uniaxial compression in the global x-direction, tension in the global y-direction, and compression in the global y-direction.

In general, the procedure described above yields multilinear stress-strain relationships like the one shown in Figure 5.4 for a hypothetical laminate with two

laminas. Assuming the stress-strain relationship shown is for uniaxial tensile stress in the global x-direction, the slope of the initial linear segment is the laminate effective elastic modulus in the global x-direction prior to first lamina failure. Point A represents failure of the first lamina. When load is applied under strain control, a vertical shift occurs from first lamina failure stress  $\sigma_A$  at point A to stress  $\sigma_B$  at point B as shown in Figure 5.4(a), where  $\sigma_B$  is the laminate stress at first lamina failure strain  $\varepsilon_A$  when the laminate effective elastic modulus is revised to account for failure of the first lamina. When load is applied under load control, a horizontal shift in the curve occurs from first lamina failure strain  $\varepsilon_A$  at point A to strain  $\varepsilon_B$  at point B as shown in Figure 5.4(b), where  $\varepsilon_B$  is the laminate strain at first lamina failure stress  $\sigma_A$  when the laminate effective elastic modulus is revised to account for failure of the first lamina. Ultimate laminate failure occurs at point C, at ultimate laminate failure stress  $\sigma_{ult}$  and strain  $\varepsilon_{ult}$ . It is important to note that each segment of the multilinear stress-strain relationship is associated with a unique set of all the laminate effective elastic properties calculated using equations 5.33 to 5.37 because all the laminate effective elastic properties change when individual laminas fail.

#### 5.2.2.2.2 Modelling Lamina and Overall Laminate Biaxial Strengths

It is assumed that the FRP shell of a concrete filled FRP tube member is subjected to a biaxial state of stress in the compression zone when combined bending moment and pure axial load or pure axial load only are applied to the member. Compressive stress in the global x-direction is caused by resultant axial

force in the FRP shell due to the applied loads. Tensile stress in the global y-direction is the hoop stress resultant of radial concrete confining pressure at the interface between the concrete core and FRP shell. Confining pressure develops when the concrete core expands due to resultant axial stress in the core from the applied loads. The biaxial state of stress in the compression zone is illustrated in Figure 5.5, for a pure axial load case. The confinement effect is discussed in more detail in section 5.2.2.3.2.

Biaxial laminate strength is described with a failure envelope or interaction curve between compressive and tensile stress in the x-direction and compressive and tensile stress in the y-direction. Each point on the curve represents a unique combination of x and y-direction stresses at failure. The biaxial strength envelopes in the quadrant corresponding to compressive stress in the global x-direction and tensile stress in the global y-direction are required for the analytical model. Failure envelopes are established point-by-point using the procedure described in section 5.2.2.2.1 with a revised step 1. Load in the global x-direction,  $N_x$ , is set equal to a negative compression value and load in the global y-direction,  $N_y$ , is set equal to an arbitrary positive tension value. The remainder of the procedure in section 5.2.2.2.1 is applied, keeping  $N_x$  constant and varying  $N_y$  to identify lamina and overall laminate failures in step 3. The procedure is repeated for a full range of  $N_x$  values between zero and ultimate uniaxial compression strength in the global x-direction, providing a family of lamina and overall laminate failure envelopes.

Typical lamina and overall laminate biaxial strength envelopes are shown in Figure 5.6. Biaxial stresses are applied and increased until the biaxial stress path intersects a lamina or overall laminate failure envelope. Revised laminate effective elastic properties are calculated when the biaxial stress path intersects a lamina failure envelope. Magnitudes of the biaxial stresses at lamina and overall laminate failure vary depending on the biaxial stress path. The shape of individual lamina failure envelopes is generally elliptical, while the shape of overall laminate failure envelopes can be highly variable and discontinuous depending on the laminate structure. Section 5.2.3.5 describes a procedure to determine the biaxial stress path for an FRP shell in the compression zone when analyzing a concrete filled FRP tube member subjected to pure axial load, pure bending moment, or a combination of axial load and bending moment. It will be shown that the shape of the biaxial stress path depends on the level of concrete confinement in the compression zone.

### 5.2.2.3 Modelling Concrete Stress-strain Response

#### *5.2.2.3.1 Unconfined Concrete Stress-strain Model*

Application of the proposed analytical model requires a suitable unconfined concrete stress-strain relationship for a given peak unconfined concrete stress  $f'_c$ . The relationship developed by Thornfeldt, Tomaszewicz, and Jensen for axially loaded concrete is used. The unconfined concrete stress  $f_c$  for normal

weight concrete at a given axial strain  $\varepsilon_c$  is related to the peak unconfined concrete stress  $f'_c$  by the following:

$$\frac{f_c}{f'_c} = \frac{n \left( \varepsilon_c / \varepsilon'_c \right)}{n - 1 + \left( \varepsilon_c / \varepsilon'_c \right)^{nk}} \quad [\text{Eq. 5.53}]$$

where  $n$  = *curve-fitting factor*

$$= \frac{E_c}{E_c - E'_c} \quad [\text{Eq. 5.54a}]$$

$$\cong 0.8 + \frac{f'_c}{17} \quad [\text{Eq. 5.54b}]$$

$E_c$  = *tangent elastic modulus*

$$= 3320\sqrt{f'_c} + 6900 \quad (f'_c \text{ in MPa}) \quad [\text{Eq. 5.55}]$$

$E'_c$  = *secant elastic modulus*

$$= \frac{f'_c}{\varepsilon'_c} \quad [\text{Eq. 5.56}]$$

$\varepsilon'_c$  = *strain at peak concrete stress  $f'_c$*

$$= \frac{f'_c}{E_c} \frac{n}{n - 1} \quad [\text{Eq. 5.57}]$$

$k$  = *post-peak decay factor*

$$= 1 \text{ for } f_c \leq f'_c \text{ and } f_c \leq 20.46 \text{ MPa} \quad [\text{Eq. 5.58a}]$$

$$= 0.67 + \frac{f'_c}{62} \quad (f'_c \text{ in MPa}) \quad [\text{Eq. 5.58b}]$$

Figure 5.7 shows typical unconfined concrete stress-strain curves established using Thornfeldt, Tomaszewicz, and Jensen's model, for peak unconfined concrete stresses between 20 and 100-MPa.

#### *5.2.2.3.2 Maximum Confinement Concrete Stress-strain Model*

In general, concrete initially experiences negative volumetric strain as it consolidates when loaded in compression, up to a compressive stress approximately half its compressive strength. At this point micro cracking in the concrete begins to cause non-linear lateral strain, at an increasing rate with increased compressive stress. The overall volumetric strain remains negative until the compressive stress reaches approximately 87-percent of the compressive strength. Above this compressive stress, the volumetric strain increases until failure due to propagation of micro cracks and formation of a dominant fracture surface.

Lateral expansion of concrete subjected to compressive stress can be partially restrained by encasing the concrete in a shell made of steel or FRP, confining the concrete. Concrete confinement delays the onset of formation of a failure surface, increasing the concrete's strength and ductility. Variable confinement occurs when concrete is encased in an elastic material. Lateral strain in the concrete subjected to compressive stress causes radial stresses at the interface between the concrete and its encasing material. The radial stress can be resolved into a hoop stress in the encasing material tangent to the surface of the



concrete, as shown in Figure 5.5. The magnitude of the confining radial stress applied to the concrete by the encasing material depends on the material's stiffness tangent to the concrete surface. When the encasing material is elastic in the tangent direction, the level of confining radial stress continuously increases with increasing compressive stress applied to the concrete, a phenomenon referred to as variable confinement.

The concrete core in axially loaded concrete filled FRP tube members experiences variable confinement caused by the FRP shell. A description of the variable confinement model by Fam and Rizkalla used in the proposed analytical model follows. Fam and Rizkalla's model was chosen because it has been shown that it accurately models concrete confinement with FRP (Fam and Rizkalla, 2001). The variable confinement model is based on a constant confinement model developed by Mander. Mander used the concrete stress-strain model originally developed by Popovics for unconfined concrete, described below:

$$f_{cc} = \frac{f'_{cc} x r}{r - 1 + x^r} \quad [\text{Eq. 5.59}]$$

$$x = \frac{\varepsilon_{cc}}{\varepsilon'_{cc}} \quad [\text{Eq. 5.60}]$$

$$r = \frac{E_{c0}}{E_{c0} - E_{\text{sec}}} \quad [\text{Eq. 5.61}]$$

where  $f_{cc}$  = *confined concrete stress*

$$f'_{cc} = \text{confined peak concrete stress}$$

$$\varepsilon_{cc} = \text{concrete strain}$$

$$\varepsilon'_{cc} = \text{concrete strain at confined peak concrete stress}$$

$$E_{c0} = \text{tangent elastic modulus}$$

$$= 5000\sqrt{f'_c} \quad [\text{Eq. 5.62}]$$

$$f'_c = \text{unconfined peak concrete stress}$$

$$E_{\text{sec}} = \text{secant elastic modulus}$$

$$= \frac{f'_{cc}}{\varepsilon'_{cc}} \quad [\text{Eq. 5.63}]$$

Mander modified Popovics expression in equation 5.59 by incorporating confinement as follows:

$$f'_{cc} = f'_c \left( 2.254 \sqrt{1 + 7.94 \frac{\sigma_R}{f'_c}} - 2 \frac{\sigma_R}{f'_c} - 1.254 \right) \quad [\text{Eq. 5.64}]$$

$$\varepsilon'_{cc} = \varepsilon'_c \left[ 1 + 5 \left( \frac{f'_{cc}}{f'_c} - 1 \right) \right] \quad [\text{Eq. 5.65}]$$

where  $\varepsilon'_c = \text{concrete strain at unconfined peak concrete stress}$

$$\sigma_R = \text{constant lateral confining pressure}$$

$f'_{cc}/f'_c$  and  $\sigma_R/f'_c$  are defined the confinement effectiveness and confinement ratio, respectively. Mander developed the model for steel confined concrete

where the confining pressure  $\sigma_R$  is constant after yielding of the steel. Fam and Rizkalla modified the expression in equation 5.64 to account for variable lateral confining pressure  $\sigma_R$ , for FRP confined concrete. They calculated  $\sigma_R$  based on radial displacement compatibility at the interface between the concrete and FRP shell. The radial displacements  $u_R$  of the components of the system are expressed:

$$\text{For the concrete core under axial pressure} \quad u_R = \nu_c R \varepsilon_{cc} \quad [\text{Eq. 5.66}]$$

$$\text{For the concrete core under radial pressure} \quad u_R = \frac{1 - \nu_c}{E_c} R \sigma_R \quad [\text{Eq. 5.67}]$$

$$\text{For the shell under internal radial pressure} \quad u_R = \frac{\sigma_R R^2}{E_{s,hoop} t} \quad [\text{Eq. 5.68}]$$

$$\text{For the shell under axial pressure} \quad u_R = \nu_s R \varepsilon_{cc} \quad [\text{Eq. 5.69}]$$

where  $\nu_c$  = concrete Poisson's ratio

$R$  = radius of concrete core and FRP shell (a thin shell with respect to the radius is assumed)

$E_c$  = concrete elastic modulus

$E_{s,hoop}$  = shell elastic modulus in the hoop direction

$t$  = shell thickness ( $t \ll R$  is assumed)

$\nu_s$  = shell Poisson's ratio

When the axial load is applied simultaneously to the concrete core and FRP shell and applying radial displacement compatibility, it can be shown that:

$$\sigma_R = \frac{(\nu_c - \nu_s)}{\frac{R}{E_s t} + \frac{1 - \nu_c}{E_c}} \varepsilon_{cc} \quad [\text{Eq. 5.70}]$$

An incremental approach is used to establish the confined concrete stress-strain curve point-by-point. The modulus of the concrete varies from one point,  $i - 1$ , to the next,  $i$ , as shown in Figure 5.8. The concrete secant modulus at the previous point is used to calculate each point:

$$(E_c)_{\text{to calculate point } i} = \left( \frac{f'_{cc}}{\varepsilon'_{cc}} \right)_{i-1} \quad [\text{Eq. 5.71}]$$

The modulus is set equal to the initial tangent modulus  $E_{c0}$  for the first point,  $i = 1$ .

The concrete Poisson's ratio also varies from point-to-point. Fam and Rizkalla have shown that the concrete Poisson's ratio at point  $i$  can be expressed:

$$(\nu_c)_i = \nu_{c0} \left[ \left( 1.914 \left( \frac{(\sigma_R)_{i-1}}{f'_c} \right) + 0.719 \right) \left( \frac{(\varepsilon_{cc})_i}{(\varepsilon'_{cc})_{i-1}} \right) + 1 \right] \quad [\text{Eq. 5.72}]$$

where  $\nu_{c0}$  = initial concrete Poisson's ratio (typically between 0.15 and 0.20)

The concrete Poisson's ratio is set equal to the initial concrete Poisson's ratio  $\nu_{c0}$  for the first point,  $i = 1$ .

Fam and Rizkalla suggest the following step-by-step procedure to establish the full variable confinement stress-strain relationship:

1. Input the axial strain  $(\varepsilon_{cc})_i$ .
2. Calculate  $(E_c)_i$  using equation 5.71;  $(E_c)_i = E_{c0}$  at  $i = 1$ .
3. Calculate  $(\nu_c)_i$  using equation 5.72;  $(\nu_c)_i = \nu_{c0}$  at  $i = 1$ .
4. Calculate  $(\sigma_R)_i$  using equation 5.70.
5. Calculate  $(f'_{cc})_i$  using equation 5.64.
6. Calculate  $(\varepsilon'_{cc})_i$  using equation 5.65.
7. Calculate  $(E_{sec})_i = (f'_{cc})_i / (\varepsilon'_{cc})_i$ .
8. Calculate  $(r)_i$  using equation 5.61.
9. Calculate  $(x)_i$  using equation 5.60.
10. Calculate  $(f_{cc})_i$  using equation 5.59.
11. Return to step 1 with  $i = i + 1$ .

Concrete failure occurs when the confining FRP shell fails. Failure detection is described in detail in section 5.2.3.5 for various load cases.

Figure 5.9 shows typical confined concrete stress-strain curves for varying confining pressures. Fam and Rizkalla (2001) presented extensive comparisons between experimental data and predictions from their variable confinement model that verified the applicability of the model to concrete filled FRP tube members subjected to pure axial loads.

#### *5.2.2.3.3 Proposed Intermediate Confinement Model*

Cross-section equilibrium is analyzed with an infinite neutral axis depth when a concrete filled FRP tube member is subjected to pure axial load, causing uniform compressive strain on the entire cross-section. As shown in Figure 5.10(a), maximum concrete confinement occurs because a maximum uniform confining pressure develops on the perimeter of the concrete core due to uniform radial expansion of the concrete.

Introducing a bending moment to the same member decreases the neutral axis depth from infinity. When the neutral axis depth lies outside the diameter of the member the entire cross-section remains in compression but strain decreases linearly from one side to the other, as shown in Figure 5.10(c). Decreasing concrete compressive strain across the section causes non-uniform decreasing concrete radial displacement and non-uniform decreasing radial confining pressure on the concrete core, reducing the overall confinement effect compared to a pure axial load case with a uniform compressive strain equivalent to the maximum compressive strain in the bending moment case. Reduction of the

confinement effect becomes more pronounced when the neutral axis depth lies within the diameter of the cross-section because tensile strains occur in a portion of the cross-section. No radial confining pressure develops in the tension region, significantly decreasing the overall confinement effect on concrete in the compression zone, as shown in Figure 5.10(d).

Due to the effects described above, the confinement model established for a pure axial load case will overestimate the concrete stress in the compression zone at a given compressive strain when a member is subjected to general axial load and bending moment because the maximum confinement effect is not developed. A simple intermediate confinement model is proposed to establish concrete stress-strain relationships in load cases including bending moment and axial load, accounting for changes in the confinement effect on concrete in the compression zone due to variable neutral axis depth.

The proposed intermediate confinement model's lower bound is the unconfined concrete stress-strain relationship described in section 5.2.2.3.1. It occurs when the applied axial load eccentricity on a member is infinite, resulting in bending moment only, as shown in Figure 5.10(b). In this case, a small portion of the concrete core is subjected to confining pressure, causing the concrete stress-strain relationship in the compression zone to approach the unconfined concrete stress-strain relationship. It will be shown in section 5.8 that modelled behaviour assuming very little concrete confinement in members subjected to bending

moment only agrees well with the beam test results. The upper bound of the model is assumed to be the maximum confinement model described in section 5.2.2.3.2, established for a pure axial load case where the axial load eccentricity is infinite. Figure 5.10 shows the effect of neutral axis depth on the shape of the concrete stress-strain curve, including the upper and lower bounds of the intermediate confinement model.

The proposed intermediate concrete confinement model is expressed in the following relationship:

$$f_{c,int} = (f_c - f_{cc}) \left( \frac{D_{out}}{D_{out} + e} \right) + f_{cc} \quad [\text{Eq. 5.73}]$$

where  $f_{c,int}$  = the concrete stress for a given strain  $\varepsilon_i$

$f_{cc}$  = confined concrete stress at strain  $\varepsilon_i$ , determined using equation 5.59 and the procedure described in section 5.2.2.3.2

$f_c$  = unconfined concrete stress at strain  $\varepsilon_i$ , determined using equation 5.53 and the procedure described in section 5.2.2.3.1

$D_{out}$  = outside diameter of the concrete filled FRP tube member

$e$  = axial load eccentricity

$= e' + \delta$  [Eq. 5.74]

$e'$  = original applied axial load eccentricity prior to member deflection

$\delta$  = cross-section deflection from original position



### ***5.2.3 Modelling Concrete Filled FRP Tube Member Response to Applied Loads***

The following section describes procedures to model concrete filled FRP tube members subjected to bending moment and axial load, and bending moment only. Modelling members subjected to axial load only is described in section 5.2.4.1.

Strain compatibility and cross-section equilibrium are used to predict the response of cylindrical concrete filled FRP tube members subjected to a general combination of bending moment and axial load. It is assumed that plane sections remain plane after bending and that the strain distribution is linear across the depth of the section. It is also assumed that the concrete core and FRP shell are fully bonded, resulting in strain compatibility between the two materials at all stages of deformation.

Cross-section equilibrium analysis of concrete filled FRP tube members is difficult to perform with hand calculations for several reasons. The problem is complicated because the width of the cross-section is non-linear with depth, stresses are non-linear with depth due to material non-linearity, and the FRP shell acts as non-discrete tension and compression reinforcement. Therefore, analysis is well suited to automated calculations.

Cross-section equilibrium calculations are applied iteratively. First, an extreme concrete compressive fibre strain is assumed. Next, an initial neutral axis depth is assumed and the equilibrium calculations described in the upcoming sections

are applied to determine if cross-section equilibrium is satisfied. If not, the assumed neutral axis depth is revised and equilibrium calculations are repeated. Iteration continues until equilibrium is satisfied. Once equilibrium is satisfied for the input extreme concrete compressive fibre strain, the strain is revised and the entire process repeated. The process is repeated for a full range of extreme concrete compressive fibre strains from zero to a strain that causes member failure, yielding the full response of the member. The following sections describe the equilibrium analysis and failure detection procedure.

#### 5.2.3.1 Analysis Geometry

Analysis begins by dividing the cross-section into a large number of horizontal strips and calculating concrete and FRP areas in each strip. As shown Figure 5.11, each strip has an equal depth  $h$  expressed:

$$h = \frac{D}{n} \quad [\text{Eq. 5.75}]$$

where  $D = \text{average cross-section diameter}$

$$= \frac{D_{out} + D_{in}}{2} \quad [\text{Eq. 5.76a}]$$

$$= D_{out} - t \quad [\text{Eq. 5.76b}]$$

$t = \text{thickness of the FRP tube}$

$n = \text{number of strips}$

A large number of strips should be selected to ensure that the depth of each strip is much less than the diameter of the cross-section. The distance from the top of the cross-section to the middle of a given strip  $i$ , shown in Figure 5.11 can be expressed:

$$h_i = h(i - 0.5) \quad [\text{Eq. 5.77}]$$

The angles  $(\phi_1)_i$  and  $(\phi_2)_i$  between a vertical line passing through the centre of the cross-section and the intersection of the top and bottom of strip  $i$  with the circle with diameter  $D$ , shown in Figure 5.11, are expressed:

$$(\phi_1)_i = \cos^{-1} \left[ \frac{0.5D - h_i + 0.5h}{0.5D} \right] \quad [\text{Eq. 5.78}]$$

$$(\phi_2)_i = \cos^{-1} \left[ \frac{0.5D - h_i - 0.5h}{0.5D} \right] \quad [\text{Eq. 5.79}]$$

The arc length  $L_i$  of the circle with diameter  $D$  between the top and bottom of strip  $i$ , shown in Figure 5.11, is calculated using the angles from equation 5.78 and equation 5.79 as follows:

$$L_i = 0.5D[(\phi_2)_i - (\phi_1)_i] \quad [\text{Eq. 5.80}]$$

The total area  $(A_f)_i$  of FRP shell within strip  $i$ , shown in Figure 5.11, is:

$$(A_f)_i = 2L_i t \quad [\text{Eq. 5.81}]$$

The angle  $\phi_i$  between a vertical line passing through the centre of the cross-section and a radial line passing through the centre of the cross-section and the intersection of the middle of strip  $i$  with the circle with diameter  $D$ , shown in Figure 5.11, is expressed:

$$\phi_i = \cos^{-1} \left[ \frac{0.5D - h_i}{0.5D} \right] \quad [\text{Eq. 5.82}]$$

Half the width  $B_i$  of strip  $i$ , shown in Figure 5.11, is calculated using:

$$B_i = 0.5D \sin \phi_i \quad [\text{Eq. 5.83}]$$

The area of concrete  $(A_c)_i$  within strip  $i$ , shown in Figure 5.11 can be expressed:

$$(A_c)_i = 2B_i h - 0.5(A_f)_i \quad [\text{Eq. 5.84}]$$

### 5.2.3.2 Cross-section Strain Distribution and Stress Calculations

Cross-section equilibrium analysis continues by calculating stresses in each strip once the location, concrete area, FRP area, and strain in each strip are determined. The strain due to a general combination of applied axial load and

bending moment varies linearly across the depth of the section, from strain  $\varepsilon_t$  at the top to strain  $\varepsilon_b$  at the bottom. The top and bottom strains are calculated from the input extreme concrete compressive fibre strain and assumed neutral axis depth using the principle of similar triangles. The strain  $\varepsilon_i$  in strip  $i$  is calculated using:

$$\varepsilon_i = \frac{\varepsilon_t(D - h_i) + \varepsilon_b h_i}{D} \quad [\text{Eq. 5.85}]$$

Material constitutive relationships are applied to calculate stresses in the concrete and FRP once strains in each strip are calculated. As described in section 5.2.2.2, compressive and tensile stress-strain relationships for an FRP shell are multilinear because laminate effective elastic properties change when individual laminas fail.

Tensile elastic moduli  $(E_f)_i$  for each strip  $i$  in the tension zone are the slopes of the FRP uniaxial tensile stress-strain relationship developed using the procedure in section 5.2.2.2.1 at strains corresponding to strains  $\varepsilon_i$ . Section 5.2.3.5 will describe a procedure to determine the state of biaxial stress in the FRP shell in the compression zone, based on the input neutral axis depth and assumed extreme concrete compressive stress, forming a point on the biaxial stress path. The procedure described in section 5.2.3.5 is applied to determine if the current state of biaxial stress in the FRP causes individual laminas to fail and to calculate

the corresponding laminate effective elastic properties, including the compressive elastic moduli  $(E_{fc})_i$ .

Once the compressive and tensile elastic moduli are determined, FRP stresses at each strip in the compression zone  $(f_{fc})_i$  and tension zone  $(f_{ft})_i$  are calculated using:

$$(f_{fc})_i = (E_{fc})_i \varepsilon_i \quad [\text{Eq. 5.86}]$$

$$(f_{ft})_i = (E_{ft})_i \varepsilon_i \quad [\text{Eq. 5.87}]$$

A concrete stress-strain relationship is used to determine the concrete stress  $(f_{cc})_i$  at a given strip  $i$ . As described in section 5.2.2.3, the concrete stress-strain relationship is non-linear with a shape that depends on the level of confinement. Either the maximum confinement model for pure axial load or intermediate confinement model for combined axial load and bending moment or bending moment only are used to determine the appropriate concrete stress-strain relationship. The concrete stress  $(f_{cc})_i$  at strip  $i$  in the compression zone is taken directly from the established concrete stress-strain relationship as the stress at a strain equivalent to strip strain  $\varepsilon_i$ .

The cross-section equilibrium analysis model also accounts for tension stiffening of the cracked concrete section. Collins and Mitchell's (1987) expression for the concrete tensile stress  $(f_{ct})_i$  for short-term monotonic loading is used:

$$(f_{ct})_i = \frac{\alpha_1 f_{cr}}{1 + \sqrt{500 \varepsilon_i}} \text{ for } \varepsilon_i \geq \varepsilon_{cr} \quad [\text{Eq. 5.88a}]$$

$$= E_{c0} \varepsilon_i \text{ for } \varepsilon_i < \varepsilon_{cr} \quad [\text{Eq. 5.88b}]$$

where  $f_{cr}$  = concrete cracking stress

$\varepsilon_{cr}$  = concrete cracking strain

$$= \frac{f_{cr}}{E_{c0}} \quad [\text{Eq. 5.89}]$$

$E_{c0}$  = tangent elastic modulus at 0 strain  
(calculated using equation 5.55)

$\alpha_1$  = factor for the bond characteristics between  
the concrete and reinforcement

The factor  $\alpha_1$  varies between 0 for unbonded reinforcement and 1.0 for deformed reinforcing bars. A value of 0.3 is used for concrete filled FRP tube members.

The concrete cracking stress  $f_{cr}$  is referred to as the modulus of rupture  $f_r$  for reinforced concrete members subjected to bending moment. CSA standard A23.3 approximates the modulus of rupture for normal weight concrete as:

$$f_r = 0.6\sqrt{f'_c} \quad [\text{Eq. 5.90}]$$

The strain distribution across the depth of a cross-section and associated concrete and FRP stresses for a general combination of applied axial load and bending moment are illustrated in Figure 5.12.

### 5.2.3.3 Cross-section Equilibrium Analysis

Concrete and FRP stresses in each compression and tension zone strip  $i$  are used to calculate internal resultant forces and moments, using the following equations, where the moments are resolved about the neutral axis:

$$\text{concrete force in compression zone} \quad CC_i = (f_{cc})_i (A_c)_i \quad [\text{Eq. 5.91}]$$

$$\text{FRP force in compression zone} \quad CF_i = (f_{fc})_i (A_f)_i \quad [\text{Eq. 5.92}]$$

$$\text{concrete force in tension zone} \quad TC_i = (f_{ct})_i (A_c)_i \quad [\text{Eq. 5.93}]$$

$$\text{FRP force in tension zone} \quad TF_i = (f_{ft})_i (A_f)_i \quad [\text{Eq. 5.94}]$$

$$\text{moment due to compression zone concrete force} \quad MCC_i = CC_i (c - (h_i + t/2)) \quad [\text{Eq. 5.95}]$$

$$\text{moment due to compression zone FRP force} \quad MCF_i = CF_i (c - (h_i + t/2)) \quad [\text{Eq. 5.96}]$$

$$\text{moment due to tension zone concrete force} \quad MTC_i = TC_i ((h_i + t/2) - c) \quad [\text{Eq. 5.97}]$$

$$\text{moment due to tension zone FRP force} \quad MTF_i = TF_i ((h_i + t/2) - c) \quad [\text{Eq. 5.98}]$$



A geometric adjustment is made in the moment arm portion of the moment equations because the neutral axis  $c$  is measured from the top of the cross-section, coinciding with the outside of the FRP shell, while the distance  $h_i$  is measured from the circle with diameter  $D$ , one-half the thickness  $t$  of the FRP shell inside the outermost surface of the shell.

Individual concrete and FRP strip forces are summed to determine total concrete compression force  $CC_{TOT}$ , total FRP compression force  $CF_{TOT}$ , total concrete tensile force  $TC_{TOT}$ , and total FRP tensile force  $TF_{TOT}$  as follows:

$$CC_{TOT} = \sum_{i=1}^{\frac{(c-t/2)}{h}} CC_i \quad [\text{Eq. 5.9}]$$

$$CF_{TOT} = \sum_{i=1}^{\frac{(c-t/2)}{h}} CF_i \quad [\text{Eq. 5.100}]$$

$$TC_{TOT} = \sum_{i=\frac{(c-t/2)}{h}}^n TC_i \quad [\text{Eq. 5.101}]$$

$$TF_{TOT} = \sum_{i=\frac{(c-t/2)}{h}}^n TF_i \quad [\text{Eq. 5.102}]$$

Force and moment equilibrium are satisfied for a general load case with applied axial load and bending moment when:

$$P = CC_{TOT} + CF_{TOT} + TC_{TOT} + TF_{TOT} \quad [\text{Eq. 5.103}]$$

$$M = MCC_{TOT} + MCF_{TOT} + MTC_{TOT} + MTF_{TOT} \quad [\text{Eq. 5.104}]$$

where  $P$  = applied axial load

$M$  = applied bending moment resolved about the neutral axis

$$MCC_{TOT} = \sum_{i=1}^h M_{CC_i} \quad [\text{Eq. 5.105}]$$

$$MCF_{TOT} = \sum_{i=1}^h M_{CF_i} \quad [\text{Eq. 5.106}]$$

$$MTC_{TOT} = \sum_{i=\frac{(c-t/2)}{h}}^n M_{TC_i} \quad [\text{Eq. 5.107}]$$

$$MTF_{TOT} = \sum_{i=\frac{(c-t/2)}{h}}^n M_{TF_i} \quad [\text{Eq. 5.108}]$$

#### 5.2.3.3.1 Bending Moment Only Load Case

The axial load term  $P$  in equation 5.103 is set equal to zero when a pure bending load case is analyzed. Equilibrium is satisfied when the sum of internal forces in the compression zone is equivalent to the sum of internal forces in the tension zone. The corresponding moment is calculated with equation 5.104 once internal force equilibrium is satisfied.

#### 5.2.3.3.2 Combined Bending Moment and Axial Load Case

Equations 5.103 and 5.104 are solved simultaneously when combined axial load and bending moment are applied. It is assumed that the bending moment  $M$  in

equation 5.104 is a result of an eccentrically applied axial load in the axial load and bending moment load case for the remainder of the discussion on the analytical model. The axial load and bending moment are coupled, with no independent bending moment applied. A case with a general combination of applied axial load and bending moment can also be analyzed if required.

As shown in Figure 5.13, the externally applied bending moment  $M_0$  at mid-height on the cross-section due to an eccentrically applied axial load can be expressed:

$$M_0 = Pe \quad [\text{Eq. 5.109a}]$$

where  $e$  = *axial load eccentricity at cross-section being analyzed (perpendicular distance between line of action of axial load and geometric centroid of the section)*

$$= e' + \delta \quad [\text{Eq. 5.110}]$$

$e'$  = *initial axial load eccentricity, prior to deflection of the member*

$\delta$  = *deflection of the cross-section relative to its original position before loading*

$M_0$  can also be expressed:

$$M_0 = P(e' + \delta) \quad [\text{Eq. 5.109b}]$$

$$= Pe' + P\delta \quad [\text{Eq. 5.109c}]$$

The  $Pe'$  and  $P\delta$  terms in equation 5.109c are referred to as the primary moment  $M_1$  and secondary moment  $M_2$ .

In order to apply cross-section moment equilibrium equation 5.104, the external moment  $M_0$  must be resolved about the neutral axis of the cross-section to be consistent with the internal moments calculated with equation 5.105 to equation 5.108. The moment due to eccentrically applied axial load, taken about the neutral axis is expressed:

$$M = P \left( e - \left( \frac{D_{out}}{2} - c \right) \right) \quad [\text{Eq. 5.111}]$$

Equilibrium is satisfied when the sum of internal moments in equation 5.104 is equivalent to the externally applied moment, given by equation 5.111 for a load case with coupled axial load and bending moment.

#### 5.2.3.4 Calculation of Member Deflection

Deflection at a point of interest along the member is calculated by evaluating the double integral of the curvature function, because the curvature function is the double derivative of the deflection function. This can be expressed:

$$\psi(x) = \frac{d^2\delta(x)}{dx^2} \quad [\text{Eq. 5.112}]$$

$$\delta(x) = \iint \psi(x) dx dx \quad [\text{Eq. 5.113}]$$

where  $x$  = distance from one end of the member

A closed form solution of equation 5.113 can be found when the curvature function with respect to distance from one end of the member is known.

Otherwise numerical integration is used to evaluate deflection  $\delta$  at point  $x$  by dividing the distance  $x$  into a number of intervals and summing the areas under the curvature diagram in each interval, up to and including the interval whose end coincides with distance  $x$ . The numerical integration procedure, illustrated in Figure 5.14, is expressed:

$$\delta @ x = \left( \frac{\psi_1 x_1 + \psi_2 x_2}{2} \right) \Delta x_1 + \cdots + \left( \frac{\psi_{i-1} x_{i-1} + \psi_i x_i}{2} \right) \Delta x_{i-1} + \cdots \quad [\text{Eq. 5.114}]$$

where  $\Delta x_{i-1}$  = length of interval  $i-1$

$\psi_{i-1}$  = curvature at the beginning of interval  $i-1$

$\psi_i$  = curvature at the end of interval  $i-1$

The curvature distribution along the length of a member is required in order to calculate the deflection at a specific cross-section of interest.

The equilibrium analysis described in section 5.2.3.3 yields a unique cross-section moment and curvature for each extreme concrete compressive fibre strain analyzed. The curvature of a cross-section is calculated once equilibrium is satisfied. Curvature is the slope of the linear strain distribution, calculated using:

$$\psi = \frac{\varepsilon_t - \varepsilon_b}{D} \quad [\text{Eq. 5.115}]$$

Analyzing a full range of extreme concrete compressive fibre strains up to member failure provides a full moment-curvature relationship for the cross-section geometry and material properties analyzed. The calculated equilibrium moment for each extreme concrete compressive fibre strain can be used to calculate the corresponding moments at any other location along the member by using the member's moment diagram, determined based on the type and location of applied loads and member supports. Moments from the established moment diagram are used to interpolate corresponding curvatures from the unique moment-curvature relationship established during cross-section equilibrium analysis. The procedure yields a complete curvature diagram along the member for each extreme concrete compressive fibre strain input to the cross-section equilibrium analysis. The calculated curvatures along the member are then used to determine the cross-section deflection with equation 5.114 for each extreme concrete compressive fibre strain analyzed. A simple example of the deflection calculation procedure is illustrated in Figure 5.15.

Because deflection does not affect cross-section equilibrium in a pure bending moment case, deflections are calculated once for each extreme concrete compressive fibre strain analyzed, after all equilibrium calculations are completed. Deflection calculations for member subjected to combined bending moment and axial load are more complicated because there are unique cross-

section moment-curvature relationships for each applied axial load, and cross-section equilibrium and deflection are related by equation 5.109. An iterative process described in section 5.2.4.3 is used to evaluate cross-section deflection for combined bending moment and axial load cases. Deflection calculations are not required when analyzing members subjected to pure axial load.

Moment diagrams for members subjected to bending moment only are typically known or can be calculated easily. However, moment diagrams for members subjected to combined axial load and bending moment are more difficult to establish due to the interdependence between deflection and equilibrium. A quadratic function is assumed to model the moments along the length of the member for the case of a concrete filled FRP tube member subjected to coupled axial load and bending moment. The derived moment function is expressed:

$$M(x) = -\frac{4(M_0 - M_1)x^2}{L^2} + \frac{4(M_0 - M_1)x}{L} + M_1 \quad [\text{Eq. 5.116}]$$

where  $x$  = distance from end of the member

$M(x)$  = applied moment at a distance  $x$  from one end of the member

$M_0$  = total moment at mid-height (see Figure 5.13)

$M_1$  = Moment at each end of the member (see Figure 5.13)  
primary moment)

$L$  = length of member

The moment function satisfies the boundary conditions  $M(x)=M_1$  at  $x=0$  and  $x=L$ , and  $M(x)=M_0$  at  $x=L/2$  shown in Figure 5.13.

### 5.2.3.5 Modelling Member Failure

#### 5.2.3.5.1 Laminate Failure in Pure Axial Load Cases

As discussed in section 5.2.2.2.2, the FRP shell of a concrete filled FRP tube member is subjected to a biaxial state of stress when a pure axial load is applied to the member. The shell experiences longitudinal compressive axial stress due to axial load on the shell and tensile hoop stress due to radial confining pressure caused by expansion of the concrete core under axial load. Following the procedure described in section 5.2.2.2.2, the radial confining pressure  $(\sigma_r)_i$  is calculated for a given incremental axial strain  $(\varepsilon_{cc})_i$ . The corresponding tensile hoop stress  $(\sigma_h)_i$  is calculated using:

$$(\sigma_h)_i = \frac{(\sigma_r)_i R}{t} \quad [\text{Eq. 5.117}]$$

The axial compressive stress  $(\sigma_a)_i$  on the FRP shell due to the applied axial load is calculated for a given incremental axial strain  $(\varepsilon_{cc})_i$  using:

$$(\sigma_a)_i = (E_{fc})_i (\varepsilon_{cc})_i \quad [\text{Eq. 5.118}]$$



Equations 5.117 and 5.118 are used to establish the biaxial stress path for increasing axial strain. As shown in Figure 5.16, the biaxial state of stress is compared to the laminate biaxial strength envelope in the quadrant for compressive axial stress  $N_x$  and tensile lateral stress  $N_y$ , determined using the Tsai-Wu failure criterion procedure described in section 5.2.2.2. A lamina in the laminate fails when the biaxial stress path intersects a lamina failure envelope. When failure of the lamina causes overall laminate failure the analysis ends because the member has failed. Analysis continues if failure of the lamina does not cause overall laminate failure. Subsequent points on the biaxial stress path are evaluated by accounting for changes in the laminate effective elastic properties in the concrete stress-strain model and equation 5.86. The procedure is repeated for increasing incremental strains until overall laminate failure is detected.

#### *5.2.3.5.2 Laminate Failure in Load Cases with Bending Moment*

Member failure occurs either when the FRP shell fails in uniaxial longitudinal tension at the extreme fibre in the tension zone, or under biaxial state of stress at the extreme fibre in the compression zone when a concrete filled FRP tube member is subjected to a pure bending moment only or combined bending moment and axial load.

It is assumed that the FRP shell is subjected to uniaxial longitudinal tensile stress in the cross-section's tension zone because the concrete in the tension zone is

cracked and no radial confining pressure occurs at the interface between the interior of the shell and the concrete core. The tensile strain in the shell at each strip, for a given extreme concrete compressive strain and neutral axis depth, is calculated using the procedure in section 5.2.3.2 and compared to the laminate's multilinear tensile stress-strain relationship determined using the procedure in section 5.2.2.2.1. When the strain in a strip exceeds the failure strain for a lamina in the laminate, the lamina is discounted from the analysis and revised laminate effective elastic properties are calculated. Once the extreme fibre tensile strain exceeds the laminate ultimate tensile strain, overall laminate failure occurs and the member fails in tension.

Member compression failure for a load case including bending moment is determined using a procedure similar to the one for member compression failure in a pure axial load case, while accounting for intermediate confinement of the concrete in the compression zone in lieu of maximum confinement. The complete intermediate confinement concrete stress-strain relationship is established using the procedure described in section 5.2.2.3.3, for a given neutral axis depth. The maximum confinement model formulation is used to back calculate radial confining pressures and resultant FRP shell hoop stresses for each point on the intermediate confinement stress-strain curve using a trial-and-error approach well suited to automated calculations. Subsequent determination of the biaxial stress path, lamina failures, and member failure then follows the procedure described

for the pure axial load case. Figure 5.17 illustrates the effect of varying neutral axis depth on the biaxial stress path in the FRP shell in the compression zone.

#### ***5.2.4 Applying the Complete Analytical Model***

Section 5.2.2 to section 5.2.3 describe the individual parts of the proposed analytical model used to describe the full response of concrete filled FRP tube members subjected to axial load, bending moment, or combined axial load and bending moment, for a general set of material properties and loads. The following sections describe the suggested step-by-step application of the complete analytical model for pure bending moment, pure axial load, and combined axial load and bending moment load cases.

The first several steps used to apply the model are common to all load cases:

1. Input desired cross-section geometry and material properties, including FRP laminate constituent properties, FRP laminate stacking sequence and lamina thicknesses, member cross-section diameter, and peak unconfined concrete stress.
2. Calculate the FRP laminate effective elastic properties using the procedure described in section 5.2.2.1, with inputs from step 1.
3. Evaluate lamina and laminate longitudinal compressive strength versus hoop tensile strength envelopes and a uniaxial tensile stress-strain

relationship for the FRP shell laminate, with inputs from step 1 and step 2.

4. Determine the unconfined and maximum confinement concrete stress-strain relationships using the procedures described in section 5.2.2.3.1 and section 5.2.2.3.2 respectively, with inputs from steps 1 to 3.

The remaining steps vary depending on the loading condition. They are presented in the following sections.

#### 5.2.4.1 Modelling a Pure Axial Load Case

5. Input a compressive strain. This strain is uniform across the entire cross-section because the neutral axis depth is infinite for a pure axial load case.
6. Evaluate the laminate biaxial stress path using the procedure in section 5.2.3.5.1, using the current laminate effective elastic properties.
7. Determine if the input extreme concrete compressive fibre strain in step 5 causes stresses on the biaxial stress path found in step 6 to exceed a lamina failure envelope calculated in step 3. If so, recalculate laminate effective elastic properties as described in section 5.2.2.1, discounting the failed lamina, and recalculate a revised maximum confinement concrete stress-strain curve. If the input compressive strain causes overall laminate failure to occur because the established point on the

- biaxial stress path exceeds the overall laminate failure envelope calculated in step 3, the member fails and analysis is stopped.
8. Repeat step 6 and step 7 until the input axial compressive strain does not cause further lamina failures.
  9. Determine the axial stress in the concrete by taking the stress from the current maximum confinement concrete stress-strain curve at the input compressive strain. Calculate the axial stress in the FRP shell by multiplying the input axial strain by the laminate effective longitudinal compressive elastic modulus for the current state of biaxial stress in the laminate.
  10. Calculate the total axial force on the member by multiplying the concrete and FRP compressive stresses determined in step 9 by their respective cross-sectional areas and summing the results.
  11. Repeat step 5 to step 10 for increasing compressive strains, until ultimate laminate failure is detected in step 7.

#### 5.2.4.2 Modelling a Pure Bending Moment Load Case

5. Input a value for the extreme concrete compressive fibre strain.
6. Input an assumed neutral axis depth.
7. Divide the cross-section into a large number of horizontal strips and calculate the FRP and concrete areas in each strip using the procedure described in section 5.2.3.1.

8. Calculate the strains in each strip using the procedure described in section 5.2.3.2, based on the extreme concrete compressive fibre strain input in step 5 and assumed neutral axis depth from step 6.
9. Calculate the intermediate confined concrete stress-strain relationship using the procedure in section 5.2.2.3.3, based on the assumed neutral axis depth in step 6.
10. Evaluate the laminate biaxial stress path using the procedure in section 5.2.3.5.2, using the current laminate effective elastic properties.
11. Determine if each compression zone strip strain calculated in step 8 causes stresses on the biaxial stress path found in step 10 to exceed a lamina failure envelope established in step 3. If so, recalculate laminate effective elastic properties at the strip as described in section 5.2.2.1, discounting the failed lamina, and recalculate a revised intermediate confined concrete stress-strain curve. If a strip strain causes overall laminate failure to occur because the established point on the biaxial stress path exceeds the overall laminate failure envelope calculated in step 3, the member fails and analysis is stopped.
12. Repeat step 10 and step 11 until strip strains in the compression zone calculated in step 8 do not cause further lamina failures.
13. Calculate stresses in the concrete and FRP for each strip, using the procedure described in section 5.2.3.2. Ensure that the appropriate intermediate confined concrete and FRP stress-strain relationships are used for each strip, accounting for changes in laminate effective elastic

properties due to individual lamina failures. In the tension zone, the FRP stress at each strip is taken directly from the multilinear uniaxial longitudinal tension stress-strain relationship for the laminate, determined using the procedure in section 5.2.2.2.1. When a tensile strain exceeds the overall laminate uniaxial tensile failure strain the member fails in tension and analysis stops.

14. Calculate total compressive and tensile concrete and FRP cross-sectional forces using equations 5.99 to 5.102. Determine if force equilibrium is satisfied by applying equation 5.103 with  $P = 0$ . The sum of cross-sectional forces will never equal exactly zero because numerical integration is used on a discrete number of strips. An allowable error tolerance must be established. Equation 5.103 is modified and equilibrium is met when:

$$|CC_{TOT} + CF_{TOT}| - |TC_{TOT} + TF_{TOT}| \leq \text{allowable error} \quad [\text{Eq. 5.119}]$$

Continue to step 15 if equation 5.119 is satisfied. Return to step 6 and input a revised value for the neutral axis depth if equation 5.119 is not satisfied.

15. Once cross-section force equilibrium is satisfied, calculate the total cross-sectional moment with equation 5.109 and curvature with equation 5.115.

16. Repeat step 5 to step 15 with increasing values of extreme compressive fibre concrete strain until overall laminate failure is detected in step 11 or step 13, resulting in member compression or tension failure.
17. Calculate cross-section deflections for each extreme concrete compressive fibre strain analyzed, using the procedure described in section 5.2.3.4.

#### 5.2.4.3 Modelling a Load Case with Bending Moment and Axial Load

5. Input a value for the initial axial load eccentricity  $e'$  prior to member deflection.
6. Assume the cross-section deflection  $\delta$  to be zero. This assumption is temporary. The true cross-section deflection will be calculated using an iterative process described in step 12 to step 14.
7. Perform step 5 to step 13 of the bending moment only procedure described in section 5.2.4.2.
8. Calculate total compressive and tensile concrete and FRP cross-sectional forces using equations 5.99 to 5.102. Sum the internal forces to obtain the resultant axial load  $P$ , using equation 5.103.
9. Determine if cross-section moment equilibrium is satisfied using equation 5.104 and equation 5.111, recalling that it was originally assumed that no cross-section deflection occurs. The sum of internal moments will never exactly equal the external moment resolved about the neutral axis because numerical integration is used on a discrete number of strips. An



allowable error tolerance must be established. Equation 5.104 is modified, and equilibrium is met when:

$$|M| - |MCC_{TOT} + MCF_{TOT} + MTC_{TOT} + MTF_{TOT}| \leq \text{allowable error} \quad [\text{Eq. 5.120}]$$

Continue to step 10 if equation 5.120 is satisfied. Return to step 7 and input a revised value for the neutral axis depth if equation 5.120 is not satisfied.

10. Once equilibrium is satisfied, calculate the external moment using equation 5.109.
11. Calculate a complete axial force-moment-curvature relationship for the equilibrium axial force calculated in step 8. The procedure is similar to steps 7 to 10 above, except that the equilibrium axial force is imposed at each extreme concrete compressive strain, and the neutral axis varied until equilibrium is satisfied. Corresponding curvatures are calculated using equation 5.115 after equilibrium is satisfied for each compressive strain analyzed. This process provides a complete moment-curvature relationship for a specific, constant axial load.
12. The external moment at equilibrium in step 10 is used to calculate the moment distribution along the member using equation 5.116. The axial load-moment-curvature relationship determined in step 11 is used to calculate the curvature distribution along the member. The numerical

- integration procedure in equation 5.114 is then used to calculate the deflection at a point of interest along the beam-column.
13. Repeat step 6 to step 12 with increasing values of extreme concrete compressive fibre strain until overall laminate failure is detected in step 7 (step 11 or step 13 of the bending moment only procedure in section 5.2.4.2) and the member fails in compression or tension.
  14. Repeat step 7 to step 13 for each extreme concrete compressive fibre strain analyzed, using the cross-section deflections calculated in step 12 when evaluating equilibrium equation 5.120 in step 9, accounting for cross-section deflection in the  $M$  term calculated using equation 5.111. Repeat this step several times, until the deflections calculated in step 12 are equivalent to the deflections calculated in the previous iteration for each extreme concrete compressive fibre strain analyzed. Two or three iterations are typically required for convergence to occur.

### 5.3 Verification of the Analytical Model

The following sections compare the behaviour of the test specimens discussed in Chapter 4 to the behaviour predicted by the proposed analytical model.

#### 5.3.1 Modelled Beam Specimen Tests

Figures 5.18 to 5.25 present the predicted moment-deflection and moment-axial strain behaviours of beam specimens BM-E-1, BM-E-2, BM-P-1, and BM-P-2.

The FRP tube longitudinal compressive and tensile elastic moduli calculated with

the LPT and from the coupon tests were applied separately when modelling each beam. The flexural stiffnesses beams BM-E-1 and BM-E-2 appear to be modelled more accurately using the FRP shell elastic moduli from the coupon tests, as shown in Figures 5.18 and 5.19. The modelled stiffness at low moments using the FRP shell elastic moduli from the coupon tests agreed well with experimental results, but over predicted the stiffness at high moments, after significant cracking and slip of the concrete core had occurred. This was expected because full bond between the concrete core and FRP shell is assumed in the model. The model does not account for loss of flexural stiffness due to concrete core cracking and slip.

The modelled flexural stiffness using FRP shell elastic moduli calculated with the LPT is initially higher than predicted using the FRP properties from the coupon tests for beams BM-P-1 and BM-P-2. A sudden change in predicted stiffness occurs when the axial tensile strain reaches approximately 3.5-millistrain, as shown in Figures 5.24 and 5.25, coinciding with first-ply failure of the laminate predicted by the Tsai-Wu failure theory, causing a significant decrease of the tensile elastic modulus of the shell. The change in calculated elastic modulus causes the predicted member flexural stiffness to decrease below the stiffness predicted using the coupon test elastic moduli. The flexural stiffness of specimens BM-P-1 and BM-P-2 is predicted more accurately using the coupon test elastic moduli because the experimental results and coupon specimens did

not demonstrate the first-ly failure in tension predicted by the Tsai-Wu failure theory.

In general, it appears that modelling the beams using the experimentally determined FRP elastic moduli is more representative of the actual behaviour than when LPT calculated properties are used. Therefore, the elastic moduli from the coupon tests are used to model the behaviour of the remainder of the test specimens in the following sections. It is important to note that modelling concrete filled FRP tubes should be performed using LPT calculated FRP properties when coupon test results are not available. However, it is essential to exercise excellent quality control during FRP shell fabrication to ensure that the laminate structure is constructed exactly as designed, allowing for accurate modelling of the laminate properties with the LPT. In the case of the test specimens in the experimental program, the fabricated shells may have differed from the designed laminate structures, causing imperfect modelling of the shells' properties using the LPT.

Figures 5.18 and 5.25 also show the predicted failure moments based on tensile rupture strains from the experimental coupon tests and calculated with the Tsai-Wu failure theory. The actual tensile failure strains were higher than the coupon and calculated values. The maximum moments in the beam tests are predicted well when modelled behaviour is extended to the measured tensile failure strains. Predicted loads and bending moments at the failure strains calculated with the

Tsai-Wu laminate failure criterion are indicated on the remainder of the plots comparing the experimental and modelled behaviours of the specimens, but the modelled behaviours are extended to the experimentally measured failure strains in cases where failure strains are under estimated by the Tsai-Wu failure theory.

### 5.3.2 Modelled Axial Load Specimens

Figures 5.26 and 5.27 compare the predicted axial load-axial strain behaviours of the pure axial load specimens to the experimental results. Predicted behaviours assuming unconfined concrete cores are also plotted for comparison. In both cases, the axial compressive failure strains predicted by the model are larger than the failure strains measured during testing. The modelled behaviour of the E-glass/epoxy FRP shell specimen indicates post-peak strain-hardening that results in a significant increase in axial load. The E-glass/polyester shell modelled behaviour exhibits a small decrease in axial load after the initial peak, followed by increasing axial load. The original peak axial load is recovered and slightly exceeded prior to failure.

The axial load specimen confined concrete predicted relationships demonstrate that a transition to confined behaviour occurs when the peak unconfined concrete stress in the concrete core is reached. The predicted axial loads at the transition point are similar to the peak axial loads of the test specimens. However, the test specimens did not exhibit the predicted confined response after the peak. The high strength of the concrete may have prevented formation of many small

cracks prior to the peak load, preventing significant radial expansion of the core, reducing the confinement effect compared to the modelled behaviour. Initiation of failure by localized effects at the load points, described in section 4.5, may have contributed to rapid failure of the specimens prior to development of significant confinement.

### 5.3.3 Modelled Combined Bending Moment and Axial Load Specimens

#### *5.3.3.1 Specimens BC-P-e10 and BC-P-e30*

Figure 5.28 and 5.29 compare the axial load-deflection relationships of beam-column specimens BC-P-e10 and BC-P-e30 to the relationships predicted by the model. The axial loads at failure are over predicted in each case. As discussed in sections 4.4.1 and 4.4.2, it is clear that the specimens did not behave as expected, as demonstrated by the fact that no deflections were initially measured for specimen BC-P-e10, and a small negative deflection was measured for specimen BC-P-e30. The experimental results were affected by possible out-of-straightness of the specimens, seating of the testing apparatus when load was applied, or some other imperfection in the test setup. The effects of the imperfections were magnified in the experimental results due to the low applied axial load eccentricities used in the tests, whereas results from higher axial load eccentricity tests were not as sensitive to such imperfections. It is concluded that the experimental results from specimens BC-P-e10 and BC-P-e30 cannot be compared reliably to the predictions from the model. However, it is interesting to note that the general shapes of the moment-axial strain relationships of the test

specimens, shown in Figures 5.30 and 5.31, resemble the shapes of the predicted behaviours, indicating that the experimental specimens would likely have performed as predicted if more ideal experimentation was possible.

#### 5.3.3.2 Specimen BC-P-e100

Figure 5.32 shows the moment-axial strain behaviour of beam-column specimen BC-P-e100. The model predicts the behaviour very well, demonstrating a bi-linear relationship attributed to post-peak ductility and strain hardening due to confinement. The figure shows that the initial peak axial load in the test occurred near the strains corresponding to the peaks of the unconfined concrete predicted relationships, followed by initiation of the confinement effect. Figures 5.33 and 5.34 also show that the model predicts the maximum axial load and moment very well. The modelled lateral deflection at failure is higher than measured in the test because the model assumes perfect bond between the concrete core and FRP shell up to failure. The model is not capable of reliably predicting the stiffness near the end of the test when significant local effects due to cracking and slip of the concrete likely affected the test results.

#### 5.3.3.3 Specimens BC-P-e200 and BC-P-e300

The predicted axial load-deflection, moment-deflection, and moment-axial strain behaviours of specimen BC-P-e200 are shown in Figures 5.35 to 5.37. The model predicts the maximum axial load and moment well, although stiffness prior to the onset of confinement is slightly under-predicted. A small drop in axial load

and moment in the experimental results coincides with the predicted peaks of the unconfined concrete relationships, followed by increasing load and moment due to confinement. The model accurately predicts the stiffness of the specimen after confinement began.

The model predicts the behaviour of specimen BC-P-e300 very well, as shown in Figures 5.38 to 5.40. The predicted onset of confinement coincides with a small change in slope on the moment-axial strain relationship from the test, shown in Figure 5.40, indicating accurate prediction of the transition point between unconfined and confined behaviour.

#### 5.3.3.4 Specimens BC-E-e30 and BC-E-e100

Figures 5.41 to 5.43 show the model predicted behaviours of beam-column specimens BC-E-e30 and BC-E-e100. In both cases, the model predicts the behaviour very well. The experimental moment-axial strain behaviour of specimen BC-E-e30 demonstrates a distinct point where slope decreases, indicating the onset of confinement, as described in section 4.4.6. The modelled behaviour also exhibits a change in slope at the beginning of confinement, when the peak of the unconfined concrete relationship is reached.

The moment-axial strain behaviour of specimen BC-E-e100 also demonstrates a similar change in slope once confinement begins, on both the experimental and modelled relationships. However, the modelled behaviour slightly over-estimates the stiffness of the specimen in this case, causing the transition point to occur



prior to the transition point in the experimental results. It also appears that the stiffness of the specimen after confinement begins is over-estimated by the model, causing the predicted maximum moment and axial load to be slightly higher, and maximum deflection slightly lower, than measured in the test. This is attributed to the fully bonded assumption in the model. Cracking and debonding of the concrete core during the test, indicated by multiple drops in load and moment past the initial peak, caused a loss in specimen stiffness, resulting in lower axial load and higher deflection at failure than predicted.

#### 5.3.3.5 Specimens BC-E-e200 and BC-E-e300

The model predicted moment-axial strain behaviours of beam-column specimens BC-E-e200 and BC-E-e300, shown in Figures 5.47 and 5.48, reflect the experimentally measured behaviours well. A drop in moment and load occurred in specimen BC-E-e200 when the strains reached those at the peak of the unconfined concrete relationships, followed by initiation of confinement causing increasing load and moment. The point at which confinement is initiated is predicted well by the model. The initiation of confinement in specimen BC-E-e300 was not accompanied by a load drop in the test.

The experimental axial load-deflection behaviours of each specimen exhibit plastic behaviour near the end of the tests, beginning near the model predicted deflections at failure. Figures 5.49 to 5.52 indicate that the model predicts the peak moments and axial loads well, but the assumptions in its formulation do not

allow the plastic deformation stages to be predicted, causing under estimation of the deflections at failure.

#### 5.3.4 Comparing Behaviour Depending on Concrete Confinement Level

Model predicted behaviours assuming full confinement and no confinement of the concrete core are shown in Figures 5.28 to 5.52, along with model calculated behaviours assuming variable concrete confinement.

The predicted behaviours assuming full confinement of the concrete core in specimens BC-P-e10 and BC-P-e30, shown in Figures 5.28 to 5.31 are similar to the predictions using variable confinement. This occurs because the axial load eccentricities are small in these cases, causing the variable concrete confinement stress-strain curves to approach the upper bound full confinement concrete stress-strain curves. The axial loads and moments past the peak of the unconfined concrete relationships are slightly overestimated by assuming full confinement. The axial load and moments drop considerably after the peak when no confinement of the concrete core is assumed because the stress-strain behaviour of the concrete is not enhanced by confinement.

The bending moments and axial loads of specimen BC-P-e100 are overestimated past the peak of the unconfined concrete relationships when full confinement is assumed, compared to the behaviour determined using variable confinement, as shown in Figures 5.32 to 5.34. The behaviours modelled with

variable concrete confinement also match the slopes of the experimental results past the peak of the unconfined concrete relationships more accurately than when full confinement is assumed. Similarly, using the variable confinement model when predicting the behaviours of specimens BC-P-e200 and BC-P-e300 results in better predictions of the slopes of the experimental relationships past the peaks of the unconfined concrete relationships than when full confinement is assumed, as shown in Figures 5.35 to 5.40. Assuming unconfined concrete in each case causes a substantial drop in axial load and bending moment past the peak, and absence of the ductility predicted when variable or full confinement are used.

Similar observations are made when comparing experimental results and model predictions for specimens BC-E-e30, BC-E-e100, BC-E-e200, and BC-E-e300. In general, use of the variable concrete confinement model generates predicted behaviours that resemble the shapes of the experimental relationships better than when full confinement is assumed, as shown in Figures 5.41 to 5.52. The experimental behaviours are not modelled well when unconfined concrete cores are assumed.

### 5.3.5 Interaction Diagrams

Figure 5.53 shows predicted axial load-bending moment interaction diagrams for each type of beam-column, calculated with the specific dimensions, laminate structures, and concrete strengths of the experimental specimens. The

interaction diagrams represent failure envelopes calculated using the proposed analytical model. The beam-columns are capable of sustaining any combinations of applied axial load and bending moment that fall within the envelopes. Failure of the members would occur if combinations of axial load and bending moment outside the envelopes were applied.

The axial loads and bending moments at failure of the specimens tested in the experimental program are also plotted in Figure 5.53. Because the experimental results describing the behaviours of specimens BC-P-e10 and BC-P-e30 are not reliable, as discussed in section 5.3.3.1, behaviour past the peak axial loads was not considered representative of the behaviour expected if an ideal test setup was used. Therefore the peak axial load and corresponding bending moment, just prior to initiation of failure of the FRP shell, are plotted in Figure 5.53.

The predicted interaction diagrams agree reasonably well with the experimental results. As described in section 5.3.2, the predicted pure axial load capacity of the E-glass/epoxy FRP tube member is higher than observed in the pure axial load test, due to premature failure prior to achieving full confinement. The interaction diagrams are similar at high axial load eccentricities due to the similarity of the two types of specimens' flexural properties. However, the E-glass/epoxy tube members can sustain higher moments and axial loads than the E-glass/polyester tube members at low eccentricities because they have higher

hoop stiffnesses and lower hoop Poisson's ratios, allowing more significant concrete confinement to develop, enhancing member capacity.

#### 5.4 Parametric Study

A parametric study was performed to examine the effect of FRP shell wall thickness, FRP laminate structure, and concrete core compressive strength on the strength of concrete filled FRP tubes subjected to axial loads, bending moments, or combinations of axial load and bending moment. Three different laminate configurations were selected, 1:1, 1:9, and 9:1, representing balanced laminates with equal amounts of fibres in the longitudinal and circumferential directions, laminates with 10-percent of the fibres in the longitudinal and 90-percent in the circumferential directions, and laminates with 90-percent of the fibres in the longitudinal and 10-percent in the circumferential directions, respectively. The thicknesses of the tubes were 1-millimetre, 6-millimetres, or 10-millimetres. The unconfined concrete compressive strengths examined were 20-MPa, 60-MPa, or 100-MPa. The diameters of the concrete cores, equivalent to the internal diameters of the FRP shells, were kept constant at 300-millimetres in each case. E-glass fibre and polyester laminate compositions, similar to the E-glass/polyester tubes used in the experimental program, were assumed in the analysis. Changing one of the variables at a time yielded 27 cases. Interaction diagrams were established using the proposed analytical model for each case.

The results of the parametric study are presented in Figures 5.54 to 5.59, in two different ways for comparison. Each plot in Figures 5.54 to 5.56 compares three interaction diagrams determined by maintaining constant FRP tube laminate configurations and unconfined concrete compressive strengths, while varying tube wall thicknesses. Figures 5.57 to 5.59 show the same interaction diagrams, but grouped by maintaining constant FRP tube wall thicknesses and unconfined concrete compressive strengths, while varying FRP tube laminate configurations.

Figures 5.54 to 5.56 demonstrate that axial load and bending moment capacities of the members increase with increasing FRP tube wall thickness, for given laminate configurations and concrete strengths. The increase in bending moment capacity is most prominent with the 9:1 laminates, as shown in Figure 5.56, because these laminates provide the most fibres in the longitudinal direction, maximizing the contribution of the shell to the bending moment. The bending moment capacity is highly sensitive to tube thickness in this case because of the shell's significant contribution to moment, especially at low axial loads. The 1:9 laminate members exhibit the smallest increases in bending moment capacities with increasing tube thickness for given concrete strengths at low axial loads because they have a small proportion of fibres oriented longitudinally. The 1-millimetre thick tubes demonstrate increasing axial load capacity with decreasing eccentricity to a peak, followed by decreasing axial load capacity as eccentricities approach zero, the pure axial load case, for 60 and 100-MPa concrete strengths. This phenomenon occurs because the concrete core contributes the majority of

the axial load capacity at high concrete strengths. The thin shell provides little confinement, causing a significant drop in concrete compressive stress when the axial strain reaches the peak unconfined concrete strength, as shown in Figure 5.60. Figure 5.60 compares the full confinement axial compressive stress-strain relationships for a 300-millimetre inside diameter 1:1 laminate tube with 1 or 10-millimetre wall thicknesses and 20 or 60-MPa unconfined concrete compressive strengths, showing the large post-peak drops in stress with small tube thicknesses and continuously increasing stresses with large tube thicknesses. When the member is subjected to axial loads at low eccentricities, the axial compressive strains significantly exceed the strains at the peak stress, causing the total axial load to decrease compared to a case when the axial load is applied at a higher eccentricity where the variable axial strains across the depth of the section may be near or at the strain at the peak concrete stress, maximizing the total axial load. This effect is not as significant at low unconfined concrete strengths because the peak strain is not followed by as sharp a drop in compressive stress, as shown in Figure 5.60. The compressive stress in the shell also contributes a larger proportion of the total axial load when the concrete strength is low, and increases with increasing axial strain, mitigating the effect of decreasing concrete stress past the peak stress. The drop in axial load carrying capacity at low eccentricities does not occur for members with higher FRP tube thicknesses because larger confinement effects occur, reducing or eliminating the decrease in compressive stress past the peak unconfined concrete stress, as shown in Figure 5.60.

Most of the modelled members' interaction diagrams are shaped similar to conventional reinforced concrete column interaction diagrams. Bending moment capacities initially increase when axial loads increase from zero, reach a peak, and begin decreasing towards pure axial load. The increasing moment portion of each curve is characterized by tensile failures of the members, and the decreasing moment portion by compression failures, as observed in the beam-column experiments reported in Chapter 4. The transition point, referred to as the balanced point, theoretically occurs when a member fails in compression and tension simultaneously. Some of the predicted interaction diagrams do not have a balanced point because the moment capacity decreases continuously with increasing axial load. This occurs in cases where a large proportion of fibres is oriented longitudinally, the concrete strength is relatively low, and the thickness of the tube is relatively high. In these cases the FRP tube sustains a significant proportion of the axial compressive stress in the internal moment couple because the tube is relatively stiff compared to low-strength concrete in the compression zone. This causes failure of the laminate at the compression side before the full tensile capacity is developed. This does not occur in the 1:9 laminate members because high proportions of fibres in the hoop direction reduce the axial stiffness of the FRP tubes, causing the majority of the internal compression force due to bending to be developed in the concrete in the compression zone, preventing premature failure of the tube at the compression side at low axial loads.



Figures 5.54 to 5.56 also demonstrate that increasing the concrete strength for given laminate configurations and tube thicknesses increases the moment and axial load capacities. Higher concrete strengths allow higher stresses to develop in the concrete in the compression zone due to higher stiffness and increased compressive strain at the peak unconfined stress. Higher concrete stresses yield higher total axial loads and increase the compressive force in the internal moment couple, increasing the bending moment.

Figure 5.57 shows interaction diagrams for the three different laminate configurations and concrete strengths studied, with 1-millimetre shell thicknesses. The 9:1 laminate members have the largest bending moment capacities at low axial loads for each concrete strength due to the high proportion of fibres in the longitudinal direction. The 1:9 laminate members have the smallest bending moment capacities at low axial loads due to the relatively small proportion of fibres in the longitudinal direction. The trend reverses near the balanced points because more compression in the concrete begins to develop at higher axial loads, and the 1:9 laminate becomes the most effective because it provides the highest degree of confinement to the concrete in the compression zone, improving the axial load and bending moment capacities of the members by enhancing the load carrying capacity of the concrete.

Figures 5.58 and 5.59 also demonstrate that increasing the proportion of fibres in the longitudinal direction increases the bending moment capacity at low axial loads. It would be expected that the axial load capacity would decrease with a

decreasing proportion of fibres in the hoop direction due to decreasing confinement. However, Figures 5.58 and 5.59 show that the axial load capacity remains approximately the same or decreases for thick FRP shells with low-strength concrete cores, as the proportion of fibres in the hoop direction decreases. This occurs because the decrease in concrete stress due to decreased confinement of the concrete core as more fibres are oriented in the longitudinal direction is overcome by the increase in stiffness of the FRP tube in the axial direction as the proportion of hoop fibres decreases and the proportion of fibres in the longitudinal direction increases. The overall stiffness of the cross-section remains constant or increases, causing equivalent or increased member axial load carrying capacity. This phenomenon is only expected in cases where the member diameter-to-FRP tube thickness ratio is high, concrete strength is low, and the tube is stiff axially, resulting in a high contributions to member axial stiffness from the tube.

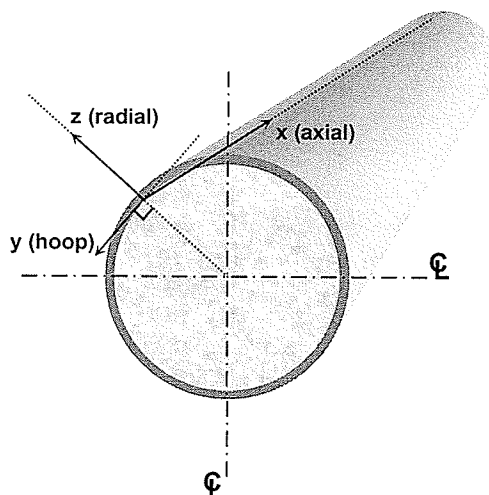
There are many possible combinations of FRP tube laminate structure, member diameter, concrete core strength, and FRP tube thickness that can satisfy the strength requirements of a specific application. Design of concrete filled FRP tube members can be optimized by determining the relative magnitudes of bending moments and axial loads expected on the member in a particular application. In most cases, laminates with larger proportions of fibres in the axial direction for a given tube wall thickness are optimal for high axial load and low bending moment cases, whereas laminates with most of the fibres oriented in the

longitudinal direction should be used for low bending moment and high axial load cases. Optimization can also be performed by varying the FRP tube wall thickness and concrete strength simultaneously. This is demonstrated in Figure 5.61, which shows the interaction diagrams for a 1:1 laminate FRP tube with various thicknesses and concrete strengths. It is advantageous to reduce the FRP wall thickness and increase the concrete compressive strength for some axial load eccentricities. For example, for the 20-millimetre axial load eccentricity shown in Figure 5.61, the following relationships are observed:

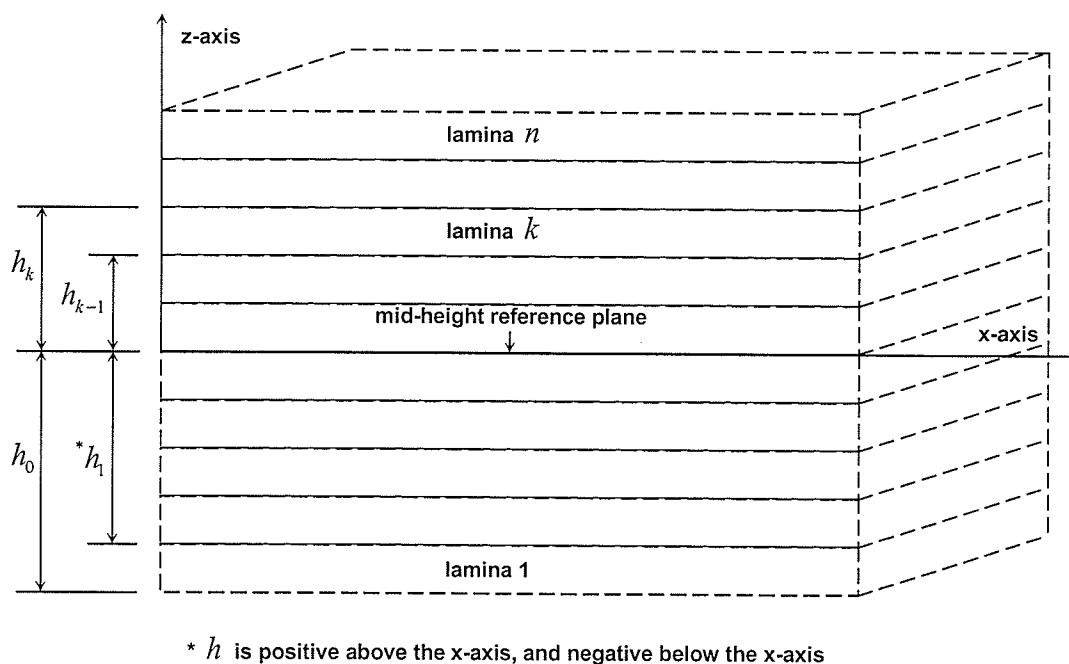
1. The axial load and bending moment capacities of a member with a 1-millimetre wall thickness and concrete strength of 60-MPa are higher than a member with a 6-millimetre wall and 20-MPa concrete.
2. The axial load and bending moment capacities of a member with a 1-millimetre thick wall and 100-MPa concrete are similar to a member with a 6-millimetre wall thickness and 60 MPa-concrete. However, both are an improvement over a member with a 10-millimetre thick shell and 20-MPa concrete.
3. The axial load and bending moment capacities of a member with a 6-millimetre thick wall and 100-MPa concrete are higher than a member with a 10-millimetre thick wall and 60-MPa concrete.

Similar relationships can be established for other eccentricities and other laminate structures. Relationships like these could significantly impact construction expenses because it may be more cost effective to use thinner

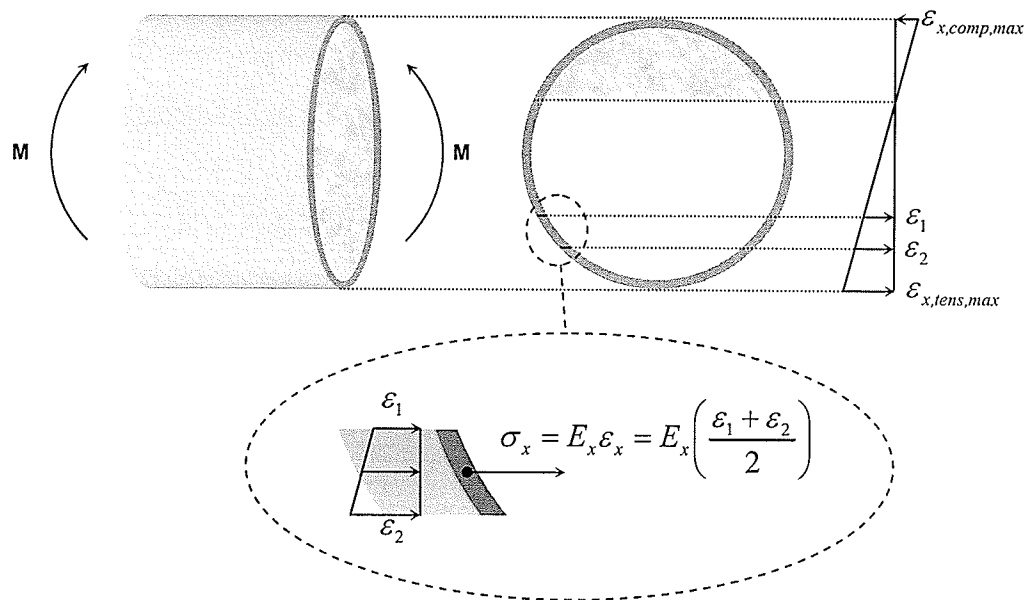
shells and higher concrete strengths. Decreasing the thickness of the FRP shells would substantially reduce the cost because significantly less material and manufacturing time would be required, while a relatively small premium would be associated with increasing the concrete strength. Overall member costs could be drastically reduced because the majority of the total cost is due to manufacturing and supply of the FRP shell. Only a small portion of the total cost is due to concrete material cost.



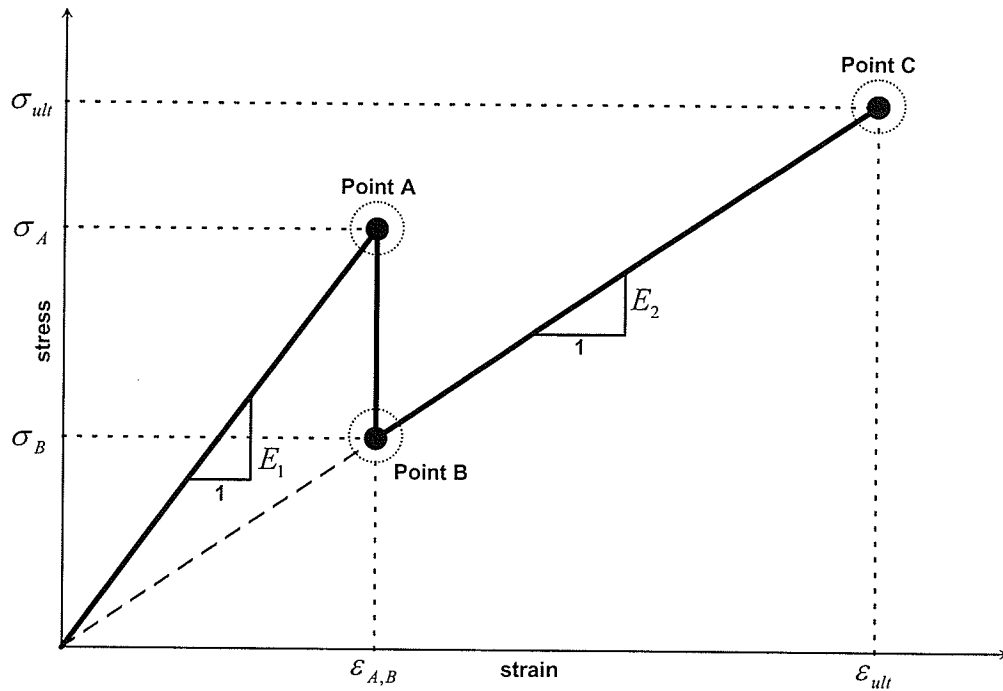
**Figure 5.1:** Laminate global coordinate axes with respect to concrete filled FRP tube member geometry.



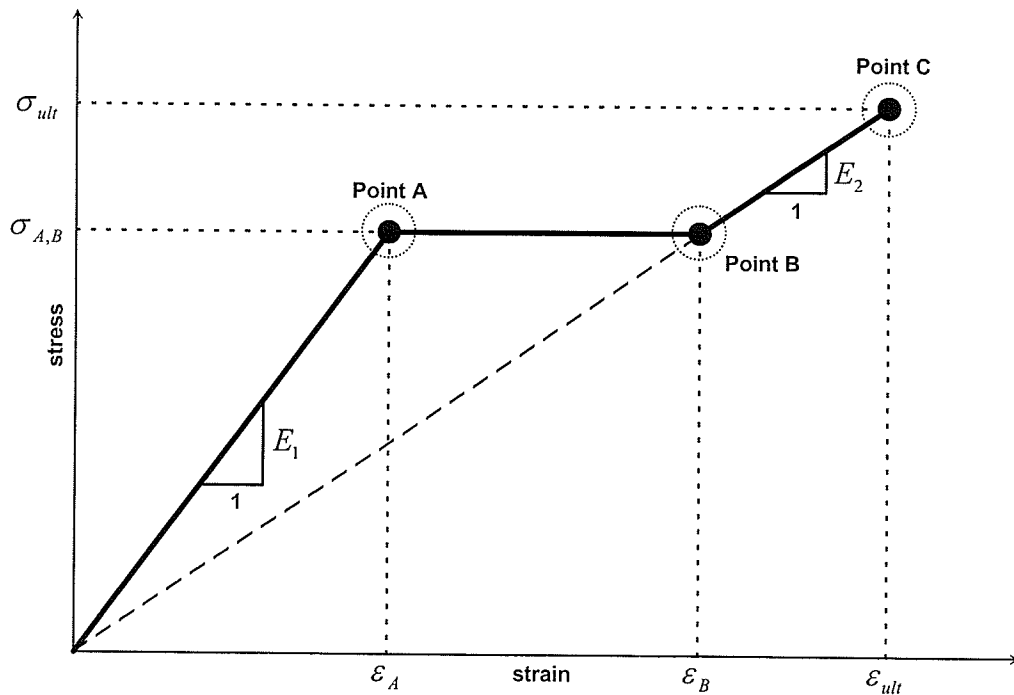
**Figure 5.2:** Laminate geometry for calculating the laminate stiffness matrix.



**Figure 5.3:** Uniaxial tensile stress at the tension side of an FRP shell of a concrete filled FRP tube member subjected to bending moment.

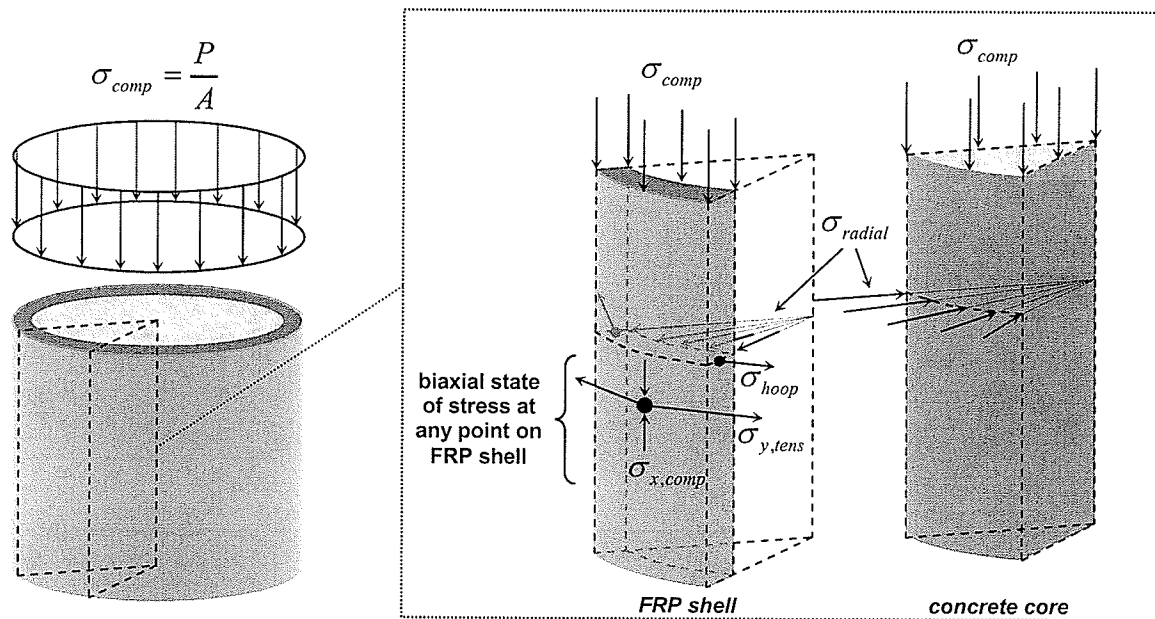


(a) Uniaxial stress-strain relationship for a laminate subjected to displacement controlled loading.

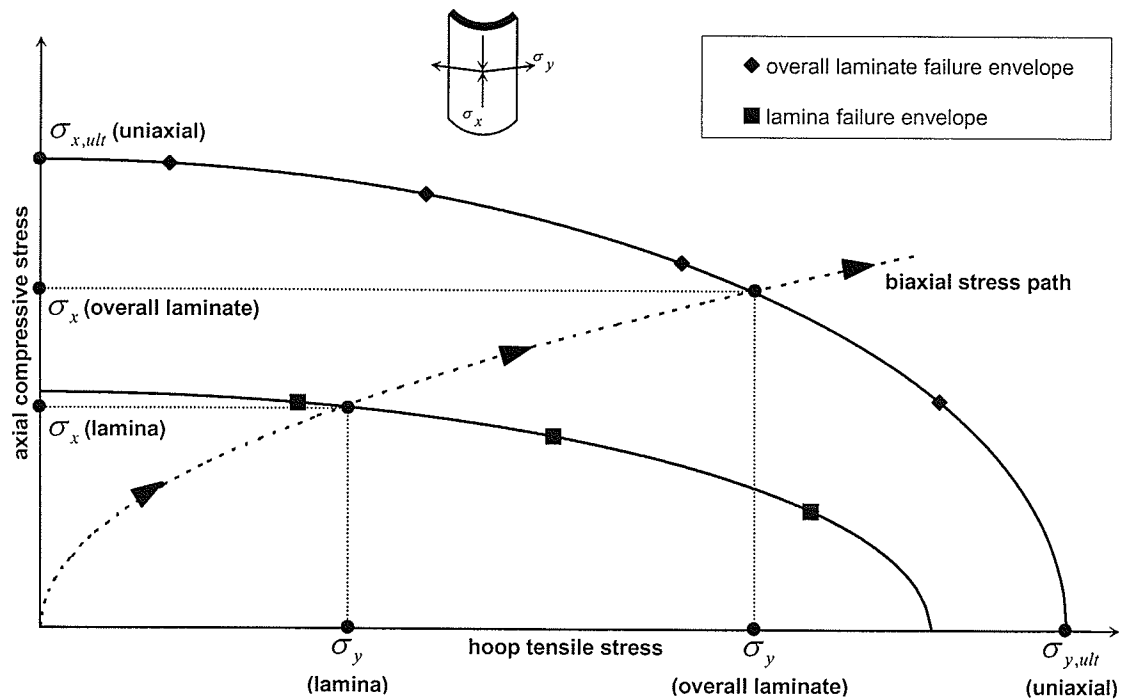


(b) Uniaxial stress-strain relationship for a laminate subjected to load controlled loading.

**Figure 5.4:** Uniaxial multilinear stress-strain relationships for a general FRP laminate with two laminas.

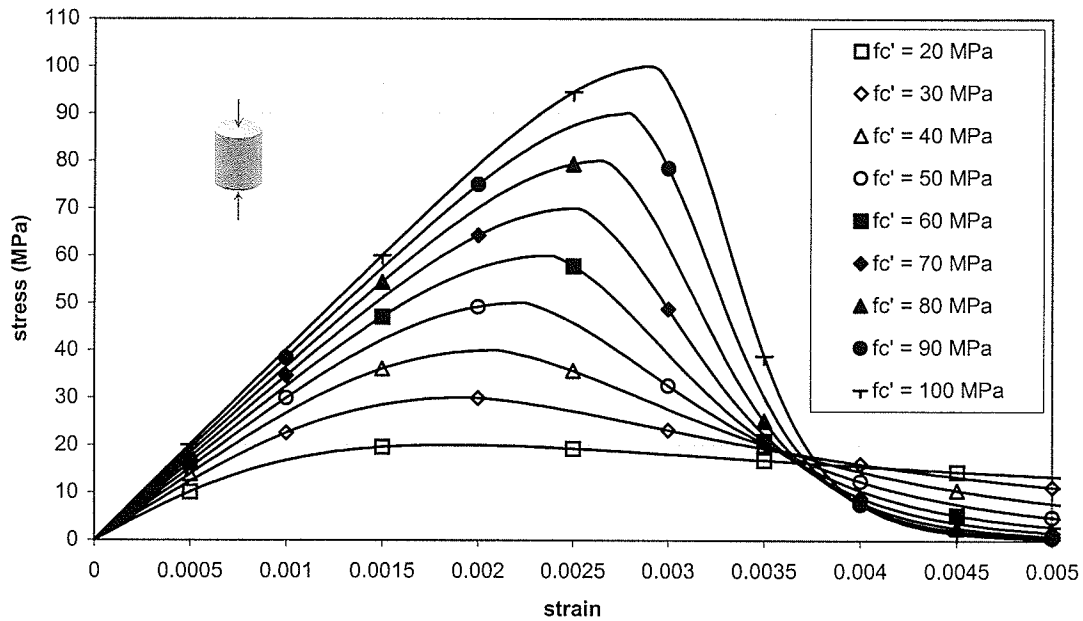


**Figure 5.5:** Biaxial state of stress on an FRP shell of a concrete filled FRP tube member subjected to an axial load.

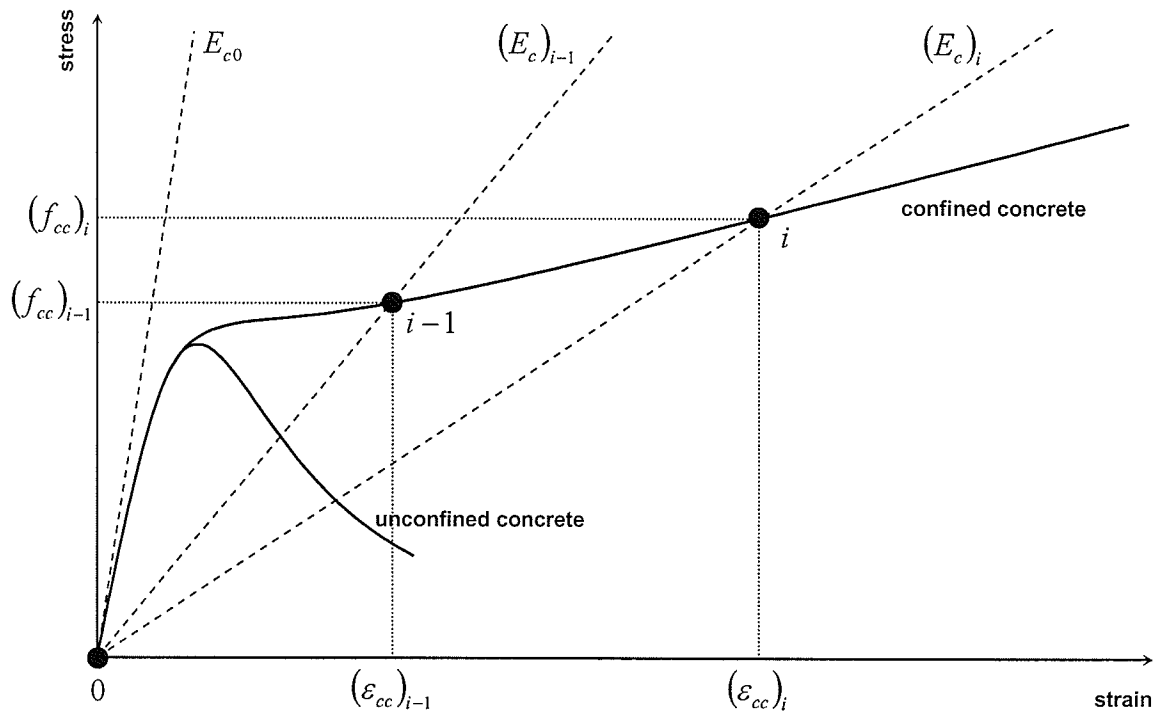


**Figure 5.6:** Lamina and overall laminate biaxial strength envelopes.

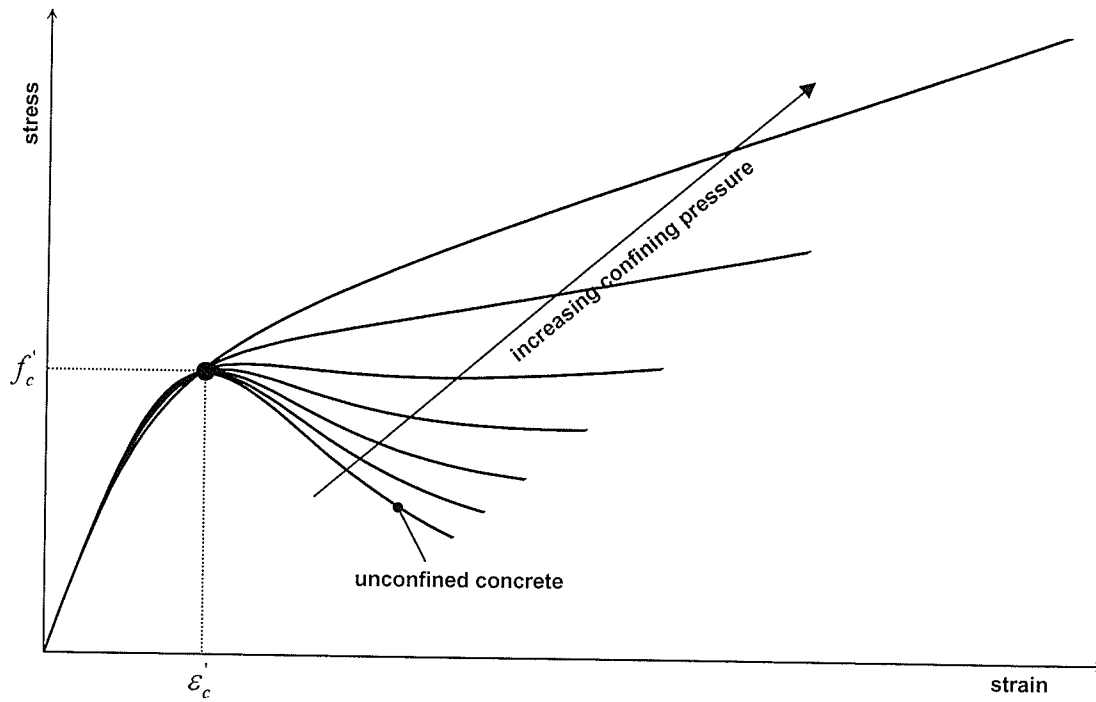




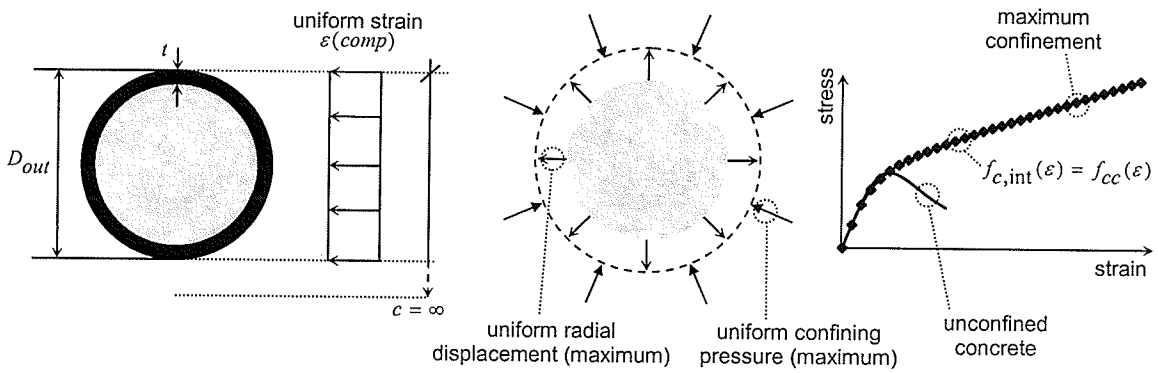
**Figure 5.7:** Unconfined concrete stress-strain curves established using Thornfeldt, Tomaszewicz, and Jensen's model.



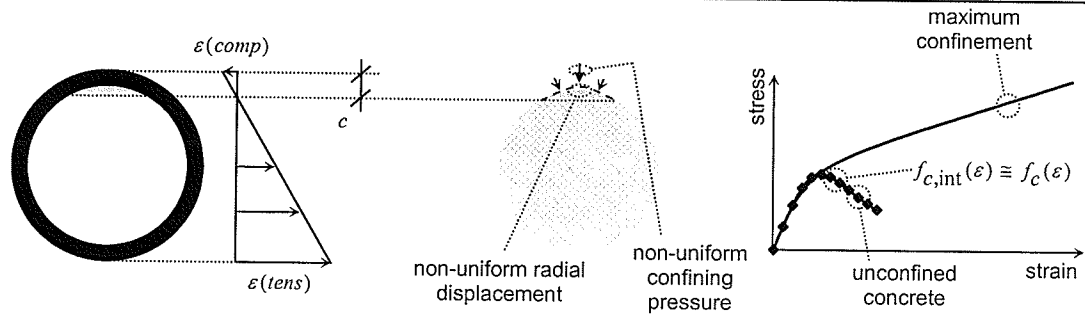
**Figure 5.8:** Determining confined concrete elastic modulus during application of Fam and Rizkalla's variable confinement model.



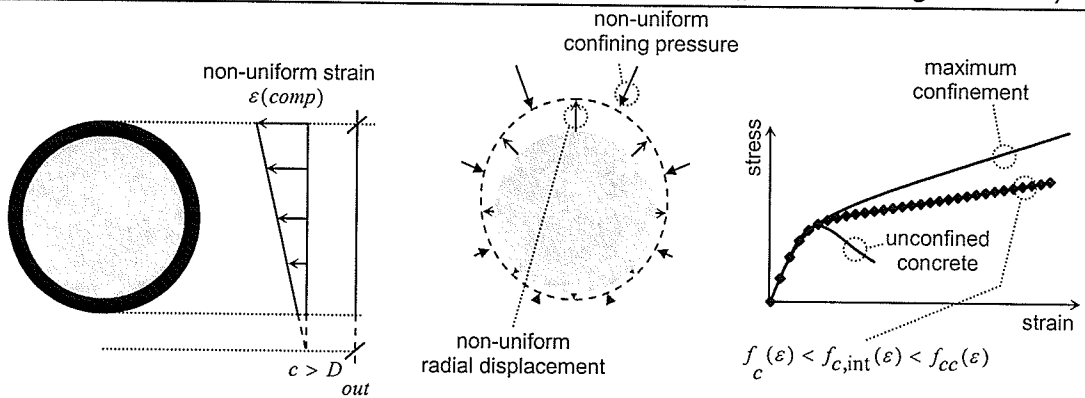
**Figure 5.9:** Confined concrete stress-strain relationships for a range of confining pressures, determined using Fam and Rizkalla's variable confinement model.



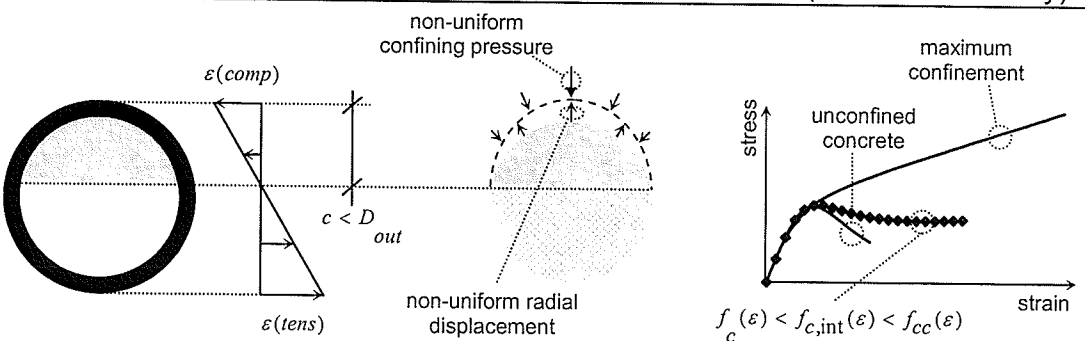
(a) Upper bound when eccentricity is 0 (pure axial load).



(b) Lower bound when axial load eccentricity is infinite (pure bending moment).



(c) Neutral axis depth greater than diameter of cross-section (small eccentricity).



(d) Neutral axis depth within limits of cross-section (large eccentricity).

**Figure 5.10:** Concrete stress-strain relationships from the intermediate confinement model for a variety of axial load eccentricities.

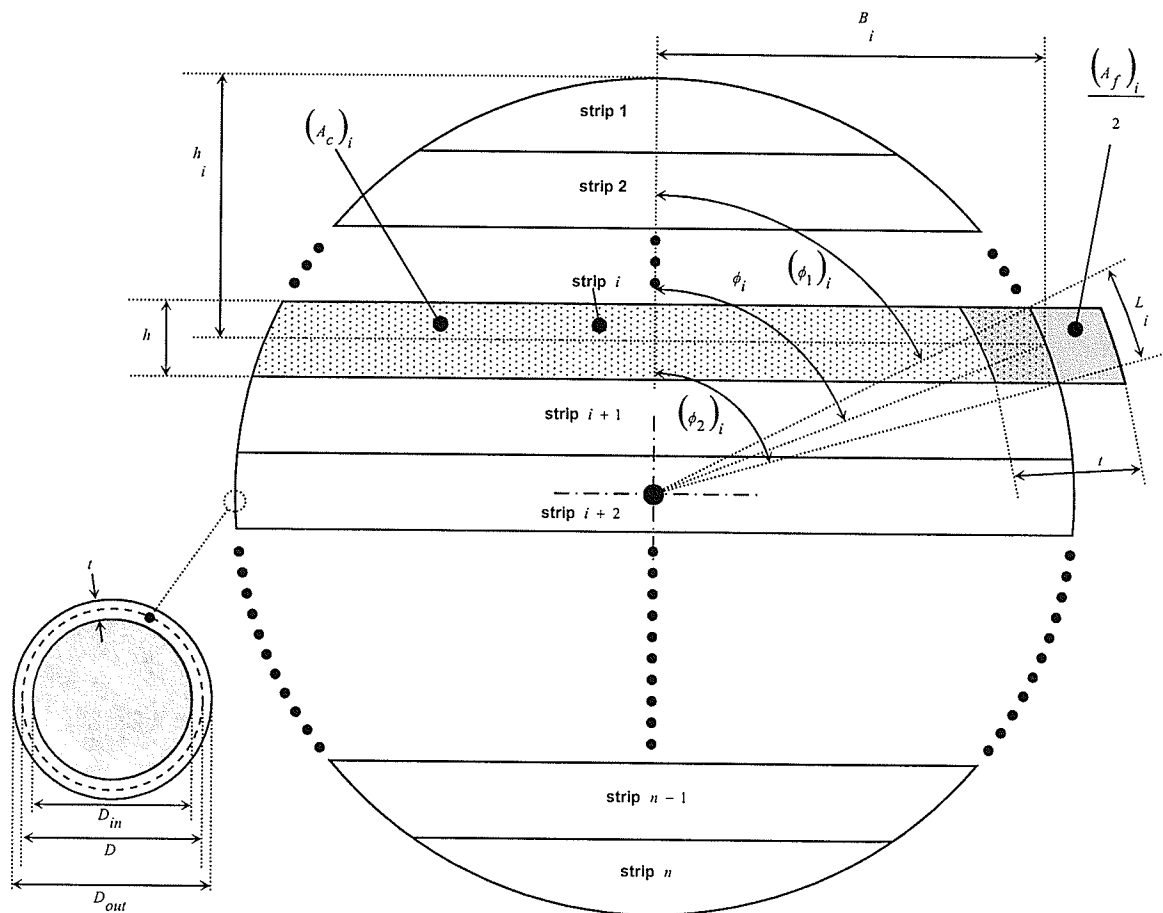


Figure 5.11: Cross-section equilibrium analysis geometry.

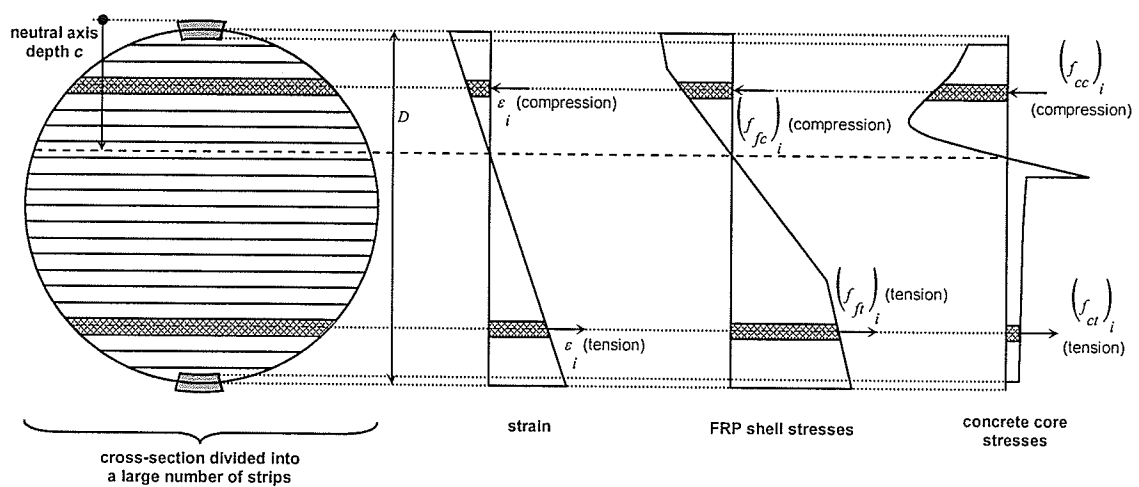
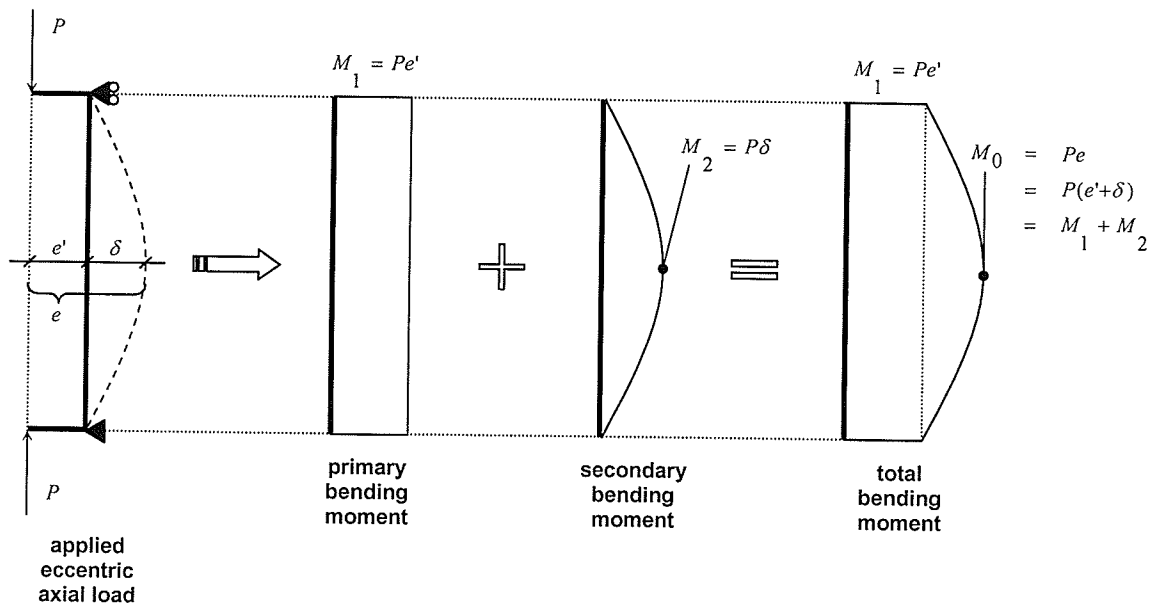
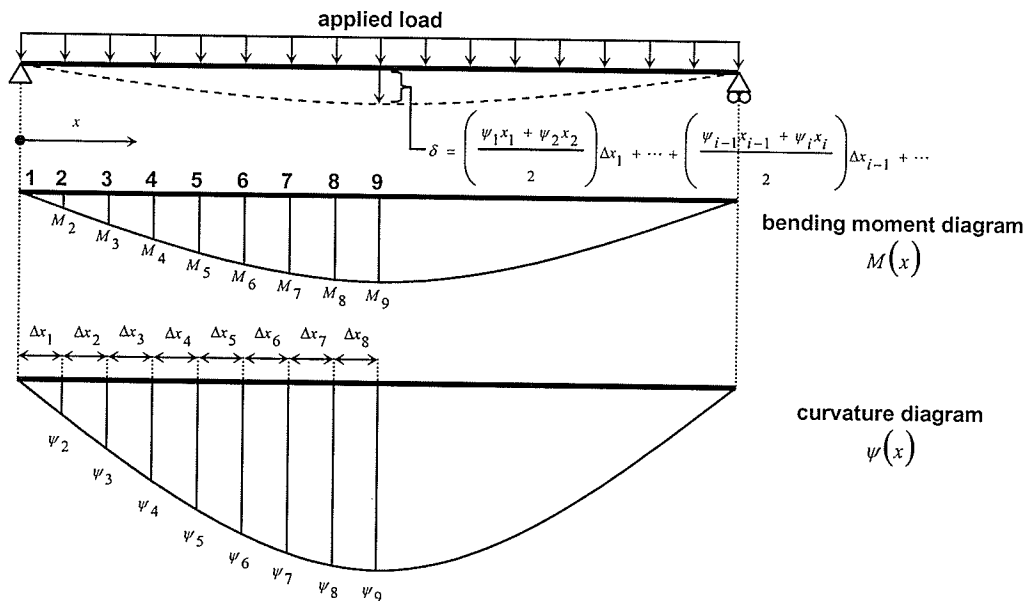


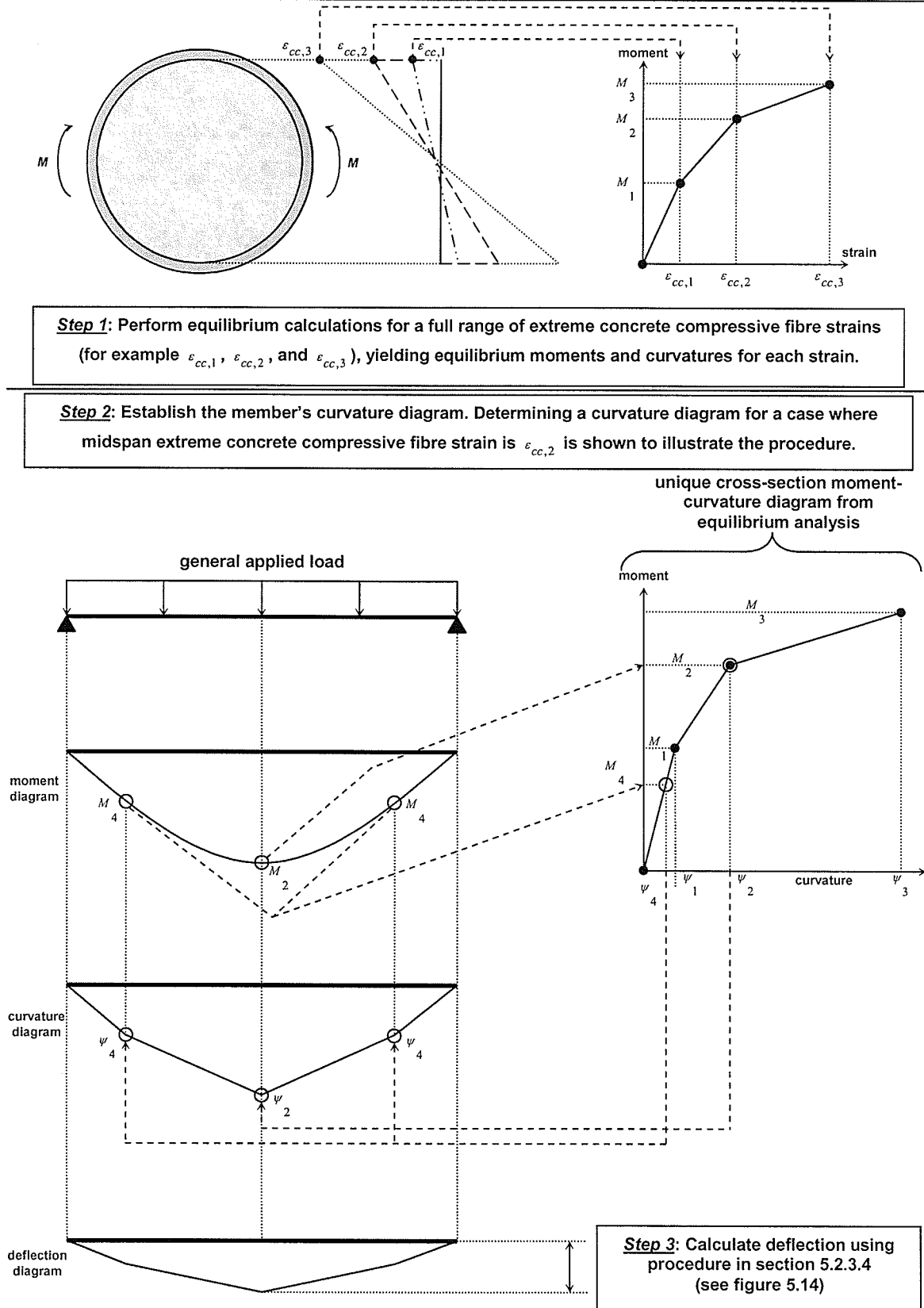
Figure 5.12: Cross-section axial compressive and tensile strains and stresses due to a general combination of applied axial load and bending moment.



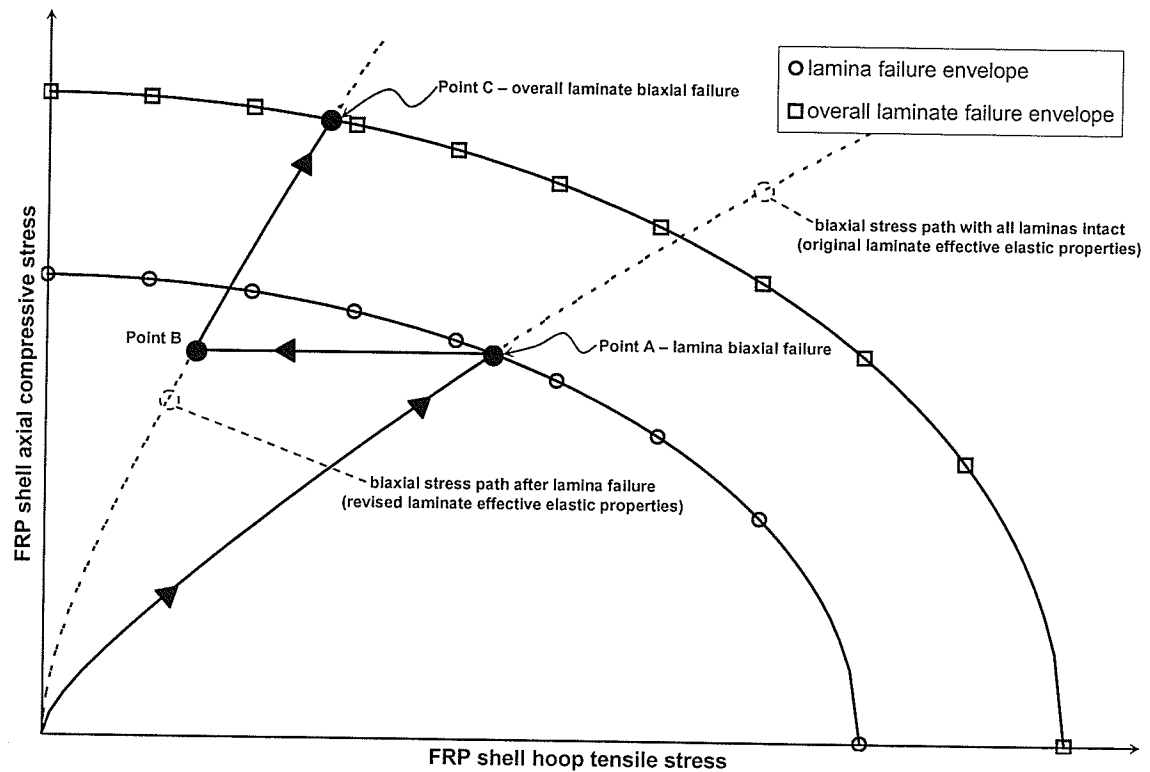
**Figure 5.13:** Calculating the applied bending moment on a member subjected to an eccentric axial load.



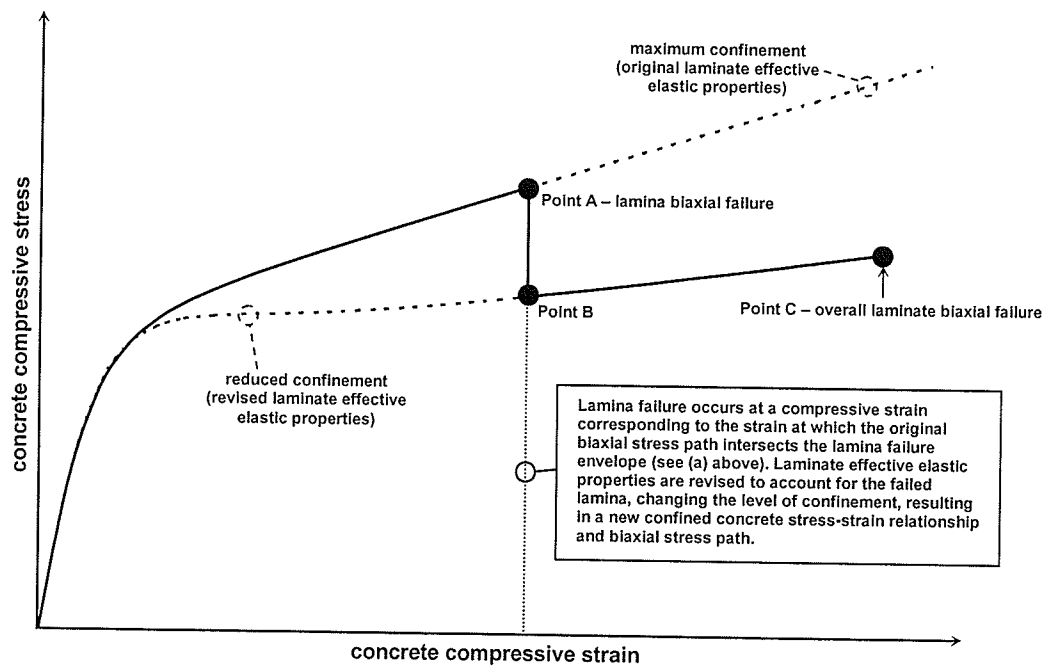
**Figure 5.14:** Numerical integration of the curvature diagram to calculate deflection of a member subjected to bending moment.



**Figure 5.15:** Calculating the member curvature diagram for use in cross-section deflection calculations.

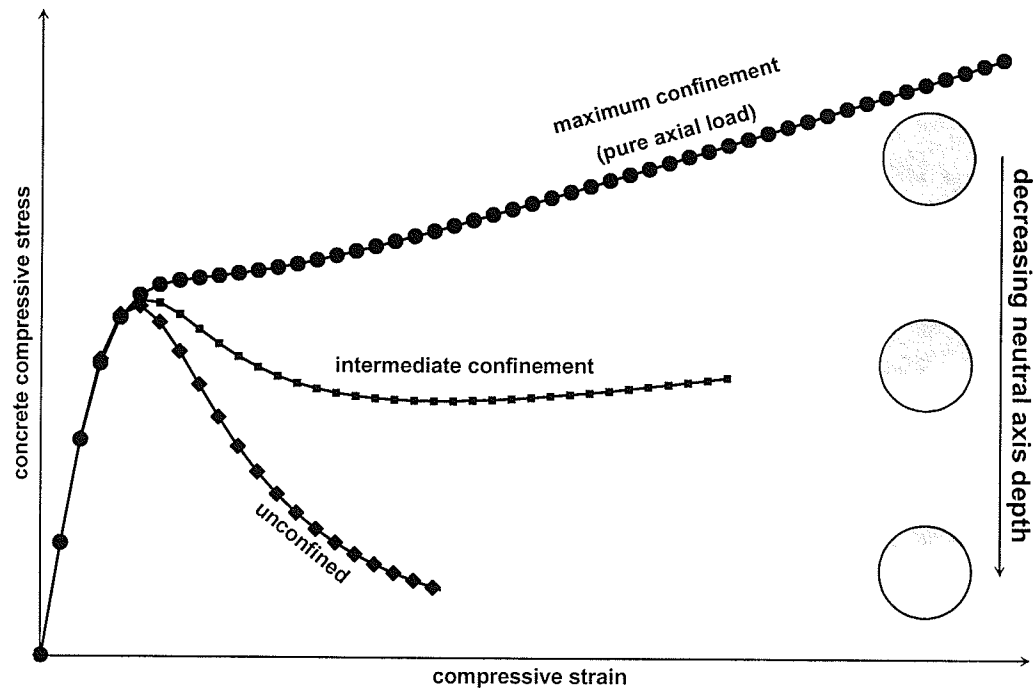


(a) Using lamina and overall laminate strength envelopes and laminate biaxial stress paths to detect failure.

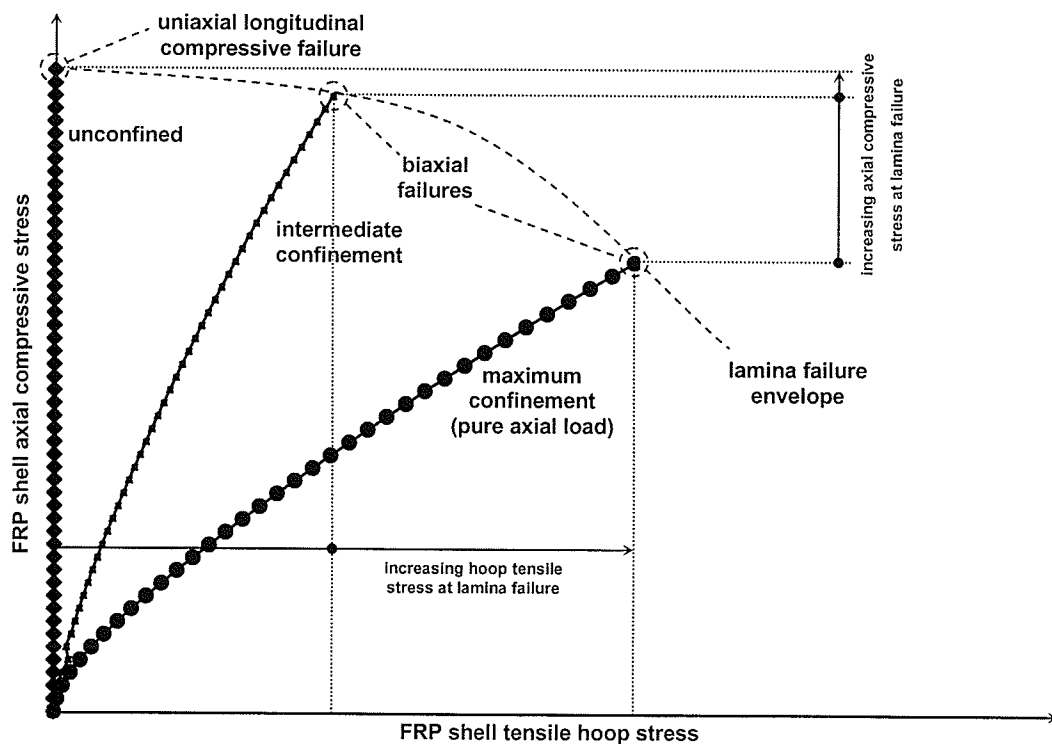


(b) Reducing the confinement effect due to changes in laminate effective elastic properties when individual laminas fail.

**Figure 5.16:** Detecting lamina and overall laminate failures in the compression zone of concrete filled FRP tube members subjected to pure axial load, pure bending moment, or combined axial load and bending moment.



(a) Concrete stress-strain relationships for various levels of confinement.



(b) Biaxial stress paths for various levels of confinement.

**Figure 5.17:** Effect of level of confinement on FRP shell biaxial stress paths and biaxial stresses at lamina failure in the compression zone.



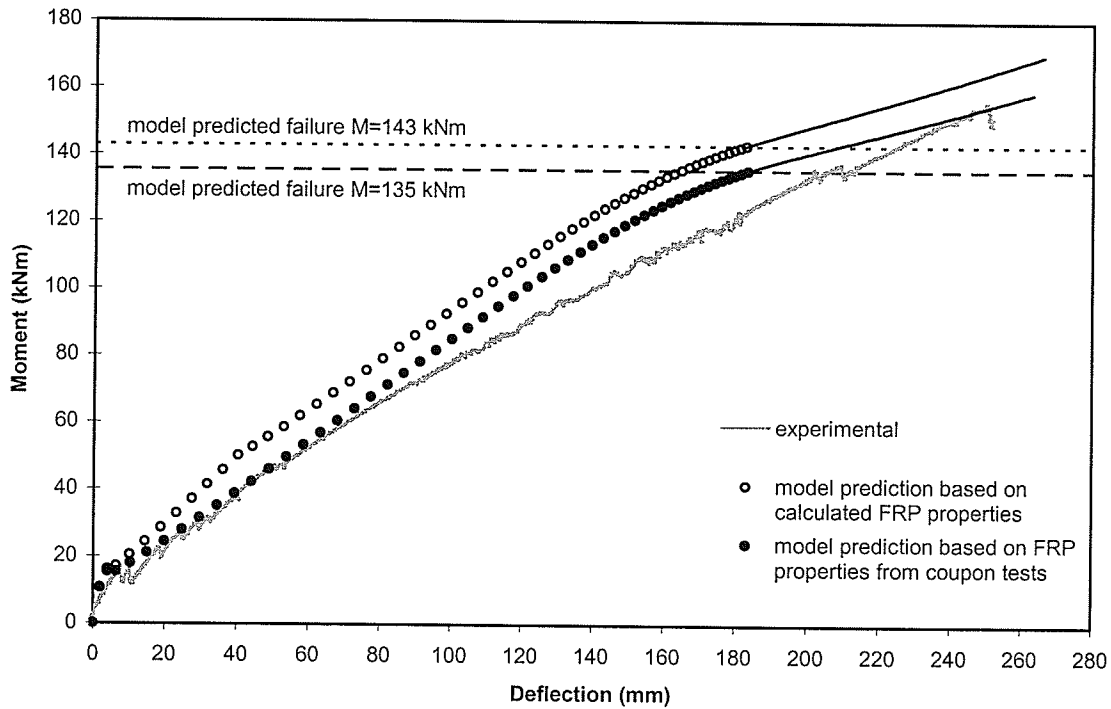


Figure 5.18: Model predicted moment-deflection behaviour of beam specimen BM-E-1.

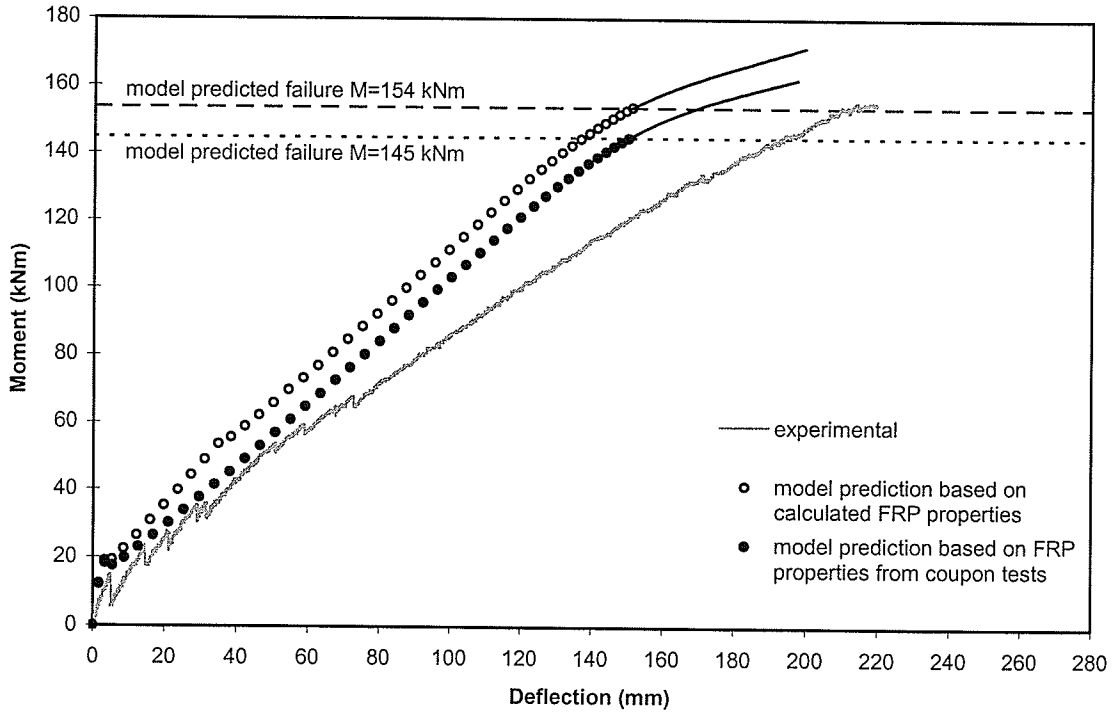


Figure 5.19: Model predicted moment-deflection behaviour of beam specimen BM-E-2.

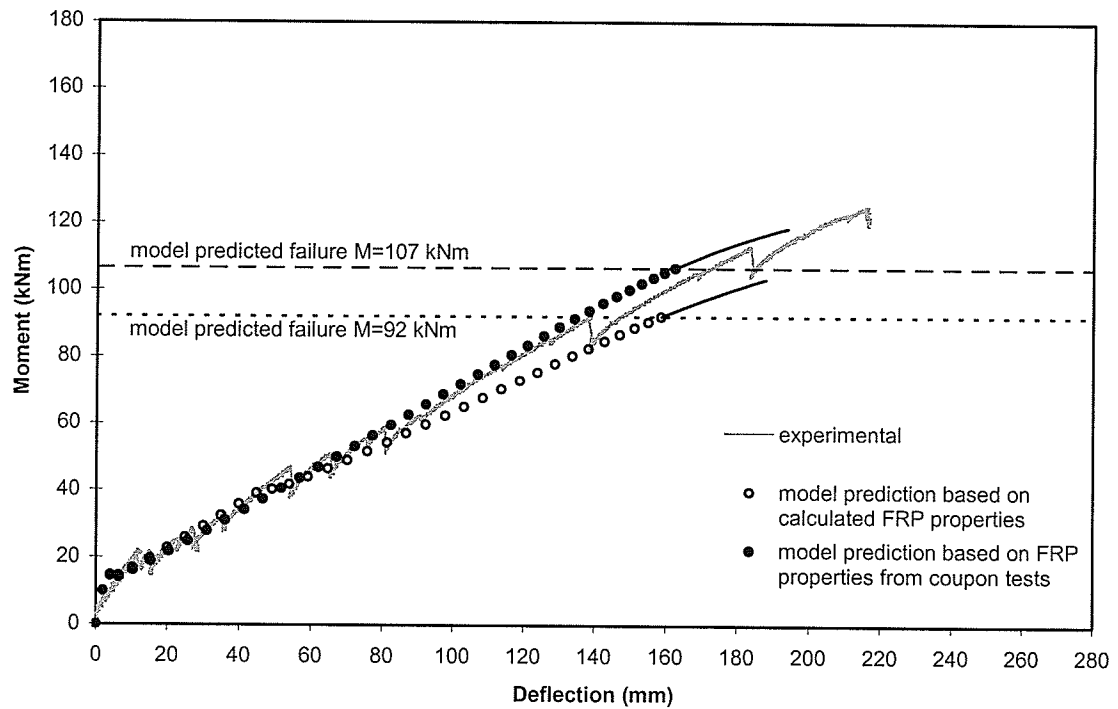


Figure 5.20: Model predicted moment-deflection behaviour of beam specimen BM-P-1.

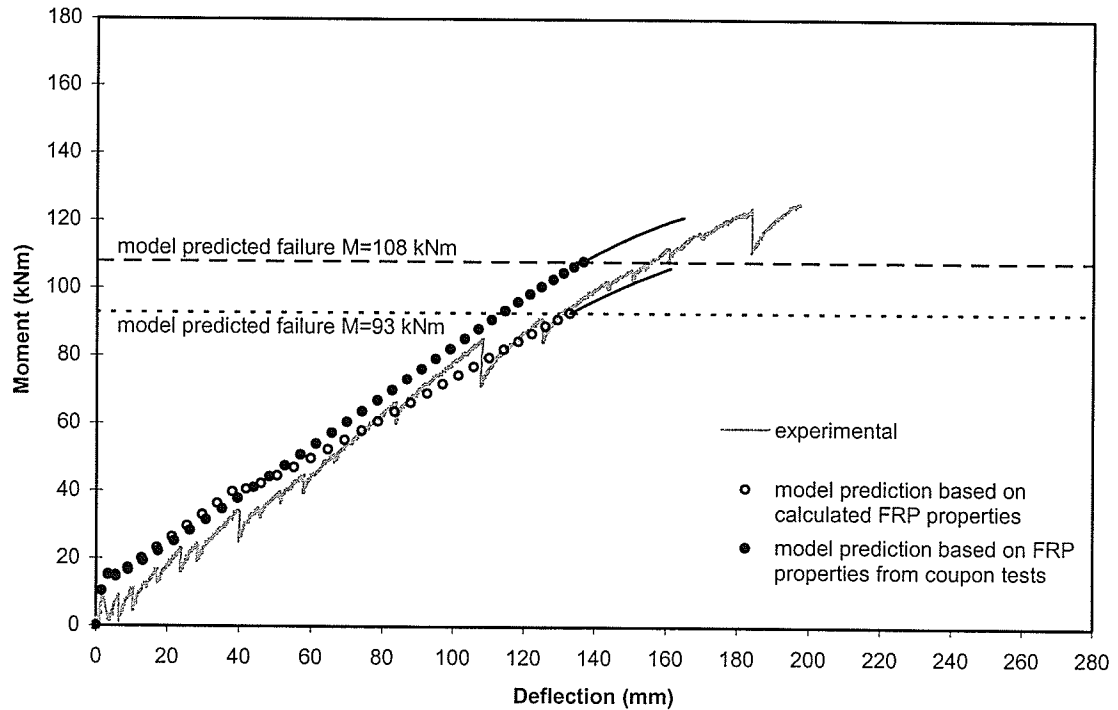
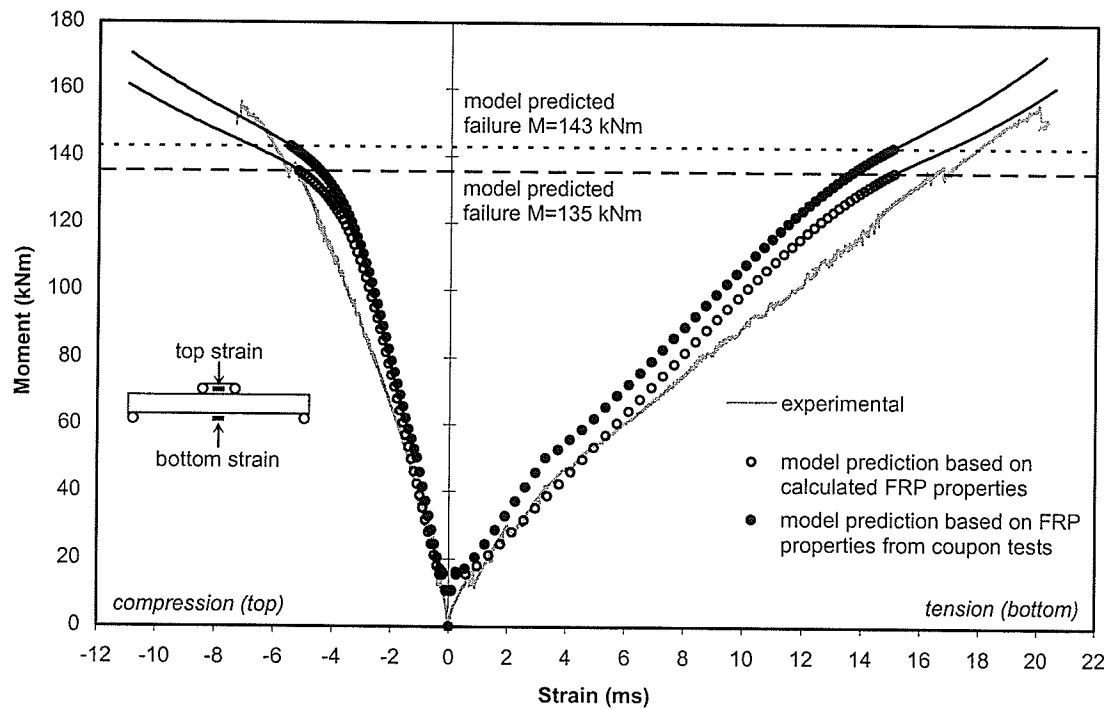
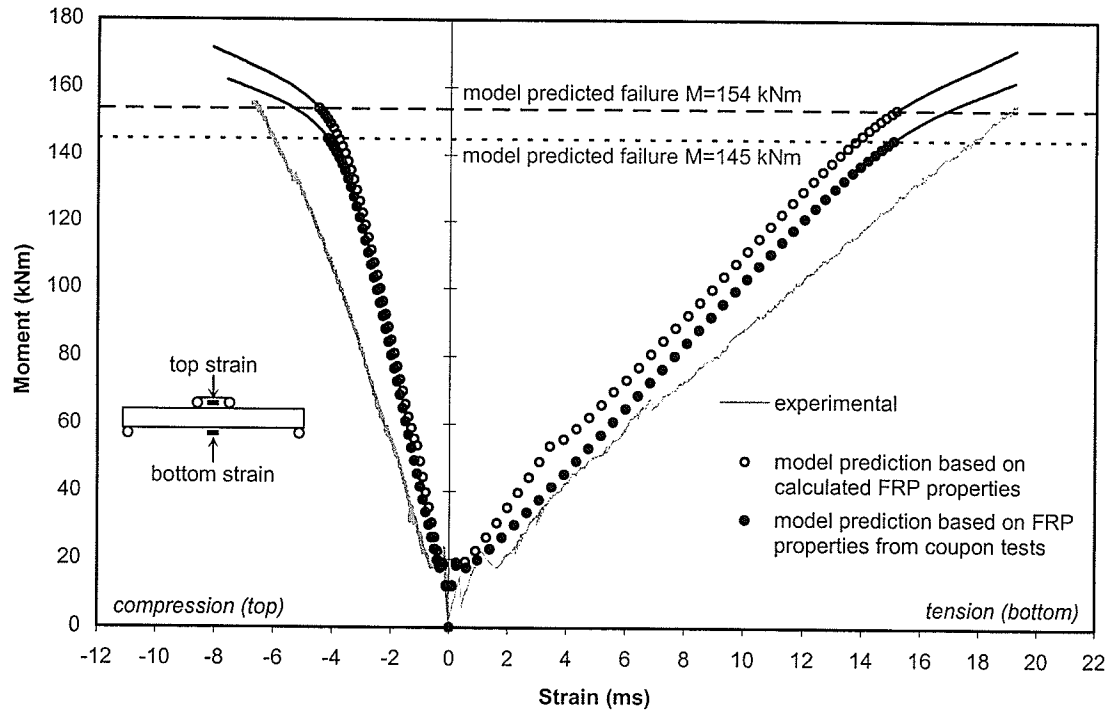


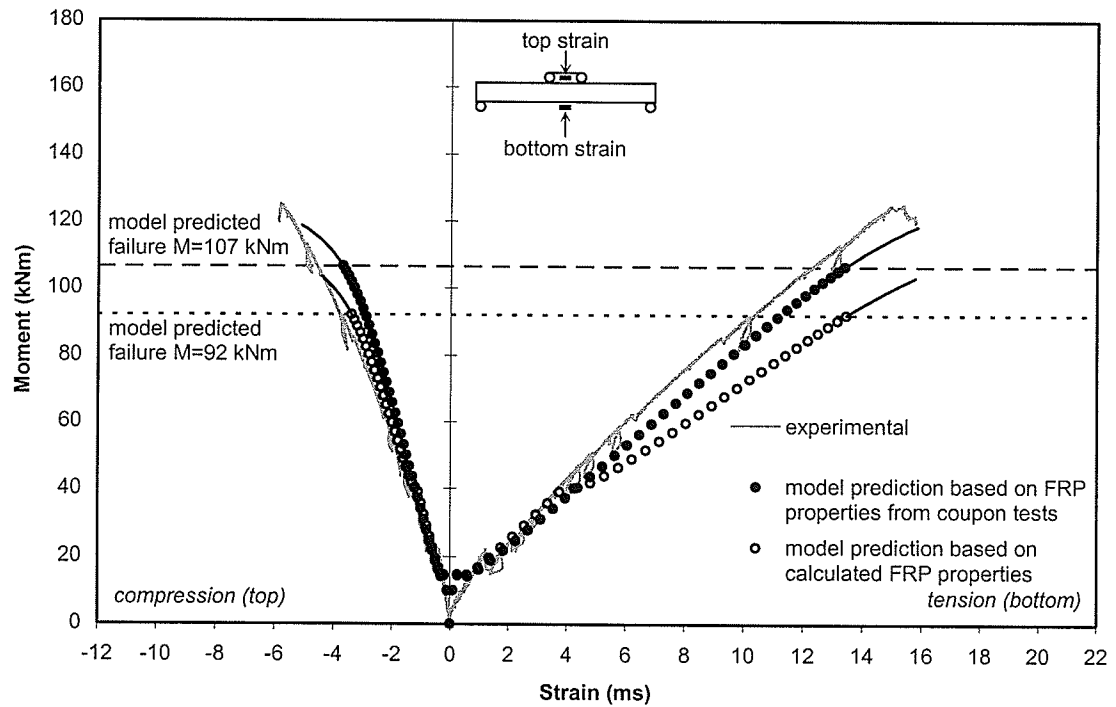
Figure 5.21: Model predicted moment-deflection behaviour of beam specimen BM-P-2.



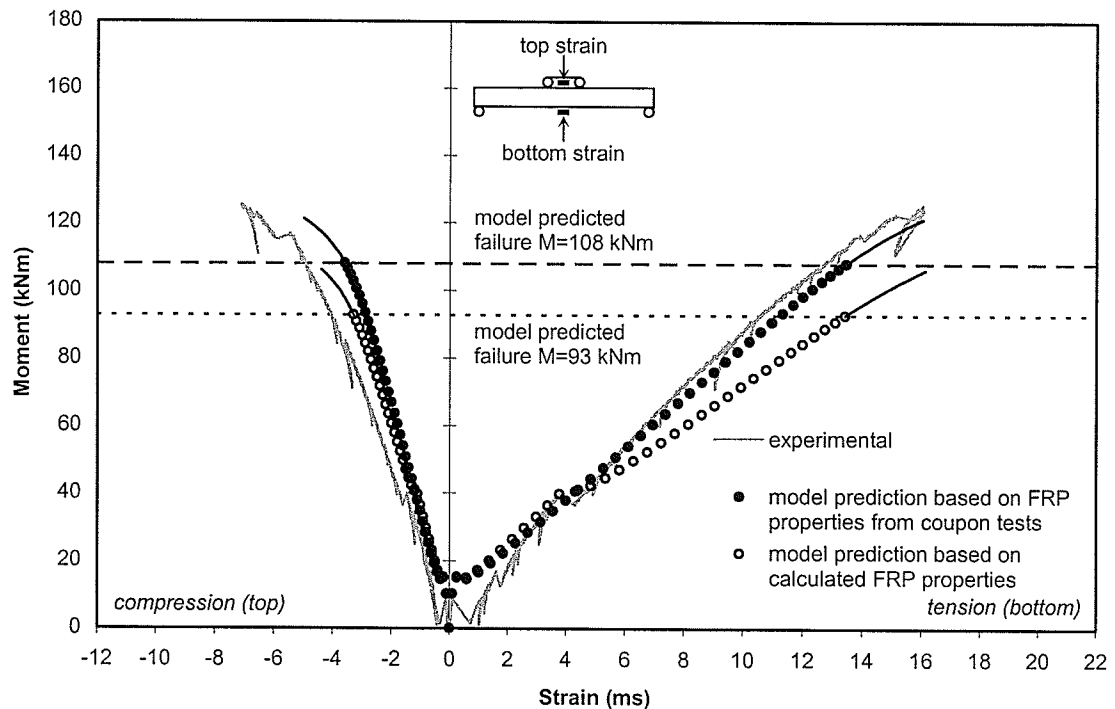
**Figure 5.22:** Predicted moment-axial strain behaviour of beam specimen BM-E-1.



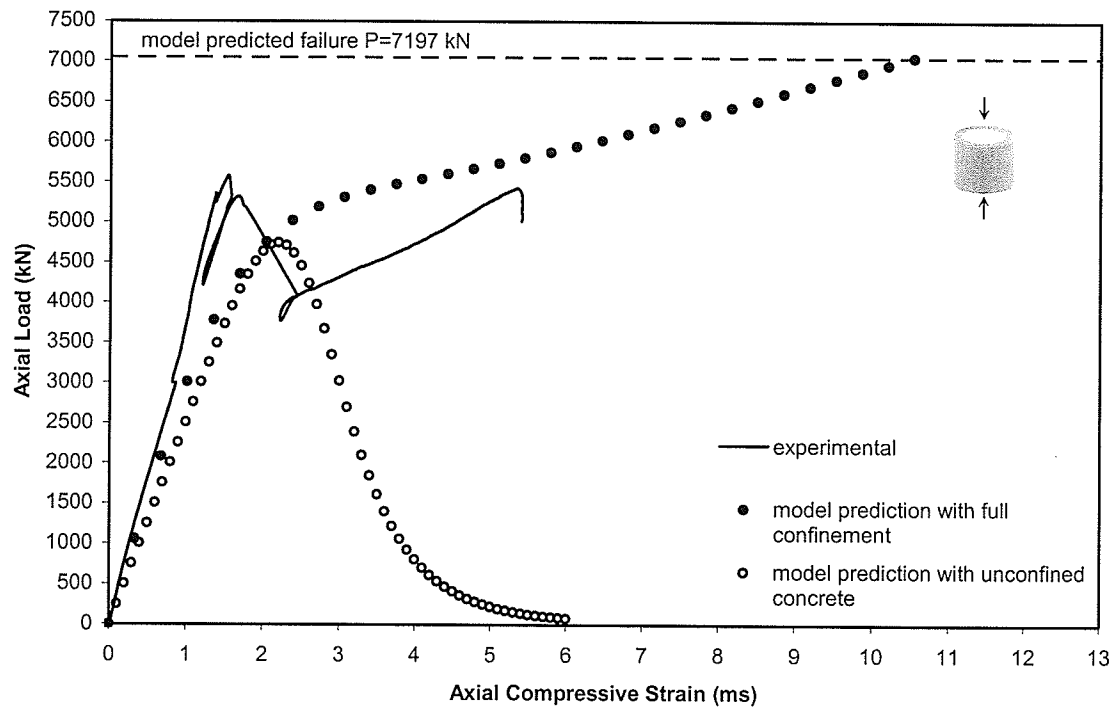
**Figure 5.23:** Predicted moment-axial strain behaviour of beam specimen BM-E-2.



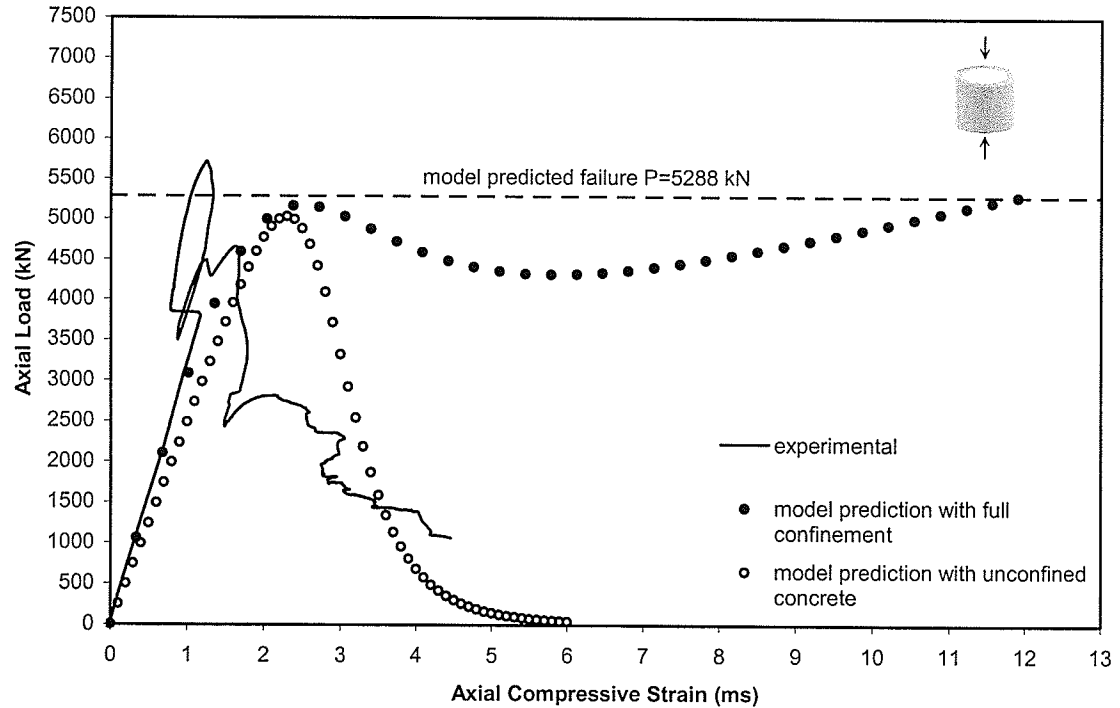
**Figure 5.24:** Predicted moment-axial strain behaviour of beam specimen BM-P-1.



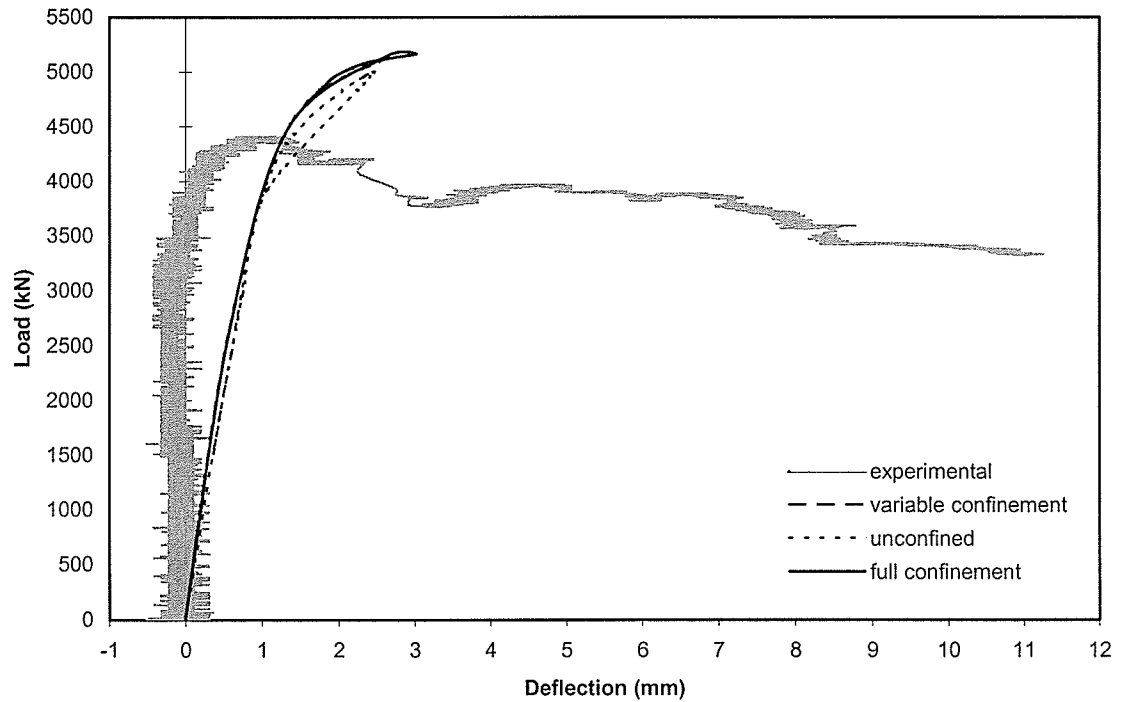
**Figure 5.25:** Predicted moment-axial strain behaviour of beam specimen BM-P-2.



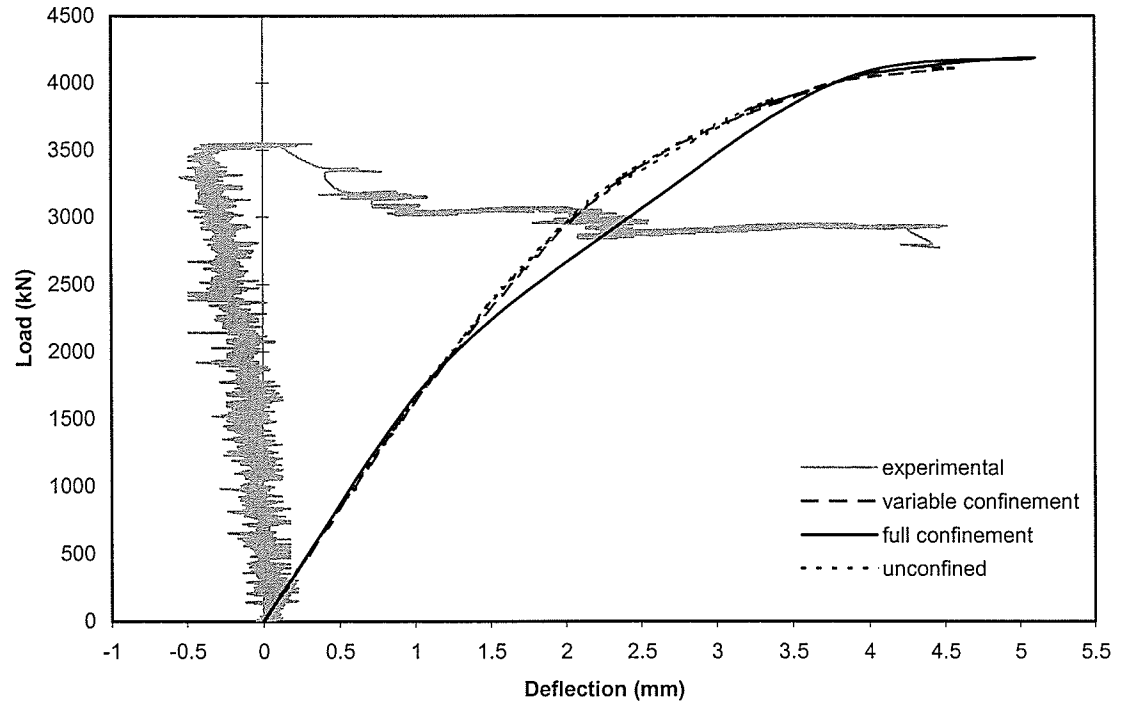
**Figure 5.26:** Model predicted axial load-axial strain behaviour of E-glass/epoxy shell pure axial load specimen.



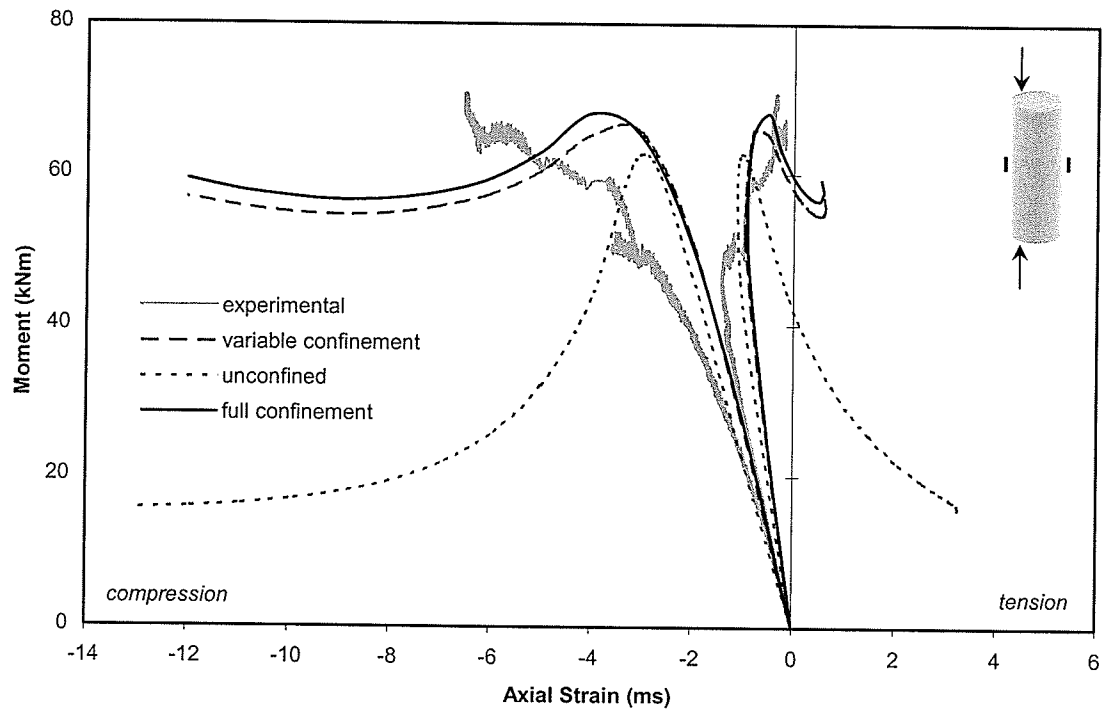
**Figure 5.27:** Model predicted axial load-axial strain behaviour of E-glass/polyester shell pure axial load specimen.



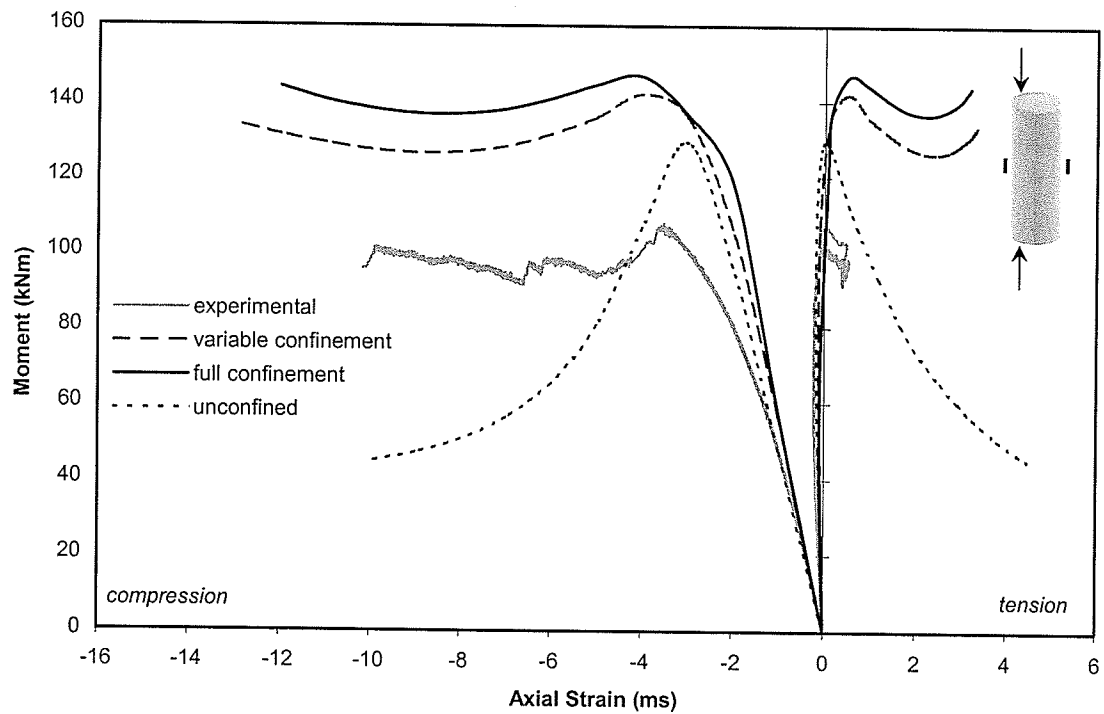
**Figure 5.28:** Predicted axial load-deflection behaviour of beam-column specimen BC-P-e10.



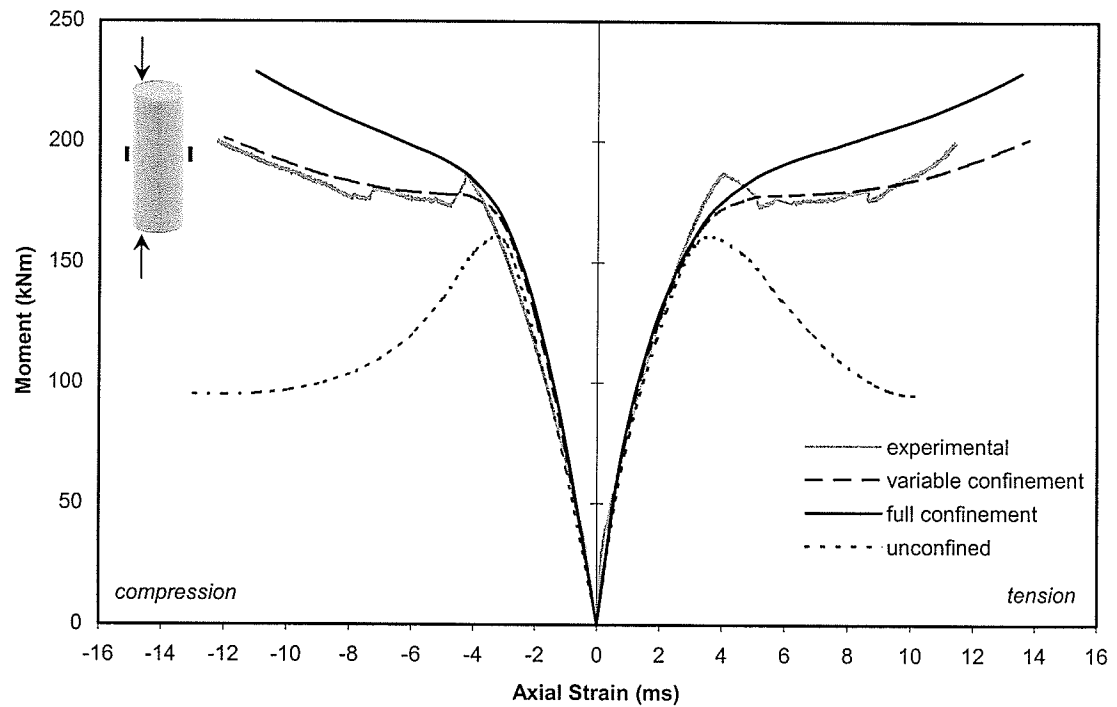
**Figure 5.29:** Predicted axial load-deflection behaviour of beam-column specimen BC-P-e30.



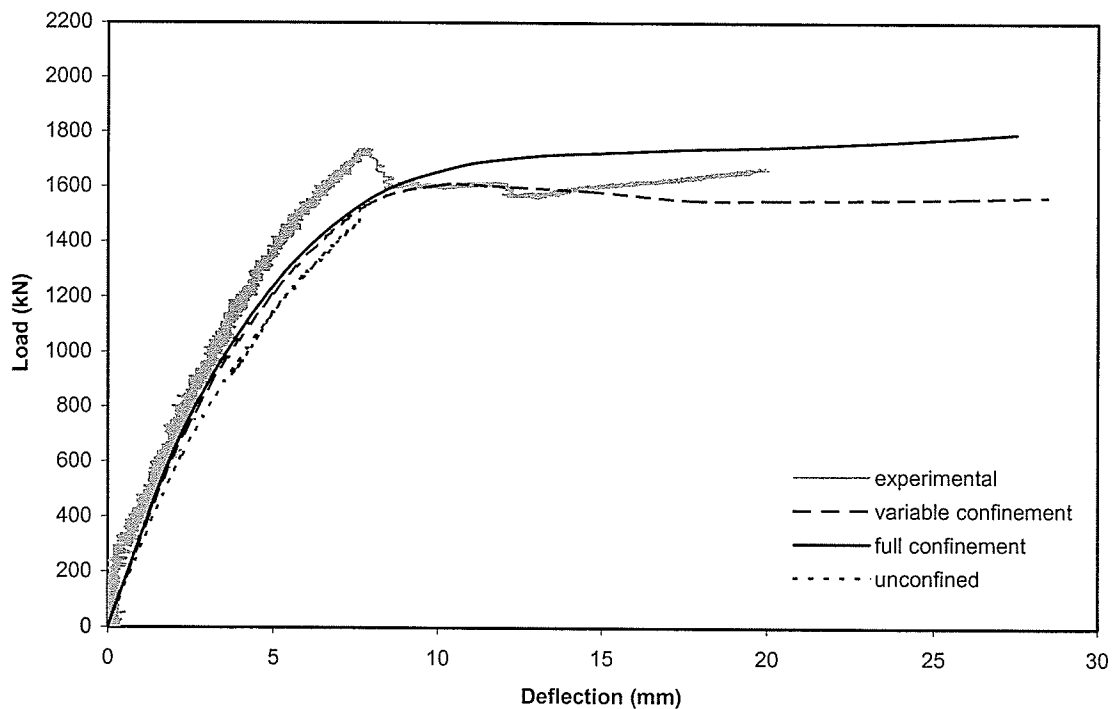
**Figure 5.30:** Predicted moment-axial strain behaviour of beam-column specimen BC-P-e10.



**Figure 5.31:** Predicted moment-axial strain behaviour of beam-column specimen BC-P-e30.

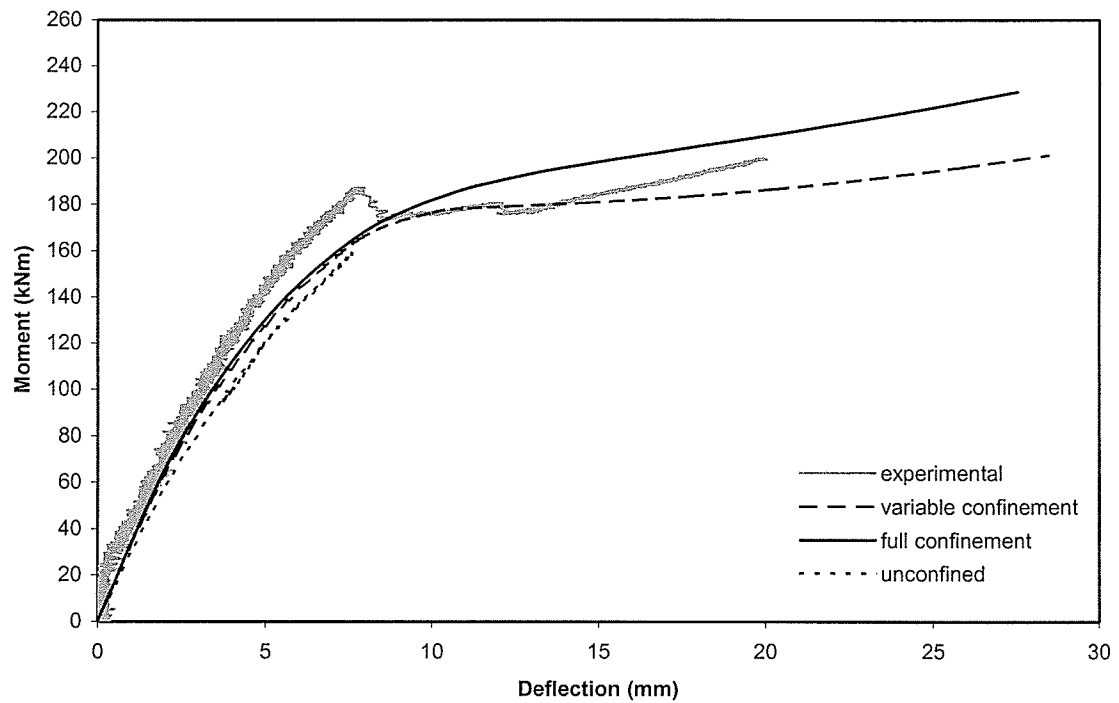


**Figure 5.32:** Predicted moment-axial strain behaviour of beam-column specimen BC-P-e100.

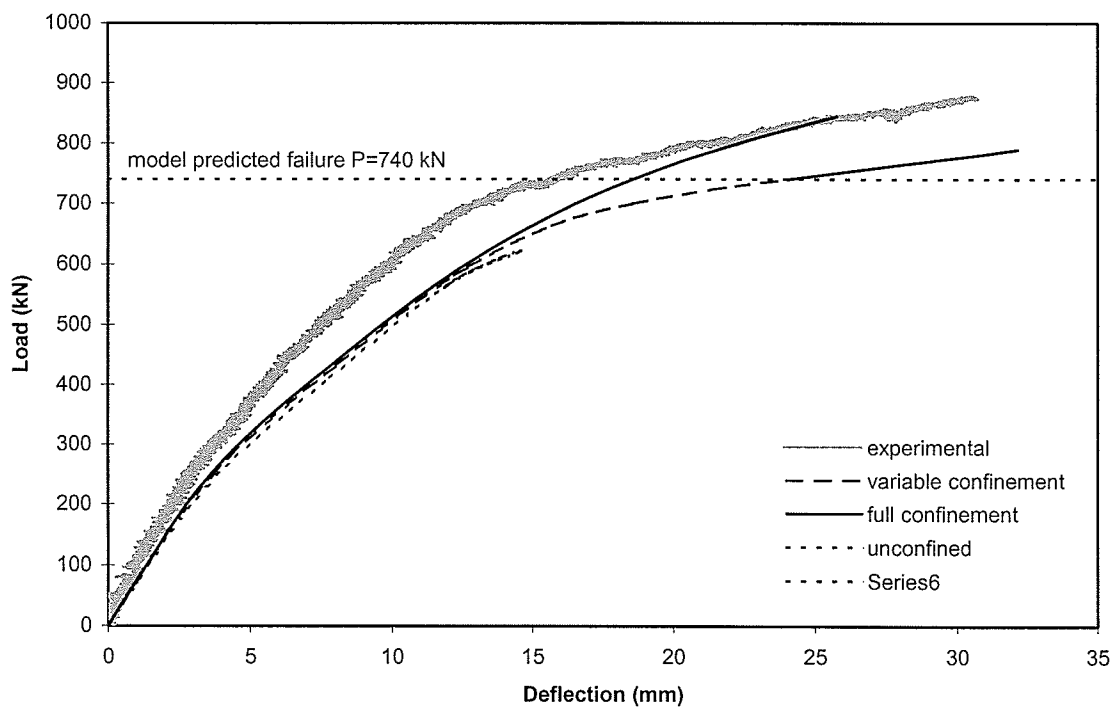


**Figure 5.33:** Predicted axial load-deflection behaviour of beam-column specimen BC-P-e100.

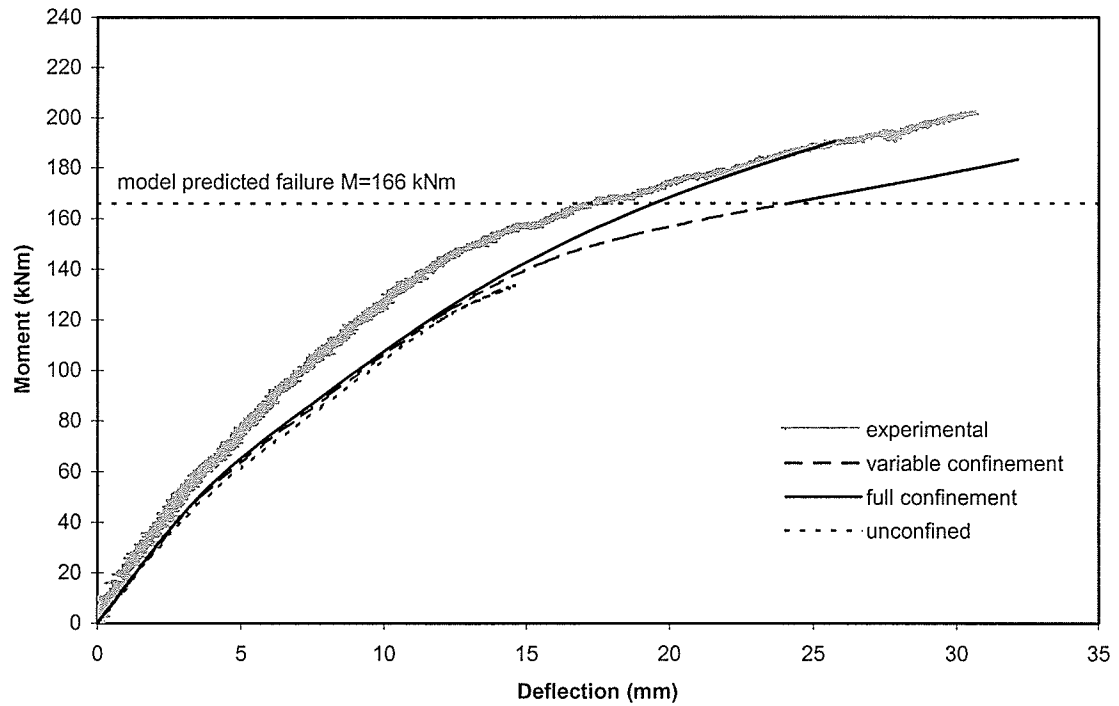




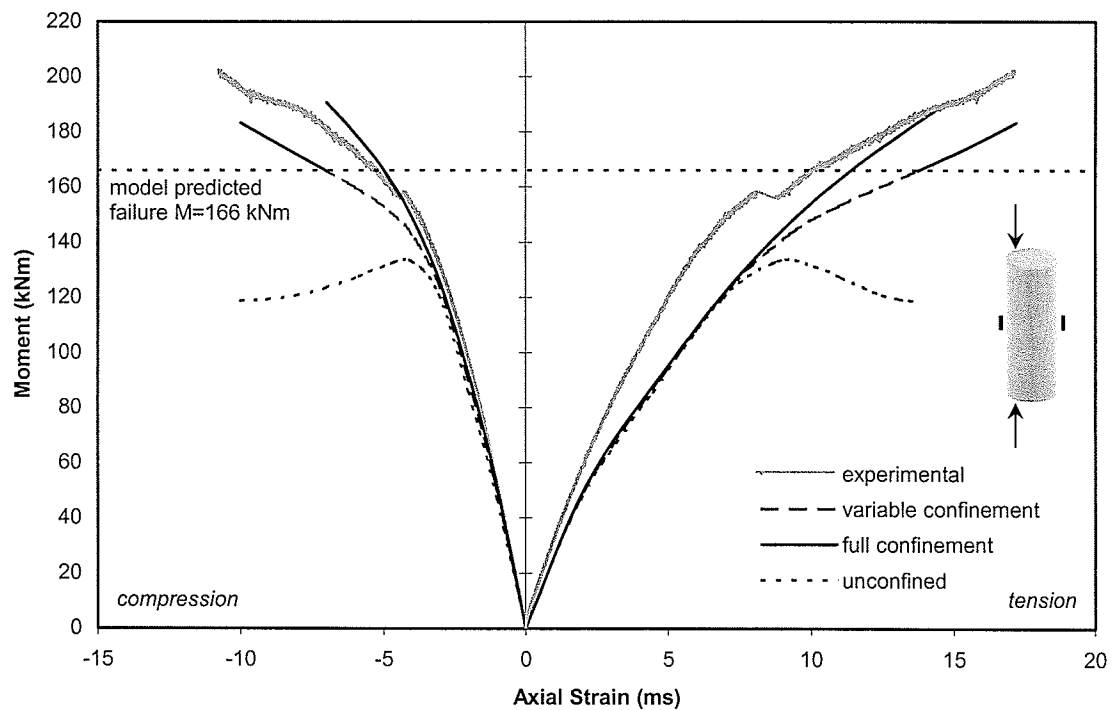
**Figure 5.34:** Predicted moment-deflection behaviour of beam-column specimen BC-P-e100.



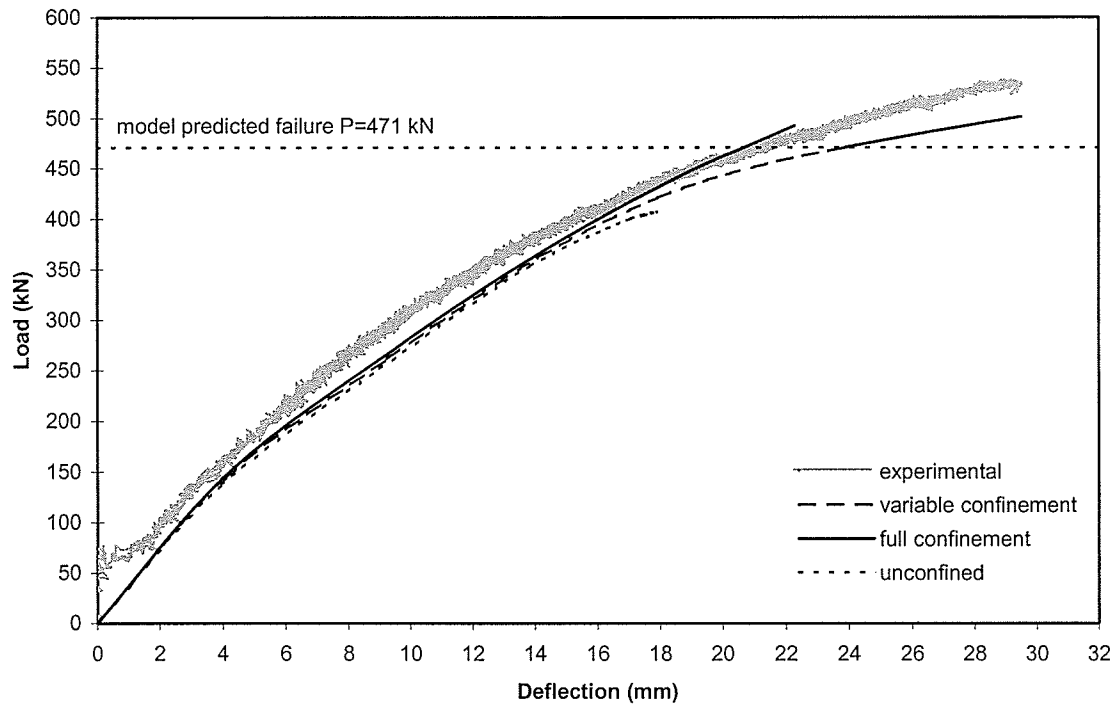
**Figure 5.35:** Predicted axial load-deflection behaviour of beam-column specimen BC-P-e200.



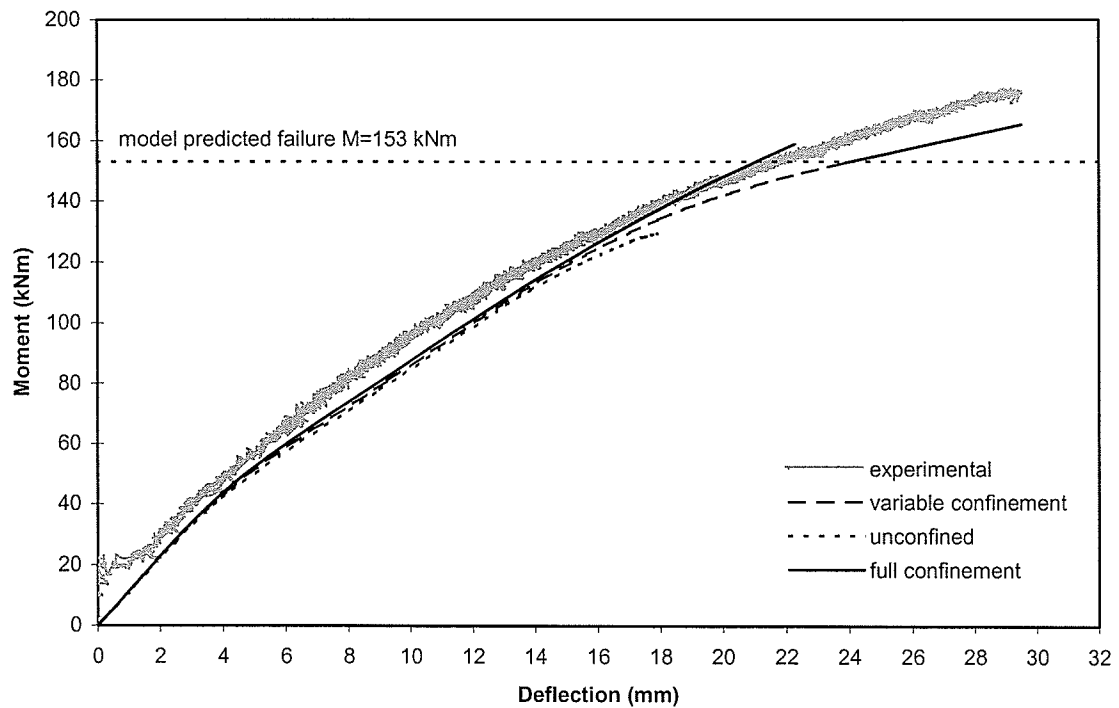
**Figure 5.36:** Predicted moment-deflection behaviour of beam-column specimen BC-P-e200.



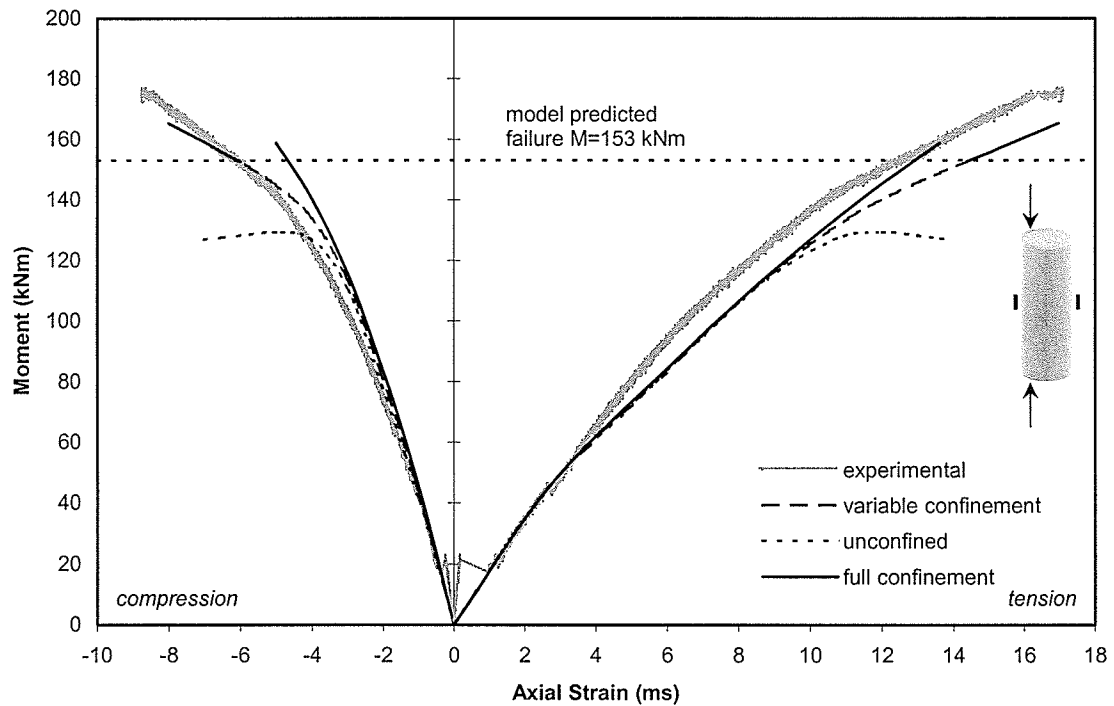
**Figure 5.37:** Predicted moment-axial strain behaviour of beam-column specimen BC-P-e200.



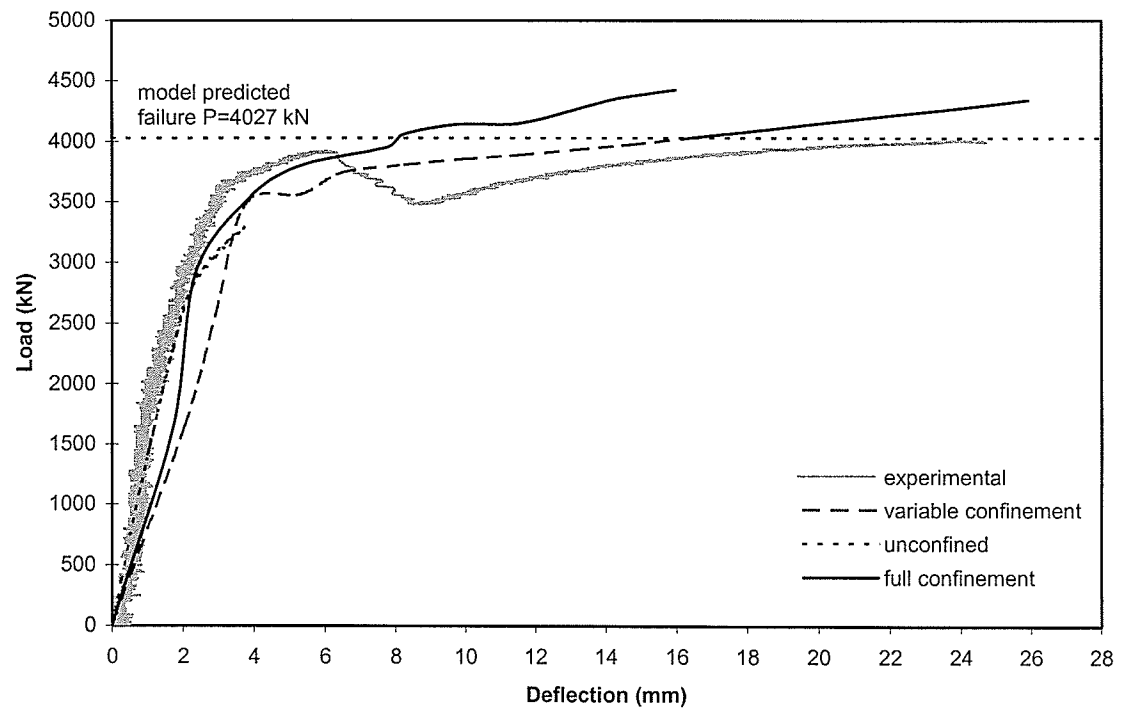
**Figure 5.38:** Predicted axial load-deflection behaviour of beam-column specimen BC-P-e300.



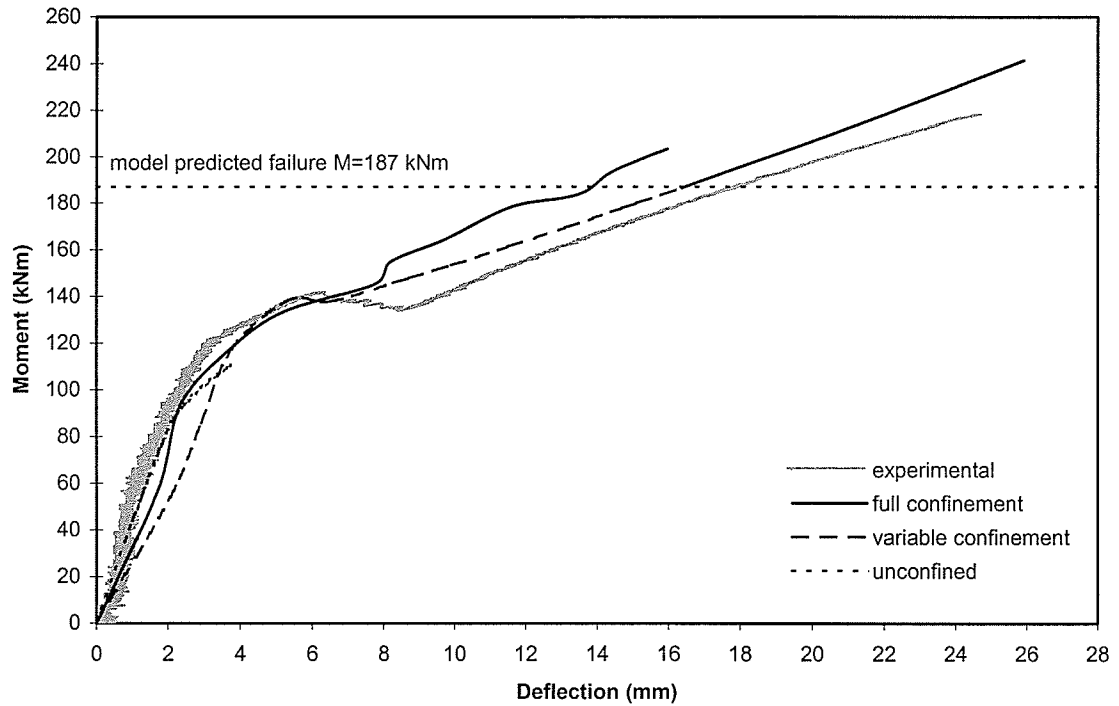
**Figure 5.39:** Predicted moment-deflection behaviour of beam-column specimen BC-P-e300.



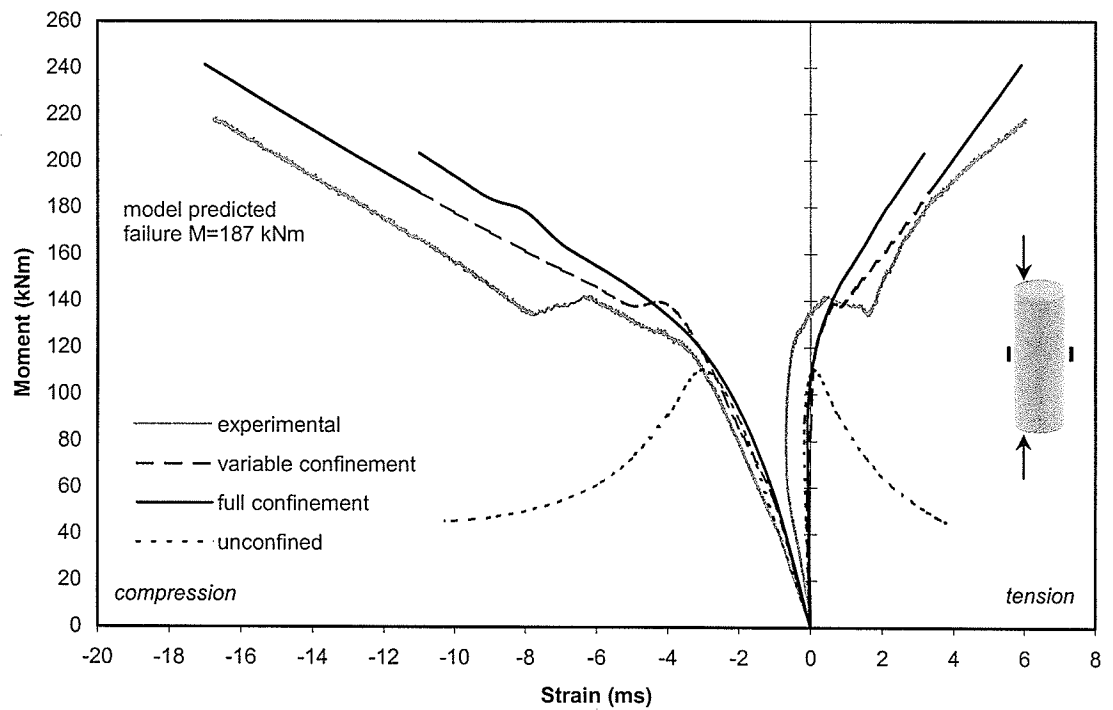
**Figure 5.40:** Predicted moment-axial strain behaviour of beam-column specimen BC-P-e300.



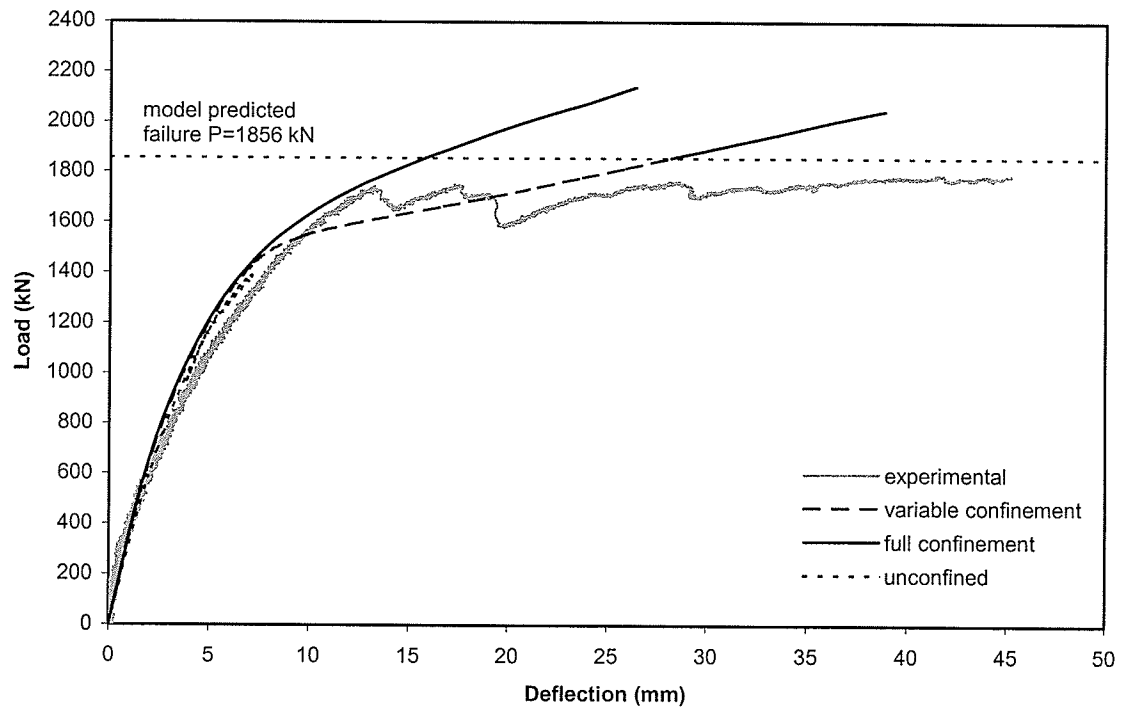
**Figure 5.41:** Predicted load-deflection behaviour of beam-column specimen BC-E-e30.



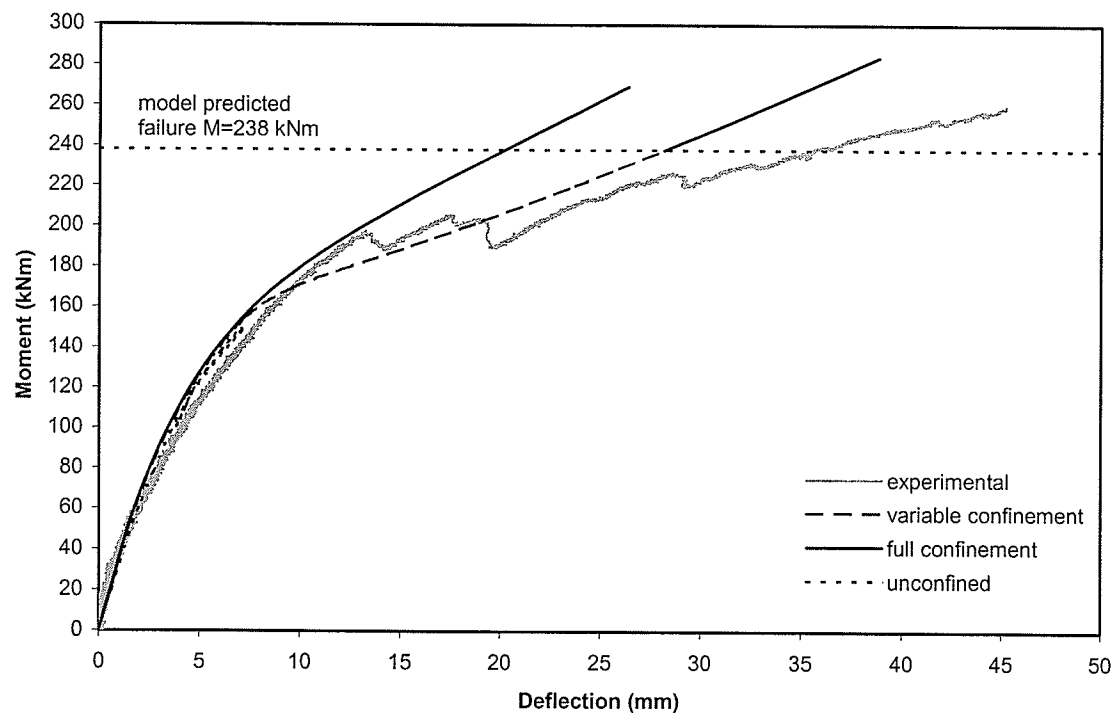
**Figure 5.42:** Predicted moment-deflection behaviour of beam-column specimen BC-E-e30.



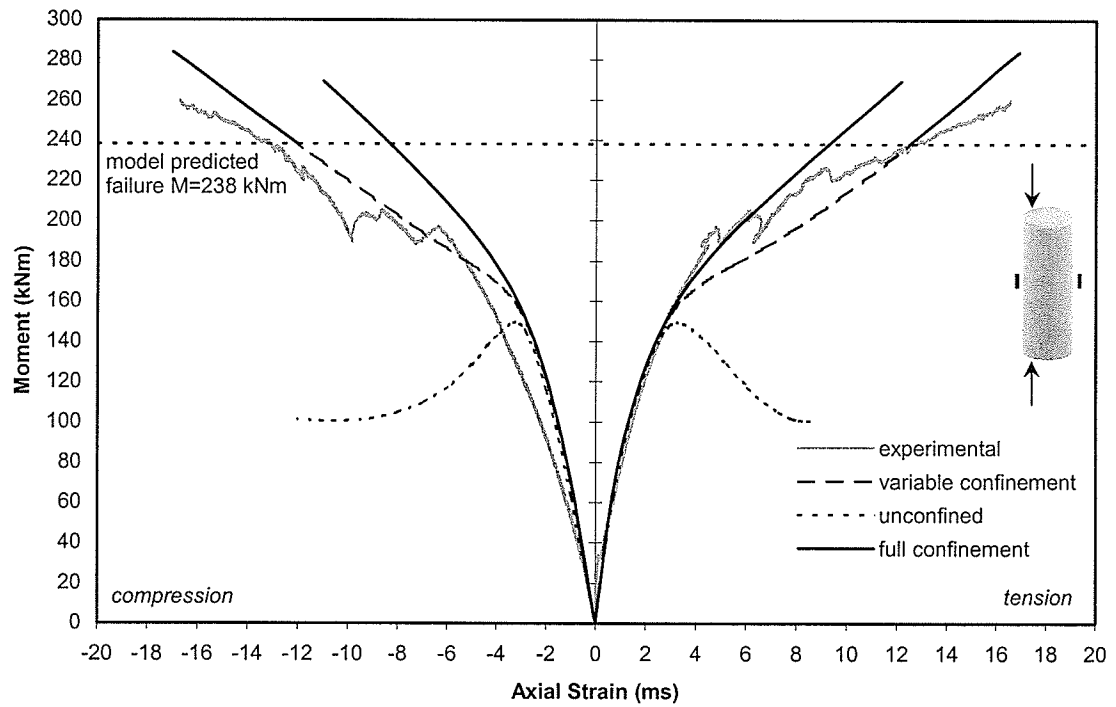
**Figure 5.43:** Predicted moment-axial strain behaviour of beam-column specimen BC-E-e30.



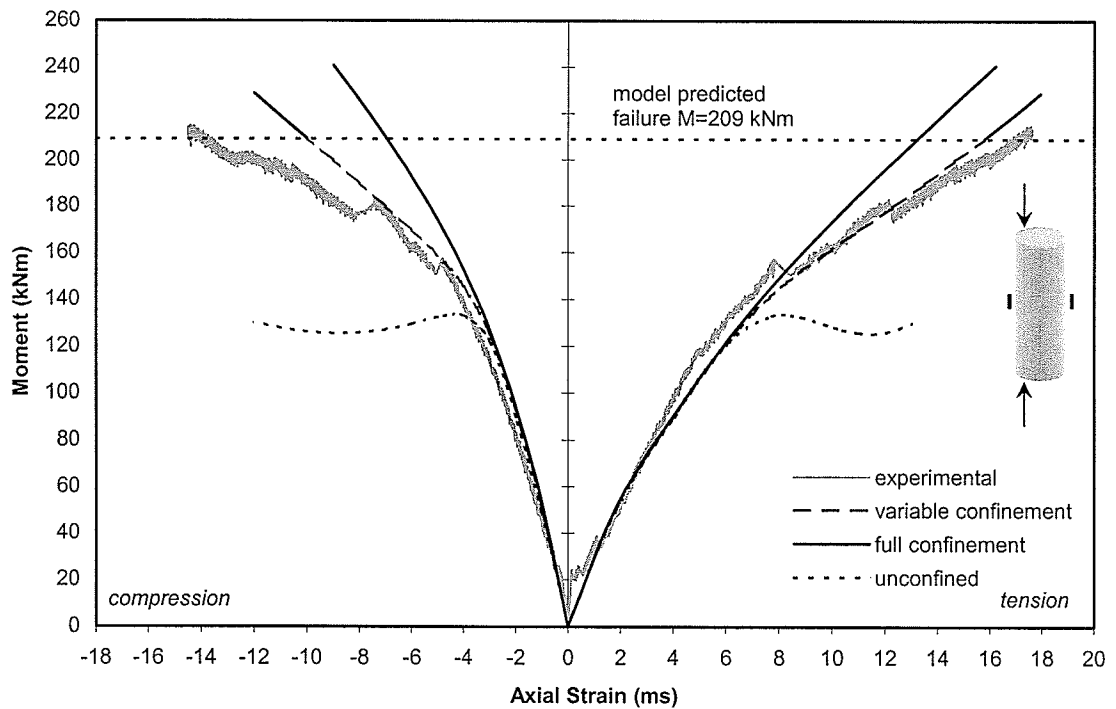
**Figure 5.44:** Predicted axial load-deflection behaviour of beam-column specimen BC-E-e100.



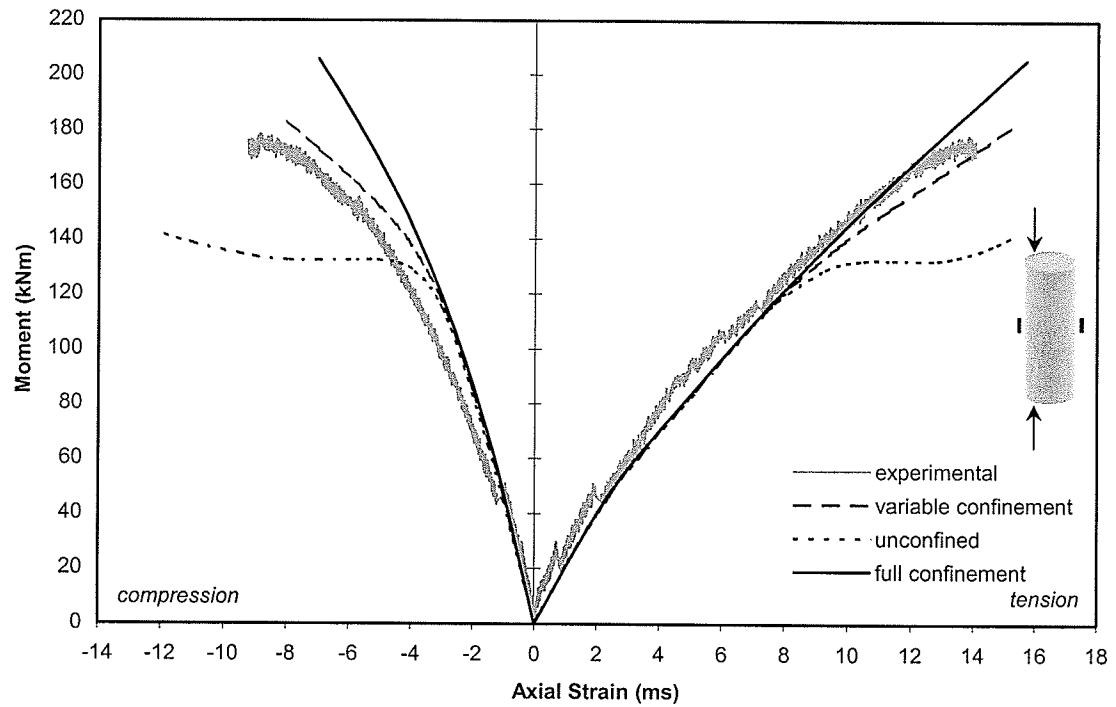
**Figure 5.45:** Predicted moment-deflection behaviour of beam-column specimen BC-E-e100.



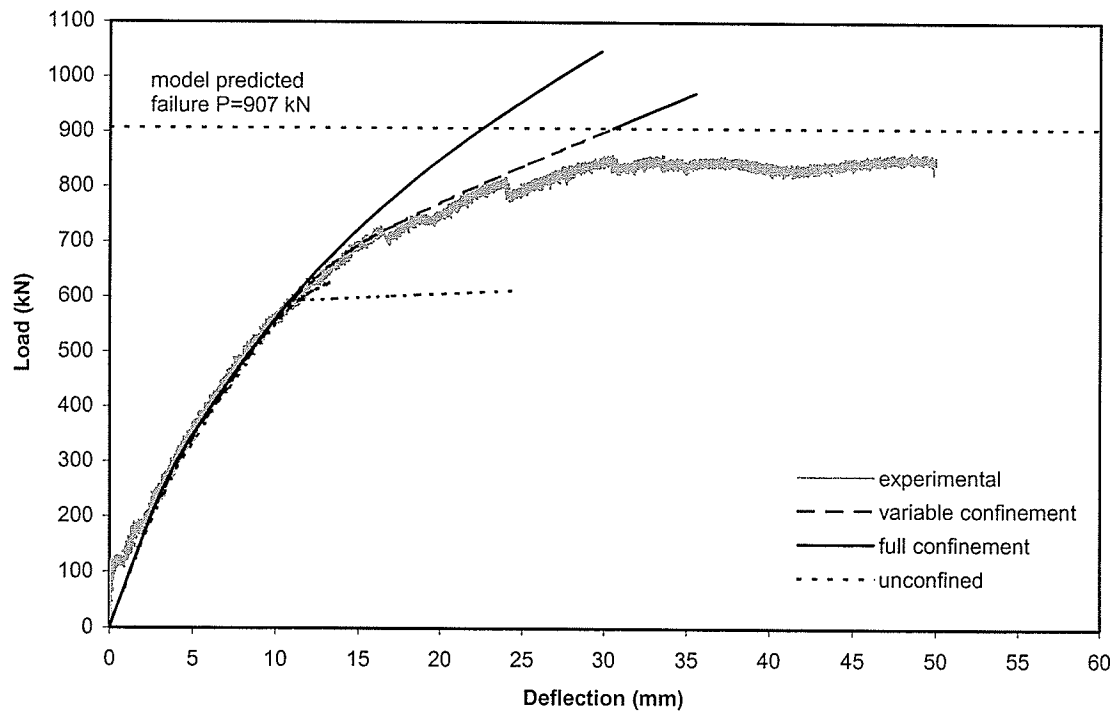
**Figure 5.46:** Predicted moment-axial strain behaviour of beam-column specimen BC-E-e100.



**Figure 5.47:** Predicted moment-axial strain behaviour of beam-column specimen BC-E-e200.

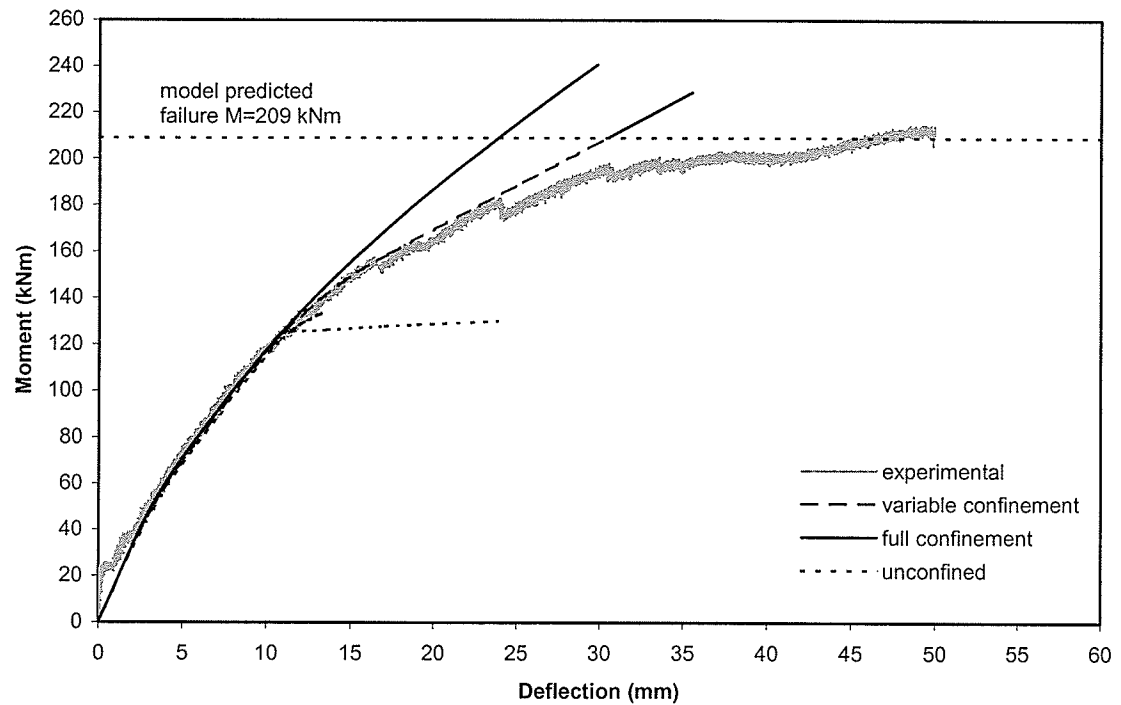


**Figure 5.48:** Predicted moment-axial strain behaviour of beam-column specimen BC-E-e300.

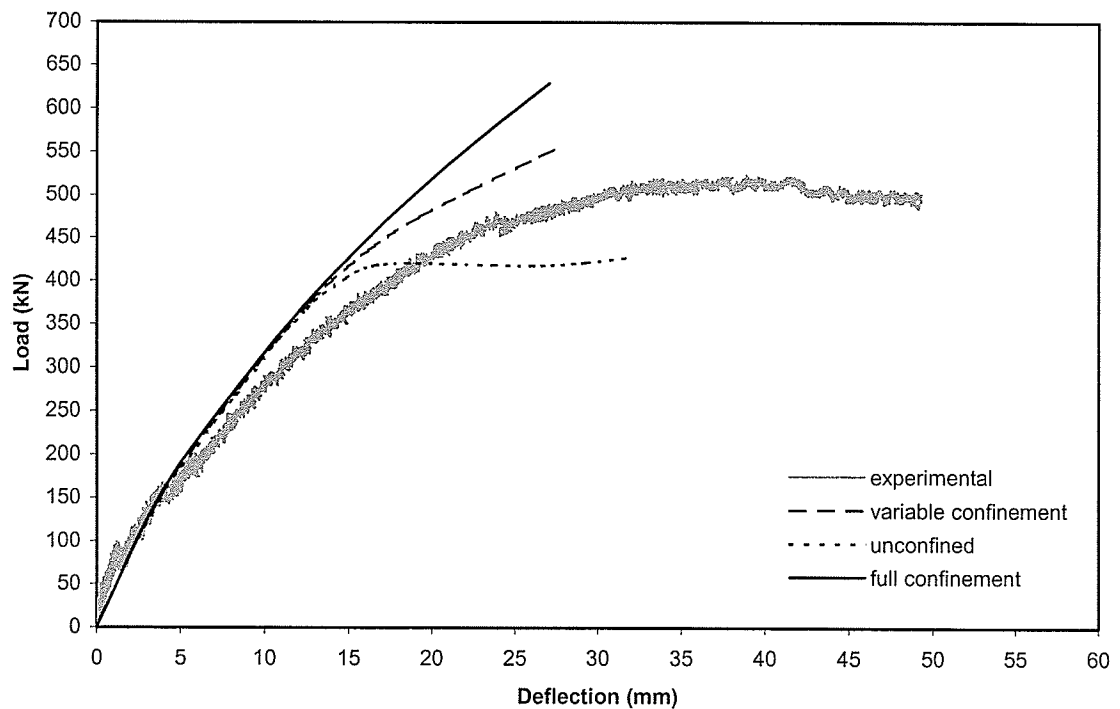


**Figure 5.49:** Predicted axial load-deflection behaviour of beam-column specimen BC-E-e200.

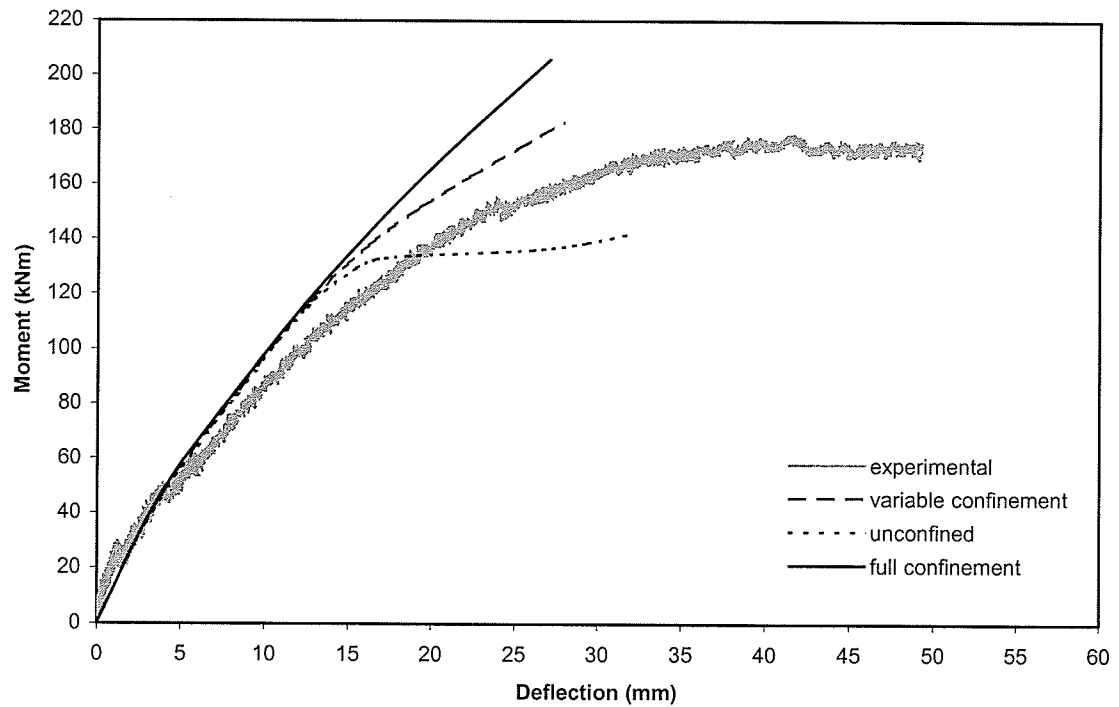




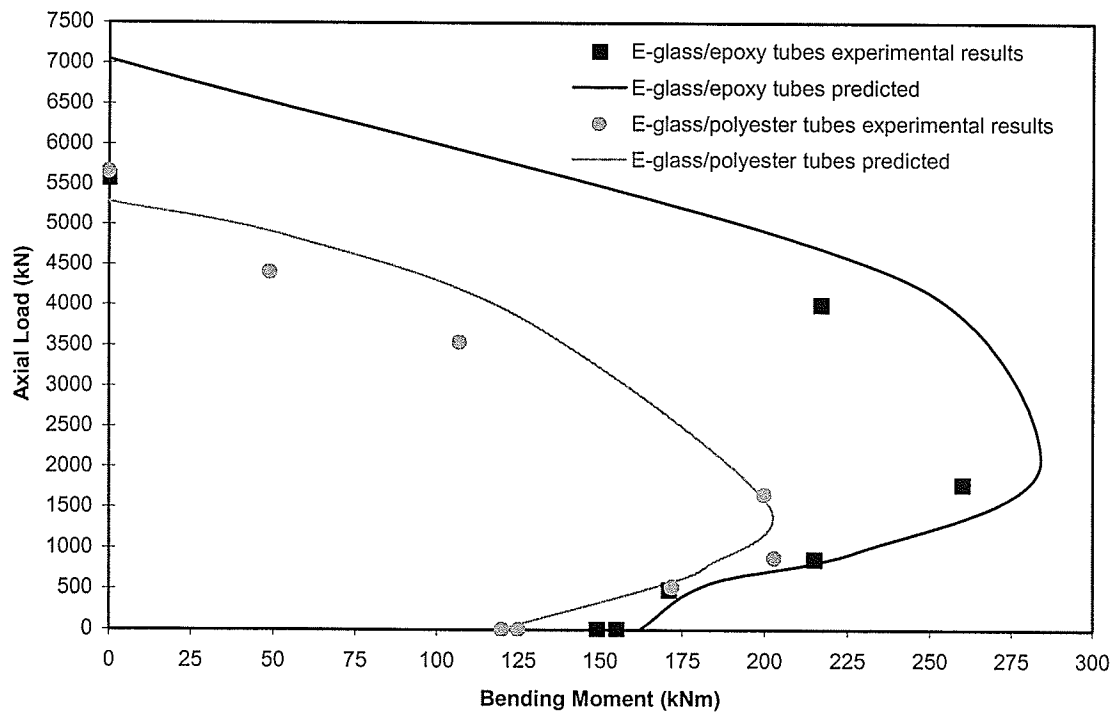
**Figure 5.50:** Predicted moment-deflection behaviour of beam-column specimen BC-E-e200.



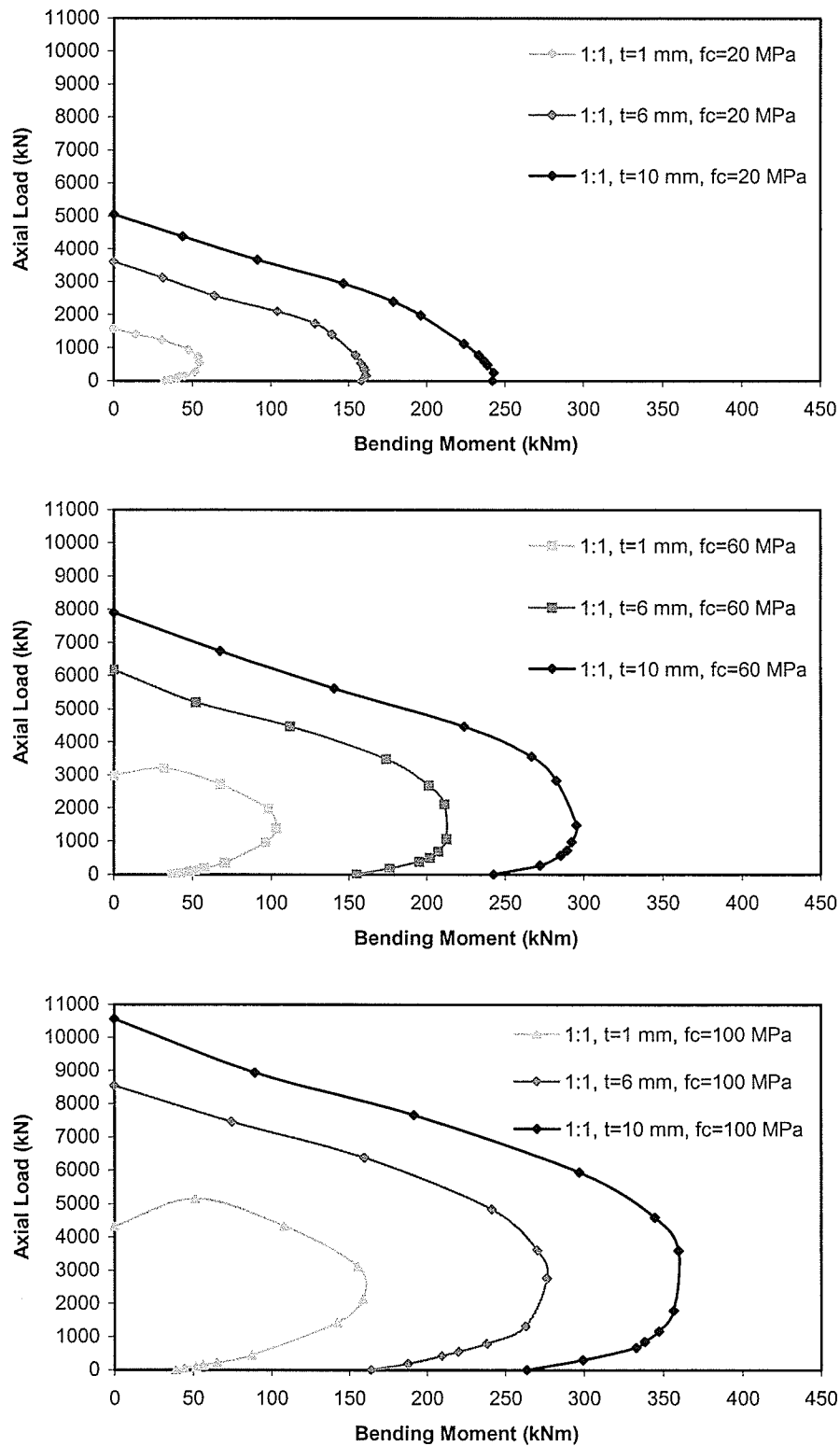
**Figure 5.51:** Predicted axial load-deflection behaviour of beam-column specimen BC-E-e300.



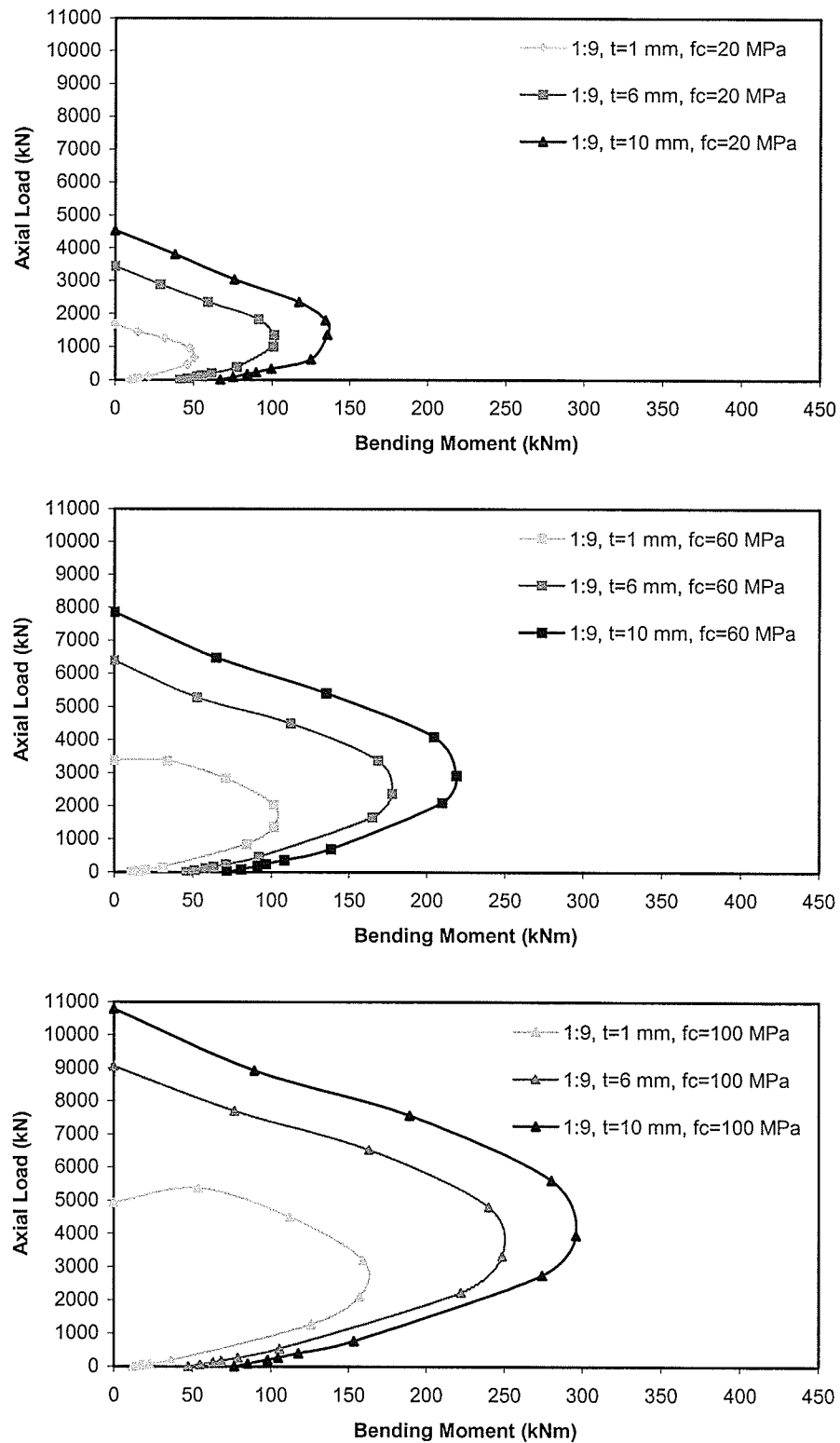
**Figure 5.52:** Predicted moment-deflection behaviour of beam-column specimen BC-E-e300.



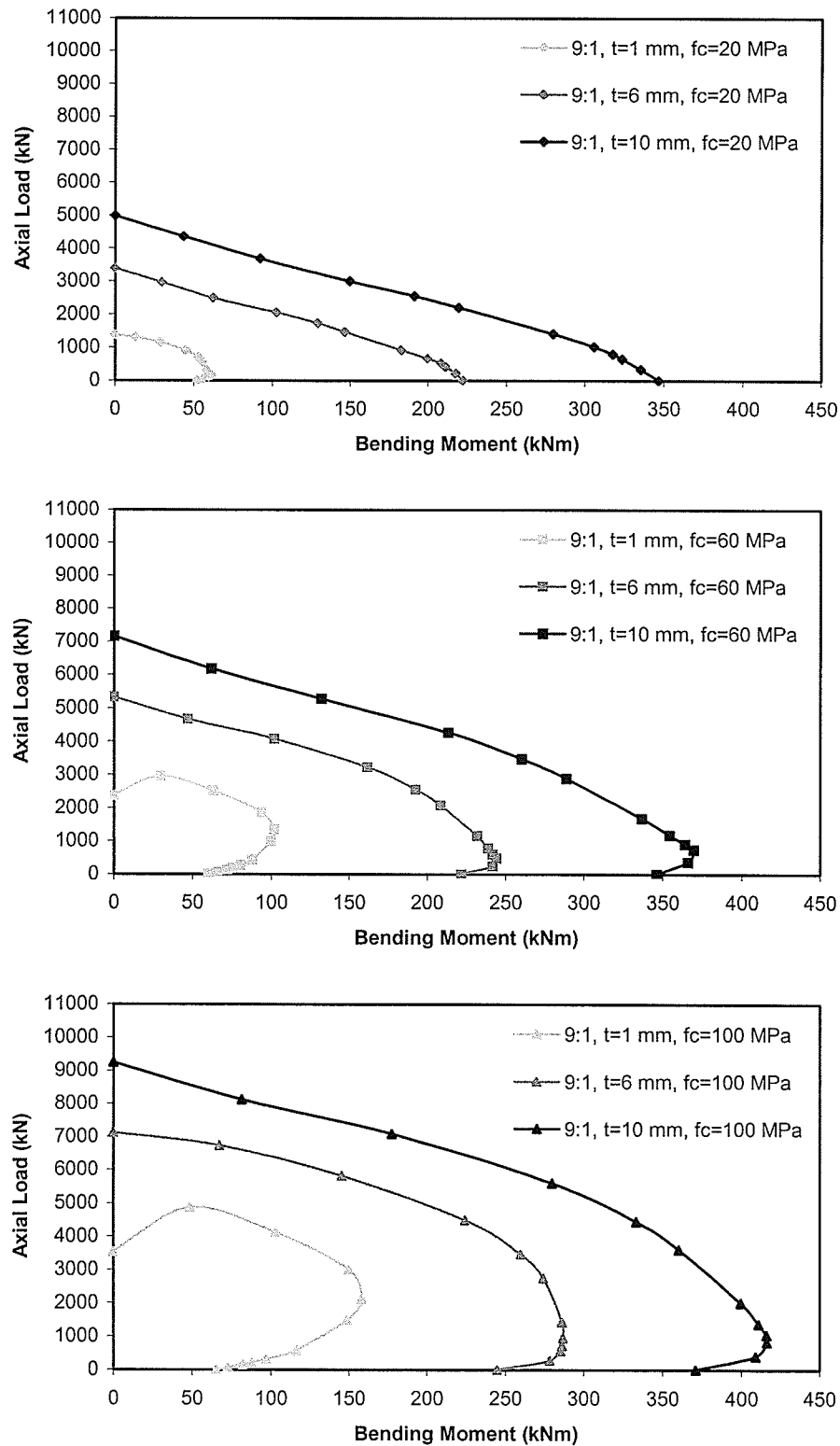
**Figure 5.53:** Predicted interaction diagrams of beam-column specimens, plotted against experimental results.



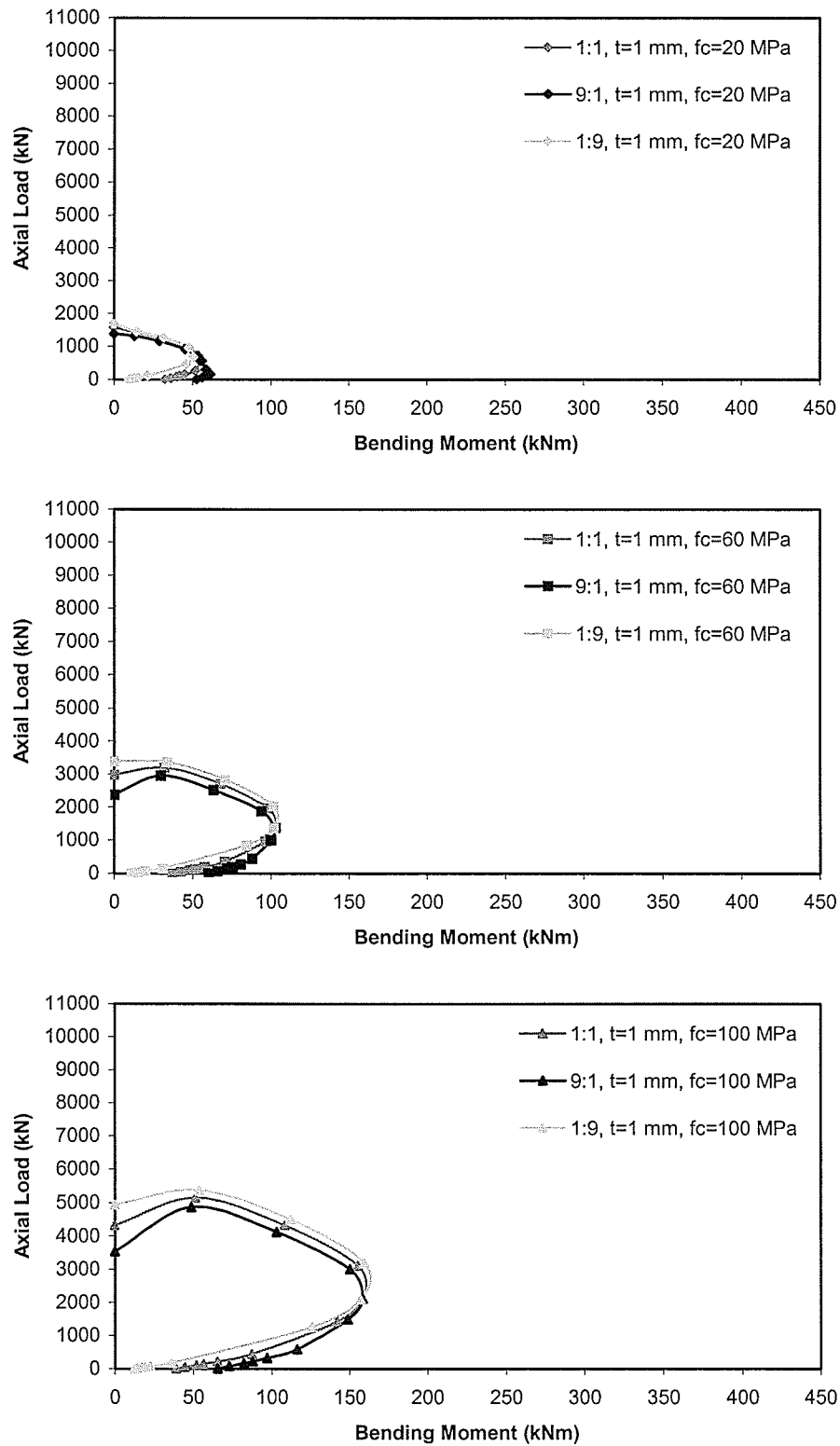
**Figure 5.54:** Modelled interaction diagrams for 300-mm diameter, 1:1 laminate concrete filled FRP tubes with varying shell thicknesses and concrete strengths.



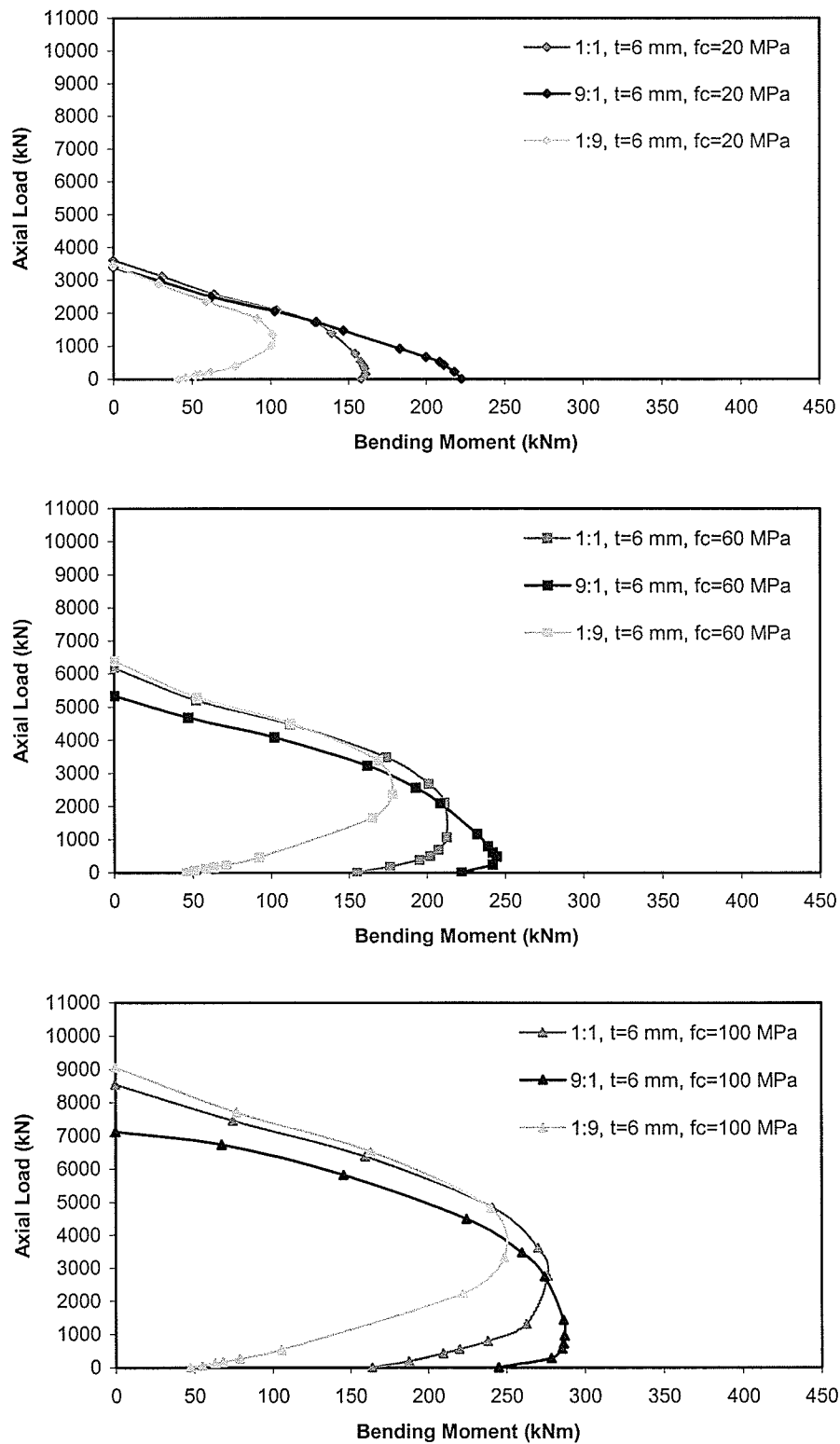
**Figure 5.55:** Modelled interaction diagrams for 300-mm diameter, 1:9 laminate concrete filled FRP tubes with varying shell thicknesses and concrete strengths.



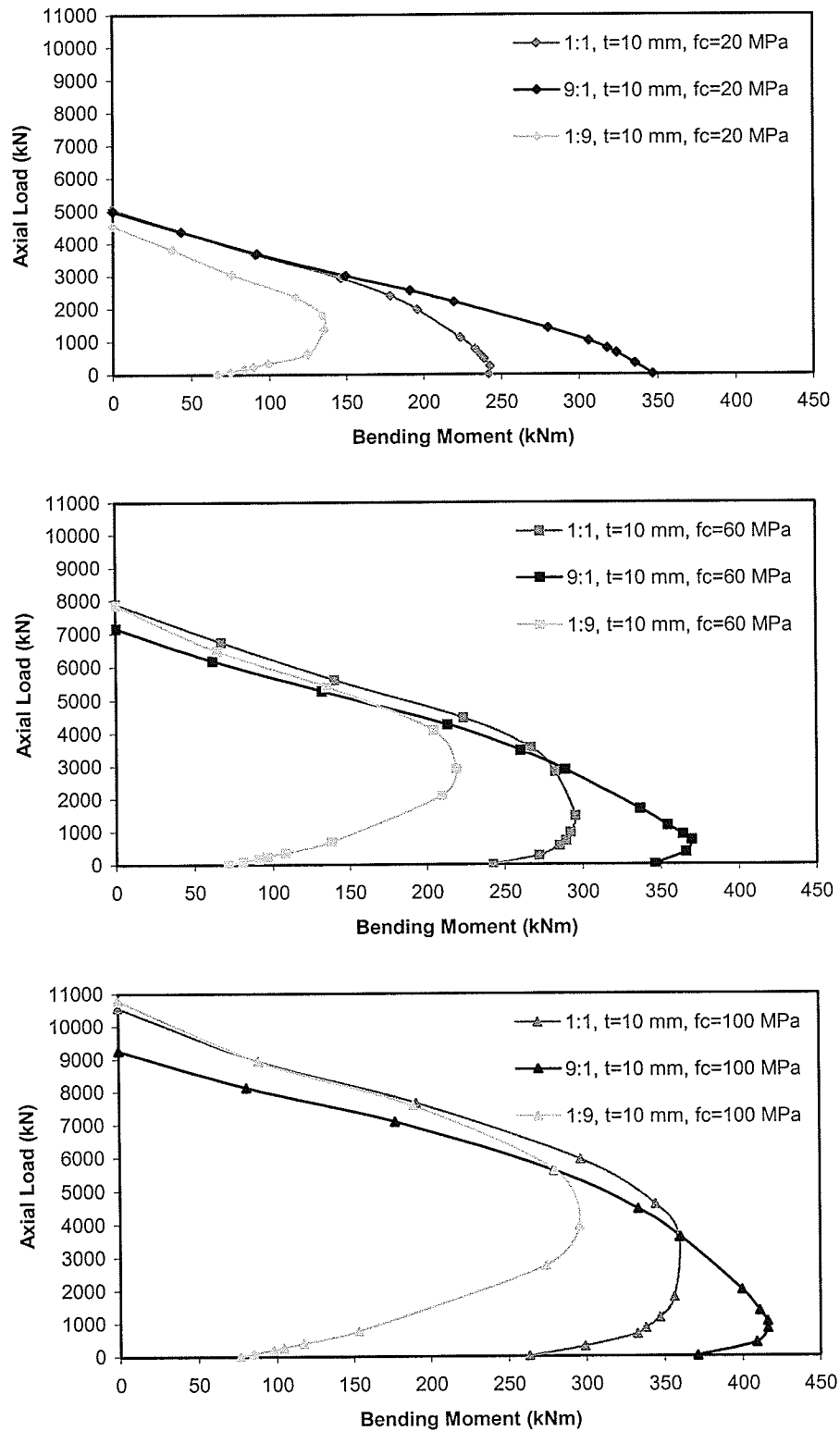
**Figure 5.56:** Modelled interaction diagrams for 300-mm diameter, 9:1 laminate concrete filled FRP tubes with varying shell thicknesses and concrete strengths.



**Figure 5.57:** Modelled interaction diagrams for 300-mm diameter, 1-mm thick concrete filled FRP tubes with varying laminates and concrete strengths.

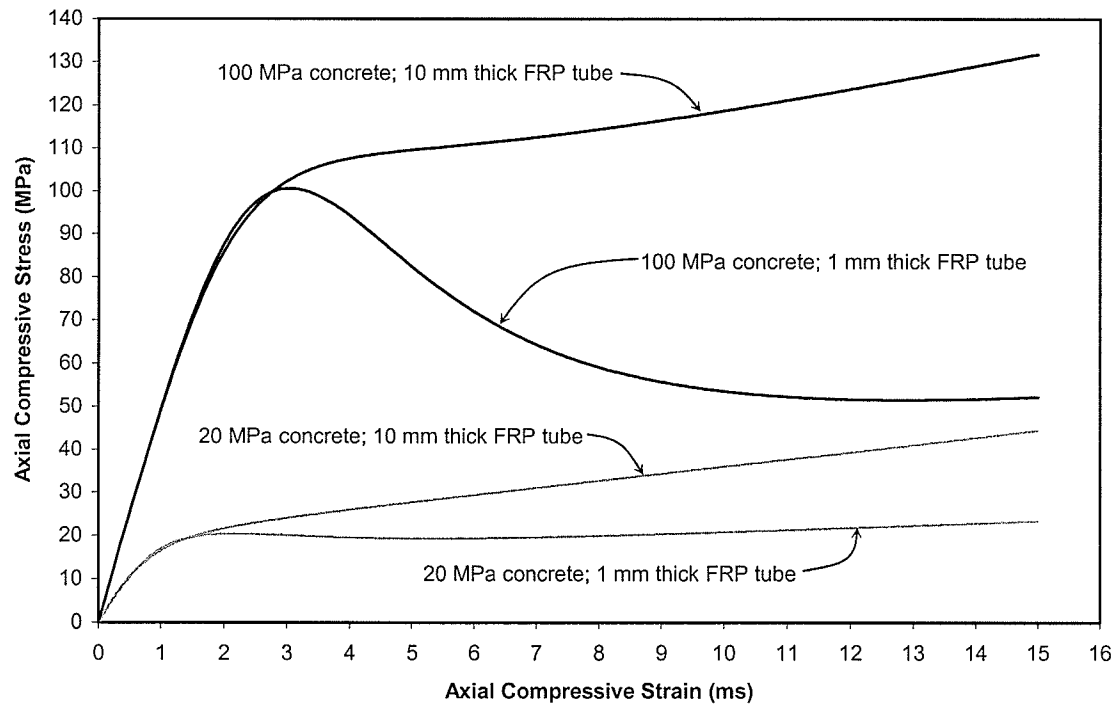


**Figure 5.58:** Modelled interaction diagrams for 300-mm diameter, 6-mm thick concrete filled FRP tubes with varying laminates and concrete strengths.

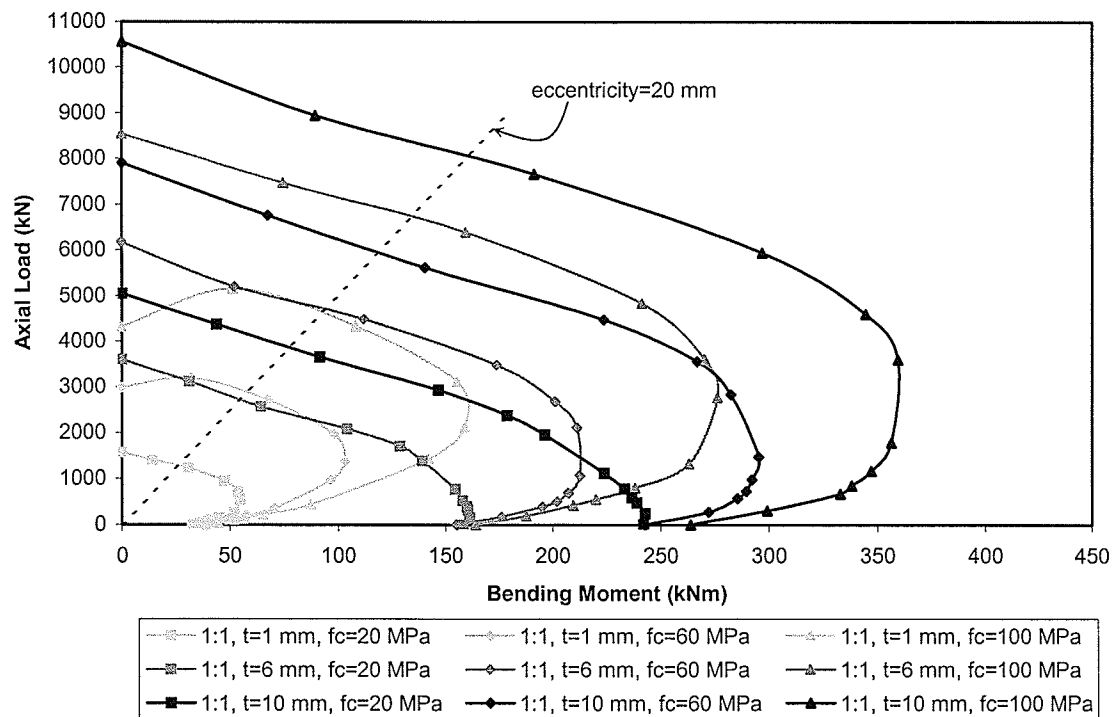


**Figure 5.59:** Modelled interaction diagrams for 300-mm diameter, 10-mm thick concrete filled FRP tubes with varying laminates and concrete strengths.





**Figure 5.60:** Full confinement concrete stress-strain relationships for 300-millimetre diameter, 1:1 laminate concrete filled FRP tubes with varying FRP tube wall thicknesses and concrete compressive strengths.



**Figure 5.61:** Modelled interaction diagrams for 300-mm diameter, 1:1 laminate concrete filled FRP tubes with varying wall thicknesses and concrete strengths.

## Chapter VI:

### Conclusions and Recommendations

This study consisted of experimental testing and analytical modelling of concrete filled FRP tubes subjected to bending moments, axial loads, and combinations of bending moments and axial loads. Four beams, two pure axial load specimens, and nine beam-column members were tested in the experimental program to study the behaviour of two types of similarly sized concrete filled FRP tubes. An analytical model is proposed to predict the behaviour of the members. The model is verified using the experimental results.

The findings in the study led to the following conclusions:

1. Ultimate failure of concrete filled FRP tube members subjected to bending moments, axial loads, or a combination of axial loads and bending moments is governed by failure of the FRP shell.
2. The failure mode, tensile or compressive, depends on the applied loads, and the strength and stiffness of the FRP tube.
3. Tensile failures were sudden and catastrophic. Compression failures were sudden in the case of the E-glass/epoxy type specimens, but

progressive in the case of the low axial load eccentricity E-glass/polyester type specimens.

4. Pure flexural capacity does not appear to be affected significantly by the concrete compressive strength since failure is governed by the FRP.
5. Pure flexural capacity depends on the strength and axial stiffness of the FRP tube, which are governed by the laminate structure.
6. Flexural stiffness may be affected by slip of the concrete core within the FRP shell. Providing a positive mechanical bond between the concrete core and FRP shell may increase the stiffness.
7. The level of concrete confinement increases with decreasing axial load eccentricity. Members subjected to pure axial loads exhibit maximum confinement, while members subjected to pure bending moments exhibit minimum confinement. The confinement effect on the concrete in the compression zone is minor when the member is subjected to pure flexure.
8. The strengths of concrete filled FRP tube beam-columns with very small axial load eccentricities and pure axial load members are affected by the end loading conditions, as demonstrated by premature initiation of failure of the FRP tube by local crushing and splitting at the interface between the specimen and machine loading plates in the pure axial load specimens and low eccentricity E-glass/polyester tube specimens.
9. An analytical model incorporating calculations for FRP tube laminate effective elastic properties and strengths, variable concrete confinement

depending on the axial load eccentricity, cross-section force and moment equilibrium, member deflection, and detection of ultimate failure was developed to predict the behaviour of concrete filled FRP tubes subjected to axial loads, bending moments, and combinations of axial loads and bending moments. The model predictions agreed well with the experimental results in most cases.

10. It is important to know the exact laminate structure and composition of the FRP shell in order to accurately model the shell's effective elastic properties with the laminated plate theory, and laminate strengths using the Tsai-Wu laminate failure criterion.
11. Bending moment and axial load capacities increase with increasing FRP tube wall thickness, for a given concrete strength, member diameter, and FRP shell laminate structure and configuration.
12. Bending moment and axial load capacities increase with increasing concrete strength, for a given FRP shell laminate structure and composition, and tube wall thickness.
13. Orienting the majority of the fibres in the FRP shell in the longitudinal direction increases the bending capacity at high axial load eccentricities for a given FRP shell thickness and concrete strength, by increasing the longitudinal strength and stiffness of the FRP tube. Increasing the proportion of hoop fibres at low eccentricities increases the axial load capacity of the member by increasing the hoop stiffness of the FRP shell,

- enhancing the concrete confinement effect. Therefore, the FRP shell laminate structure can be optimized for specific, expected applied loads.
14. In general, the interaction diagrams of concrete filled FRP tube members resemble those of conventional reinforced concrete columns. Bending moment capacities initially increase with increasing axial loads, at low axial loads, and members fail by rupture of the shell in the tension zone. A balanced point is reached after which bending moment capacities decrease with increasing axial loads, and FRP shell compression failures occur.
  15. In cases where a large proportion of fibres are oriented in the longitudinal direction, concrete strengths are relatively low, and FRP shell wall thickness-to-diameter ratios are relatively large, FRP shell compression failures occur along the entire interaction curve.
  16. Member designs, including tube thickness and concrete strength can be optimized for specific expected loading conditions. In some cases, substantially decreasing the FRP tube wall thickness while increasing the concrete strength can improve member bending moment and axial load capacities, allowing for cost efficient designs.
  17. There are many possible combinations of concrete strength, FRP shell laminate structure, and FRP tube wall thickness that can satisfy member strength requirements for specific combinations of applied axial loads and bending moments.

Although this study represents a significant contribution to the state-of-the-art in concrete filled FRP tube members, there are several key areas that require further investigation. Further research is recommended on the following:

1. Behaviour of members with different types of laminates, including carbon and aramid fibre laminates, and possibly hybrid laminates containing combinations of glass, carbon, and aramid fibres.
2. Cyclic loading and fatigue behaviour.
3. Effect of slenderness ratio.
4. Effect of bond strength between the concrete core and FRP shell.
5. Behaviour of members reinforced with steel or FRP bars.
6. Behaviour of pre-stressed and post-tensioned members.
7. Use of members in structural systems like composite girder/bridge decks.
8. Design of connections between beams and columns to transfer moments and shear between members.
9. Durability under long-term exposure to severe environmental effects like UV radiation, water, freeze-thaw cycles, and aggressive chemicals.
10. Member fire resistance.
11. The effects of shear on member behaviours and capacities.
12. Development of reliable, repeatable experimental methods to determine FRP shell effective elastic properties and laminate strengths.
13. Development of efficient construction techniques including concrete casting and pile driving.

There are numerous advantages of using concrete filled FRP tube members in place of conventional systems for foundations, columns, overhead sign structures, poles, and other structural members that require high strengths and excellent durability in aggressive environments. Further studies building on the experience from this and other similar research programs will lead to the development of a strong knowledge base on concrete filled FRP tube member technology. Once a comprehensive understanding is developed, knowledge transfer to designers and infrastructure owners can occur through design codes and guidelines, ensuring that the benefits of concrete filled FRP tube members are realized in the infrastructure of the future.

ACI Committee 440, 1996, *State-of-the-art Report on Fibre Reinforced Plastic Reinforcement for Concrete Structures*, ACI 440R-96, American Concrete Institute, Detroit.

ACI Committee 318, 2002, *Building Code Requirements for Structural Concrete and Commentary*, ACI 318M-02, American Concrete Institute, Detroit.

Addax, summer 2000, "Filament Winding Process,"  
[http://www.addax.com/technology/filament\\_winding.html](http://www.addax.com/technology/filament_winding.html).

American Composites Manufacturers Association, summer 2000, "Composites Industry Overview," <http://www.compositetek.com/composites.htm>.

ASTM Subcommittee C09.61, 1996, *Standard Test Method for Compressive Strength of Cylindrical Concrete Specimens*, ASTM, 5 pp.

Barber, E.; Kennedy, S.; Laurie Kennedy, D.; and MacGregor, J., 1987, "Flexural Strength of Concrete-filled Steel Hollow Structural Sections," *Proceedings of the 1987 CSCE Centennial Conference*, Montreal, May, pp. 494-511.

Becque, Jurgen, 2000, "Analytical Modelling of Concrete Columns Confined by FRP," MSc thesis, the University of Manitoba.



Black, Sara, 2000, "A Survey of Composite Bridges," *Composites Technology*, April-May, pp. 14-18.

Canadian Standards Association, 1994, *CSA Standard A23.3-94 Design of Concrete Structures*, CSA, Canada, 220 pp.

Canning, L.; Holloway, L. and Thorne, A.M., 1999, "Manufacture, Testing and Numerical Analysis of an Innovative Polymer Composite/Concrete Structural Unit," *Proc. Instn. Engrs. Structs. & Bldgs.*, Paper 11826, 134, August, pp. 231-241.

Collins, Michael P. and Mitchell, Denis, 1987, *Prestressed Concrete Structures*, Response Publications, Canada, 766 pp.

Composites Institute of the Society of Plastics Industry Inc., 1995, *Introduction to Composites*, SPI Literature Sales Department, 109 pp.

Composites Solutions LLC, summer 2000, "Filament Winding,"  
[www.composite-solutions.com/whenfilament.htm](http://www.composite-solutions.com/whenfilament.htm).

Daniel, Isaac M. and Ishai, Ori, 1994, *Engineering Mechanics of Composite Materials*, Oxford University Press, 395 pp.

Deskovic, N. and Triantafillou, T.C., 1995, "Innovative Design of FRP Combined with Concrete: Short-term Behaviour," *Journal of Structural Engineering*, July, pp. 1069-1078.

Fam, Amir Z., 2000, "Concrete-filled Fiber Reinforced Polymer Tubes for Axial and Flexural Structural Members," PhD thesis, the University of Manitoba, 261 pp.

Fam, Amir Z.; Flisak, Bart and Rizkalla, Sami H., 2003, "Experimental and Analytical Modelling of Concrete-Filled Fiber-Reinforced Polymer Tubes Subjected to Combined Bending and Axial Loads," *ACI Structural Journal*, Jul-Aug, pp. 499-509.

Fam, Amir Z. and Rizkalla, Sami H., 2001, "Confinement Model for Axially Loaded Concrete Confined by FRP Tubes," *ACI Structural Journal*, Vol. 98, No. 4, Jul-Aug, pp. 451-461.

Fardis, M.N. and Khalili, H., 1981, "Concrete Encased in Fibreglass-reinforced Plastic," *ACI Structural Journal*, Title No. 78-38, Nov-Dec, pp. 440-446.

Furlong, R.W., 1967, "Strength of Steel-encased Concrete Beam Columns," *Proceedings of the ASCE*, Vol. 93, No. ST5, October, pp. 113-124.

Gardner, Noel J. and Jacobson, E. Ronald, 1967, "Structural Behaviour of Concrete Filled Steel Tubes," *ACI Journal*, Title No. 64-38, July, pp. 404-416.

Han, L., 2000, "Tests on Concrete Filled Steel Tubular Columns with High Slenderness Ratio," *Advances in Structural Engineering*, Vol. 3, No. 4, pp. 337-344.

ISIS Canada, winter 2004, "Field Demonstration Projects,"  
[http://www.isiscanada.com/field/main.htm?field\\_projects.htm](http://www.isiscanada.com/field/main.htm?field_projects.htm).

Iskander, Magued G. and Hassan, Moataz, 1998, "State of the Practice Review in FRP Composite Piling," *Journal of Composites for Construction*, August, pp. 116-120.

Iyengar, K.T.S.R.; Desayi, P. and Reddy, K.N., 1971, "Flexure of Reinforced Concrete Beams with Confined Compression Zones," *ACI Journal*, Vol. 68, No. 9, September, pp. 719-725.

Izbal, M. and Hatcher, D.S., 1977, "Post-crushing Behaviour of Bound Concrete Beams," *Proceedings of the ASCE*, Vol. 103, No. ST8, August, pp. 1643-1654.

Kanatharana, J. and Lu, L., 1998, "Strength and Ductility of Concrete Columns Reinforced with FRP Tubes," *Proceedings of the First International Conference on Composites in Infrastructure (ICCI'96)*, Tucson, Arizona, January, pp. 370-384.

Karbhari, V.M et al, 1998, "Structural Characterization of Fiber-reinforced Composite Short- and Medium-span Bridge Systems," *Proceedings of European Conference on Composite Materials (ECCM-8)*, June, V. 2, pp. 116-120.

Kilpatrick, Andrew E. and Rangan, B. Vijaya, 1999, "Tests on High-strength Concrete-filled Steel Tubular Columns," *ACI Structural Journal*, Vol. 96, No. 2, Mar-Apr, pp. 268-274.

Knowles, Robert B. and Park, R., 1969, "Strength of Concrete Filled Steel Tubular Columns," *Proceedings of the ASCE*, Vol. 95, No. ST12, December, pp. 2565-2587.

Kurt, C.E., 1978, "Concrete Filled Structural Plastic Columns," *Proceedings of the ASCE*, Vol. 104, No. ST1, January, pp. 55-63.

Mallick, P.K., 1993, *Fiber-reinforced Composites: Materials, Manufacturing and Design*, Dekker, 566 pp.

Mander, J.B.; Priestley, M.J.N., and Park, R., 1988, "Theoretical Stress-strain Model for Confined Concrete," *Journal of Structural Engineering*, Vol. 114, No. 8, August, pp. 1804-1826.

Martin Marietta Materials, summer 2000, "Composites,"  
[http://www.martinmarietta.com/corpsite/about\\_mmm/technologies/  
tl\\_comp\\_technology.asp](http://www.martinmarietta.com/corpsite/about_mmm/technologies/tl_comp_technology.asp).

Mirmiran, Amir, 1998, "Length Effect on FRP-Reinforced Concrete Columns," *Proceedings of the Second International Conference on Composites in Infrastructure (ICCI'98)*, Tucson, Arizona, pp. 518-532.

Mirmiran, Amir and Shahawy, Mohsen, 1997, "Behaviour of Concrete Columns Confined by Fiber Composites," *Journal of Structural Engineering*, May, pp. 583-590.

Mirmiran, Amir and Shahawy, Mohsen, 2000, "Large Beam-column Tests on Concrete-filled Composite Tubes," *ACI Structural Journal*, Title No. 97-S29, Mar-Apr, pp 268-276.

Mirmiran, Amir; Shahawy, Mohsen; Samaan, M.; El Echary, H.; Mastrapa, J.C. and Pico, O., 1998, "Effect of Column Parameters on FRP-confined Concrete," *Journal of Composites for Construction*, November, pp. 175-185.

Okamoto, T. and Maeno, T., 1988, "Experimental Study on Rectangular Steel Tube Columns Infilled with Ultra High Strength Concrete Hardened by Centrifugal Force," *Annual Meeting of the AIJ, Proceedings*, Chiba, October, pp. 1359.

Owens Corning, summer 2000, "Composite Introduction,"  
<http://www.owenscorning.com/composites/about/introduction.asp>.

Owens Corning, winter 2004, "Composite Solutions,"  
[http://secure.owenscorning.net/cgi-bin/bvprd.dll/portal/homepage/customer.jsp?BV\\_SessionID=@@@@0270677736.1074988955@@@@&BV\\_EngineID=ccciadckhfegdjfcefecfegdgdgndfhg.0](http://secure.owenscorning.net/cgi-bin/bvprd.dll/portal/homepage/customer.jsp?BV_SessionID=@@@@0270677736.1074988955@@@@&BV_EngineID=ccciadckhfegdjfcefecfegdgdgndfhg.0).

Parent, S. and Labossiere Pierre, 1997, "Finite Element Analysis of Reinforced Concrete Columns Confined with Composite Materials," Paper, University of Sherbrooke.

Parvathaneni, H.K.; Iyer, S. and Greenwood, M., 1996, "Design and Construction of Test Mooring Pile Using Superprestressing," *Proceedings of Advanced Composite Materials in Bridges and Structures (ACMBS)*, Montreal, pp. 313-324.

Picher, F.; Rochette, P. and Labossiere, Pierre, 1996, "Confinement of Concrete Cylinders with CFRP," *Proceedings of the First International Conference on Composites in Infrastructure (ICCI'96)*, Tucson, Arizona, January, pp. 829-841.

Prion, Helmut G.L. and Boehme, J., 1994, "Beam-column Behaviour of Steel Tubes Filled With High Strength Concrete," *Canadian Journal of Civil Engineering*, Vol. 21, pp. 207-218.

Purba, B.K. and Mufti, A.A, 1998, "Reinforcement of Circular Concrete Columns with Carbon Fiber Reinforced Polymer (CFRP) Jackets," *Proc., Canadian Society of Civil Engineering Second Structural Specialty Conference*, Vol. 3b, June, pp. 561-569.

Rangan, B.V. and Joyce, M., 1992, "Strength of Eccentrically Loaded Slender Steel Tubular Columns Filled with High-strength Concrete," *ACI Structural Journal*, Vol. 89, No. 6, Nov-Dec, pp. 676-681.

Rochette, P., 1996, "Confinement of Short Square and Rectangular Columns with Composite Materials," MSc thesis, the University of Sherbrooke.

Saaman, M.; Mirmiran, Amir, and Shahawy, Mohsen, 1998, "Model of Concrete Confined by Fiber Composites," *Journal of Structural Engineering*, September, pp. 1025-1032.

Sakino, K.; Tomii, M. and Watanabe, K., 1985, "Sustaining Load Capacity of Plain Concrete Stub Columns by Circular Steel Tubes," *Proc., Int. Spec. Conf. On Concrete-filled Steel Tubular Struct.*, pp. 112-118.

Schneider, Stephen P., 1998, "Axially Loaded Concrete-filled Steel Tubes," *Journal of Structural Engineering*, October, pp. 1125-1138.

Scott, D.F., 1998, *Visual Basic for Applications 5 Bible*, IDG Books Worldwide Inc., Foster City, California, USA, 629 pp.

Seible, Frieder, 1996, "Advanced Composite Materials for Bridges in the 21<sup>st</sup> Century," *Proceedings of the First International Conference on Composites in Infrastructure (ICCI'96)*, Tucson, Arizona, January, pp. 17-30.

Shams, M. and Saadeghvaziri, M.A., 1997, "State of the Art of Concrete-filled Tubular Columns," *ACI Structural Journal*, Vol. 94, No. 5, Sept-Oct, pp. 558-571.

Spoelstra, Marijn R. and Monti, Giorgio, 1999, "FRP-confined Concrete Model," *Journal of Composites for Construction*, ASCE, August, pp. 143-150.

Stapleman, Jan, 1997, "Pile on the Abuse," *Composite Technology*, Sep-Oct.

Tomii, Masahide; Yoshimura, K. and Morishita, Y., 1977, "Experimental Studies on Concrete Filled Steel Tubular Stub Columns Under Concentric Loading," *Proc., Int. Colloquium on Stability of Struct. Under Static and Dyn. Load*, pp. 718-741.



Trival Kompoziti, winter 2004, "Trivavit Filament Wound Products,"

<http://www.trival-kompoziti.si/ang/winding.htm>

Williams, Brea K., 2000, "The Development of GFRP Bridge Deck Modules,"

MSc thesis, the University of Manitoba, 182 pp.